Copernicus Marine Service Ocean State Report, Issue 3

Karina von Schuckmann ((Editor)), Pierre-Yves Le Traon ((Editor)), Neville Smith (Chair) ((Review Editor)), Ananda Pascual ((Review Editor)), Samuel Djavidnia ((Review Editor)), Jean-Pierre Gattuso ((Review Editor)), Marilaure Grégoire ((Review Editor)), Glenn Nolan ((Review Editor)), Signe Aaboe, Eva Aguiar, Enrique Álvarez Fanjul, Aida Alvera-Azcárate, Lotfi Aouf, Rosa Barciela, Arno Behrens, Maria Belmonte Rivas, Sana Ben Ismail, Abderrahim Bentamy, Mireno Borgini, Vittorio E. Brando, Nathaniel Bensoussan, Anouk Blauw, Philippe Bryère, Bruno Buongiorno Nardelli, Ainhoa Caballero, Veli Çağlar Yumruktepe, Emma Cebrian, Jacopo Chiggiato, Emanuela Clementi, Lorenzo Corgnati, Marta de Alfonso, Álvaro de Pascual Collar, Julie Deshayes, Emanuele Di Lorenzo, Jean-Marie Dominici, Cécile Dupouy, Marie Drévillon, Vincent Echevin, Marieke Eleveld, Lisette Enserink, Marcos García Sotillo, Philippe Garnesson, Joaquim Garrabou, Gilles Garric, Florent Gasparin, Gerhard Gayer, Francis Gohin, Alessandro Grandi, Annalisa Griffa, Jérôme Gourrion, Stefan Hendricks, Céline Heuzé, Elisabeth Holland, Doroteaciro Iovino, Mélanie Juza, Diego Kurt Kersting, Silvija Kipson, Zafer Kizilkaya, Gerasimos Korres, Mariliis Kõuts, Priidik Lagemaa, Thomas Lavergne, Heloise Lavigne, Jean-Baptiste Ledoux, Jean-François Legeais, Patrick Lehodey, Cristina Linares, Ye Liu, Julien Mader, Ilja Maljutenko, Antoine Mangin, Ivan Manso-Narvarte, Carlo Mantovani, Stiig Markager, Evan Mason, Alexandre Mignot, Milena Menna, Maeva Monier, Baptiste Mourre, Malte Müller, Jacob Woge Nielsen, Giulio Notarstefano, Oscar Ocaña, Ananda Pascual, Bernardo Patti, Mark R. Payne, Marion Peirache, Silvia Pardo, Begoña Pérez Gómez, Andrea Pisano, Coralie Perruche, K. Andrew Peterson, Marie-Isabelle Pujol, Urmas Raudsepp, Michalis Ravdas, Roshin P. Raj, Richard Renshaw, Emma Reyes, Robert Ricker, Anna Rubio, Michela Sammartino, Rosalia Santoleri, Shubha Sathyendranath, Katrin Schroeder, Jun She, Stefania Sparnocchia, Joanna Staneva, Ad Stoffelen, Tanguy Szekely, Gavin H. Tilstone, Jonathan Tinker, Joaquín Tintoré, Benoît Tranchant, Rivo Uiboupin, Dimitry Van der Zande, Karina von Schuckmann, Richard Wood, Jacob Woge Nielsen, Mikel Zabala, Anna Zacharioudaki, Frédéric Zuberer & Hao Zuo

Julie Deshayes, Emanuele Di Lorenzo, Jean-Marie Dominici, Cécile Dupouy, Marie Drévillon, Vincent Echevin, Marieke Eleveld, Lisette Enserink, Marcos García Sotillo, Philippe Garnesson, Joaquim Garrabou, Gilles Garric, Florent Gasparin, Gerhard Gayer, Francis Gohin, Alessandro Grandi, Annalisa Griffa, Jérôme Gourrion, Stefan Hendricks, Céline Heuzé, Elisabeth Holland, Doroteaciro Iovino, Mélanie Juza, Diego Kurt Kersting, Silvija Kipson, Zafer Kizilkaya, Gerasimos Korres, Mariliis Kõuts, Priidik Lagemaa, Thomas Lavergne, Heloise Lavigne, Jean-Baptiste Ledoux, Jean-François Legeais, Patrick Lehodey, Cristina Linares, Ye Liu, Julien Mader, Ilja Maljutenko, Antoine Mangin, Ivan Manso-Narvarte, Carlo Mantovani, Stiig Markager, Evan Mason, Alexandre Mignot, Milena Menna, Maeva Monier, Baptiste Mourre, Malte Müller, Jacob Woge Nielsen, Giulio Notarstefano, Oscar Ocaña, Ananda Pascual, Bernardo Patti, Mark R. Payne, Marion Peirache, Silvia Pardo, Begoña Pérez Gómez, Andrea Pisano, Coralie Perruche, K. Andrew Peterson, Marie-Isabelle Pujol, Urmas Raudsepp, Michalis Ravdas, Roshin P. Raj, Richard Renshaw, Emma Reyes, Robert Ricker, Anna Rubio, Michela Sammartino, Rosalia Santoleri, Shubha Sathyendranath, Katrin Schroeder, Jun She, Stefania Sparnocchia, Joanna Staneva, Ad Stoffelen, Tanguy Szekely, Gavin H. Tilstone, Jonathan Tinker, Joaquín Tintoré, Benoît Tranchant, Rivo Uiboupin, Dimitry Van der Zande, Karina von Schuckmann, Richard Wood, Jacob Woge Nielsen, Mikel Zabala, Anna Zacharioudaki, Frédéric Zuberer & Hao Zuo (2019) Copernicus Marine Service Ocean State Report, Issue 3, Journal of Operational Oceanography, 12:sup1, S1-S123, DOI: 10.1080/1755876X.2019.1633075

To link to this article: https://doi.org/10.1080/1755876X.2019.1633075

Published online: 13 Sep 2019.

Submit your article to this journal ☐

Article views: 8822

View related articles ☐

View Crossmark data ☐

Citing articles: 2 View citing articles ☐

COPERNICUS MARINE SERVICE

OCEAN STATE REPORT

Issue 3, 2019

Journal of Operational Oceanography
Volume 12, Supplement 1

Journal of Operational Oceanography

Aims and scope

The *Journal of Operational Oceanography* will publish papers which examine the role of oceanography in contributing to the fields of:

- Numerical Weather Prediction
- Development of Climatologies
- Implications of Ocean Change
- Ocean and Climate Forecasting
- Ocean Observing Technologies
- Eutrophication
- Climate Assessment
- Shoreline Change
- Marine and Sea State Prediction
- Model Development and Validation
- Coastal Flooding
- Reducing Public Health Risks
- Short-Range Ocean Forecasting
- Forces on Structures
- Ocean Policy
- Protecting and Restoring Ecosystem health
- Controlling and Mitigating Natural Hazards
- Safe and Efficient Marine Operations

The *Journal of Operational Oceanography* will also publish papers which address the requirements of the:

- Global Ocean Observing System (GOOS)
- Global Climate Observing System (GCOS)
- Global Monitoring for Environment and Security (GMES)
- Global Earth Observing System of Systems (GEOSS)

The *Journal of Operational Oceanography* will also publish papers which address the needs of one or more of a wide range of end user communities including:

- Shipping
- Marine Energy
- Weather Services
- Fishing
- Port Management
- Wastewater Management
- Search and Rescue
- National Security
- Charting and Navigational Services
- Public Health
- Conservation
- Insurance and Re-insurance
- Recreation and tourism
- Marine Mineral Extraction
- Environmental Regulation
- Education
- Aquaculture
- Coastal Management

All submitted manuscripts are subject to initial appraisal by the Editor, and, if found suitable for further consideration, enter peer review by independent, anonymous expert referees. All peer review is single blind.

Authors are requested to submit manuscripts via the journal's online submission system following the Instructions for Authors.

Submitting to *Journal of Operational Oceanography*
For more information about the journal and guidance on how to submit, please see www.tandfonline.com/tjoo

Journal of Operational Oceanography

Subscription information
For information and subscription rates please see www.tandfonline.com/pricing/journal/tjoo

Informa UK Limited, trading as Taylor & Francis Group, has a flexible approach to subscriptions enabling us to match individual libraries' requirements. This journal is available via a traditional institutional subscription (either print with online access, or online only at a discount) or as part of our libraries, subject collections or archives. For more information on our sales packages please visit www.tandfonline.com/page/librarians

All current institutional subscriptions include online access for any number of concurrent users across a local area network to the currently available backfile and articles posted online ahead of publication. Subscriptions purchased at the personal rate are strictly for personal, non-commercial use only. The reselling of personal subscriptions is prohibited. Personal subscriptions must be purchased with a personal check or credit card. Proof of personal status may be requested.

Back issues: Taylor & Francis Group retains a two-year back issue stock of journals. Older volumes are held by our official stockists to whom all orders and enquiries should be addressed: Periodicals Service Company, 351 Fairview Ave., Suite 300, Hudson, New York 12534, USA. Tel: +1 518 537 4700; fax: +1 518 537 5899; email: psc@periodicals.com.

Ordering information: Please contact your local Customer Service Department to take out a subscription to the Journal: USA, Canada: Taylor & Francis, Inc., 530 Walnut Street, Suite 850, Philadelphia, PA 19106, USA. Tel: +1 800 354 1420; Fax: +1 215 207 0050. UK/Europe/Rest of World: T&F Customer Services, Informa UK Ltd, Sheepen Place, Colchester, Essex, CO3 3LP, United Kingdom. Tel: +44 (0) 20 7017 5544; Fax: +44 (0) 20 7017 5198; Email: subscriptions@tandf.co.uk.

Dollar rates apply to all subscribers outside Europe. Euro rates apply to all subscribers in Europe, except the UK where the pound sterling price applies. If you are unsure which rate applies to you please contact Customer Services in the UK. All subscriptions are payable in advance and all rates include postage. Journals are sent by air to the USA, Canada, Mexico, India, Japan and Australasia. Subscriptions are entered on an annual basis, i.e. January to December. Payment may be made by sterling check, dollar check, euro check, international money order, National Giro or credit cards (Amex, Visa and Mastercard).

Airfreight and mailing in the USA by agent named WN Shipping USA, 156-15 146th Avenue, 2nd Floor, Jamaica, NY 11434, USA.

Periodicals postage paid at Jamaica NY 11431.

US Postmaster: Send address changes to *Journal of Operational Oceanography*, WN Shipping USA, 156-15 146th Avenue, 2nd Floor, Jamaica, NY 11434, USA.

Subscription records are maintained at Taylor & Francis Group, 4 Park Square, Milton Park, Abingdon, OX14 4RN, United Kingdom.

Air Business Ltd is acting as our mailing agent.

All Taylor and Francis Group journals are printed on paper from renewable sources by accredited partners.

COPERNICUS MARINE SERVICE OCEAN STATE REPORT, ISSUE 3

Editors

Karina von Schuckmann   Pierre-Yves Le Traon

Review Editors

Neville Smith (Chair)   Ananda Pascual   Samuel Djavidnia

Jean-Pierre Gattuso   Marilaure Grégoire   Glenn Nolan

AUTHOR AFFILIATIONS (ALPHABETICAL BY NAME)

Signe Aaboe, MET, Tromso, Norway
Eva Aguiar, SOCIB, Illes Balears, Spain
Enrique Álvarez Fanjul, Puertos del Estado, Madrid, Spain
Aida Alvera-Azcárate, Université de Liège, Liege, Belgium
Lotfi Aouf, Météo-France, Toulouse, France
Rosa Barciela, Met Office, Exeter, United Kingdom
Arno Behrens, Helmholtz-Zentrum Geesthacht (HZG), Geesthacht, Germany
Maria Belmonte Rivas, KNMI, GA De Bilt, Netherlands
Sana Ben Ismail, INSTM, Tunis, Tunisia
Abderrahim Bentamy, IFREMER, Plouzané, France
Mireno Borgini, Consiglio Nazionale delle Ricerche, Istituto di Scienze Marine (CNR-ISMAR), Pozzuolo di Lerici (SP), Itlay
Vittorio E. Brando, Institute of Marine Sciences (ISMAR) – National Research Council (CNR), Rome, Italy
Nathaniel Bensoussan, Institute of Marine Sciences-CSIC, Barcelona, Spain
Anouk Blauw, Deltares, Delft, Netherlands
Philippe Bryère, Argans, Brest, France
Bruno Buongiorno Nardelli, Institute of Marine Sciences – CNR, Napoli, Italy
Ainhoa Caballero, AZTI, Pasaia – GIPUZKOA (Spain)
Veli Çağlar Yumruktepe, NERSC, Bergen, Norway
Emma Cebrian, Universitat de Girona, Girona, Spain
Jacopo Chiggiato, Consiglio Nazionale delle Ricerche, Istituto di Scienze Marine (CNR-ISMAR), Venezia, Italy
Emanuela Clementi, CMCC, Bologna, Italy
Lorenzo Corgnati, Institute of Marine Sciences – National Research Council ISMAR-CNR, La Spezia, Italy
Marta de Alfonso, Puertos del Estado, Madrid, Spain
Álvaro de Pascual Collar, Puertos del Estado, Madrid, Spain
Julie Deshayes, LOCEAN/CNRS, Paris, France
Emanuele Di Lorenzo, Georgia Institute of Technology, États-Unis, USA
Jean-Marie Dominici, Parc Naturel Régional de Corse, Galeria, France
Cécile Dupouy, MIO, IRD, Marseille, France
Marie Drévillon, Mercator Ocean International, Ramonvill St-Agne, France
Vincent Echevin, LOCEAN/IRD, PARIS, France
Marieke Eleveld, Deltares, Delft, Netherlands
Lisette Enserink, Rijkswaterstaat, Delft, Netherlands
Marcos García Sotillo, Puertos del Estado, Madrid, Spain
Philippe Garnesson, ACRI-ST, Sophia-Antipolis, France
Joaquim Garrabou, ICM/CSIC, Barcelona, Spain
Gilles Garric, Mercator Ocean, Ramonville Saint-Agne, France
Florent Gasparin, Mercator Ocean International, Ramonville Saint-Agne, France
Gerhard Gayer, Helmholtz-Zentrum Geesthacht (HZG), Geesthacht, Germany
Francis Gohin, IFREMER, Plouzané, France
Alessandro Grandi, CMCC, Bologna, Italy
Annalisa Griffa, CNR-ISMAR, La Spezia, Italy
Jérôme Gourrion, Oceanscope, Incheon, South Korea
Stefan Hendricks, Alfred-Wegener-Institut, Bremerhaven, Germany
Céline Heuzé, University of Gothenburg, Gothenburg, Sweden
Elisabeth Holland, University of South Pacific, Fiji, Australia
Doroteaciro Iovino, CMCC, Bologna, Italy
Mélanie Juza, SOCIB, Illes Balears, Spain
Diego Kurt Kersting, Freie Universität, Berlin, Germany
Silvija Kipson, PMF, Zagreb, Croatia
Zafer Kizilkaya, Mediterranean Conservation Society, Bornova/İzmir, Turkey
Gerasimos Korres, HCMR, Attica, Greece
Mariliis Kõuts, Marine Systems Institute at Tallinn University of Technology, Tallinn, Estonie
Priidik Lagemaa, Marine Systems Institute at Tallinn University of Technology, Tallinn, Estonia
Thomas Lavergne, MET, Tromso, Norway
Heloise Lavigne, RBINS, Brussels, Belgium
Jean-Baptiste Ledoux, ICM/CSIC, Barcelona, Spain
Jean-François Legeais, Collecte Localisation Satellite (CLS), Ramonville-Saint-Agne, France
Patrick Lehodey, Collecte Localisation Satellite (CLS), Ramonville-Saint-Agne, France
Cristina Linares, University of Barcelona, Barcelona, Spain
Ye Liu, Swedish Meteorological and Hydrological Institute, Norrköping, Sweden

(Continued from previous page)

Julien Mader, AZTI, Pasaia – GIPUZKOA (Spain)
Ilja Maljutenko, Marine Systems Institute at Tallinn University of Technology, Tallinn, Estonie
Antoine Mangin, ACRI-ST, Sophia-Antipolis, France
Ivan Manso-Narvarte, AZTI, Pasaia – GIPUZKOA (Spain)
Carlo Mantovani, CNR-ISMAR, La Spezia, Italy
Stiig Markager, Aarhus University, Roskilde, Denmark
Evan Mason, IMEDEA (CSIC-UIB), Illes Balears, Spain
Alexandre Mignot, Mercator Ocean International, Ramonville Saint-Agne, France
Milena Menna, Istituto Nazionale di Oceanografia e di Geofisica Sperimentale (OGS), Sgonico (TS), Italy
Maeva Monier, CELAD/Mercator Ocean International, Ramonville St-Agne, France
Baptiste Mourre, SOCIB, Illes Balears, Spain
Malte Müller, MET, Tromso, Norway
Jacob Woge Nielsen, Danish Meteorlogical Institute, Copenhagen, Denmark
Giulio Notarstefano, Istituto Nazionale di Oceanografia e di Geofisica Sperimentale (OGS), Sgonico (TS), Italy
Oscar Ocaña, Fundación Museo del Mar de Ceuta, Ceuta, Spain
Ananda Pascual, IMEDEA (CSIC-UIB), Illes Balears, Spain
Bernardo Patti, CNR-IAS, Campobello di Mazara, Italy
Mark R. Payne, Technical University of Denmark (DTU-Aqua), Denmark
Marion Peirache, Parc National de Port-Cros, Hyeres cedex, France
Silvia Pardo, PML, UK
Begoña Pérez Gómez, Puertos del Estado, Madrid, Spain
Andrea Pisano, CNR-ISMAR, Roma, Italy
Coralie Perruche, Mercator Ocean International, Ramonville Saint-Agne, France
K. Andrew Peterson, ECCC, Québec, Canada
Marie-Isabelle Pujol, Collecte Localisation Satellites (CLS), Ramonville St-Agne, France
Urmas Raudsepp, Marine Systems Institute at Tallinn University of Technology, Tallinn, Estonie
Michalis Ravdas, HCMR, Attica, Greece
Roshin P. Raj, Nansen Environmental and Remote Sensing Center, Bergen, Norway
Richard Renshaw, Met Office, Exeter, United Kingdom
Emma Reyes, SOCIB, Palma, Spain
Robert Ricker, Alfred-Wegener-Institut, Bremerhaven, Germany
Anna Rubio, AZTI, Pasaia – GIPUZKOA (Spain)
Michela Sammartino, CNR-ISMAR, Rome, Italy
Rosalia Santoleri, CNR-ISMAR, Rome, Italy
Shubha Sathyendranath, PML, United Kingdom
Katrin Schroeder, CNR-ISMAR, Venezia, Italy
Jun She, Danish Meteorological Institute (DMI), Copenhagen, Denmark
Stefania Sparnocchia, CNR-ISMAR, Trieste, Italy
Joanna Staneva, Helmholtz-Zentrum Geesthacht (HZG), Geesthacht, Germany
Ad Stoffelen, KNMI, GA De Bilt, Netherlands
Tanguy Szekely, Oceanscope, Incheon, South Korea
Gavin H. Tilstone, Plymouth Marine Laboratory, Plymouth, UK
Jonathan Tinker, Met Office, Exeter, United Kingdom
Joaquín Tintoré, SOCIB/IMEDEA (CSIC-UIB), Balears, Spain
Benoît Tranchant, Collecte Localisation Satellites (CLS), Ramonville St-Agne, France
Rivo Uiboupin, TalTech, Tallinn, Estonia
Dimitry Van der Zande, RBINS, Brussels, Belgium
Karina von Schuckmann, Mercator Ocean International, Ramonville St-Agne, France
Richard Wood, Met Office, Exeter, United Kingdom
Jacob Woge Nielsen, Danish Meteorlogical Institute, Copenhagen, Denmark
Mikel Zabala, UB/IRBIO, Barcelona, Spain
Anna Zacharioudaki, HCMR, Attica, Greece
Frédéric Zuberer, OSU PYTHEAS, Cedex, France
Hao Zuo, ECMWF, United Kingdom

Journal of Operational Oceanography

CONTENTS

Taylor & Francis
Taylor & Francis Group

�osOPEN ACCESS   Check for updates

Copernicus Marine Service Ocean State Report, Issue 3

Chapter 1: Introduction

The fundamental role of the ocean for life and well-being on Earth is more and more recognised at the highest political level. In 2015, the United Nations (UN) Sustainable Development Goals (SDGs) of the 2030 Agenda for Sustainable Development were adopted by world leaders. The SDG 14 'Conserve and sustainably use the oceans, seas and marine resources for sustainable development' is dedicated to the oceans. The mention of the ocean in the Paris Agreement signed in 2016 marked a decisive milestone. In 2018, the UN Decade of Ocean Science for Sustainable Development (2021–2030) has been proclaimed (https://en.unesco.org/ocean-decade): The Intergovernmental Oceanographic Commission of UNESCO will gather ocean stakeholders worldwide behind a common framework to foster evidence-based policy-making. In fall 2019, the IPCC special report on ocean and cryosphere will be published, and will provide an opportunity to increase awareness and action before COP25[1] (already claimed as 'Blue COP').

This unprecedented ocean agenda is a timely one: multiple anthropogenic stressors such as climate change, over-exploitation and pollution are becoming a major threat on the marine environment and its services for human benefits and biodiversity at large. The annual Ocean State Report of the European Union's Copernicus Marine Service contributes to this unrivalled mobilisation of the global scientific community, and is one of the priority tasks given by the EU Delegation Agreement for CMEMS implementation (CMEMS 2014). Ocean observing, monitoring and forecasting are key to unravel the ocean's responses to pressures, understand and predict the evolution of the oceans and develop management actions for sustainable development, including for mitigation and adaptation to climate change.

Since its launch in 2016 with the publication of the first issue (von Schuckmann et al. 2016a), a fundamental baseline of regular science-based ocean reporting has been established. It covers the blue ocean (i.e. physical processes driven by changes in temperature, salinity and currents), the green ocean (i.e. biogeochemical processes such as fluctuations of ocean chlorophyll identifying changes at the base of the marine food chain,

eutrophication processes, the uptake of carbon by the ocean, and ocean deoxygenation), and the white ocean (i.e. the rapid evolution of ice-covered polar regions). The evaluations in the Copernicus Marine Ocean State Report span local scales (e.g. extreme variability of sea level, sea surface temperature and significant wave height at the coast), the European regional seas (e.g. monitoring of key essential variables and interpretation of variations and trends), large scale (e.g. analysis of the unusual cold and fresh conditions or the Meridional Overturning Circulation in the North Atlantic), to global scale (e.g. delivering an Earth system view on the uptake of heat and carbon by the ocean). The assessments cover climate-relevant time scales (e.g. ocean deoxygenation since the 1960s), multi-decadal time scales (e.g. global mean sea level rise over the past three decades), and the evaluation of specific events taking place in the marine environment close to real time (e.g. extreme sea ice conditions in the Arctic ocean in 2016, or the polynya event in the Weddell Sea during 2017).

The scientific assessments developed in the Copernicus Marine Ocean State Report are based on a wide range of reprocessed in-situ and satellite observation data products and ocean reanalysis model products in seven ocean regions (Figure 1.1). A large fraction of these products are distributed via the Copernicus Marine Service web portal (http://marine.copernicus.eu/). In addition, products from the Copernicus Climate Change Service are used, in particular for climate-related studies such as sea level rise (i.e. a Global Climate Indicator as identified by WMO/GCOS, https://gcos.wmo.int/en/global-climate-indicators). Additional data products have been included in the Ocean State Report analyses aiming to strengthen the scope of the report, e.g. to take an Earth system perspective (i.e. the role of the ocean heat uptake in the Earth energy budget), to further investigate exchanges and processes with other components of the Earth system (e.g. air-sea exchanges), or to complement the analyses with biological data for impact studies on the marine ecosystem. All products used in each section are listed in a specific product table, which includes data source information and
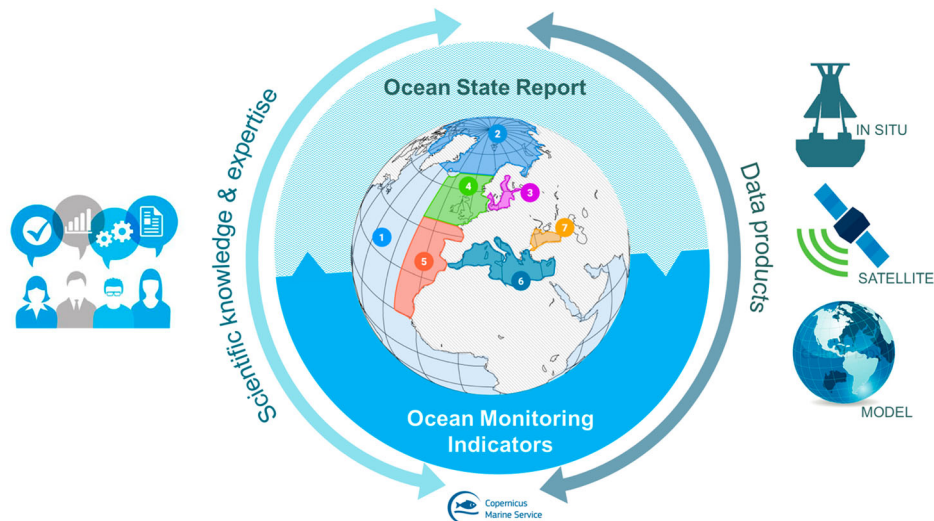
Figure 1.1. Schematic overview on the Copernicus Marine Ocean State Report and Ocean Monitoring Indicator activities, which are both linked to each other, and cover seven principal regions. The interplay of scientific knowledge and expertise, as well as the data products (*in situ*, satellite, model) from Copernicus services and other sources is the key ingredient for the Copernicus Marine scientific evaluation and reporting. See text for more details. Regions include: 1 – Global Ocean; 2 – Arctic Ocean from 62°N to the North Pole; 3 – Baltic Sea, including Kattegat at 57.5°N from 10.5°E to 12.0°E; 4 – European North West Shelf Sea, which includes part of the North East Atlantic Ocean from 48°N to 62°N and from 20°W to 13°E. The border with the Baltic Sea is situated in the Kattegat Strait at 57.5°N from 10.5°E to 12.0°E; 5 – Iberia-Biscay-Ireland Regional Seas, which includes part of the North East Atlantic Ocean from 26°N to 48°N and 20°W to the coast. The border with the Mediterranean Sea is situated in the Gibraltar Strait at 5.61°W; 6 – Mediterranean Sea until the Gibraltar Strait at 5.61°W and the Dardanelles Strait; 7 – Black Sea until the Bosporus Strait.

documentations (product manuals, quality assessment documents, and scientific publications).

The major objective of the Copernicus Marine Ocean State Report activity is to provide scientifically assessed added-value information, for a wide range of topical domains in the marine environment and at different space and time scales. Expert collaboration is indispensable to achieve this goal. Since the launch of this activity, more than 150 European scientific experts from more than 25 European institutions have joined forces to develop the Copernicus Marine Ocean State Report and the number of new collaborators is steadily increasing with the evolution of the reporting activity. This activity is a breeding ground for new and innovative science activities across multidisciplinary expertise (e.g. joint analysis on physical and biogeochemical topics), space scales (e.g. between different European basins), and time scales (e.g. interplay of climate change and natural variability).

The Ocean State Report content is designated to a specific audience, including scientists, expert stakeholders and European and International environmental agencies and organisations (e.g. EEA, WMO, IPCC, …). In order to enlarge the audience, two supplement tools have been established by the Copernicus Marine Service. The first tool is the preparation of a summary for each issue of the Ocean State Report in collaboration with communication and graphical experts, highlighting and synthetising key outcomes of the scientific

publication. This summary is aiming to reach out to policy and decision-makers, as well as to increase general public awareness about the status of, and changes in, the marine environment. These documents are freely available at the Copernicus Marine web portal (http://marine.copernicus.eu/science-learning/ocean-state-report/).

The second tool includes the dissemination of numerical values, quality and background documentation and figures of key variables used to track the vital health signs of the ocean and changes in line with climate change and natural variability. All elements (data, documentation, figures) are regularly updated, and build the Copernicus Marine Ocean Monitoring Indicator framework (http://marine.copernicus.eu/science-learning/ocean-monitoring-indicators/). For example, close-to-real-time knowledge of how much heat is stored in the ocean, the pH of the ocean, how fast sea level is rising and sea ice is melting, is essential to understanding the current state and changes in the ocean and climate. This information is critical for assessing and confronting ocean and climate changes associated with global warming and they can be used by scientists, decision-makers, environmental agencies, economy, the general public, and in measuring our responses to environmental directives. The Ocean Monitoring Indicators were developed through a long process of scientific analysis and validation, with the consensus

of scientific experts after review as part of the Ocean State Report. The online publication of an Ocean Monitoring Indicator generally requires that the scientific rationale, validation and interpretation went through the Ocean State Report peer review.

A general rule is that a scientific topic already addressed in one of the issues of the Ocean State Report should not be repeated in upcoming new issues. However, in order to maintain a comprehensive review on the variations and changes in the blue, green and white ocean as part of the Ocean State Report, the Ocean Monitoring Indicator framework is indispensable. From the third issue of the Ocean State Report onwards, two synthesis figures based on the Ocean Monitoring Indicator information, as well as on scientific evaluations in the corresponding issue will be included in Chapter 1 (i.e. the introduction). One figure will summarise the long-term changes reported over the past decades (Figure 1.2), and the second figure is dedicated to deliver an overview of the anomalies close to real time for the European regional seas and the global ocean (Figure 1.3).

What else is new in the third issue of the Copernicus Marine Ocean State Report? Beside the new strategy for Chapter 1 as described above, a large number of new topics have been gathered in this new issue. In Chapter 2 – which addresses the state, variability and change in the marine environment – topics such as sea wind, coastal and regional current systems, phytoplankton blooms, hydrographic pressure on cod stocks and extreme variability have been analysed. Chapter 3 discusses selected case studies that analyse specific aspects of the ocean change that are of scientific and more general interest. For example, this issue proposes a marine atlas for the Pacific Ocean Island states, which responds directly to Fiji's requests at the 2017 United Nation Oceans for SDG 14, life below water and the 2017 COP23 for SDG13, climate action. A review on the use of ocean data in European fishery management is developed in this issue as well. Other specific studies include for example a joint analysis between Copernicus Marine and Marine Protected Areas (e.g. t-mednet.org) to analyse the impact of thermal stress on marine biodiversity, and reported environmental changes and their impact on aquaculture. Chapter 4 reports on specific events during the year 2017, including for example the Weddell Sea polynya, marine heat waves and the 2017 coastal El Niño.

1.1. Trends over the past decades

Continuous reporting of trends contribute to the understanding of observed changes in the marine environment around the world, and improves knowledge of the likely responses to climate change affecting social,

environmental and economic systems, i.e. the three pillars of sustainable development. As also reported in the second issue of the Ocean State Report, the results of the third issue show ocean surface and subsurface warming, rising total and thermosteric sea level and a decrease in global sea ice extent over the past 25 years (Figure 1.2). Ocean deoxygenation is shown to take place over the past decades. Decreasing and increasing regional trends since the year 2007 are reported for chlorophyll-a. These changes can be observed not only at global scale, but also in the seven European regional seas. The following changes are highlighted:

- The ocean surface continues to warm, and sea surface temperature trends for the European regional seas range from 0.03 to 0.07°C year^{-1} at 0.002–0.005°C year^{-1} uncertainty ranges. Sea surface temperature trends have also been evaluated as part of the Copernicus Marine Atlas for Pacific Islands (Section 3.1), as sea surface temperature is a much-needed variable for assessing coral reef health and bleaching, as well as for tropical cyclone forecasting. While the ocean surface is warming in the Western and Central Pacific Islands areas, we note a strong variability over various time scales, such as for example the El Niño Southern Oscillation.

- The subsurface ocean continues to warm (von Schuckmann et al. 2016b, 2018). Global ocean heat content of the upper 700 m increases currently at a rate of 0.9 ± 0.1 Wm^{-2} as obtained over the period 1993–2017 (Figure 1.2). Over the shorter time window 2005–2017 during which Argo provides the best available coverage of the global ocean observing system (e.g. Riser et al. 2016), this rate of change is smaller (0.6 ± 0.1 Wm^{-2}), and needs correction for short-term climate variability (Cazenave et al. 2014). Increasing the integration depth to 2000 m yields a rate of change of ocean heat content of 1.2 ± 0.1 Wm^{-2} due to the excess heat sequestered into the deeper layers of the oceans (e.g. Meehl et al. 2011; Abraham et al. 2013). By adding a contribution of 0.1 Wm^{-2} for the deep ocean below 2000 m depth (Purkey and Johnson 2010; Desbruyères et al. 2016), we obtain an estimate of the Earth energy imbalance of $0.5–0.7 \pm 0.1$ Wm^{-2} based on the CMEMS reporting (1993–2017, 0–700 m: 0.7 Wm^{-2}; 2005–2017, 0–700 m: 0.5 Wm^{-2}; 0–2000 m: 0.7 Wm^{-2}, taking into account that the heat content is related to the ocean surface only i.e. multiplied by 0.7). At regional scales, subsurface ocean warming in the upper 700 m depth increases at rates close to the global value in the Mediterranean Sea and the Central Pacific Islands area, and doubles for the Western Pacific Islands area (Figure 1.2).

Copernicus Marine Service

TREND VALUES

THERMOSTERIC SEA LEVEL ⬆ *Units: mm year⁻¹*

GLOBAL (0-700M) **+1.4** ±0.1

GLOBAL (0-2000M) **+1.2** ±0.1

GLOBAL (0-700M) **+0.9** ±0.1

Trend from 1993 to 2017   *Trend from 2005 to 2017*

SEA SURFACE TEMPERATURE ⬆

Units: °C year⁻¹ - Trend from 1993 to 2017

Mediterranean Sea	Baltic Sea	Black Sea
+0.04 ±0.002	+0.03 ±0.003	+0.07 ±0.005

Western Pacific Islands	Central Pacific Islands	Pacific Islands total area
+0.02 ±0.01	+0.01 ±0.02	+0.02 ±0.01

SEA LEVEL ⬆

Units: mm year⁻¹
Trend from 1993 to 2017

GLOBAL **+3.2** ±0.4

Mediterranean Sea	Black Sea	Baltic Sea	North West Shelf
+2.4 ±2.2	+1.9 ±2.2	+4.3 ±2.2	+2.7 ±2.0

Iberian Biscay Irish	Western Pacific Islands	Central Pacific Islands	Pacific Islands total area
+3.4 ±2.0	+4.8 ±2.5	+2.8 ±2.5	+3.5 ±2.5

CHLOROPHYLL-a ⬆

Units: % year⁻¹ - Trend from 1997 to 2017

GLOBAL **+0.63** ±0.01

Western Pacific Islands	Central Pacific Islands	Pacific Islands total area	Mediterranean Sea
-0.4 ±0.02	-0.7 ±0.001	-0.4 ±0.001	+0.5 ±0.002

Black Sea	Baltic Sea	North Atlantic Ocean	Arctic Ocean
-0.7 ±0.01	+2.5 ±0.01	+1.1 ±0.01	+1.72 ±0.01

OXYGEN INVENTORY ⬇

Units: mol m⁻² year⁻¹
Trend from 1955 to 2017

Black Sea
-0.15 ±0.02

OCEAN HEAT CONTENT ⬆ *Units: Watts m⁻²*

GLOBAL (0-700M) **+0.9** ±0.1

GLOBAL (0-2000M) **+0.9** ±0.1

GLOBAL (0-700M) **+0.6** ±0.1

Trend from 1993 to 2017   *Trend from 2005 to 2017*

Trend from 1993 to 2017 - 0-700m

Mediterranean Sea	Western Pacific Islands	Central Pacific Islands	Pacific Islands total area
+0.8 ±0.1	+1.9 ±1.5	+0.8 ±0.7	+1.2 ±0.7

SEA ICE EXTENT

Units: km² decade⁻¹ (% decade⁻¹)
Trend from 1993-2017

Nothern Hemisphere ⬇
-0.77·10⁶ ±0.06·10⁶
(-5.89 ±0.47)

Southern Hemisphere ⬆
+0.07·10⁶ ±0.12·10⁶
(+0.57 ±0.94)

Figure 1.2. Overview on trend values reported in the third issue of the CMEMS Ocean State Report, and in the CMEMS Ocean Monitoring Indicator framework (http://marine.copernicus.eu/science-learning/ocean-monitoring-indicators/). Upward arrow indicates increasing trends, downward arrow decreasing trends. Time intervals for trend evaluation are indicated for each parameter, respectively.
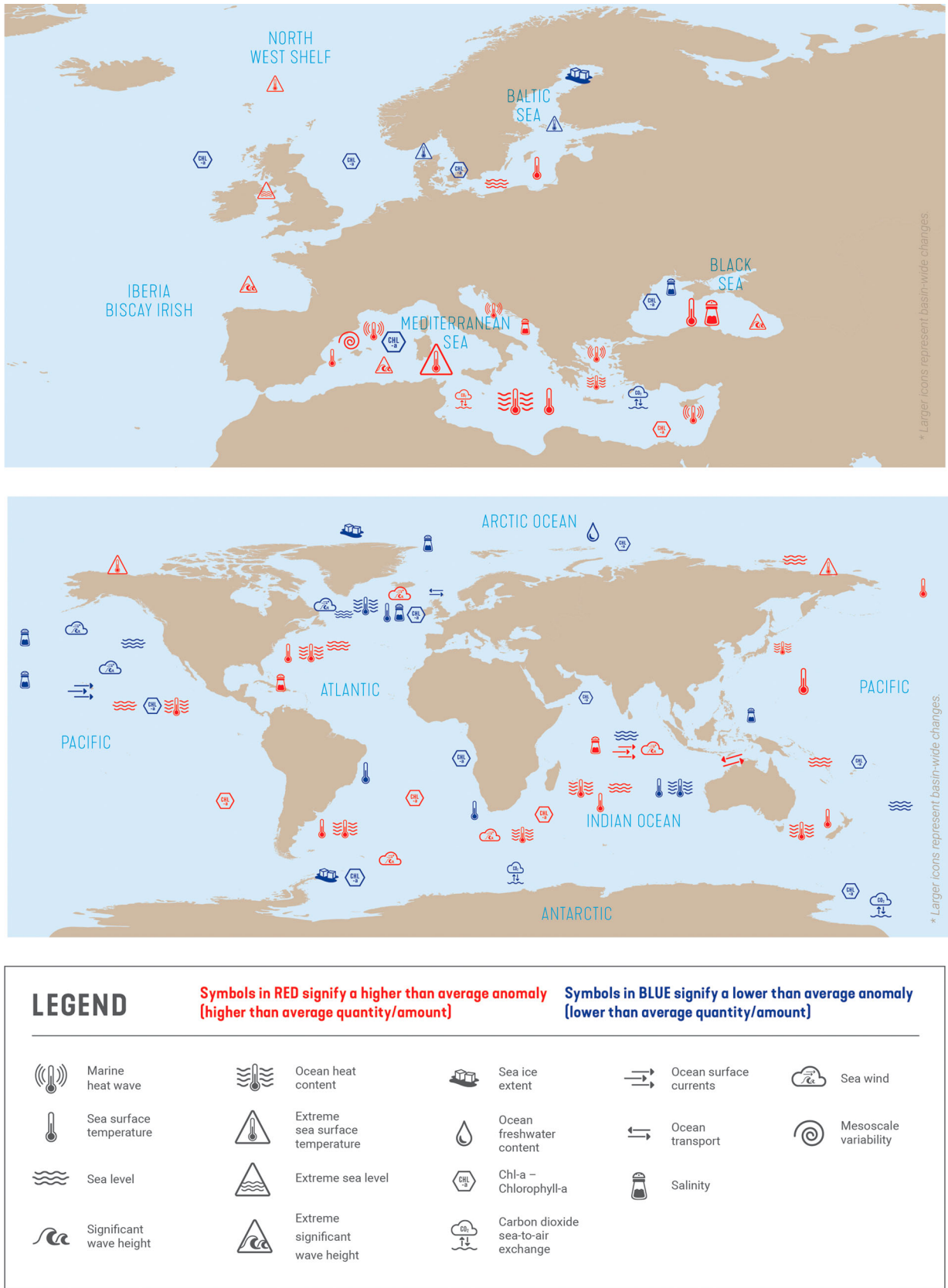
Figure 1.3. Anomalies and extreme events during the year 2017 as reported in the third issue of the CMEMS Ocean State Report and from the Copernicus Marine Ocean Monitoring Indicator framework (see text for more details) for the global ocean (upper panel), and the European regional seas (lower panel). A legend for all icons is included. Red coloured icons signify higher-than-average anomalies and extremes, and blue coloured icon show lower-than-average values.

- Global sea level continues to rise at a rate of 3.2 ± 0.4 mm year^{-1} (Figure 1.2). As the ocean warms, its volume expands (thermosteric effect), which is a major cause of global mean sea level rise. The upper ocean (0–700 m) thermosteric sea level has been rising since 1993 at a rate of 1.4 ± 0.1 mm year^{-1}. Sea level rises also in all European regional seas at rates that even exceed the global mean rate (e.g. the Baltic Sea). Sea level has been also included in the Copernicus Marine Atlas for the Pacific Islands areas as it is a key ocean variable to better inform climate adaptation and coastal planning. Sea level in these areas is rising as well and a strong rate of 4.8 ± 2.5 mm year^{-1} can be noticed in the western part (Chapter 3).
- Since 1993, there has been a sea ice extent loss of nearly 770,000 km^2 decade^{-1} in the northern hemisphere, and a sea ice extent gain of 80,000 km^2 decade^{-1} in the southern hemisphere (Figure 1.2).
- Chlorophyll-a, the main photosynthetic pigment contained in all phytoplankton, has shown increasing and decreasing trends over the past 19 years (1998–2017). At global scale, chlorophyll-a has been increasing by $0.6 \pm 0.01\%$ year^{-1} (Figure 1.2). Increasing trends are also reported in the Mediterranean Sea, Baltic Sea, North Atlantic and Arctic Ocean. Decreasing trends occur in the Black Sea, as well as in the areas of the Pacific Islands. However, given that the chlorophyll-a time series from remote sensing used here is only 19 years long characterised by large signals of decadal variability, the time series are too short to disentangle the effect of interannual variability and longer-term climate change.
- There is an ongoing deoxygenation trend reported in the Black Sea, with a decrease at a rate of -0.16 ± 0.02 mol m^{-2} year^{-1} (Figure 1.2).

1.2. Anomalies and extreme events

Anomalies and extreme events observed in 2017 are summarised in Figure 1.3. The results have been drawn from the third issue of the CMEMS OSR, as well as from the CMEMS OMIs. Chapters 2, 3 and 4 contain reported anomalous changes in the marine environment during the year 2017. Some specific events have been highlighted and described in Chapter 4. The anomalous changes are summarised in Figure 1.3, which include:

- The northern parts of the European regional seas (e.g. the Baltic Sea, the North West Shelf Sea) have been characterised by lower-than-average sea ice extent and chlorophyll-a values respectively during 2017. Moreover, extreme cold temperature conditions have been reported in these areas, together with higher-than-average ocean temperature and sea level in the Baltic Sea.
- The southern parts of the European regional seas have undergone significant changes during the year 2017: the Mediterranean Sea has been impacted by strong heat wave events during boreal summer in the eastern and western basins (Section 4.4), several events of extreme variability in the western basin, and higher-than-average ocean surface and subsurface water temperature. Chlorophyll-a values have been larger than previous years. Air-to-sea carbon fluxes show higher-than-average values in this area. Higher-than-average significant wave height, surface water temperature and salinity have been reported in the Black Sea.
- The Arctic Ocean has experienced lower-than-average sea ice extent and ocean freshwater content during the year 2017. In addition, extreme sea surface temperature anomalies of values up to +6°C have been reported, for example in the East Siberian Sea and the Beaufort Sea (Section 2.6).
- In the Antarctic region, a large hole in the winter sea ice cover (polynya) appeared in the Weddell Sea and stayed open for almost three months (Section 4.1). This was the first occurrence of such an event since 1976. Additionally, the Antarctic ocean area has showed lower-than-average air-to-sea carbon flux. Chlorophyll-a concentration was below its average value.
- At global scale, surface and subsurface temperature and sea level are particularly high in several areas such as the southwestern Indian Ocean, eastern tropical Pacific, subtropical and southwestern Atlantic and southeast of Australia. Anomalous cold and fresh conditions together with low sea level have prevailed in the subpolar North Atlantic, the western tropical and north Pacific, and in the northeastern Indian Ocean. Higher-than-average chlorophyll-a is reported in the southeastern Pacific and in the Indian Ocean south of Madagascar, while chlorophyll-a was anomalously low in the northwestern Indian Ocean, and in the eastern tropical Atlantic and Pacific. The tropical Pacific was in neutral El Niño Southern Oscillation conditions in 2017. However, coastal El Niño conditions have been reported along the coast of Peru and Ecuador at the beginning of the year.

Note

1. *25th meeting of the Conference of the Parties to the United Nations Framework Convention on Climate Change.*

References

Abraham JP, Baringer M, Bindoff NL, Boyer T, Cheng LJ, Church JA, Conroy JL, Domingues CM, Fasullo JT, Gilson J, et al. 2013. Monitoring systems of global ocean heat content and the implications for climate change, a review. Rev Geophys. 51:450–483. doi:10.1002/rog.20022.

Cazenave A, Dieng H-B, Meyssignac B, von Schuckmann K, Decharme B, Berthier E. 2014. The rate of sea level rise. Nat Geosci. 4(5). doi:10.1038/NCLIMATE2159.

CMEMS. 2014. Technical annex to the delegation agreement with Mercator Ocean for the implementation of the Copernicus Marine Environment Monitoring Service (CMEMS). http://www.copernicus.eu/sites/default/files/library/CMEM_TechnicalAnnex_PUBLIC.docx.pdf.

Desbruyères DG, Purkey SG, McDonagh EL, Johnson GC, King BA. 2016. Deep and abyssal ocean warming from 35 years of repeat hydrography. Geophys Res Lett. 43:10356–10365. doi:10.1002/2016GL070413.

Meehl GA, Arblaster JM, Fasullo JT, Hu A, Trenberth KE. 2011. Model-based evidence of deep-ocean heat uptake during surface-temperature hiatus periods. Nat Clim Chang. 1:360–364.

Purkey SG, Johnson GC. 2010. Warming of global abyssal and deep southern ocean waters between the 1990s and 2000s: contributions to global heat and sea level rise budgets. J Clim. 23:6336–6351. doi:10.1175/2010JCLI3682.1.

Riser SC, Freeland HJ, Roemmich D, Wijffels S, Troisi A, Belbéoch M, Gilbert D, Xu J, Pouliquen S, Thresher A, et al. 2016. Fifteen years of ocean observations with the global Argo array. Nature Clim Change. 6(2):145–153. doi:10.1038/nclimate2872.

von Schuckmann K, Le Traon P, Alvarez-Fanjul E, Axell L, Balmaseda M, Breivik L-A, Brewin RJW, Bricaud C, Drevillon M, Drillet Y, et al. 2016a. The Copernicus marine service ocean state report issue 1. J Oper Oceanogr. 9. doi:10.1080/1755876X.2016.1273446.

von Schuckmann K, Cazenave A, Chambers D, Hansen J, Josey S, Kosaka Y, Loeb N, Mathieu P-P, Meyssignac B, Palmer M, et al. 2016b. An imperative to monitor Earth's energy imbalance. Nat Clim Chang. 6:138–144. doi:10.1038/nclimate2876.

von Schuckmann K, Storto A, Simoncelli S, Raj RP, Samuelsen A, de Pascual Collar A, Garcia Sotillo M, Szerkely T, Mayer M, Peterson KA, et al. 2018. Ocean heat content, in CMEMS ocean state report 2. J Oper Oceanogr. 11(sup1):S1–S142. doi:10.1080/1755876X.2018.1489208.

Chapter 2: State, variability and change in the marine environment: new monitoring indicators

2.1. Sea surface winds and Ekman pumping

Authors: Maria Belmonte Rivas, Ad Stoffelen, Abderrahim Bentamy

Statement of main outcome: Sea surface wind stress and Ekman transport changes are assessed that imply changes in both large-scale and smaller-scale ocean forcing. During 2017 a transition from gradually warming El Niño Southern Oscillation conditions to non-El-Niño-Southern-Oscillation conditions in the tropical Pacific is observed. The North Atlantic is influenced by sustained high North Atlantic Oscillation conditions, with higher-than-average Azores High and south-easterly wind anomalies in the Labrador Sea. We note sustained high westerlies in the Southern Ocean, and increased south-easterly trades in the South Indian Ocean, with enhanced wind convergence off Sumatra. Trends and anomalies in Ekman pumping (ocean circulation forcing) are consistent with the respective trends and anomalies observed in the wind. Inter-annual variability is dominated by changes in mean large-scale conditions, rather than changes in transient smaller-scale wind activity, without any substantial trends in globally averaged annual mean or transient winds. Regional trends and anomalies in wind variability are generally of opposite sign to those in the mean wind, as they feed on the mean flow and counterbalance it. These wind stress changes imply changes in both large-scale and smaller-scale ocean forcing.

Products used

Ref. No.	Product name and type	Documentation
2.1.1	Product: WIND_GLO_WIND_L3_REP_ OBSERVATIONS_012_005/ Dataset (reprocessed ASCAT-A 25 km Ascending): KNMI-GLO-WIND_L3-REP-OBS_METOP-A_ASCAT_25_ASC Remote sensing	PUM: http://marine. copernicus.eu/ documents/PUM/ CMEMS-WIND-PUM-012-002-005.pdf QUID: http://marine. copernicus.eu/ documents/QUID/ CMEMS-WIND-QUID-012-002-003-005.pdf

Winds blowing over the ocean induce sheared flows and waves that generate ocean turbulence. This turbulence transfers the momentum imparted by the winds down into the ocean and transports heat and constituents. In addition, ocean winds evaporate water and thus affect heat and mass fluxes and ocean salinity. Changing winds and associated air–sea interaction, currents and waves strongly affect the ocean state, both on global and local scales. Monitoring changes in ocean winds and stress on all spatial scales is therefore crucial to understand how changes in the ocean state (waves, currents, sea surface temperature, sea surface salinity, chlorophyll) are related to its atmospheric forcing. More in particular, Earth rotation causes the wind to generate the so-called Ekman ocean transport, which vertical component (pumping/suction) forces the Antarctic Circumpolar Current and ocean gyres through the wind stress curl.

In climate modelling and ocean applications ocean forcing is provided by atmospheric general circulation models. Although these models often use scatterometer observations as input, unresolved or poorly determined processes, such as wind dynamics or structure related to moist convection, the stable surface layer and atmospheric drag, cause both mean and variable errors in ocean wind forcing. Given the importance of model winds for this report on the ocean state, an assessment of the errors in atmospheric general circulation models forcing is provided with respect to the scatterometer observations.

Global monitoring of ocean mean winds, stress, its local variability and the associated Ekman pumping is introduced in this section. We provide a summary view of the current conditions and recent evolution in global sea surface winds from observational scatterometer data, highlighting major large-scale events in the context of climatology and trends, and exposing potential connections with the other ocean variables (such as waves, currents, sea surface temperature, sea surface salinity, chlorophyll) and global climate indicators (such as El Niño Southern Oscillation, North Atlantic Oscillation, Pacific Decadal Oscillation, Indian Ocean Dipole index, monsoons or tropical convection).

An approach to describing mean and variability of sea surface winds consists of resolving the field of motion into a time-mean component (called mean or steady wind, $<u>$) and a time-variable component (called transient eddy wind, u') superposed upon it (Lorenz 1955) as:

$$u(t) = \langle u \rangle + u_s(t) + u'(t)$$

$$v(t) = \langle v \rangle + v_s(t) + v'(t)$$

where $u_s(t)$ is a seasonally dependent quantity representing the departure of the monthly mean from the annual mean wind, satisfying $<u_s(t)> = 0$. The total wind kinetic energy is partitioned in mean, seasonal and transient eddy components as:

$$\mathrm{TKE} = \frac{1}{2} \langle u^2 + v^2 \rangle = \mathrm{MKE} + \mathrm{SKE} + \mathrm{TEKE}$$

$$\text{MKE} = \frac{1}{2}(\langle u \rangle^2 + \langle v \rangle^2)$$

$$\text{SKE} = \frac{1}{2}(\langle u_s^2 \rangle + \langle v_s^2 \rangle)$$

$$\text{TEKE} = \frac{1}{2}(\langle u'^2 \rangle + \langle v'^2 \rangle)$$

In this section, the mean wind climatology is determined from the annual mean zonal and meridional wind components as

$$u_{\text{mean}} = \langle u \rangle$$

$$v_{\text{mean}} = \langle v \rangle$$

And the transient eddy wind climatology is determined as the square root of the annual mean variance of the zonal and meridional wind components around monthly means as

$$u_{\text{eddy}} = \sqrt{\langle u'^2 \rangle}$$

$$v_{\text{eddy}} = \sqrt{\langle v'^2 \rangle}$$

Accordingly, we show how the total wind kinetic energy is partitioned in mean and transient eddy components, since both affect ocean circulation and its gyres, the former through large-scale Ekman transport and upwelling/downwelling, the latter through vertical mixing via ocean eddies, surface and internal wave motions, etc. (Large et al. 1994). Aside from mean and transient wind statistics, this section introduces Ekman pumping as ocean-monitoring parameter. Ekman pumping is defined as curl($\tau/\rho_0 f$) (Ekman 1905), and it relates to the curl of the wind stress vector, τ (de Kloe et al. 2017), scaled by a reference ocean density, ρ_0, and the Coriolis parameter f. As a rule of thumb, cyclonic winds will induce a net divergence in Ekman transport and upwelling, or Ekman suction, while anticyclonic winds will induce a net convergence and downwelling, or Ekman pumping.

In this chapter, the reference climatology is calculated over the period 2007–2014. The 2017 anomalies in mean wind, transient eddy wind and Ekman pumping are interpreted in the context of the 2007–2014 climatology and the 2007–2017 trend.

2.1.1. Global mean wind

The climatology, 2007–2017 trends and 2017 anomaly in the global mean sea surface winds are illustrated in Figure 2.1.1, with major features listed in Table 2.1.1. In the tropical Pacific, the 2007–2017 trend is dominated by a general shift from cold (La Niña) to warm (El Niño) Southern Oscillation conditions, with a gradual

deceleration of easterlies in the central and western Tropical Pacific (Tag A1 in Figure 2.1.1(b)), along with enhanced easterlies and mean wind convergence in the eastern Pacific (Tag A2 in Figure 2.1.1(b)). 2017 is a year with a short or aborted warm El Niño Southern Oscillation event and a return to more neutral conditions, showing weak westerly anomalies in the western Tropical Pacific and a more easterly flow with reduced wind convergence in the eastern Tropical Pacific (Figure 2.1.1(c)), connected to cooling of sea surface temperatures in the central and eastern Tropical Pacific (cf. http://marine.copernicus.eu/science-learning/ocean-monitoring-indicators/). In the eastern Tropical Pacific, northwesterly wind anomalies are also associated with the onset of a 'Coastal El Niño' in 2017 (Tag A3 in Figure 2.1.1, cf. Section 4.7 of this report).

Connected to the gradually warmer El Niño Southern Oscillation conditions (reversed Walker Circulation) during the climatology period, the 2007–2017 mean wind trend is dominated by cyclonic anomalies over the North and South Pacific subtropical gyres (Tag B in Figure 2.1.1(b)). In line with the trend, the 2017 mean wind anomaly registers cyclonic anomalies over the Pacific subtropical gyres, together with a reduction of the Aleutian Sea Low in the North Pacific (Tag C), and an intensification of the South Pacific High (Tag D). Cyclonic anomalies in the North Pacific are associated with a weakening of the central and eastern branches of the North Pacific Gyre (cf. Section 2.7) and related to the Pacific Decadal Oscillation index, which projects onto a warm phase in 2017, connected with warm SST anomalies along the US Coast and cold SST anomalies across the northern Pacific (cf. Section 1.1.1).

The 2007–2017 mean wind trend in the Southern Ocean is dominated by a shift towards higher Southern Annular Mode indices (Thompson and Solomon 2002), corresponding to stronger-than-average westerlies over the mid-high latitudes (50S–70S, see Tag F in Figure 2.1.1(b)) and weaker westerlies in the mid-latitudes (30S–50S). The higher Southern Annular Mode indices have been associated with large but statistically insignificant meridional wind anomalies (northerly near the Antarctic Peninsula, Tag E1, and southerly in the Ross Sea, Tag E2) during the 1992–2010 period (Holland and Kwok 2012) suggesting that a deepening of the autumn Amundsen Sea Low is connected with the evolution of West-Antarctic climate and sea ice in the Pacific sector (Raphael et al. 2016). The variability and change of the Amundsen Sea Low remains complex (Turner et al. 2013), and it fails to provide a consistent deepening trend over the 2007–2014 period analysed here.

The 2007–2014 climatology over the Atlantic Ocean is dominated by a shift to higher North Atlantic Oscillation

Figure 2.1.1. Global map of annual mean wind (product reference 2.1.1, ASCAT observations): 2007–2014 climatology (top), 2007–2017 decadal trend (middle, arrows at 95% significance level) and anomaly in 2017 relative to the climatology (bottom). Tagged features are listed in Table 2.1.1.

conditions, which are associated to increasing westerlies along the 55N–60N band (Tag G in Figure 2.1.1(b)). In line with the trend, the 2017 mean wind anomaly

shows enhanced westerlies in the North Atlantic, accompanied by an enhancement of the Azores High and deepening of the Icelandic Low. In contrast to the general trend of increasing southerly meridional anomalies observed in the Greenland and Norwegian Seas, the 2017 anomaly shows enhanced subpolar north-easterlies (Tag H in Figure 2.1.1(c)). We also observe southeasterly wind anomalies in the Labrador Sea (Tag I in Figure 2.1.1(c)), weakening the local mean flow and connected to the weakening of the North Atlantic cold sea surface temperature anomaly as it is pushed further into the subpolar gyre (cf. Section 4.2). The 2007–2017 mean wind trend and anomalies are dominated by anticyclonic anomalies over the North and South Atlantic subtropical gyres (Tag J in Figure 2.1.1 (b)), with an intensification of the South Atlantic High near the Brazil-Malvinas Confluence, connected to unusually high sea surface temperatures in that region (http://marine.copernicus.eu/science-learning/ocean-monitoring-indicators) and associated with the Azores High near the Gulf Stream.

Finally, no significant trends are observed over the South Indian Ocean during the 2007–2017 period, except for a small cyclonic trend over the Mascarenes High off Madagascar (Tag K1 in Figure 2.1.1(b)). The 2017 mean wind anomaly is opposite to the trend, with a large anticyclonic anomaly over the South Indian gyre (Tag K2 in Figure 2.1.1(c)), enhancing the prevailing south-easterly trades and connected with unusually strong wind convergence off Sumatra. The enhanced south-easterly trades in the southern Indian Ocean are connected to colder than average sea surface temperatures on the eastern side, and warmer sea surface temperatures to the west (http://marine.copernicus.eu/science-learning/ocean-monitoring-indicators), also associated with the Indian Ocean Dipole Index, which projects into a positive phase in 2017.

2.1.2. Global transient eddy winds
The climatology, trends and 2017 anomaly in the global transient eddy winds are illustrated in Figure 2.1.2 below. Attending to their lower amplitude, we note that regional trends and anomalies in transient eddy winds are generally smaller than in the mean winds, indicating that most of the inter-annual variability in wind power is dominated by changes in persistent large-scale conditions, rather than changes in transient wind activity. We also note that trends and anomalies in transient wind are generally of opposite sign to trends and anomalies in the mean wind, indicating that changes in the mean wind are counterbalanced by changes in wind transience, which is reasonable when one considers that transient disturbances feed on the mean flow.

Table 2.1.1. Major features in global sea surface wind trends and anomalies, with associated ocean features as indicated in Figure 2.1.1.

TAG	Wind feature	Ocean feature
A1	El Niño Southern Oscillation trend: deceleration of easterlies in the central/western Tropical Pacific	Sustained extra-equatorial upwelling anomalies at latitudes from 3 to 7 deg.
A2	El Niño Southern Oscillation trend: enhanced easterlies and mean wind convergence in the eastern Pacific	Sustained extra-equatorial downwelling anomalies at latitudes from 3 to 7 deg.
A3	Coastal El Niño Southern Oscillation in 2017	Coastal circulation and production
B	Cyclonic anomalies over the North and South Pacific subtropical gyres	Upwelling trend and anomaly
C	Reduction of the Aleutian Sea Low	Downwelling anomaly Bering Strait
D	Intensification of the South Pacific High	Downwelling trend
E1	Deep Amundsen Sea Low anomalies: northerly near the Antarctic Peninsula	Ocean circulation and sea ice
E2	Deep Amundsen Sea Low anomalies: southerly in the Ross Sea	Ocean circulation and sea ice
F	Higher Southern Annular Mode	Northerly Ekman flow trend with associated down(up)welling to S(N)
G	Higher North Atlantic Oscillation conditions	Gulf Stream Dynamics
H	Increased subpolar north-easterlies in Greenland and Norwegian Seas	Enhanced ocean circulation/transport
I	Southeasterly wind anomalies in the Labrador Sea	Downwelling anomaly & trend off Newfoundland
J	Intensification of the Azores High and South Atlantic High	Atlantic Meridional Overturning
K1	Cyclonic trend over the Mascarenes High off Madagascar	Upwelling trend in Indian Ocean Gyre
K2	Anticyclonic anomaly in eastern tropical Indian Ocean	Positive phase of the Indian Ocean Dipole index

In connection with the trends in annual mean wind, we observe increasing wind variability over the central and western Tropical Pacific during the 2007–2017 period (Tag A1 in Figure 2.1.1 and Table 2.1.1), spatially correlated with the slowdown of trades and connected to the shift towards warmer El Niño Southern Oscillation conditions. Also note the localised regions of increased wind variability around Newfoundland and the Kamchatka Peninsula, both in the trends and the 2017 anomaly, and decreased wind variability over the Gulf of Alaska. We moreover observe a generally lower wind variability over the Southern Ocean (Tag F in Figure 2.1.1 and Table 2.1.1), in connection with a higher Southern Annular Mode – except in the Pacific sector. We also note a trend of increased wind variability over the subtropical Pacific gyres (Tag B in Figure 2.1.1 and Table 2.1.1) in connection with cyclonic anomalies in the mean winds, and lower wind variability in the eastern tropical Indian Ocean (Tag K2 in Figure 2.1.1 and Table 2.1.1) in 2017 connection with a strong anticyclonic anomaly in the mean wind.

Time series of globally averaged annual mean and eddy kinetic energy contributions for the 2007–2017 period split into zonal and meridional components for ASCAT observations and the ERA-Interim spatio-temporally interpolated collocations (product reference 2.1.1) have been computed (but not shown). It is interesting to compare the representation of the globally averaged wind kinetic energy provided by reanalyses to that of observations, since the accuracy of the former is limited by inhomogeneities introduced by changes in the observing system, as well as systematic errors inherited from the underlying model physics. Despite the regional trends noted earlier, there are no significant trends in globally averaged annual mean wind or wind variabilities over the 2007–2017 period. The partition of kinetic energy into mean and transient eddy components is however pictured somewhat differently in the ERA-Interim reanalysis, with a 6% higher mean wind energy and an 8% lower transient eddy wind energy than in the ASCAT measurements. The partition of mean wind energy into zonal and meridional components is also different in ERA-Interim, with stronger mean zonal winds and weaker meridional winds than in the ASCAT measurements, along with weaker zonal and meridional wind variabilities (not shown here, see Belmonte Rivas and Stoffelen 2019).

2.1.3. Ekman pumping

The climatology, trends and 2017 anomaly in Ekman upwelling are illustrated in Figure 2.1.3. We recall that trends and anomalies in Ekman suction/pumping, as derived from the curl of the wind stress vector, follow from the cyclonic/anticyclonic trends and anomalies in the annual mean wind. As an indication of large-scale vertical motions in the global oceans, ocean upwelling influences biological productivity (upwelling waters are usually rich in nutrients) and brings about changes in sea surface temperature that may affect weather and climate.

Due to their biological impact, a lot of research has focused on eastern boundary upwelling systems and their modes of variability, namely, the California and Peru-Humboldt systems, which are particularly impacted by El Niño Southern Oscillation; the Benguela system, which is affected by El-Niño-Southern-Oscillation-like variability and the Southern Annular Mode; or the Canary/Iberian system, which is impacted by the North Atlantic Oscillation and the Atlantic Multidecadal Oscillation (Bakun et al. 2015). Note that current scatterometer products lack data values closer than 25 km off the coast, as depicted in all figures. Some other
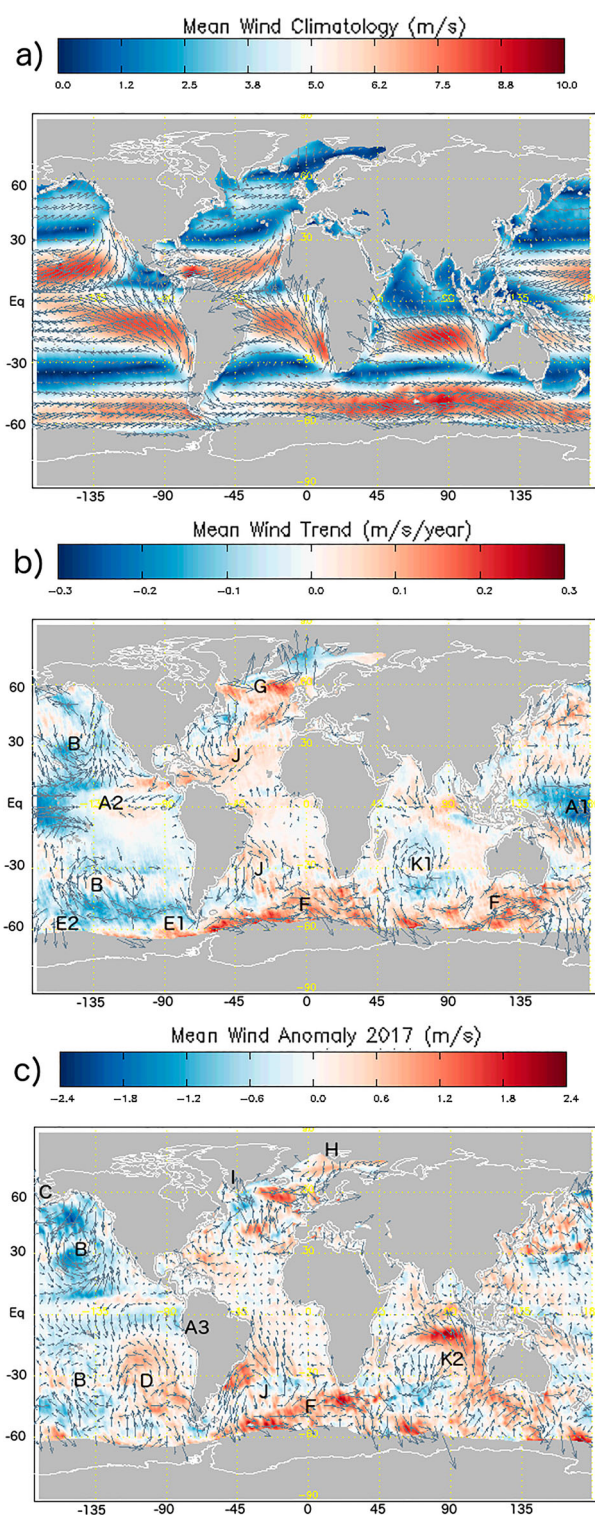
Figure 2.1.2. Global map of observed annual transient eddy wind (product reference 2.1.1, ASCAT observations): 2007–2014 climatology (top), 2007–2017 decadal trend (middle, arrows at 95% significance level) and anomaly in 2017 (bottom) with horizontal/vertical arrows showing the relative weight of the zonal/ meridional components.
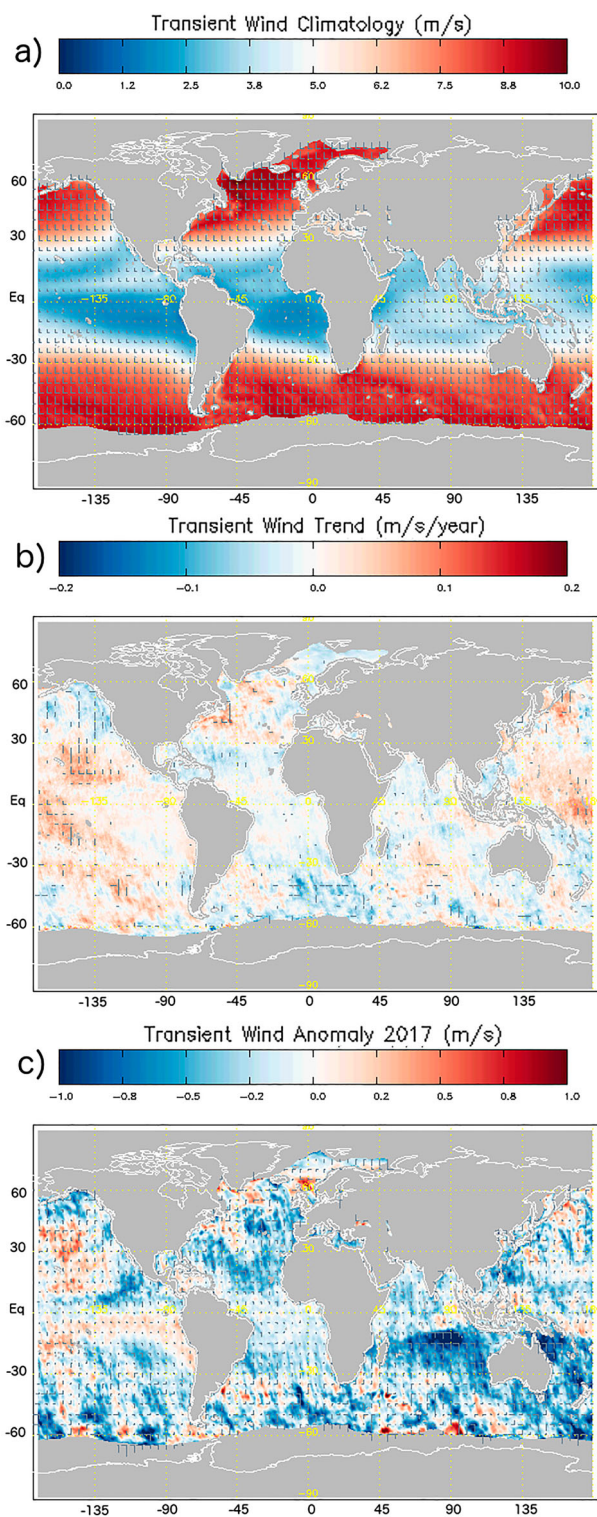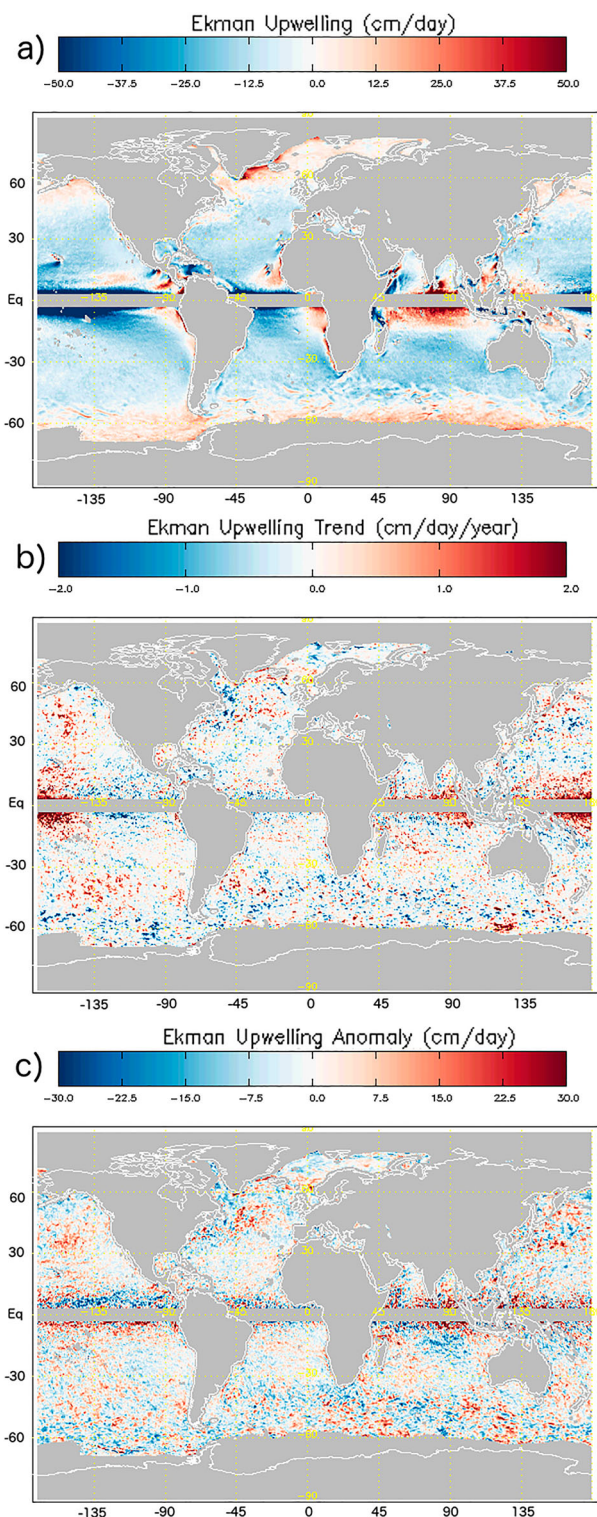
Figure 2.1.3. Global map of observed annual mean Ekman Upwelling (product reference 2.1.1, ASCAT observations): 2007–2014 climatology (top), 2007–2017 trend (middle, colours enhanced at 95% significance level) and anomaly in 2017 (bottom). Estimates between 5N and 5S are shaded as in (Risien and Chelton 2008) because the Coriolis force is small there.

researchers have focused on describing inter-annual variability in open-ocean upwelling.

In the tropical Pacific, we observe a persistent easterly flow that should create a thin tongue of upwelling cold water around the equator due to divergent Ekman transport approximately between 3S and 3N (within the shaded region in Figure 2.1.3). The trend of reduced easterlies in the central and western Tropical Pacific (associated to the general shift to warmer El Niño Southern Oscillation conditions during the 2007–2017 period) should result in downwelling anomalies (i.e. less upwelling) along the equatorial strip (Bograd and Lynn 2001), also within the shaded region in Figure 2.1.3. What we can see are the compensating downwelling zones North and South of the Equator (i.e. the extra-equatorial bands between 3 and 7 deg in both hemispheres) sustaining strong upwelling anomalies in the central and western Tropical Pacific (Tag A1 in Figure 2.1.1 and Table 2.1.1). These upwelling trends are indirectly related to reduced upwelling along the equatorial strip during the 2007–2017 period. In 2017, we still observe weak upwelling anomalies in the western extra-equatorial tropical Pacific, and somewhat more remarkable downwelling anomalies in the eastern extra-equatorial Pacific connected to enhanced easterlies there (Tag A2 in Figure 2.1.1 and Table 2.1.1).

Over the North and South Pacific Subtropical Gyres, we observe small upwelling trends and anomalies associated to persistent cyclonic anomalies in the mean wind (Tag B in Figure 2.1.1 and Table 2.1.1), along with a downwelling anomaly in the Bering Sea connected to the reduction of the Aleutian Sea Low (Tag C in Figure 2.1.1 and Table 2.1.1), and a downwelling anomaly (Tag D in Figure 2.1.1 and Table 2.1.1) connected with the intensification of the South Pacific High.

The strengthening of westerly winds over the Southern Ocean creates a band of enhanced northward Ekman flow with increased subpolar upwelling (trends and anomalies) to the south and enhanced downwelling to the north (Tag F in Figure 2.1.1 and Table 2.1.1) in connection with a stronger Southern Annular Mode (Hall and Visbeck 2002). In the Atlantic Ocean, we observe downwelling trends and anomalies off Newfoundland associated to a high pressure anomaly there (Tag I in Figure 2.1.1 and Table 2.1.1) (Spall and Pickart 2003), and upwelling trends and anomalies further east across the North Atlantic and around Iceland (Pelegri et al. 2006). Finally, we observe increased upwelling trends and anomalies in the eastern tropical Indian Ocean, which previous research has connected to Indian Ocean Dipole and El Niño Southern Oscillation conditions (Chen et al. 2016), along with a strong downwelling anomaly over the southern Indian Ocean connected to a large anticyclonic anomaly in the mean wind observed in 2017.

2.1.4. Concluding remarks

Wind, stress and Ekman variations are important in so far as they may be driving changes in other components (SST, SSS, sediment, biology) or initiate (local or remote) coupled processes that may push the climate system towards new states of equilibrium. Coupled processes, coastal processes, etc., have a host of relevant applications in economy and society. While these processes are best studied locally, we show that local changes, affecting ocean users, are strongly associated to changes in global atmospheric circulation. We moreover depict that the input used by most oceanographers suffers from large-scale forcing issues, in addition to the well-documented regional issues in processes and resolution. The associations between ocean indicators in other domains (sections) and the tagged features in this section's figures, appear a good way to connect the global atmospheric circulation changes to regional and local ocean circulation features and indicators. We also imply that for many of our users, the large-scale mean and transient errors in NWP forcing will be relevant in user applications, as it will provide errors in the time-dependent ocean response. It will be useful to further document and monitor these errors and the temporal changes in them. Finally, we note that efforts are ongoing to improve the coastal processing of scatterometer data, hence enhancing the usefulness of our products for ocean applications.

2.2. The seasonal intensification of the slope Iberian Poleward Current

Authors: Anna Rubio, Ivan Manso-Narvarte, Ainhoa Caballero, Lorenzo Corgnati, Carlo Mantovani, Emma Reyes, Annalisa Griffa and Julien Mader
Statement of main outcomes: The combination of surface HF radar data and data from ADCP moorings is showcased as a promising approach for the monitoring of the slope currents in the southeastern Bay of Biscay and the Iberian Poleward Current seasonal intensification. Persistent and intense eastward currents are observed during winter periods and affect the measured water column down to 150 m depth. During summer time, stronger vertical shear is observed, both during eastward and westward current events. Strong fluctuations occur in parallel to intense north-northwestern and southern wind changes in both seasons. This variability is expected to have a significant impact on the residence time and the water exchanges between the coast and the open ocean in the area.

Products used:

Ref. No.	Product name and type	Documentation
2.2.1	INSITU_IBI_NRT_OBSERVATIONS_ 013_033	QUID: http://marine.copernicus. eu/documents/QUID/CMEMS-INS-QUID-013-030-036.pdf PUM: http://marine.copernicus. eu/documents/PUM/CMEMS-INS-PUM-013.pdf
2.2.2	Insitu total surface currents from HF radar	NRT data to be included in CMEMS v5 portfolio, REP data to be included in CMEMS v7 portfolio. REVIEW PAPER: https://doi.org/ 10.3389/fmars.2017.00008 EUROPEAN HF STANDARD FOR HF RADAR DATA AND METADATA: http://www. marineinsitu.eu/wp-content/ uploads/2018/02/EGU2018-13317_presentation.pdf

The Iberian Poleward Current drives the ocean slope circulation in the southeastern Bay of Biscay form the surface down to 300 m depth. The intensification and variability of this current at seasonal and shorter scales can have a significant impact on the marine environment in this coastal area, since it can modulate the residence time of nutrient-rich waters, pollutants, planktonic organisms as well as the water exchange between the coast and the open ocean. The monitoring and forecast of the surface and subsurface variability of currents in coastal areas is key for their accurate management where a myriad of socio-economic activities coexist (e.g. commercial and recreational fisheries and navigation, tourism, industry, ports and harbours, etc.). While coastal numerical models can provide three-dimensional fields of currents and enable the computation of Lagrangian quantities with application to biological, geochemical and environmental issues, the joint analysis of multi-platform observations, with complementary spatial coverage, is an interesting approach for a better understanding of the three-dimensional coastal circulation and the validation of the models. In this contribution we combine HF radar-derived hourly surface current maps with ADCP data and wind measurements from three moorings to showcase their use to continuously monitor and analyse the IPC seasonal variability along the period 2009–2017 and its intensification under certain prevailing wind conditions.

The Iberian Poleward Current is one of the main along-slope flows that promote trans-boundary interactions along the Atlantic margin of Europe. In the southeastern Bay of Biscay (see Figure 2.2.1), the Iberian Poleward Current is a persistent feature and affects the 0–300 m depth layer in the area. Together with the presence of slope eddies that grow from current instabilities
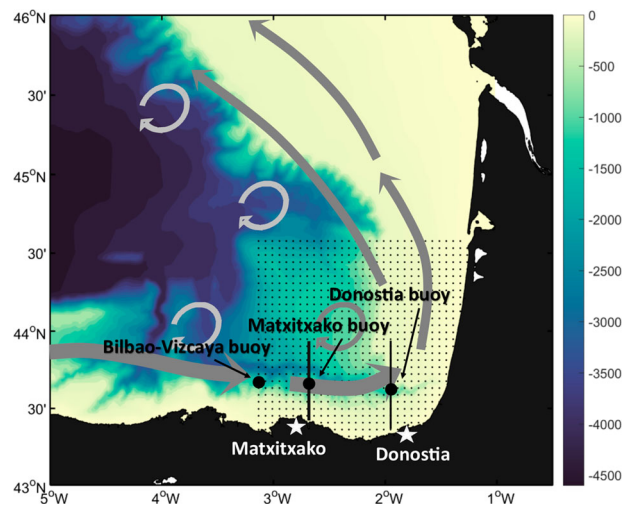
Figure 2.2.1. Study area corresponding to the southeastern Bay of Biscay (northeastern Iberian Peninsula) and schematic view of the winter shelf-slope current and mesoscale regime (grey arrows, note that although only anticyclonic arrows are represented, eddies of anticyclonic and cyclonic polarity are observed in different locations along the slope). The nodes for the computation of HF radar total currents (product ref. 2.2.2) are shown by the grey dots. The stars provide the location of the HF radar antennas in Matxitxako and Higer (Donostia) Capes. The black dots provide the location of the slope moorings (product ref. 2.2.1) used in this study and the black lines the surface cross-transects used to plot HF radar along-slope currents in Figure 2.2.2. Bathymetry is given by the contours (in metre).

and the wind-induced circulation, this has a significant impact on the surface transport patterns, the residence times and the water exchange between the coast and the open ocean (Rubio et al. 2018).

The Iberian Poleward Current flows over the slope, advecting warm surface waters eastwards (northwards) along the Spanish (French) coast (Le Cann and Serpette 2009; Herbert et al. 2011; Charria et al. 2013) during winter. The flow is reversed and three times weaker (Solabarrieta et al. 2014) during summer. In addition to this markedly seasonal density-driven circulation, variability at shorter scales is observed linked to wind-induced currents (e.g. Solabarrieta et al. 2015), mesoscale eddies (e.g. Rubio et al. 2018), tides and inertial motions (e.g. Rubio et al. 2013). The generation of slope eddies occurs mainly in winter, when the intensified Iberian Poleward Current interacts with the abrupt bathymetry (Pingree and Le Cann 1992; Teles-Machado et al. 2016). During autumn and winter, southwestern winds dominate and generate northward and eastward drift over the shelf. The rest of the year the winds are much weaker and less persistent, which makes wind-driven currents more variable (Lazure 1997; González et al. 2004; Solabarrieta et al. 2015). The observation and monitoring of the surface and

subsurface current, together with its variability is thus crucial to obtain accurate estimation of the coastal transport in this area and to evaluate its potential impacts on the coastal ecosystem.

Several previous works have focused on the study of different aspects of the Iberian Poleward Current variability in the area by using remote sensing data (e.g. Herbert et al. 2011), moorings (Rubio et al. 2011), drifters (e.g. Charria et al. 2013) and HF radar data (e.g. Solabarrieta et al. 2014) independently. The main contribution of this study is the use of multi-platform observing systems with complementary spatial coverage for observing and monitoring the surface and subsurface currents and their variability, to accurately estimate the coastal transport in the southeastern Bay of Biscay. Particularly, in this case, we combine data from emerging technologies as the HF radar-derived hourly surface current maps (product ref. 2.2.2) with ADCP water column velocity profiles from two slope moorings and wind velocity from a third mooring (product ref. 2.2.1) to monitor the Iberian Poleward Current seasonal variability along the period 2009–2017 and its intensification under certain prevailing wind conditions.

HF radar is a land-based remote sensing technology which can infer ocean surface currents over wide areas (distances from the coast over 150 km) with high spatial (300 m–5 km) and temporal (≤1 h) resolution. Nowadays, HF radars are the unique technology that can offer such a continuous observation of surface coastal current patterns over wide areas at high-spatial resolution and thus the possibility to monitor the associated transports. The combination of HF radar data with water-column data is especially interesting since it can broaden the application of this technology to biological, geochemical and environmental issues, since plankton or pollutants can be located deeper in the water column and not only follow surface dynamics. The inclusion of near-real-time and reprocessed HF radar data into the European Copernicus Marine Environment Monitoring Service is foreseen in 2019 and 2021, respectively. It will enable a sustained delivery of HF radar data and related products, including the expansion of the approach presented here to other coastal areas.

The HF radar system located in the southeastern Bay of Biscay (www.euskoos.eus) emits at a central frequency of 4.5 MHz and a 40-kHz bandwidth and provides surface hourly current maps in an area up to 150 km from the coast (Figure 2.2.1). HF radar-derived surface currents are quality controlled using advanced procedures based on velocity and variance thresholds, noise to signal ratios and radial and total coverage (Rubio et al. 2011, 2018; Solabarrieta et al. 2014, 2015, 2016), and re-processed (for obtaining gap-filled surface currents)

using the Open-boundary Modal Analysis (Kaplan and Lekien 2007). The historical HF radar data used here cover the whole period 2009–2017. Wind data and current profiles in the water column are obtained from the CMEMS reference product 2.2.1. Winds are obtained from the Bilbao Vizcaya mooring (location shown in Figure 2.2.1) and we use current data from two buoys moored over the upper part of the slope with a downward looking ADCP (150 kHz, 8 m vertical bins, up to 200 m): Matxitxako mooring historical data spanning the period 2007–2013 and Donostia mooring the period 2007–2017 (see locations in Figure 2.2.1).While the slope buoys' data time coverage is irregular, and no data are available for the Matxitxako buoy after August 2013, the HF radar data coverage is quite good from the end of 2010.

To explore the variability of the current we follow a two-step approach. First, the data series are analysed jointly to identify the main variability patterns in relation to the seasonal cycle and winds, exploiting the spatial complementarity of the measurements for characterising the variability in the horizontal and vertical extension of the current. Second, we compute spatial maps and vertical profiles of temporal cross-correlation between the velocity measurements at the moorings location and the rest of the nodes within the HF radar and vertical levels to obtain an estimation of the area and levels where the point-wise current measurements from the moorings and the surface currents from the HF radar can be considered as representative of the whole slope area. The areas and levels containing high cross-correlation values between measurements provide thus the 3D volume that can be well monitored by the combination of the two observing systems.

The along-slope current is marked by strong seasonal variability (Figure 2.2.2). Persistent and intense eastward currents are observed during winter periods, and affect the measured water column down to 150 m depth. The cross-shore extension of the winter eastward current shows significant variability, being some of the winter events constricted to the shelf-slope area of the Matxitxako mooring (W2), while others show higher extension being observed up to 43.9°N (W3, W4 or W5). Remarkable differences between the two mooring locations are also observed (see also Rubio et al. 2011): the signature of the slope current is much stronger at Matxitxako, and generally weaker and less stable at Donostia mooring. Moreover, observed intensifications of the eastward winter current are also weaker at the Donostia location and more constrained to the slope (latitudes between 43.5 and 43.75° N). The strongest eastward currents are observed in periods of intense north-northwestern winds, particularly during winter time. During some of the winter periods the (e.g. W1 in Donostia or W4, see Figure 2.2.2) strong

fluctuations together with altering east/west intense currents occur in parallel to intense north-northwestern and southern wind changes. In December 2014, the wind-induced intensification of the slope current and its subsequent relaxation triggered the generation of an intense anticyclonic eddy described in Rubio et al. (2018) (see also Figure 2.2.2(a): intense countercurrent after W4 event). The signature of the eddy at Donostia latitudinal transect is less intense and less persistent but can be observed to be vertically coherent down to 150 m depth.

During summer time, stronger vertical shear is observed, both during eastward (S1, S2) and westward (S3 and S4) current events. In 2014, 2015 and 2016 intense summer westward currents (S3, S4) are observed in both locations. The westward event during July and August 2016 is especially remarkable because of its intensity and persistence, although it is limited to the surface (of a few tens of meters).

The cross-correlation maps for the sub-inertial along-slope component (Figure 2.2.3(a–d)) show high correlation between Matxitxako and Donostia locations and the nearby areas over the self and slope, from 1°30′ to 3°W, and from the coast to 43°50′. In winter, cross-correlation values over 0.6 are observed in the area between 43°50′N and the Spanish coast. This is due
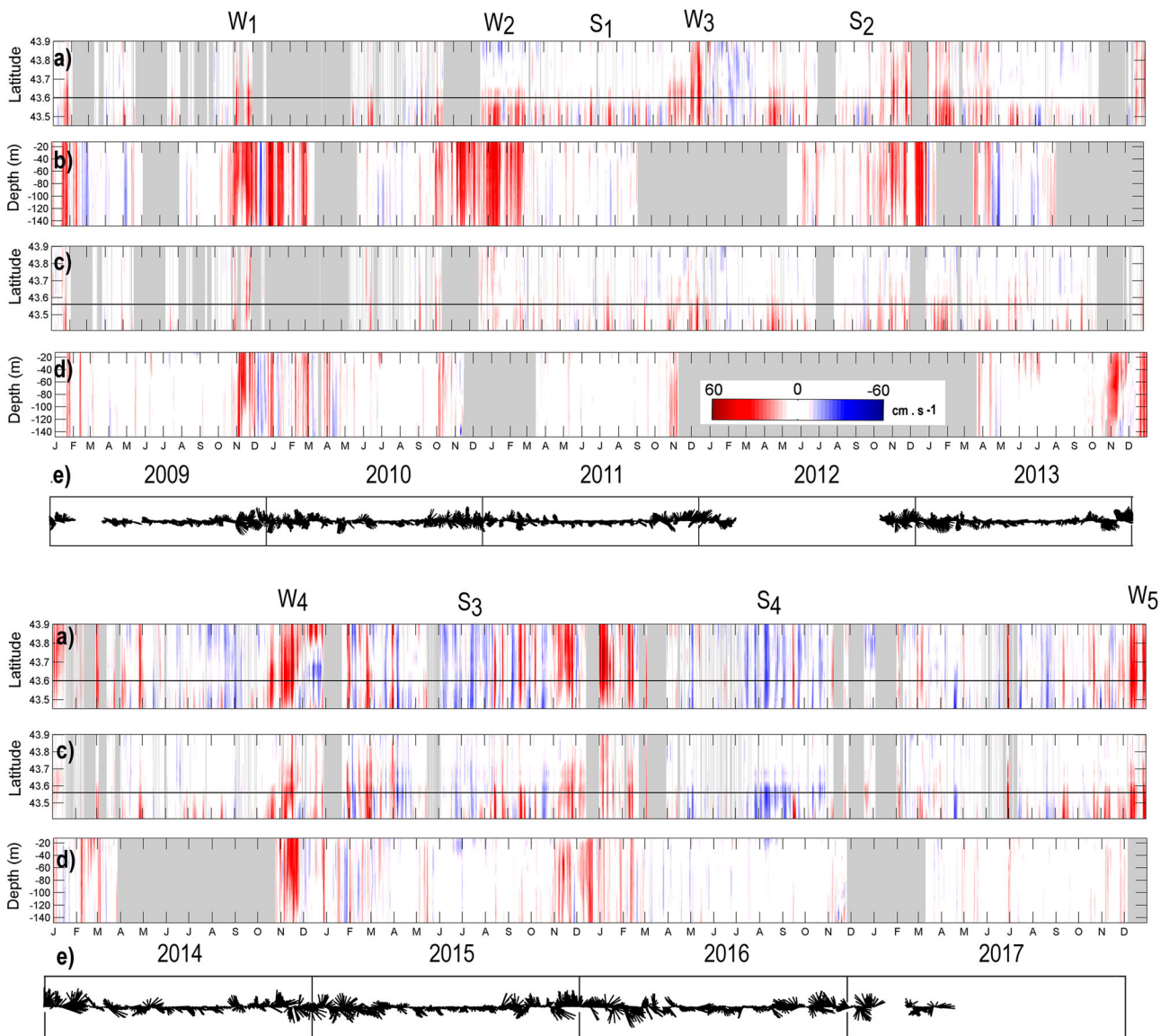
Figure 2.2.2. Hovmöller diagrams of along-slope surface currents derived from the HF radar (product ref. 2.2.2) along the surface cross-transects shown in Figure 2.2.1, at the longitude of the (a) Matxitxako and (c) Donostia moorings. Hovmöller diagrams of along-slope current profiles up to 150 m depth from downward looking ADCP data in (b) Matxitxako (only for the period 2009–2013) and (d) Donostia moorings (product ref. 2.2.1). Low-pass filtered wind vectors (product ref. 2.2.1)) from Bilbao Vizcaya mooring are shown in (e). A selection of winter (W*) and summer (S*) current events discussed more in detail in the text are identified at the top of (a) panel.

to the persistent and spatially homogeneous surface signature of the winter slope current flowing eastwards along the Spanish slope. In the case of Matxitxako mooring (which samples very well the core of the slope current) an area of high cross-correlation values (over 0.5) is also observed along the French slope (Figure 2.2.3(a)). We relate this to the surface signature of the slope current in this area where, due to the change of orientation of the bathymetry, it flows to the north-northwest (so the variability of the east–west component of the flow over the French slope is well correlated with east–west flow changes at Matxitxako mooring location). As mentioned before, the seasonal variability is weaker at Donostia location, being less evident the influence of the winter current regime. Vertically, the cross-correlation is also seasonally modulated (Figure 2.2.3(e,f)), and shows significant spatial differences. The highest cross-correlations at 150 m are observed in winter in Matxitxako, which is again in coherence with a stronger slope current influence at this location. The strongest stratification in summer leads to a higher vertical shear, and makes the correlation drop up to 0.5 at 60 and 50 m in

Matxitxako and Donostia, respectively. From this level to 150 m the decay in the correlation is again much higher in Donostia, which indicates that other than the absence of a vertically coherent slope regime is favouring a stronger vertical shear in this area of complex bathymetry.

Recent work has shown the impact of the slope circulation and its variability on the residence time and the water exchange between the coast and the open ocean in the southeastern Bay of Biscay (Rubio et al. 2018; Declerck et al. 2019). The monitoring and forecast of the surface ocean variability is key for the accurate assessment of the distribution and transport of organic and inorganic matter, in this area where different human activities coexist (commercial and recreational fisheries and navigation, tourism, industry, etc.). From our results, the combination of surface HF radar data (product ref. 2.2.2) and data from ADCP moorings (product ref. 2.2.1) arises as a promising approach for the monitoring and characterisation of the Iberian Poleward Current seasonal variability and its intensification under certain prevailing wind directions. Moreover, our analysis on the spatial and temporal
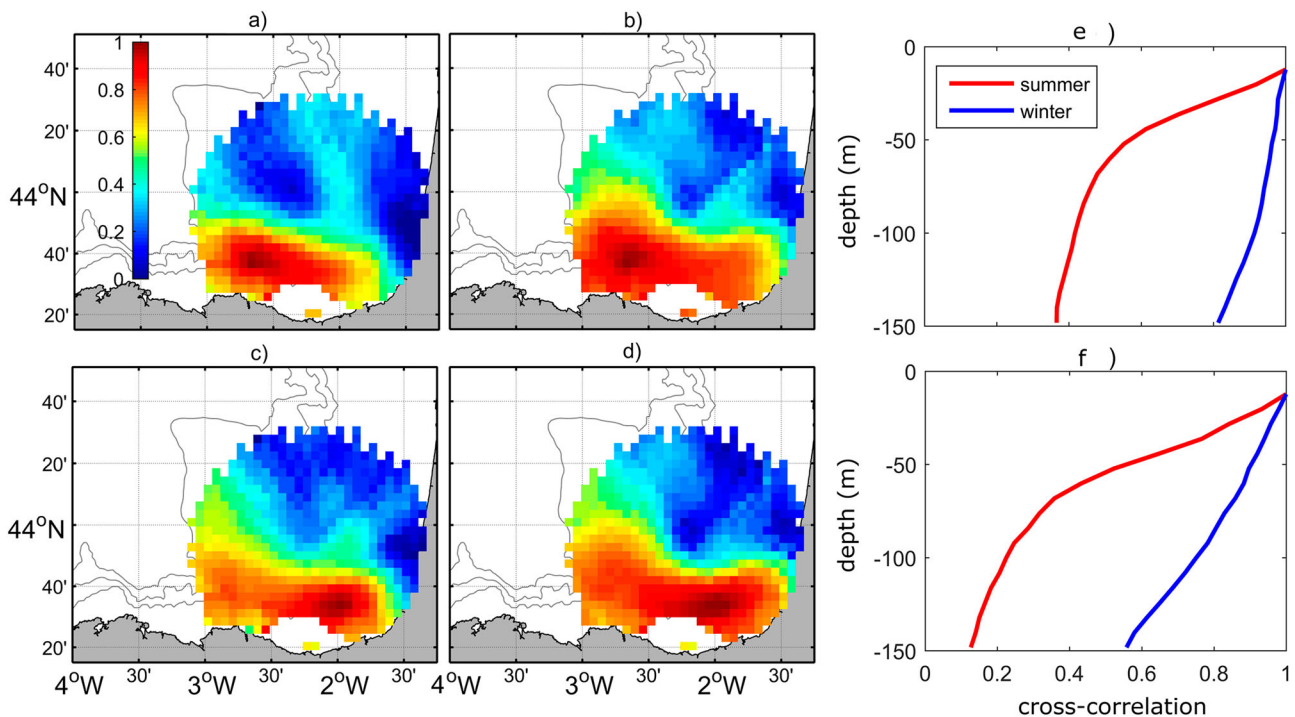
Figure 2.2.3. Spatial maps of cross-correlations between the low-pass filtered time series of the HF radar along-slope velocity component (product ref. 2.2.2) at (a,b) Matxitxako and (c,d) Donostia locations and the rest of the nodes within the HF radar footprint area for total currents (the maps for winter/summer are shown in (a) and (c)/(b) and (d) subplots, respectively). ADCP data cross-correlations along the vertical range of ADCP data (product ref. 2.2.1) for (e) Matxitxako and (f) Donostia and the along-slope velocity component for summer (stratified) and winter (well-mixed) periods. A 10th order digital Butterworth filter was applied to obtain sub-inertial current previous to the computation of cross-correlation between time series. The significance level is over 0.99 for all the cross-correlations values plot in the figure.

coherence in the seasonal and mesoscale variability observed by independent observing systems is a first step in the blending of both data sets, for an improved real-time monitoring of three-dimensional coastal transports in the area. Besides, the use of these data sets for the improvement of the existing numerical models, through validation and data assimilation, would potentially enable enhanced forecast skills. Operational gap-filled HF radar coastal surface currents could also be used to monitor the transport properties of the surface flow, based on the Lagrangian approach, aiming to identify the different scenarios that favour the local retention and dispersal of shelf waters.

2.3. Mediterranean deep and intermediate water mass properties

Authors: Katrin Schroeder, Jacopo Chiggiato, Sana Ben Ismail, Mireno Borghini, Bernardo Patti, Stefania Sparnocchia

Statement of outcome: The Mediterranean Sea is a mid-latitude marginal sea which has been recognised to be a climatic hotspot. During the past decade, its water masses have experienced strong and fast increases in temperature and salinity, evidencing the tendency of this area to respond very rapidly to global warming and to changes in the regional freshwater budget. Based on *in situ* data here it is shown where and how fast these changes occur, with a particular focus on the Western Mediterranean Deep Water, the Levantine Intermediate Water and the upper Eastern Mediterranean Deep Water. Such trends are at least one order of magnitude higher than the global mid-latitude average trends. Indicator-type curves, routinely updated, for subsurface temperature and salinity evolution represent an outcome that is envisaged to be important for climate science, environmental agencies, concerned citizens as well as regional policy-makers.

Products used:

Ref. No.	Product name and type	Documentation
2.3.1	INSITU_MED_NRT_OBSERVATIONS_ 013_035 *In situ* data ftp://nrt.cmems-du.eu/Core/ INSITU_MED_NRT_OBSERVATIONS_ 013_035/history/mooring/MO_ TS_MO_6101022.nc	QUID: http://cmems-resources.cls.fr/ documents/QUID/ CMEMS-INS-QUID-013-030-036.pdf PUM: http://cmems-resources.cls.fr/ documents/PUM/ CMEMS-INS-PUM-013.pdf

(*Continued*)

Continued.

Ref. No.	Product name and type	Documentation
2.3.2	INSITU_MED_NRT_OBSERVATIONS_ 013_035 *In situ* data ftp://nrt.cmems-du.eu/Core/INSITU_ MED_NRT_OBSERVATIONS_013_ 035/history/mooring/MO_TS_MO_ SardiniaChannel.nc	QUID: http://cmems-resources.cls.fr/ documents/QUID/ CMEMS-INS-QUID-013-030-036.pdf PUM: http://cmems-resources.cls.fr/ documents/PUM/ CMEMS-INS-PUM-013.pdf
2.3.3	INSITU_MED_NRT_OBSERVATIONS_ 013_035 *In situ* data Monthly files from ftp://nrt.cmems-du.eu/Core/INSITU_ MED_NRT_OBSERVATIONS_013_035/ monthly/mooring/MO_201301_ TS_MO_SardiniaChannel.nc to ftp://nrt.cmems-du.eu/Core/INSITU_ MED_NRT_OBSERVATIONS_013_035/ monthly/mooring/MO_201711_TS_ MO_SardiniaChannel.nc	QUID: http://cmems-resources.cls.fr/ documents/QUID/ CMEMS-INS-QUID-013-030-036.pdf PUM: http://cmems-resources.cls.fr/ documents/PUM/ CMEMS-INS-PUM-013.pdf
2.3.4	INSITU_MED_NRT_OBSERVATIONS_ 013_035 *In situ* data Yearly files as ftp://nrt.cmems-du.eu/Core/ INSITU_MED_NRT_OBSERVATIONS_ 013_035/history/vessel/ MO_PR_CT_AlgerianBasin_yyyy.nc ftp://nrt.cmems-du.eu/Core/ INSITU_MED_NRT_OBSERVATIONS_ 013_035/history/vessel/ MO_PR_CT_SardiniaChannel_yyyy.nc ftp://nrt.cmems-du.eu/Core/ INSITU_MED_NRT_OBSERVATIONS_ 013_035/history/vessel/ MO_PR_CT_SicilyChannel_yyyy.nc	QUID: http:// cmems-resources. cls.fr/documents/ QUID/CMEMS-INS-QUID-013-030-036.pdf PUM: http://cmems-resources.cls.fr/ documents/PUM/ CMEMS-INS-PUM-013.pdf
2.3.5	INSITU_MED_NRT_OBSERVATIONS_ 013_035 *In situ* data Monthly files as ftp://nrt.cmems-du.eu/Core/ INSITU_MED_NRT_OBSERVATIONS_ 013_035/monthly/vessel/ MO_yyyymm_PR_CT_AlgerianBasin.nc ftp://nrt.cmems-du.eu/Core/ INSITU_MED_NRT_OBSERVATIONS_ 013_035/monthly/vessel/ MO_yyyymm_PR_CT_SardiniaChannel.nc ftp://nrt.cmems-du.eu/Core/ INSITU_MED_NRT_OBSERVATIONS_ 013_035/monthly/vessel/ MO_yyyymm_PR_CT_SicilyChannel.nc	QUID: http://cmems-resources.cls.fr/ documents/QUID/ CMEMS-INS-QUID-013-030-036.pdf PUM: http://cmems-resources.cls.fr/ documents/PUM/ CMEMS-INS-PUM-013.pdf

Strong increases in evaporation and reduction in precipitation and river runoff have greatly modified the freshwater budget of the Mediterranean Sea and a further increase of net evaporation is projected to occur during the twenty-first century in this region, as a result of anthropogenic climate change (Giorgi 2006).

Long-term changes in temperature, but also in salinity, are observed in all water masses, from the inflowing Atlantic Water, to the intermediate water
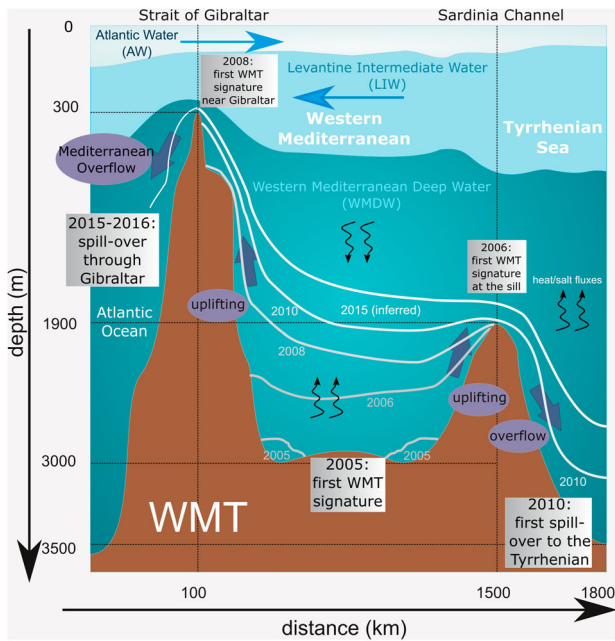
Figure 2.3.1. Temporal and spatial evolution of the processes associated to the Western Mediterranean Transition: white/light-grey curves denoted by years indicate the upper interface of the new Western Deep Water. Updated from Schroeder et al. (2016).

and the deep waters (e.g. Vargas-Yáñez et al. 2017). In the western basin, the rather homogeneous layer of Western Mediterranean Deep Water has always been considered a stable medium in which precise quantification of trends in heat and salt contents is possible. Indeed, it has been observed that deep temperature and salinity have increased almost steadily for about half a century, due to different and concurrent factors (Bethoux and Gentili 1999; Rixen et al. 2005; Josey et al. 2011). However *in situ* data gathered between 2005 and 2017, during dozens oceanographic cruises (CTD casts) and by means of submerged moorings in key areas, revealed a decade of enhanced thermohaline variability in the deep and intermediate western Mediterranean water masses (Schroeder et al. 2016): the gradual increasing trend in the western deep water was interrupted by an abrupt shift towards higher temperature and salinity (with yearly increases during 2005–2017 that are more than 2.5 times faster than during 1961–2004). The onset of this shift (Figure 2.3.1), called the Western Mediterranean Transition, has been a major dense water formation event in winter 2004/2005 in the north-western
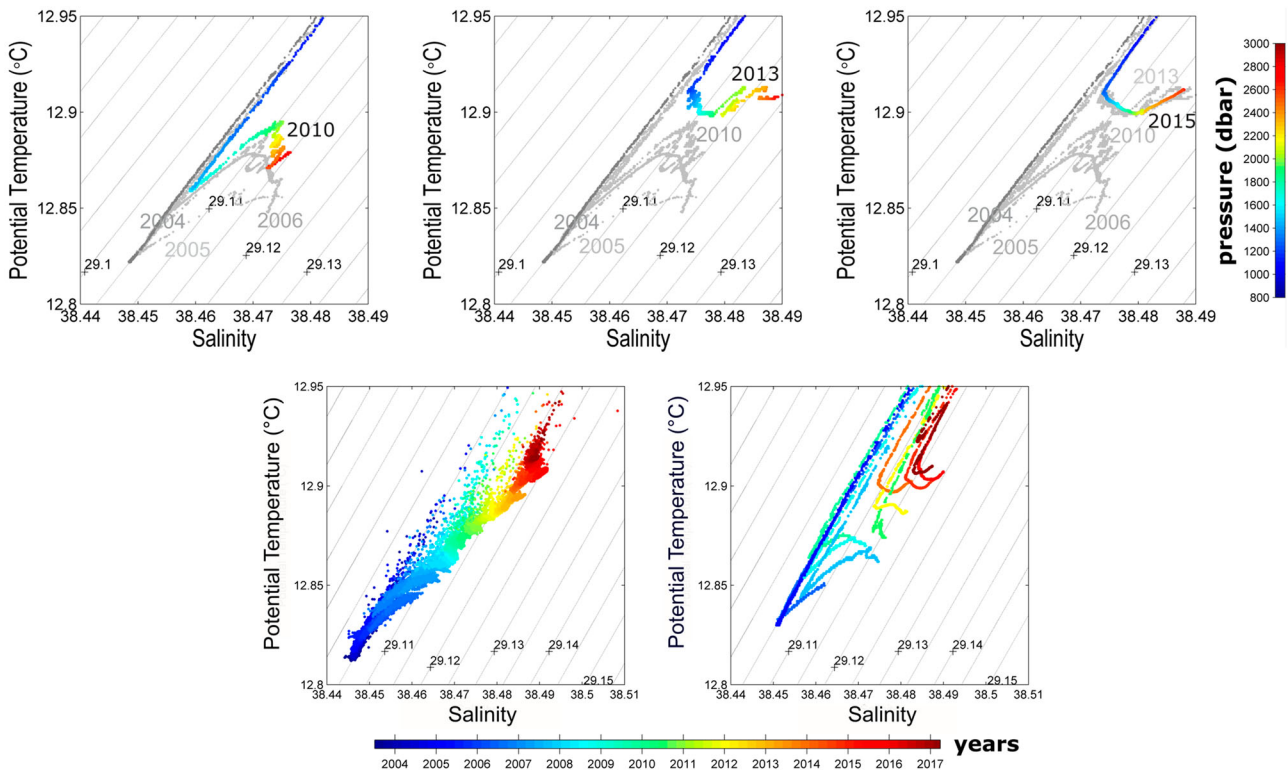
Figure 2.3.2. (upper panels) θS diagrams from 800 m depth to the bottom, in a repeat station (2800 m, 37.98°N, 4.65°E, product ref. 2.3.4–2.3.5) of the southern western Mediterranean (pressure is colour coded) in 2010 (left, light grey points refer to preceding years, i.e. 2005–2009, dark grey points refer to 2004, the pre-existing situation), 2013 (middle, light grey 2005–2010, dark grey 2004) and 2015 (right, light grey 2005–2014, dark grey 2004); (lower panels) θS diagrams at the sill in the Sardinia Channel (1915 m, 38.33°N, 9.33°E), (left) from bottom mooring data (product ref. 2.3.2–2.3.3) and (right) from repeated CTD profiles (years 2003–2017 are colour-coded, product ref. 2.3.4–2.3.5). Updated from Schroeder et al. (2016).

Mediterranean. Following winters also have contributed to the formation of anomalously warm and salty dense water.

Since then this anomaly started to spread from its formation region into the interior of the sea. The formation of large amounts of anomalously warm and salty deep water continued during the following winters and the new deep water started to fill up the entire basin (Figure 2.3.1). The increases of temperature and salinity in the deep western basin keep evolving stepwise, with the deep temperature-salinity diagrams becoming more and more complex (Figure 2.3.2, upper panels). From these diagrams it is possible to note how the Western Mediterranean Transition has changed the basic structure and the properties of the deep layers in the western basin. Over time, these waters eventually spread westward to flow out through the Strait of Gibraltar towards the Atlantic Ocean (Figure 2.3.1), as has been detected by a monitoring site at the sill where the characteristics of the outflowing waters in years 2015–2016 are consistently saltier and warmer than in 2005–2006 (Naranjo et al. 2017).

The new deep water spread also eastward: the Sardinia Channel allows exchanges of the upper part of the deep waters to occur between the western basin interior and the Tyrrhenian Sea. At the sill a CTD cast has been performed about once a year and a deep sea mooring
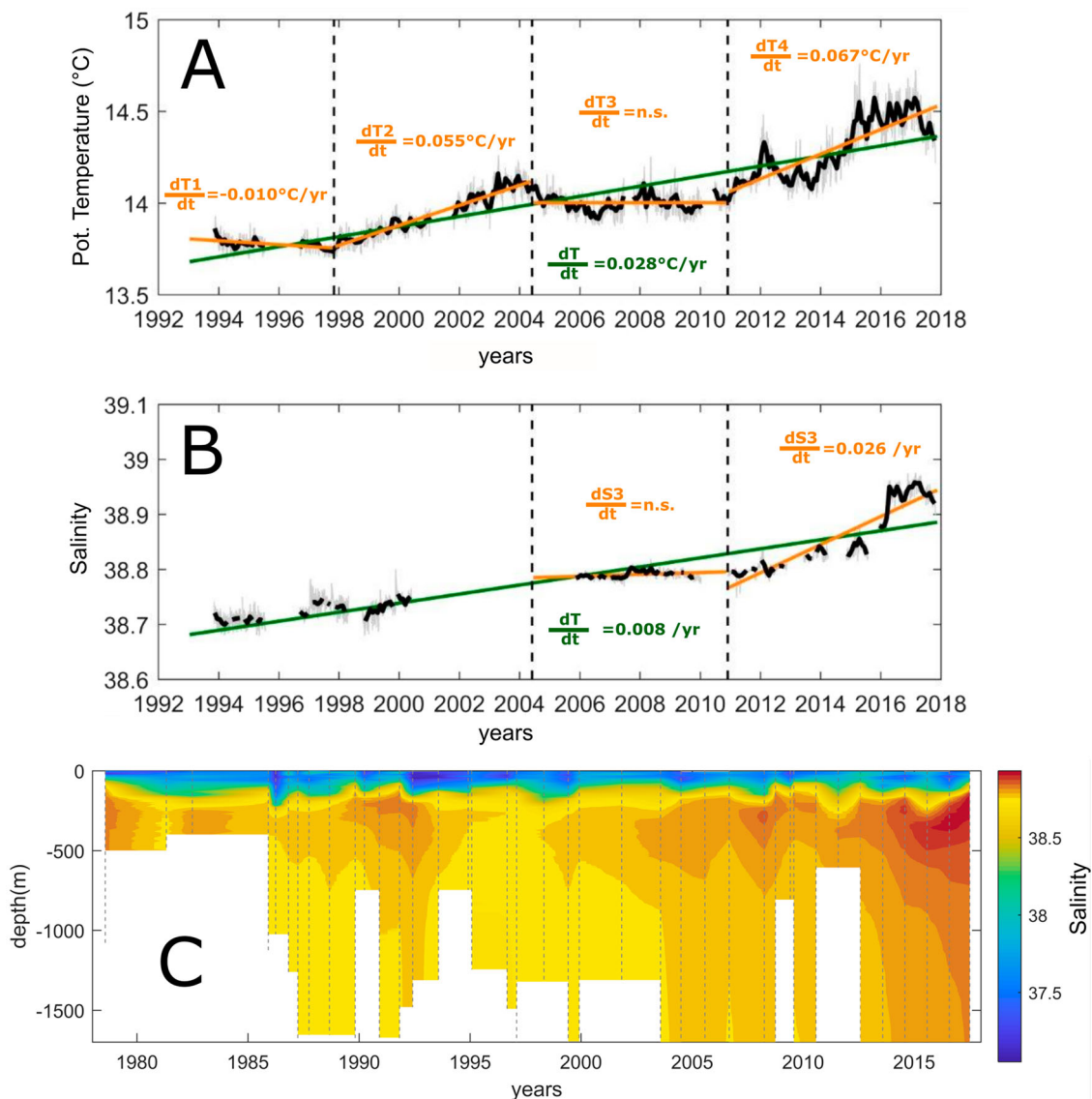
Figure 2.3.3. Daily (grey) and monthly (black) time series (1993–2017) of (A) temperature and (B) salinity at 400 m in the Sicily Channel (mooring, product ref. 2.3.1), updated from Schroeder et al. (2017); (C) Hovmöller diagram of the *in situ* salinity in the central part of the Sicily Channel (36.5°N, 13.2°E, north-west of Malta) from repeated CTD casts, 1978–2017 (product ref. 2.3.4–2.3.5). Updated from Gačić et al. (2013).

(belonging to the CIESM Hydrochanges network, see Schroeder et al. 2013) monitors the overflowing dense waters in detail since 2003. While until 2005 only the 'classical' old deep water was found at the sill, the new denser ones started to cross it since then (Figure 2.3.2 lower panels), being uplifted by even denser new deep waters that were produced in the following winters (Figure 2.3.1). By 2014 the whole layer below 500 m, i.e. the halocline/thermocline and the deep water, has densified to values of 29.11–29.12 kg m^{-3}, becoming denser than the 'classical' resident water found at <3000 m in the Tyrrhenian Sea (Schroeder et al. 2016).

Given that all processes of dense water formation involve Atlantic and Intermediate Water to some extent, the latter being the main contributor to the heat and salt contents of the newly formed waters, all Mediterranean water masses are intimately related to each other, so that significant modifications to one will also affect the others sooner or later. Indeed, recent studies have also focused on the long-term strong warming and salinification of intermediate water: since the mid-1990s its temperature and salinity have increased by 0.28°C/decade and 0.08/decade in the Sicily Channel (respectively Figure 2.3.3(A–B)), a key site where the intermediate water flowing from east to west may be intercepted. Such trends are at least one order of magnitude higher than the average values reported for the global ocean intermediate layer at mid-latitudes (Schroeder et al. 2017). These outcomes are also of great benefit for intercomparisons with numerical model results (as those in von Schuckmann et al. 2018, their Figure 3.4.3).

Warmer and drier regional climatic conditions over the eastern basin are favouring the formation of increasingly warmer and saltier intermediate water: indeed, the Levantine region in particular is undergoing a dramatic drought since the late 1990s (Cook et al. 2016), the driest period in the past 500 years. As a result, also the upper part of the Eastern Mediterranean deep waters is experiencing a warming (not shown) and a salinification (Figure 2.3.3(C)), as is evident from repeated CTD casts in the central Sicily Channel (between the islands of Pantelleria and Malta) that reach depths below 1700 m, where the upper part of the eastern deep water is found. The thermohaline evolution at this location has already been discussed in Gasparini et al. (2005), Ben Ismail et al. (2014) and Gačić et al. (2013). At any moment, the salinity profile shows a maximum at around 300 m depth, associated with the Levantine Intermediate Water. The temporal evolution reveals two maxima before the very recent period (until

2011), around 1992 and 2008, while since 2011 the layer is warming and becoming saltier at a much higher rate than before, each year reaching higher peak values within the water mass core. Since 2010–2011 this pattern is involving the whole water column down to 1700 m, where the deep water is now as warm and salty as it was the intermediate water during the peak in 2008.

2.4. Phytoplankton blooms in the Baltic Sea

Authors: Urmas Raudsepp, Jun She, Vittorio E. Brando, Rosalia Santoleri, Michela Sammartino, Mariliis Kõuts, Rivo Uiboupin, Ilja Maljutenko

Statement of outcome: The Baltic Sea phytoplankton bloom characteristics are evaluated based on spring and summer bloom statistics, summer chlorophyll-a and attenuation coefficient (Kd). Over the past 20 years, the mean start day of the spring bloom changed from day 120 in 1998 to around days 80–60 from the year 2003 onward. The intensity and spatial coverage of summer blooms decreased since 2009, and they tend to be more intensified in the subsurface layer. Low attenuation coefficient and chlorophyll-a anomaly, a late start date and early end date of the spring bloom, as well as low spatiotemporal coverage of the bloom show that the spring bloom in 2017 was exceptionally weak. Summer phytoplankton bloom was strong in the Gulf of Bothnia and dominated by subsurface bloom in 2016, but shifted to the northern Baltic Proper in 2017.

Products used:

Ref. No.	Product name and type	Documentation
2.4.1	OCEANCOLOUR_BAL_OPTICS_ L3_REP_OBSERVATIONS_ 009_097 Remote sensing	PUM: http://marine.copernicus.eu/ documents/PUM/CMEMS-OC-PUM-009-ALL.pdf QUID: http://marine.copernicus.eu/ documents/QUID/CMEMS-OC-QUID-009-080-097.pdf
2.4.2	OCEANCOLOUR_BAL_CHL_ L3_REP_OBSERVATIONS_ 009_080 Remote sensing	PUM: http://marine.copernicus.eu/ documents/PUM/CMEMS-OC-PUM-009-ALL.pdf QUID: http://marine.copernicus.eu/ documents/QUID/CMEMS-OC-QUID-009-080-097.pdf

Recently comprehensive classifications of eutrophication status of the Baltic Sea were made using the third version of the HELCOM Eutrophication Assessment Tool (HEAT 3.0), applying indicators with commonly agreed targets of good environmental status (HELCOM

2015). The indicators were grouped under three 'criteria': (1) nutrient levels (i.e. winter dissolved inorganic phosphate and nitrogen in the upper 10 m of the water column), (2) direct effects (summer chlorophyll-a in the upper 10 m and secchi depth) and (3) indirect effects (annual oxygen debt below the halocline and benthic invertebrates). Spring bloom has been less considered for the assessment of the Baltic Sea eutrophication. Here we propose that spring and summer bloom statistics, summer chlorophyll-a and attenuation coefficient (Kd) from the products 2.4.1 and 2.4.2 of the product table could be successfully used as one of the relevant indicators in evaluating the Baltic Sea eutrophication status. Annual oxygen content and nutrient conditions in the Baltic Sea will be subject of the forthcoming studies to complete the set of eutrophication status indicators of the Baltic Sea.

CMEMS ocean colour product references 2.4.1 and 2.4.2 provide a good spatiotemporal coverage of the surface bio-optical features in the Baltic Sea, although their uncertainties are still high ($r^2 = 0.4$, for chlorophyll-a, see Pitarch et al. 2016). The phytoplankton abundance and succession in the Baltic Sea are characterised by dinoflagellate- and diatom-dominated spring bloom and cyanobacterial summer bloom (Kahru and Nõmmann 1990; Kahru et al. 2018). The spring bloom (spring is from days 31 to 160) is detected using the Siegel (2002) approach (i.e. it is a spring bloom if chlorophyll-a > median + 5%) for each pixel in the basin, after which the statistics for the bloom onset are calculated as in Groetsch et al. (2016) and presented as distribution of the start, peak and end days over the whole basin per each year. The spring and summer bloom spatiotemporal coverage (day km^2) is aggregated from daily subsurface and surface bloom following Hansson and Håkansson (2007). Summer blooms are detected by applying the thresholds defined by Hansson et al. (2010) on remote sensing reflectance spectra (Rrs) at the wavelength of 550 nm and Rrs at 676 nm for the subsurface and surface blooms, respectively. Although 20 years of satellite data are available in the Baltic Sea, it should be noted that the remote sensing indexes computed by SMHI for HELCOM, recorded from 2010 onwards, should not be directly compared with the 1997–2009 values, as an improved detection method is now used (i.e. Hansson et al. 2010). The time series for Rrs, chlorophyll-a and attenuation coefficient (Kd490) used in this study are fully homogeneous as they are based on a merged product from different satellites that corrects for inter-sensor differences (Mélin et al. 2017; Sathyendranath et al. 2017). Attenuation coefficient values are proxies for Secchi depth, accounting for water transparency.

During 1998–2001, only SeaWiFS (O'Reilly et al. 1998) was available; while from the year 2002 onwards there are two or three sensors available (Brewin et al. 2015).

We observed the start, peak and end day of the spring bloom during the period of 1998–2017 from product reference 2.4.2 (Figure 2.4.1). In most years, the spring bloom starts first in the western and southern Baltic Sea, then in the central Baltic, and the latest in the Bothnian Sea and Bothnian Bay (Fennel 1999; Wan et al. 2013). This gives significant spatial variability to the starting date of the spring bloom in the Baltic Sea. However, there are also years when the spring bloom starts early, e.g. in 1985 and 1986 as shown by Kahru and Nõmmann (1990). The mean start day of the spring bloom shifted earlier during the observation period (from day 120 in 1998 to day 50 in 2015). According to the start day and spatial variability, most of the spring bloom can be divided into three types:

- late onset spring bloom (later than day 100) that shows small spatial variability in the Baltic Sea, evident in 1998–2002;
- medium onset spring bloom (around day 80) that has large spatial variability, mostly found in 2003–2011;
- early onset spring bloom (around day 60) with rather small spatial variability, mostly found in 2012–2016 (Figure 2.4.1(a)).

The year 2017 deviates from this trend of declining start day by a late onset spring bloom (days 80–120). It also differs from the previously mentioned three types of spring blooms due to its high spatial variability that can be inferred by the interquartile range (Figure 2.4.1 (a)). There is a good consistency between the start day and spatiotemporal coverage of spring bloom (Figure 2.4.2(a)) – in general, later start day results in smaller spatiotemporal coverage. The seven late onset spring bloom years, 1998–2002, 2006 and 2017 (Figure 2.4.1 (a)) also represent the lowest spatiotemporal coverage (Figure 2.4.2(a)). Although the top two years with the largest spatiotemporal coverage (2008 and 2011) are marked with earlier start day (day 55 and day 65), earlier start day does not always result in large spatiotemporal coverage, as found in the years 2012–2016. These years also have quite small spatial variability of the start day in the Baltic Sea. The end day of spring bloom has shifted slightly later, from days 145–148 to day 150 from 2002 onwards. The peak day of spring bloom has fluctuated with no clear trend.

Since 2002 the spring bloom spatiotemporal coverage has shown general tendency to increase until
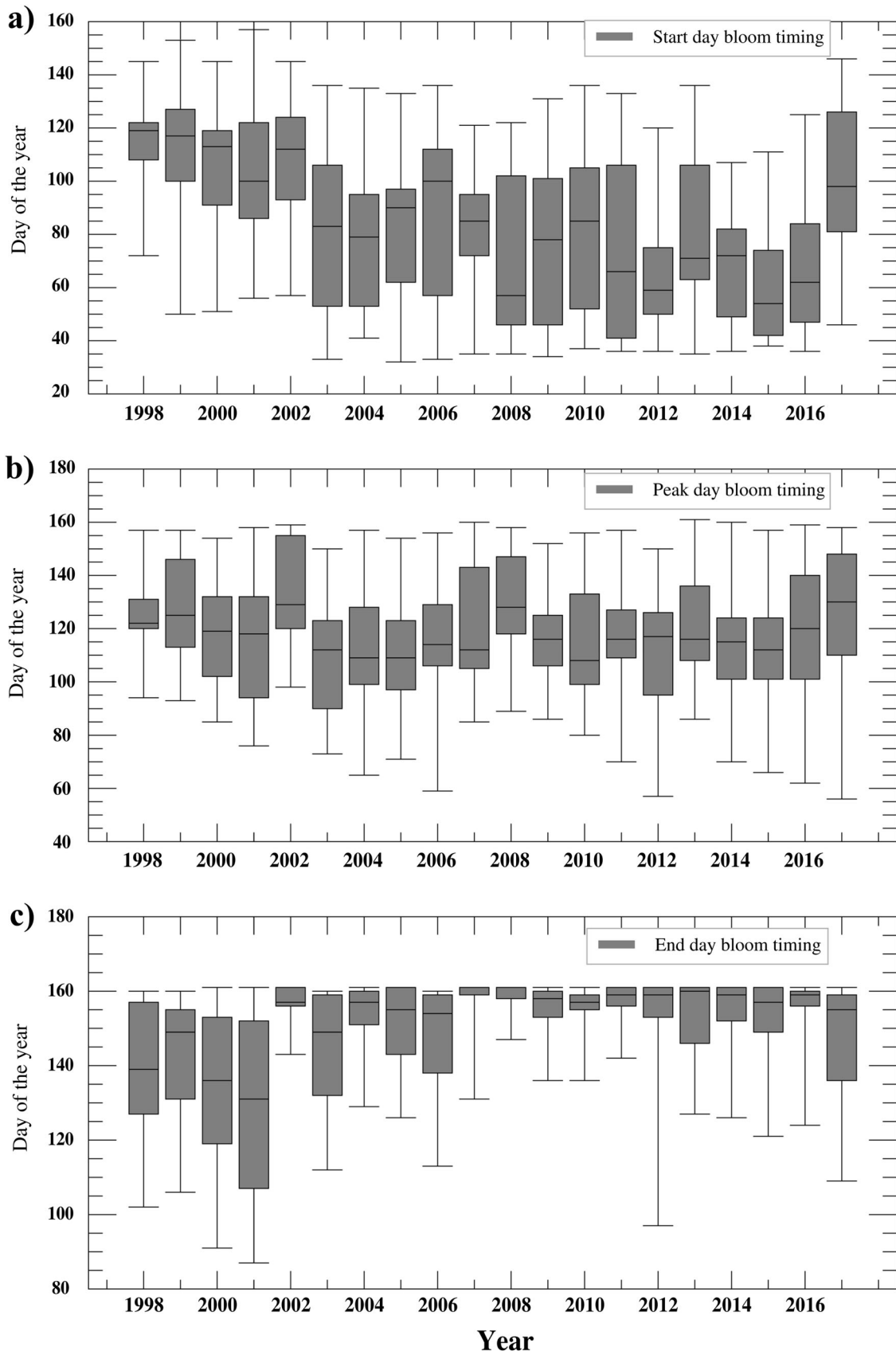
Figure 2.4.1. Time series of the spring bloom statistics (Siegel 2002; Groetsch et al. 2016) for start day (a), peak day (b), end day (c) for the period of 1998–2017 of the Baltic Sea from product reference 2.4.2. The bar refers to first quartile, median (black line) and third quartile, while the whiskers are the 5th and 95th percentiles respectively for start, peak and end days over the basin.
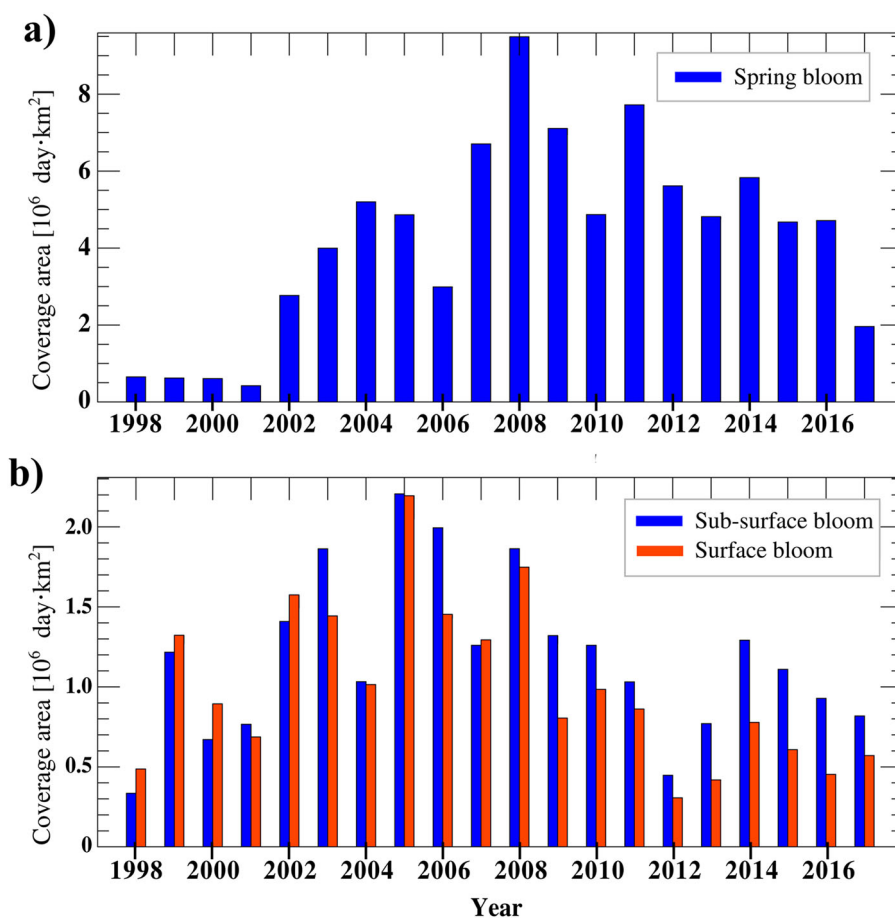
Figure 2.4.2. Time series of spring (a) and summer bloom (b) spatiotemporal coverage (day km^2) (1998–2017) using method by Hansson and Håkansson (2007). Results are based on CMEMS product reference 2.4.2 and 2.4.1 respectively.

2008–2011, followed by a decrease afterwards (Figure 2.4.2(a)). Spring blooms have been reported to weaken in intensity but lengthen during the period of 2000–2014 (Groetsch et al. 2016). Summer bloom coverage, however, increased from 1998 until 2005, and then decreased practically until present with a local minimum in 2012 (Figure 2.4.2(b)). Thus, high spatiotemporal coverage of the spring bloom is detected in 2007, 2008, 2009 and 2011, but peak years of the summer bloom spatiotemporal coverage are 2002, 2003, 2005 and 2008. There are several sub-periods of co-changes of the spatiotemporal coverage of the spring and summer blooms. For instance, the spring and summer blooms have a positive correlation in the period of 2013–2017. There is a slight positive trend in the spring bloom spatiotemporal coverage for the period of 2002–2011, whereas summer bloom shows a decreasing trend during the partially overlapping period of 2005–2012. Over the longer period of 1979–2017, the summer (cyanobacteria) blooms are reported to

be oscillating without a clear, significant trend (Kahru et al. 2018).

Since 2009, the summer bloom has been on a relatively low level, featured by more subsurface than surface bloom. The previous years (1998–2008) were dominated by the opposite feature (Figure 2.4.2(b)). The subsurface bloom declined continuously from 2014 to 2017, whereas the surface bloom increased in 2017, compared to the previous year.

One of the indicators of the eutrophication status of the Baltic Sea is secchi depth (HELCOM 2015) for which we use light attenuation coefficient (Kd) as proxy in this study. Summer mean attenuation coefficient (Kd) values in the Baltic Sea from the period of 1998–2017 derived from product reference 2.4.1. In open water light attenuation is mainly caused by phytoplankton species, while coloured dissolved organic matter (CDOM) and resuspended particulate matter are the main optically active substances in the coastal zone. Summer mean attenuation coefficient values derived from satellite remote sensing reflectance
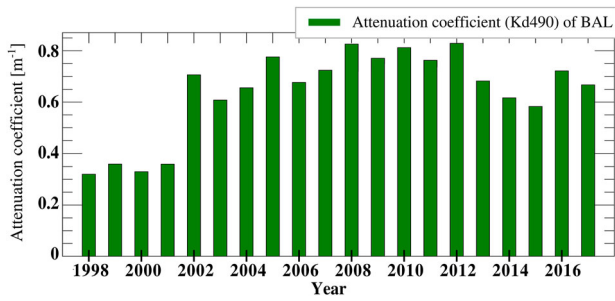
Figure 2.4.3. Time series of the attenuation coefficient (Kd490) averaged over the Baltic Sea in summer of 1998–2017 (product reference 2.4.1).

(Figure 2.4.3) stand for high values in the coastal zones, as reflected on the chlorophyll-a anomaly also (Figure 2.4.5).

In general, low attenuation coefficient values are observed in 1998–2001, followed by an increasing trend until 2010 and a decline until present. Last two years, i.e. 2016 and 2017, indicate an increase in summer mean attenuation coefficient values again. The attenuation coefficient anomaly in the summer of 2016 is positive over the entire sea area except for the eastern part of the Gulf of Finland (Figure 2.4.4(b)). Especially high values are observed in the Bay of Bothnia. In summer 2017, the area with positive attenuation coefficient anomaly has been reduced to the northern and eastern Baltic Proper and southern Gulf of Riga (Figure 2.4.4 (d)). The attenuation coefficient anomaly in the springs of 2016 and 2017 shows strong inter-annual changes (Figure 2.4.4(a,c)). Excluding the coastal areas close to the major river inlets, where coloured dissolved organic
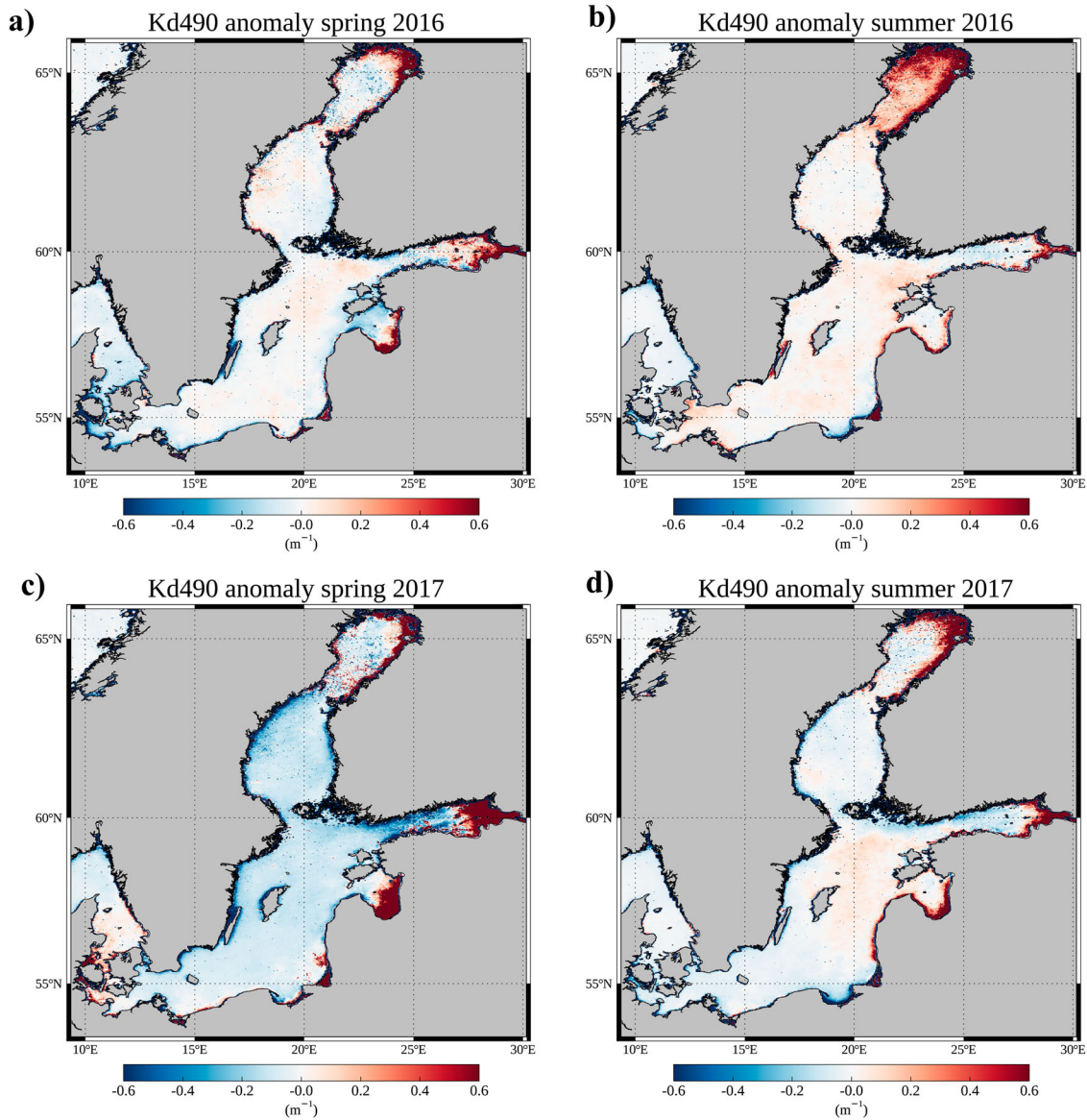
Figure 2.4.4. Attenuation coefficient (Kd) anomaly fields in spring 2016 (a) and 2017 (c) relative to the 1998–2014 spring mean field, and in summer 2016 (b) and 2017 (d) relative to the 1998–2014 summer mean field in the Baltic Sea. Data from product reference 2.4.1.
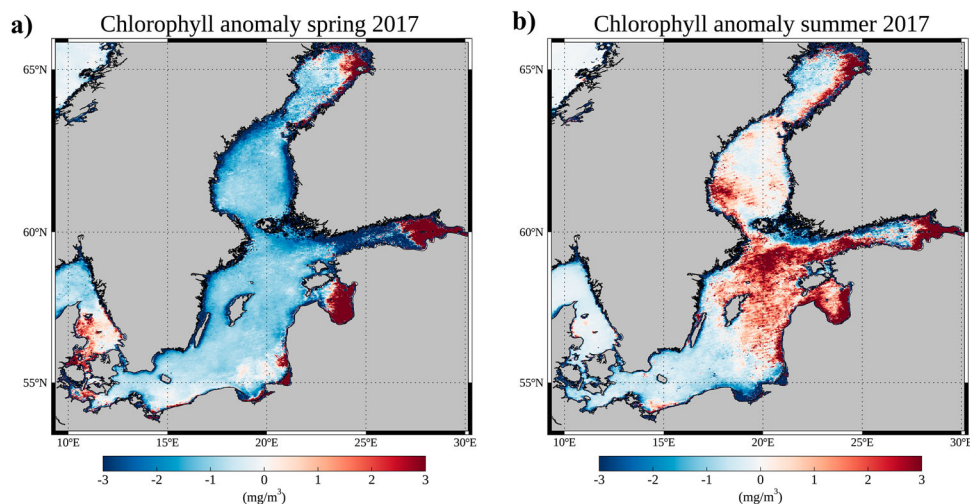
Figure 2.4.5. Chlorophyll-a anomaly fields in the Baltic Sea in spring 2017 relative to the 1998–2014 spring mean field (a) and in summer 2017 relative to the 1998–2014 summer mean field (b). Data from product reference 2.4.2.

matter could be a major contributor to the high attenuation coefficient values, elevated attenuation coefficient values are seen in the entire Baltic Proper and the Bothnian Sea. In spring 2017, attenuation coefficient anomaly is negative all over the Baltic Sea (Figure 2.4.4(c)). A very high positive attenuation coefficient anomaly in the southeastern Gulf of Riga and eastern Gulf of Finland could include contamination of attenuation coefficient values from ice coverage. The differences in the attenuation coefficient anomaly in the springs of 2016 and 2017 are well reflected in the spatio-temporal coverage of the spring bloom, with the 2017 spring bloom being less than half of the spring bloom in 2016 (Figure 2.4.2(a)). The attenuation coefficient anomaly in summer 2016 is higher than in 2017 (Figure 2.4.4(b,d)), which is reflected also in the summer mean attenuation coefficient values (Figure 2.4.3) and in the spatiotemporal coverage of subsurface bloom, but not in the surface bloom (Figure 2.4.2(b)). Measured phytoplankton wet weight during spring bloom has been substantially higher in 2016 than in 2017, but comparable in the summers of 2016 and 2017 (Wasmund et al. 2017, 2018). In general, by comparing time series of summer mean attenuation coefficient values and summer bloom spatiotemporal coverage (Figures 2.4.2(b) and 2.4.3), we conclude no obvious match of these two parameters.

Chlorophyll-a spring anomaly in 2017 showed high values in the Gulf of Riga and the eastern part of the Gulf of Finland. High values with a smaller extent were visible in the northern coastal area of the Bothnian Bay and coastal areas of the Gulf of Gdansk and the Curonian Lagoon. To a larger extent, lower values are evident in the western part of the Gulf of Finland. The spatial distributions of measured chlorophyll-a are versatile in the spring of 2017 (Wasmund et al. 2018). In March, chlorophyll-a concentrations show higher values near the Danish Straits, with decreasing gradient towards the Gotland Basin. In May, the spatial gradient of chlorophyll-a was reversed – chlorophyll-a concentrations were significantly higher in the eastern and southern Gotland basin and lower near the Danish Straits.

Chlorophyll-a summer anomaly in 2017 has highest values in the eastern part of the Gulf of Finland and the Gulf of Riga, which extend further in space, compared to same areas in 2016 (Raudsepp et al. 2018). Extensive high chlorophyll-a values in the northern Baltic Proper in 2017 are not visible in 2016. At the same time, high chlorophyll-a values, which are seen across the Bothnian Bay in 2016, are only limited to the eastern coast in 2017. Both years share similarly low summer chlorophyll-a anomaly values in the Gulf of Gdansk and on the coasts of Lithuania and Kaliningrad, except for the outflow area from Curonian lagoon. In summer 2017, spatial differences in measured chlorophyll-a concentrations were relatively uniform in the southern Baltic, but much higher in the Eastern Gotland basin (Wasmund et al. 2018).

2.5. Cod reproductive volume potential in the Baltic Sea

Authors: Urmas Raudsepp, Ilja Maljutenko, Mariliis Kõuts

Statement of outcome: Cod (*Gadus morhua*) is a characteristic fish species in the Baltic Sea with major economic importance. The Baltic cod stocks have
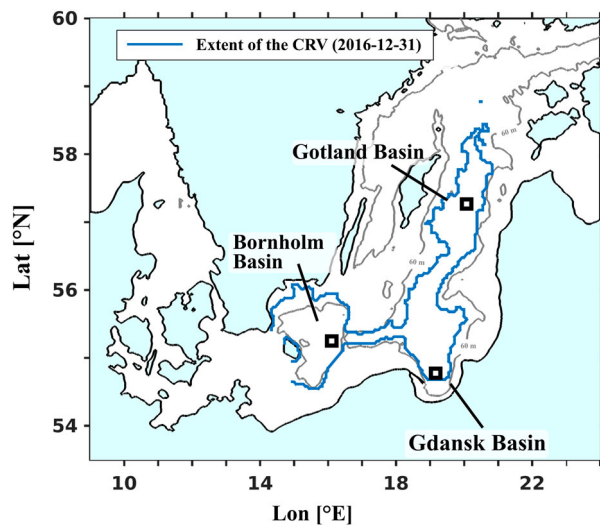
Figure 2.5.1. Map of the Southern Baltic Sea showing locations of the basins. Sixty metre isodepth is marked with grey line. Blue contour show geographical extent of cod reproductive volume (CRV) for 2016-12-31 based on CMEMS product reference 2.5.1 and 2.5.2.

gone through a steep decline in the late 1980s (ICES 2016). In this section we focus on the impact of the Major Baltic Inflows on the eastern cod population. Hydrographic conditions affect cod directly through the survival of eggs. Our results indicate that the water volume with suitable conditions for cod reproduction has stayed mostly on the same level during the period of 1993–2017. We verify the importance of the Major Baltic Inflows shaping a suitable environment for cod reproduction and the Bornholm basin as the most important spawning ground. Cod reproductive volume is on a relatively stable level in the Bornholm basin, while highly dependent on inflows in the downstream basins. Available data about the Major Baltic Inflows can be used as an indicator of important biological processes.

Products used:

Ref. No.	Product name and type	Documentation
2.5.1	BALTICSEA_REANALYSIS_PHY_ 003_011 Reanalysis	PUM: http://marine.copernicus.eu/ documents/PUM/CMEMS-BAL-PUM-003-011.pdf QUID: http://marine.copernicus.eu/ documents/QUID/CMEMS-BAL-QUID-003-011.pdf
2.5.2	BALTICSEA_REANALYSIS_PHY_ 003_012 Reanalysis	PUM: http://marine.copernicus.eu/ documents/PUM/CMEMS-BAL-PUM-003-012.pdf QUID: http://marine.copernicus.eu/ documents/QUID/CMEMS-BAL-QUID-003-012.pdf

Atlantic cod (*Gadus morhu*a) is a major fish species of the Baltic Sea with high economic importance. The Baltic Sea cod consists of two genetically different populations – eastern and western Baltic cod. We focus on the eastern cod as it contributes to the landing numbers the most and has several spawning grounds in the deep areas of the Baltic Sea, east of Bornholm island. The eastern Baltic cod stock has been at the absolute low since the 1980s (ICES 2005; FishSource). There are two sets of governing factors – anthropogenic and natural. Anthropogenic effects mostly manifest through high fishing pressure. Natural conditions vary in the Baltic Sea in relation to water exchange with the North Sea – the Major Baltic Inflows in particular, which create the specific environmental conditions for cod to reproduce. We focus on the Major Baltic Inflows, the most important controlling factor of cod recruitment in the Baltic Sea (MacKenzie et al. 1996; Köster et al. 2005). The dramatic decline of cod stocks overlaps with the decrease in the frequency and intensity of the North Sea advections in the late 1980s (Heikinheimo 2008). Recruitment started to decline in the mid-1980s despite the spawning stock and the number of eggs produced by old females still being high (Cardinale and Arrhenius 2000). There was no significant change in fishing pressure during that period (ICES 2005). This implies that other factors besides fishing might have been important (Heikinheimo 2008). Hydrographic factors affect cod recruitment directly through the survival of eggs, and indirectly via species composition and availability of the prey organisms which are essential for cod larvae survival (Heikinheimo 2008). As a result, cod reproduction in the eastern areas of the sea, including the Gdansk Deep, almost completely ceased and continued only in the Bornholm Basin (Nielsen 1998). Karasiova (2011) found a positive correlation between the interannual fluctuations of egg production and water volumes with conditions favourable for cod reproduction in the four main spawning areas in the Baltic Sea.

The Bornholm Basin is the most important spawning ground for the eastern Baltic cod stock, followed by the Gotland and Gdansk basins (MacKenzie et al. 1996; Hinrichsen et al. 2017) (Figure 2.5.1). In order to describe the relationship between cod reproduction and the Major Baltic Inflows we use 'cod reproductive volume' (CRV), which is based on previous research and takes into account the three most important influencing factors of cod reproductive success: salinity over 11 g/kg (product reference 2.5.1), oxygen content > 2 ml/l (product reference 2.5.2) and water temperature over 1.5°C (product reference 2.5.1) (MacKenzie et al. 1996; Heikinheimo 2008; Plikshs

et al. 2015). Our aim is to derive the reproductive potential of the eastern Baltic cod from dynamics, characteristics and volume of the inflowing water and compare these results with the published numbers. This approach enables to use available data about Major Baltic Inflows as an indicator for important biological processes, which could be of use in evaluating the status and development of Baltic cod stocks in the future. The boundary of the Baltic Sea has been taken from the western boundary of the Bornholm Basin according to the ICES fishery subdivisions.

Our results show that the cod reproductive volume has been more or less stable in the Bornholm Basin during the period of 1993–2017 (Figure 2.5.2(a)). There were periods of elevated cod reproductive volume in the Baltic Sea in 2003–2004, 2006–first half of the 2007, 2014–first half of the 2015 and 2016, which contribute to a small positive trend of 8.8 km^3/year over the study period. Saline water volume of the Baltic Sea, however, shows considerable increase since the 1993 Major Baltic Inflow (Figure 2.5.2(a)) and due to the following inflows in 1997, 2003 and 2014. Cod biomass values were estimated to be slightly higher around 2010, which might reflect the period with sufficient conditions after 2003 (Karasiova 2011). This is in an agreement with the

highest values of cod stock size indicator (Figure 2.5.2(a)). The ICES stock size indicator is a combined biomass index, in kg/h, of cod ≥30 cm from the Baltic International Trawl Survey (BITS) in quarters 1 and 4 in the Baltic Sea subdivisions of 25–28 (ICES 2018). Also, egg counts responded to Major Baltic Inflows with higher values in 1994, 1997 and 2003 (Karasiova 2011). The cod reproductive volume is in minimum in 2000 and in 2011 with the values comparable to low cod reproductive volume values at the end of the stagnation period in the Baltic. The saline water volume has never dropped to a value comparable to the value at the end of the stagnation period. The lowest saline water volume values can be seen in the Baltic Sea in 2002 and 2013.

There is a strong positive correlation between cod reproductive volume and saline water volume in the Bornholm Basin ($R^2 = 0.82$) and the two volumes vary less compared to the rest of the Baltic Sea (Figure 2.5.2(a)). In the Bornholm Basin, average saline water volume and cod reproductive volume are 315 km^3 (SD = 59 km^3) and 220 km^3 (SD = 80 km^3), respectively. In the rest of the Baltic Sea, the saline water volume is associated with Major Baltic Inflows – the larger the inflow, the bigger the volume of salty water that goes to other basins. The impact of the inflow events was bigger following the inflows of
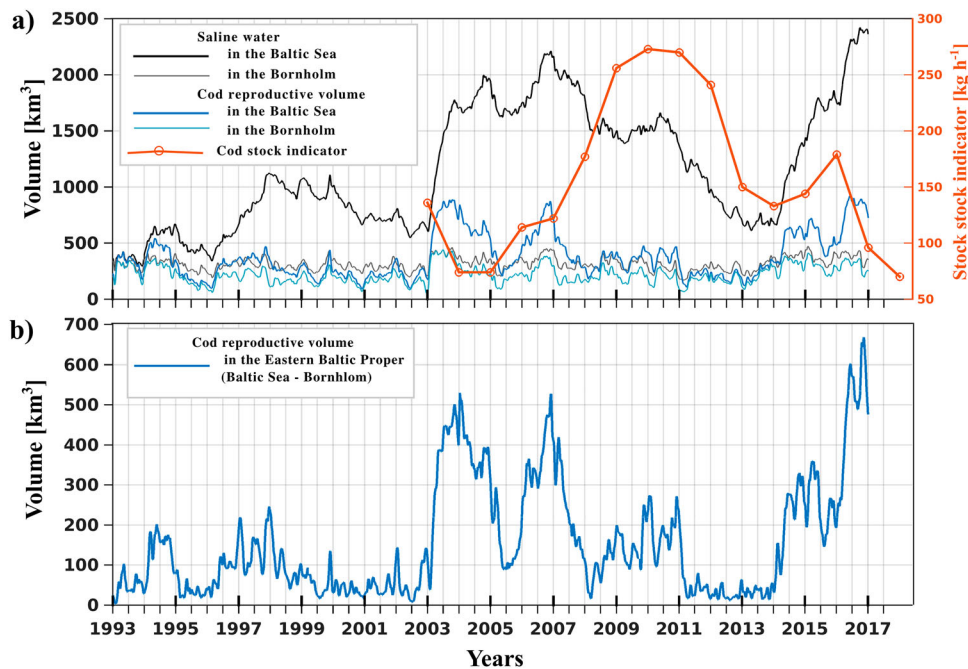
Figure 2.5.2. (a) Time series of saline water volumes (SWV, S > 11 g/kg) black line and cod reproductive volumes (CRV) in the Baltic Proper (thick lines), excluding Arkona Basin; and in Bornholm Basin (thin lines); and cod stock size indicator. Dots in the red line represent the geometric mean of the biomass of ≥30 cod specimens in the previous year from the Baltic International Trawl Survey in subdivisions 25–28. (b) Time series of cod reproductive volume (CRV, S > 11 g/kg, O$_2$ > 2 ml/l) extending outside the Bornholm Basin. Time series are calculated from CMEMS product reference 2.5.1 and 2.5.2.

2003 and 2014. Similarly to salinity, increase in cod reproductive volume reflects the impact of the Major Baltic Inflows to the basins downstream of the Bornholm Basin (Figure 2.5.2(a,b)). Suitable conditions for cod reproduction persist for a shorter time period (Figure 2.5.2(b)) than that of the saline water volume (Figure 2.5.2(a)) which means that oxygen content declines faster than salinity in the bottom layers of the Baltic Sea (Raudsepp et al. 2018).

The effect of the Major Baltic Inflows on cod reproduction has been studied earlier and results indicate that the effect can be small to important based on the pre-existing hydrological conditions, which determine how big the potential spawning area will be. The inflow of 1993–1995 had a small effect because the conditions before did not predispose the formation of large spawning areas, while the effect of the Major Baltic Inflow in 2003 was bigger (Karaseva and Zezera 2016). We used data from ICES to compare our values with the stock size indicator. The data fits our model results with increased cod reproductive volume having a positive effect on cod reproduction success, which reflects in an increase of stock size indicator ca. 4–5 years after the Major Baltic Inflow. The inflow in 2003 resulted in an increased stock size between 2007 and 2012 (Figure 2.5.2(a)). Eastern Baltic cod reaches maturity around age 2–3, depending on the population density and environmental conditions. Lack of oxygen and low salinity cause stress, which negatively affects cod recruitment, whereas sufficient conditions may bring about male cod maturation even at the age of 1.5 years (Cardinale and Modin 1999; Karasiova et al. 2008). Since there was a Major Baltic Inflow again in 2014, which increased the cod reproductive volume up to 900 km^3 in the Baltic Sea (Figure 2.5.2(a)), we expect an increase of cod stock size starting from 2018–2019.

2.6. The North Pacific Gyre Oscillation

Authors: Benoît Tranchant, Isabelle Pujol, Emanuele Di Lorenzo, Jean-François Legeais

Statement of main outcome: The North Pacific Gyre Oscillation is defined as the second dominant mode of variability of SSH anomaly and SST anomaly in the North East Pacific. This mode emerges as the leading mode of decadal variability for surface salinity and upper ocean nutrients, and is in a negative phase since 2014. This condition reflects a reduced amplitude of the central and eastern branches of the North Pacific gyre, corresponding to a reduced coastal upwelling and thus a lower sea surface salinity and concentration of nutrients. Here, this indicator is inferred from a long time series of

SSH anomalies over the North East Pacific (25°–62°N, 180°–250°E) and will be regularly updated.

Product used:

Ref. No.	Product name and type	Documentation
2.6.1	SSH anomalies Numerical Ocean Model	Di Lorenzo et al. (2008)
2.6.2	SSS anomalies Observations	Scripps Pier measurements collected by the Birch Aquarium at Scripps staff and volunteers. Data provided by the Shore Stations Program sponsored at Scripps Institution of Oceanography by California State Parks, Division of Boating and Waterways. Contact: shorestation@ucsd.edu.
2.6.3	NCEP wind stress 1950–2004 Numerical Atmospheric Model	The NCEP/NCAR 40-Year Reanalysis Project (Kalnay et al. 1996)
2.6.4	Altimeter data: previous version of SEALEVEL_GLO_PHY_L4_REP_OBSERVATIONS_008_047 (see below) Remote sensing	Product User Manual (CMEMS-SL-PUM-008-032-051) http://marine.copernicus.eu/documents/PUM/CMEMS-SL-PUM-008-032-051.pdf Quality Information Document (CMEMS-SL-QUID-008-032-051) http://marine.copernicus.eu/documents/QUID/CMEMS-SL-QUID-008-032-051.pdf
2.6.5	SEALEVEL_GLO_PHY_L4_REP_OBSERVATIONS_008_047 Remote sensing	Product User Manual (CMEMS-SL-PUM-008-032-051) http://marine.copernicus.eu/documents/PUM/CMEMS-SL-PUM-008-032-051.pdf Quality Information Document (CMEMS-SL-QUID-008-032-051) http://marine.copernicus.eu/documents/QUID/CMEMS-SL-QUID-008-032-051.pdf
2.6.6	SEALEVEL_GLO_PHY_L4_REP_OBSERVATIONS_008_046 Remote sensing	Product User Manual (CMEMS-SL-PUM-008-032-051) http://marine.copernicus.eu/documents/PUM/CMEMS-SL-PUM-008-032-051.pdf Quality Information Document (CMEMS-SL-QUID-008-032-051) http://marine.copernicus.eu/documents/QUID/CMEMS-SL-QUID-008-032-051.pdf

The Decadal North Pacific Gyre Oscillation is a climate pattern defined by Di Lorenzo et al. (2008). The North Pacific Gyre Oscillation term is used because its
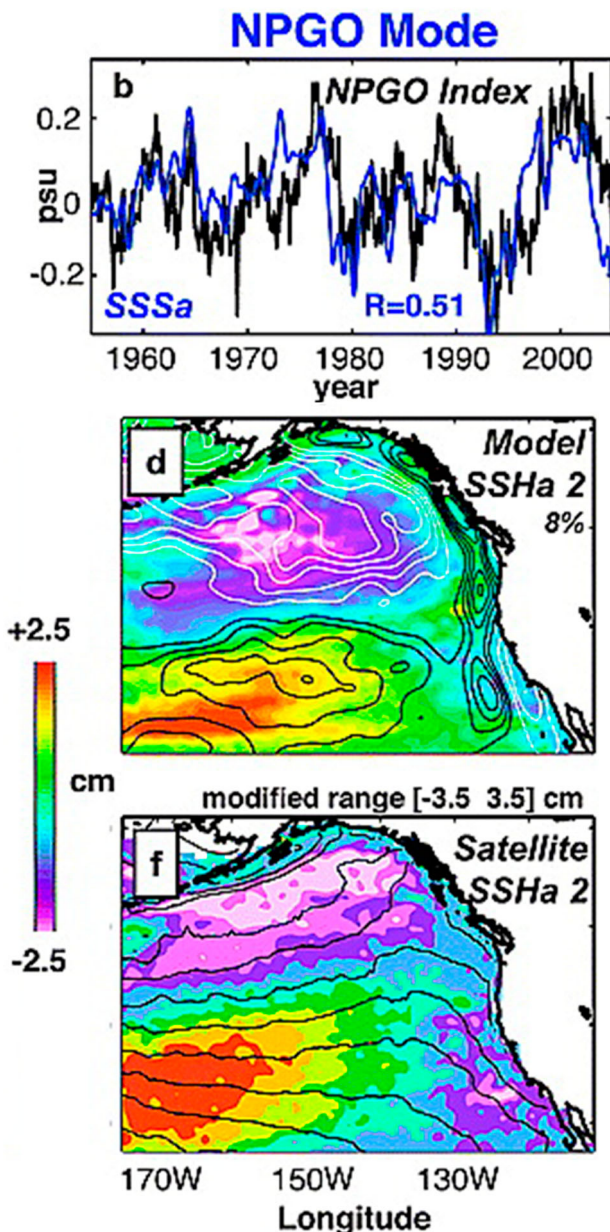
Figure 2.6.1. (b) Time series of La Jolla Scripps Pier SSSa (reference product 2.6.2) (blue) compared to the NPGO index (correlation $R = 0.51$, 99% significance), defined as the second PC of model SSHa (black). The SSSa records are detrended and a 12 months running mean is applied. (d) Regression maps of model NPGO indices with the model SSHa. The white (black) contours indicate regions of positive (negative) wind stress curl (Ekman upwelling) as inferred from a regression of the model PCs with the NCEP wind stress curl (reference product 2.6.3). The % variance accounted for by each regression map is indicated. (f) Regression maps of the model NPGO index with satellite altimeter data gathered between 1993 and 2004 (reference product 2.6.4). The colour range is modified to [3.5 3.5] in Figure 2(f) to properly display the map (black contours are satellite/drifter-derived mean dynamic height [Niiler et al. 2003]). Credit from Di Lorenzo et al. (2008).

fluctuations reflect changes in the intensity of the central and eastern branches of the North Pacific gyre circulations. Thus, it has been defined as the 2nd dominant mode of sea surface height variability in the Northeast Pacific (25°–62°N, 180°–250°E, see Figure 2.6.1(d,f)). The North Pacific Gyre Oscillation index has been defined as the second Principal Component of model Sea Surface Height anomaly calculated over the period 1950–2004 (reference product 2.6.1), see Figure 2.6.1(b). Di Lorenzo et al. (2008) suggest that the North Pacific Gyre Oscillation is the oceanic expression of the atmospheric North Pacific Oscillation (Walker and Bliss 1932). This seems reinforced by the recent work of Yi et al. (2018) that show consistent pattern feature between the atmospheric North Pacific Oscillation and the oceanic North Pacific Gyre Oscillation.

This index measures change in the North Pacific gyres circulation and explains key physical-biological ocean variables including temperature, salinity, sea level, nutrients, chlorophyll-a. One example is the coherent variation of model and observed/modelled SSS (Sea Surface Salinity) in the Northeast Pacific (Di Lorenzo et al. 2008), see Figure 2.6.1(b). Like the Pacific decadal oscillation, the North Pacific Gyre Oscillation is a basin-scale feature and captures prominent low-frequency changes in the Pacific physical and biological fields. This is why the North Pacific Gyre Oscillation index provides a strong indicator of fluctuations in the mechanisms driving planktonic ecosystem dynamics.

A positive North Pacific Gyre Oscillation phase is a dipole pattern with negative SSH anomaly north of 40°N and the opposite south of 40°N. The North Pacific Gyre Oscillation index is presently in a negative phase, associated with a positive SSH anomaly north of 40°N and negative south of 40°N. This reflects a reduced amplitude of the central and eastern branches of the North Pacific gyre, corresponding to a reduced coastal upwelling and thus a lower sea surface salinity and concentration of nutrients.

The EOF's amplitude pattern (pers. Comm. Di Lorenzo) has been inferred from the principal component analysis. This regression map of the model North Pacific Gyre Oscillation index is used/projected with normalised satellite altimeter delayed-time sea level anomalies to calculate and update the NPGO index. An example is given on Figure 2.6.2 where the NPGO index has been projected on the last version of the reprocessed altimeter sea level record (CMEMS reference product 2.6.5).

North Pacific Gyre Oscillation indicator
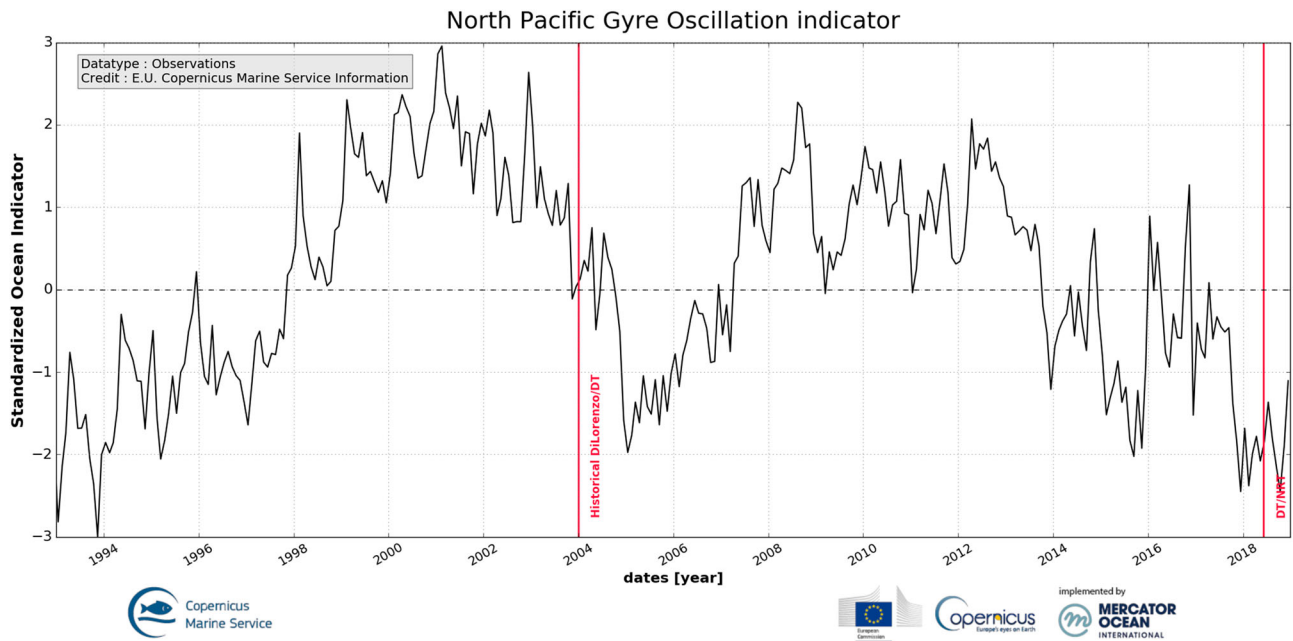
Figure 2.6.2. NPGO index monthly averages. From 1993 to 2003, the NPGO index is calculated from ref. 2.6.4, see Di Lorenzo et al. (2008). From 2004 onward, the NPGO index has been projected on normalised satellite altimeter Delayed-Time (DT) (CMEMS reference product 2.6.5) and Near-Real-Time (NRT) (CMEMS reference product 2.6.6).

2.7. Sea level, sea surface temperature and SWH extreme percentiles: combined analysis from model results and in situ observations

Authors: Enrique Álvarez Fanjul, Álvaro de Pascual Collar, Begoña Pérez Gómez, Marta De Alfonso, Marcos García Sotillo, Joanna Staneva, Emanuela Clementi, Alessandro Grandi, Anna Zacharioudaki, Gerasimos Korres, Michalis Ravdas, Richard Renshaw, Jonathan Tinker, Urmas Raudsepp, Priidik Lagemaa, Ilja Maljutenko, Gerhard Geyer, Malte Müller, Veli Çağlar Yumruktepe

Statement of main outcome: This section explores the temporal and spatial variability of the extremes of sea level, waves and sea surface temperature over European seas and the Arctic region. The analysis combines information from both in-situ observations and model data available through CMEMS, demonstrating the potential of the service and the benefits of merging observational and modelled products. The main outcomes of this joint analysis of anomalies in 2017 relative to long-term average conditions include: (i) sea level extremes variability was near average in all coastal areas of Europe and the Arctic except for a few stations in the UK, west of Normandy and the northwestern Gulf of Bothnia in the Baltic, (ii) wave extremes were larger than usual in most of the Iberia-Biscay-Ireland region (anomalies of significant wave height about +0.5 m) and in the western Mediterranean Sea (+0.75 m) and lower than usual in the eastern Mediterranean and near the Irish coast (−0.5 m). In the Black Sea,

the usual spatial pattern is inverted, being the largest extremes on the eastern and central areas (up to 0.7 m). (iii) Sea surface temperature extremes anomalies were strongly positive in most of the Mediterranean Sea, typically by +1°C, and in the Northern Arctic regions reaching as high as +6°C. Negative anomalies were found in the Baltic (up to −3°C) and the North Sea (∼−1°C).

Products used:

Ref. No.	Product name and type	Documentation
2.7.1	INSITU_IBI_TS_REP_ OBSERVATIONS_013_040 Observations reprocessed	PUM: http://marine.copernicus.eu/ documents/PUM/CMEMS-INS-PUM-013.pdf QUID: http://marine.copernicus.eu/ documents/QUID/CMEMS-INS-QUID-013-040.pdf
2.7.2	INSITU_NWS_TS_REP_ OBSERVATIONS_013_043 Observations reprocessed	PUM: http://marine.copernicus.eu/ documents/PUM/CMEMS-INS-PUM-013.pdf QUID: http://marine.copernicus.eu/ documents/QUID/CMEMS-INS-QUID-013-043.pdf
2.7.3	INSITU_MED_TS_ REP_OBSERVATIONS_ 013_041 Observations reprocessed	PUM: http://marine.copernicus.eu/ documents/PUM/CMEMS-INS-PUM-013.pdf QUID: http://marine.copernicus.eu/ documents/QUID/CMEMS-INS-QUID-013-041.pdf
2.7.4	INSITU_BAL_TS_ REP_OBSERVATIONS_ 013_038 Observations reprocessed	PUM: http://marine.copernicus.eu/ documents/PUM/CMEMS-INS-PUM-013.pdf QUID: http://marine.copernicus.eu/ documents/QUID/CMEMS-INS-QUID-013-038.pdf

(*Continued*)

Continued.

Ref. No.	Product name and type	Documentation
2.7.5	INSITU_IBI_NRT_ OBSERVATIONS_ 013_033 Observations	PUM: http://marine.copernicus.eu/ documents/PUM/CMEMS-INS-PUM-013.pdf QUID: http://marine.copernicus.eu/ documents/QUID/CMEMS-INS-QUID-013-030-036.pdf
2.7.6	INSITU_NWS_NRT_ OBSERVATIONS_013_036 Observations	PUM: http://marine.copernicus.eu/ documents/PUM/CMEMS-INS-PUM-013.pdf QUID: http://marine.copernicus.eu/ documents/QUID/CMEMS-INS-QUID-013-030-036.pdf
2.7.7	INSITU_MED_NRT_ OBSERVATIONS_013_035 Observations	PUM: http://marine.copernicus.eu/ documents/PUM/CMEMS-INS-PUM-013.pdf QUID: http://marine.copernicus.eu/ documents/QUID/CMEMS-INS-QUID-013-030-036.pdf
2.7.8	INSITU_BAL_NRT_ OBSERVATIONS_013_032 Observations	PUM: http://marine.copernicus.eu/ documents/PUM/CMEMS-INS-PUM-013.pdf QUID: http://marine.copernicus.eu/ documents/QUID/CMEMS-INS-QUID-013-030-036.pdf
2.7.9	INSITU_GLO_NRT_ OBSERVATIONS_013_030 Observations	PUM: http://marine.copernicus.eu/ documents/PUM/CMEMS-INS-PUM-013.pdf QUID: http://marine.copernicus.eu/ documents/QUID/CMEMS-INS-QUID-013-030-036.pdf
2.7.10	IBI_REANALYSIS_ PHYS_005_002 Model reanalysis	PUM: http://marine.copernicus.eu/ documents/PUM/CMEMS-IBI-PUM-005-002.pdf QUID: http://marine.copernicus.eu/ documents/QUID/CMEMS-IBI-QUID-005-002.pdf
2.7.11	IBI_ANALYSIS_ FORECAST_ WAV_005_005 Model analysis	PUM: http://marine.copernicus.eu/ documents/PUM/CMEMS-IBI-PUM-005-005.pdf QUID: http://marine.copernicus.eu/ documents/QUID/CMEMS-IBI-QUID-005-005.pdf
2.7.12	IBI_ANALYSIS_ FORECAST_PHYS _005_001 Model analysis	PUM: http://marine.copernicus.eu/ documents/PUM/CMEMS-IBI-PUM-005-001.pdf QUID: http://marine.copernicus.eu/ documents/QUID/CMEMS-IBI-QUID-005-001.pdf
2.7.13	BLKSEA_ANALYSIS _FORECAST_WAV_ 007_003 Model analysis	PUM: http://marine.copernicus.eu/ documents/PUM/CMEMS-BS-PUM-007-003.pdf QUID: http://marine.copernicus.eu/ documents/QUID/CMEMS-BS-QUID-007-003.pdf
2.7.14	BLKSEA_REANALYSIS_ WAV_007_006 Model reanalysis	PUM: http://marine.copernicus.eu/ documents/QUID/CMEMS-BS-QUID-007-006.pdf QUID: http://marine.copernicus.eu/ documents/PUM/CMEMS-BS-PUM-007-006.pdf
2.7.15	MEDSEA_REANALYSIS_ PHYS_006_004 Model reanalysis	PUM: http://marine.copernicus.eu/ documents/PUM/CMEMS-MED-PUM-006-004.pdf QUID: http://marine.copernicus.eu/ documents/QUID/CMEMS-MED-QUID-006-004.pdf DOI: https://doi.org/10.25423/ medsea_reanalysis_phys_006_ 004, Simoncelli et al. (2014)

(Continued)

Continued.

Ref. No.	Product name and type	Documentation
2.7.16	MEDSEA_HINDCAST_ WAV_006_012 (period 2006–2017) Model hindcast	PUM: http://marine.copernicus.eu/ documents/PUM/CMEMS-MED-PUM-006-012.pdf QUID: http://marine.copernicus.eu/ documents/PUM/CMEMS-MED-QUID-006-012.pdf
2.7.17	NORTHWESTSHELF_ ANALYSIS_FORECAST_ PHYS_004_001_b Model analysis	PUM: http://marine.copernicus.eu/ documents/PUM/CMEMS-NWS-PUM-004-001.pdf QUID: http://marine.copernicus.eu/ documents/QUID/CMEMS-NWS-QUID-004-001-b.pdf
2.7.18	NORTHWESTSHELF_ REANALYSIS_PHYS _004_009 Model reanalysis	PUM: http://marine.copernicus.eu/ documents/PUM/CMEMS-NWS-PUM-004-009-011.pdf QUID: http://marine.copernicus.eu/ documents/QUID/CMEMS-NWS-QUID-004-009-011.pdf
2.7.19	BALTICSEA_ANALYSIS _FORECAST_PHY _003_006 Model analysis	PUM: http://marine.copernicus.eu/ documents/QUID/CMEMS-BAL-QUID-003-006.pdf QUID: http://marine.copernicus.eu/ documents/PUM/CMEMS-BAL-PUM-003-006.pdf
2.7.20	BALTICSEA_REANALYSIS _PHY_003_011 Model reanalysis	PUM: http://marine.copernicus.eu/ documents/PUM/CMEMS-BAL-PUM-003-011.pdf QUID: http://marine.copernicus.eu/ documents/QUID/CMEMS-BAL-QUID-003-011.pdf
2.7.21	BALTICSEA_ANALYSIS _FORECAST_WAV_ 003_010 Model analysis	PUM: http://marine.copernicus.eu/ documents/PUM/CMEMS-BAL-PUM-003-010.pdf QUID: http://marine.copernicus.eu/ documents/QUID/CMEMS-BAL-QUID-003-010.pdf
2.7.22	IBI_REANALYSIS_ WAV_005_006 Model reanalysis	PUM: http://marine.copernicus.eu/ documents/PUM/CMEMS-IBI-PUM-005-006.pdf QUID: http://marine.copernicus.eu/ documents/QUID/CMEMS-IBI-QUID-005-006.pdf
2.7.23	MEDSEA_ANALYSIS_ FORECAST_PHY_ 006_013 Model analysis	PUM: http://marine.copernicus.eu/ documents/PUM/CMEMS-MED-PUM-006-013.pdf QUID: http://marine.copernicus.eu/ documents/QUID/CMEMS-MED-QUID-006-013.pdf
2.7.24	MEDSEA_ANALYSIS _FORECAST _WAV_006_017 Model analysis	PUM: http://marine.copernicus.eu/ documents/PUM/CMEMS-MED-PUM-006-017.pdf QUID: http://marine.copernicus.eu/ documents/QUID/CMEMS-MED-QUID-006-017.pdf
2.10.21	ARCTIC_ANALYSIS _FORECAST_PHYS _002_001_a Model analysis	PUM: http://marine.copernicus.eu/ documents/PUM/CMEMS-ARC-PUM-002-ALL.pdf QUID: http://marine.copernicus.eu/ documents/QUID/CMEMS-ARC-QUID-002-001a.pdf
2.10.22	ARCTIC_REANALYSIS _PHYS_002_003 Model reanalysis	PUM: http://marine.copernicus.eu/ documents/PUM/CMEMS-ARC-PUM-002-ALL.pdf QUID: http://marine.copernicus.eu/ documents/QUID/CMEMS-ARC-QUID-002-003.pdf

The first step of the methodology employed is to compute the 99th mean annual percentile for each Essential Ocean Variables, and for both observations and models. This is calculated as the mean of the 99th percentile from

Figure 2.7.1. Map of mean 99th percentile significant wave height computed from reanalysis model data and *in situ* measurements (inset circles) for the Iberian-Biscay-Ireland region (a) (product ref. 2.7.22 and 2.7.1), Mediterranean Sea (c) (product ref. 2.7.16 and 2.7.3) and Black sea (e) (product ref. 2.7.14). Map of 99th percentile anomaly in 2017 for the Iberian-Biscay-Ireland region (b) (product ref. 2.7.11 and 2.7.5), Mediterranean Sea (b) (product ref. 2.7.24 and 2.7.7) and Black sea (f) (product ref. 2.7.13).

each year of data, from 1993 to 2016 for sea level, and from 2000 to 2016 for waves and sea surface temperature. Once the datasets based on models and observations are obtained, results from buoys and tide gauges are superimposed on the percentile maps generated from the model multi-year products (Figures 2.7.1–2.7.3 – left panels). In a second step, this process is repeated for the data of year 2017. Finally, 2017 and mean data are subtracted, producing, for each variable, a 2017 anomaly map (Figures 2.7.1–2.7.3 – right panels). For in-situ data, a minimum number of years (15 for tide

gauges and 10 for buoys) with a percentage of valid measurements larger than 70% is required for a station to be included in the study. To avoid problems related to changes in reference level, all sea level data was detrended by subtracting each year the annual mean. This does not affect the main objective of the study, to analyse how anomalous 2017 was in terms of extremes.

For several regions the lack of data at CMEMS made impossible the analysis of some variables, as shown in the following sections.

2.7.1. Extremes variability in the Iberian-Biscay-Ireland area.

Waves

Figure 2.7.1(a) shows that wave extremes vary with latitude (Pontes 1998), being larger in northern seas (99th percentile larger than 8 m). The buoys in the area show results consistent with the model. Some exceptions are present, corresponding to some stations that are moored in shallow water (i.e. Gijón coastal buoy to the north of Spain), were local effects are not resolved by the model.

The year 2017 shows positive anomalies in most of the domain (Figure 2.7.1(b)), with values up to 1 m. In contrast, the anomalies are negative west of Ireland (−1 m) and around 34°N. The map of 2017 anomalies, presenting bands of positive and negative values depending on latitude, is consistent with the well-known yearly North–South displacement of the storm tracks. These latitudinal displacements alter the wind patterns over the region and, therefore, the extreme waves.

In general, there is good agreement between the 2017 data from model (product ref. 2.7.11) and from observations (product ref. 2.7.5), but with some exceptions. Off the North coast of Spain, some buoys show negative anomalies in a region where the model shows positive values. This is most likely linked to extreme values not captured by the buoys due to malfunction during severe individual storm events.

Sea Surface Temperature

Sea surface temperature mean 99th percentile in the Iberian-Biscay-Ireland area (Figure 2.7.2(a)) is strongly dependent on latitude, with higher values towards the South (Locarnini et al. 2013). Also visible is the upwelling signal off the African and western Iberian Peninsula coasts, present because the maximum extreme values
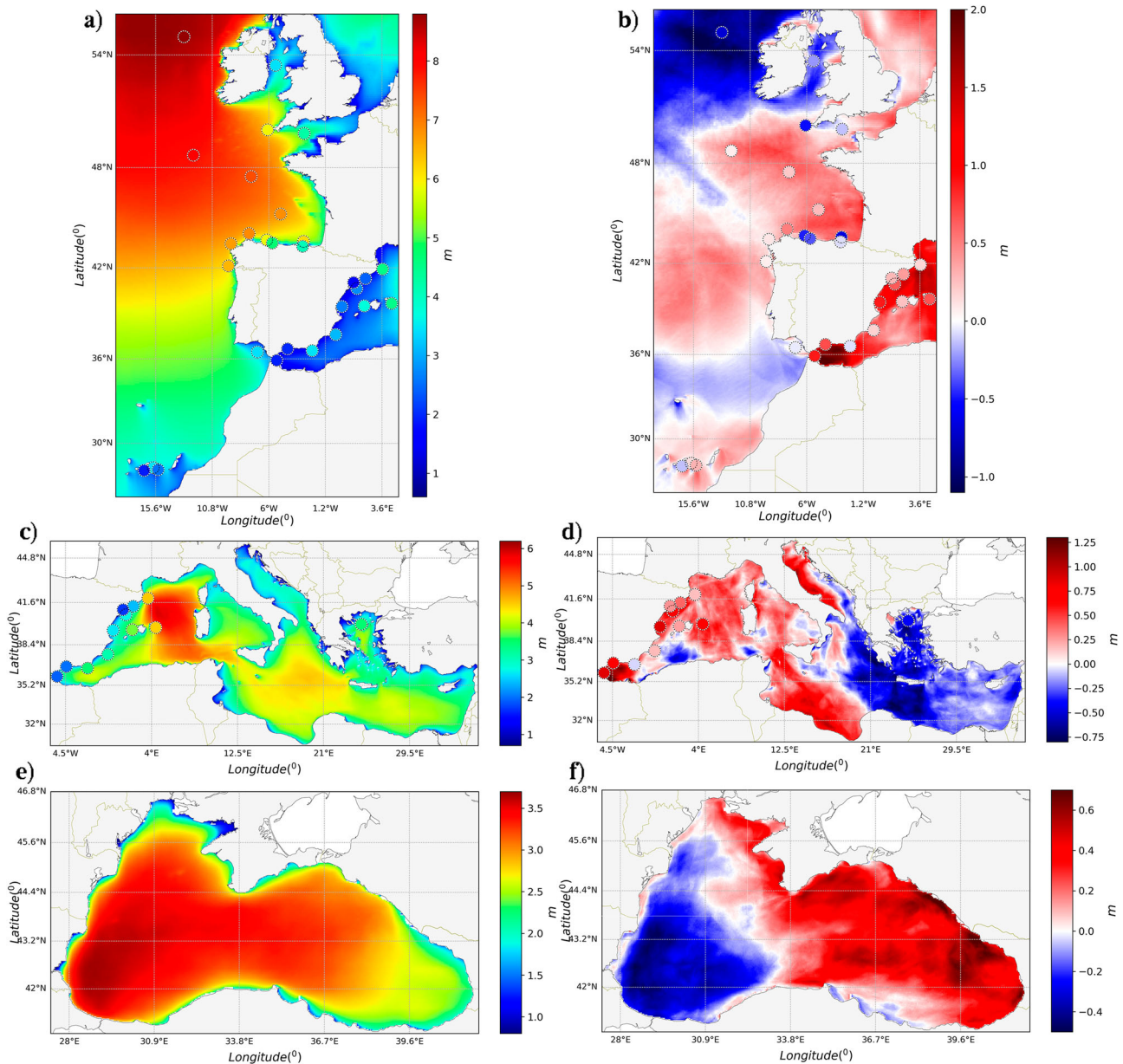

Figure 2.7.2. Map of mean 99th percentile sea surface temperature computed from reanalysis model data and *in situ* measurements (inset circles) for the Iberian-Biscay-Ireland region (a) (product ref. 2.7.10 and 2.7.1), North-West Shelf region (b) (product ref. 2.7.18 and 2.7.2), Mediterranean Sea (e) (product ref. 2.7.15 and 2.7.3), Baltic Sea (g) (product ref. 2.7.20 and 2.7.4) and Arctic Ocean (h) (product ref. 2.7.26). Map of 99th percentile anomaly in 2017 for the Iberian-Biscay-Ireland region (c) (product ref. 2.7.12 and 2.7.5), North-West Shelf region (d) (product ref. 2.7.17 and 2.7.6), Mediterranean Sea (f) (product ref. 2.7.23 and 2.7.7), Baltic Sea (g) (product ref. 2.7.19 and 2.7.8) and Arctic Ocean (h) (product ref. 2.7.25).

occur in summer, coinciding with upwelling events (Ambar and Días 2008)

The level of consistency with in-situ measurements (product ref. 2.7.1) is excellent. This agreement is due to the accuracy of the modelled product and because sea surface temperature extremes occur in the summer, when malfunctions on the buoys are rare due to mild weather conditions, and therefore high values are usually properly captured.

Results for 2017 (Figure 2.7.2(c)) show negative anomalies in most of the Atlantic domain, with values around −1°C, except in a band centred at 42°N and in the south, around the Canary Islands, where positive values can be found (∼1°C). The African coast shows a positive anomaly of the extremes, reflecting a weaker than usual upwelling during the extreme temperature events at the region. Positive anomalies can also be seen in the English Channel. Buoy and model results for 2017 extremes are in good agreement.

Sea Level

Spatial differences in the mean 99th percentile of sea level reflect mainly the large differences in tidal amplitude in the region (Figure 2.7.3(a)): highest sea levels are found in the waters surrounding the British Isles and in the English Channel, where the astronomical tide is amplified (Pugh 2004). The mean 99th percentile of sea level is in considerable agreement for both model and *in situ* data at most of the stations.

Figure 2.7.3(b) shows positive anomalies (<0.1 m) for year 2017 below 40°N in the Atlantic, and negative values northwards. These anomalies agree well for both model and tide gauge data along the Spanish coast (very small and even negative anomalies in year 2017) and in the Mediterranean part of the Iberian-Biscay-Ireland domain, where sea level variability is lower (tide amplitude <0.5 m). Largest positive and negative anomalies for year 2017 (−0.3 to 0.5 m) are present around the British Isles and the English Channel.

In the Western coast of the British Isles the mean percentiles from the model are in generally good agreement with tide gauge data. This is clear in higher resolution plots (not shown). However, the anomalies for year 2017 reveal differences between tide gauge data (very small or zero values) and model data (larger positive and negative values). Differences in this overlapping region between this model and the one used for the North-West Shelf analysis (product ref. 2.7.17 and 2.7.18) are also evident. This is due to different astronomical tide propagation in the two different configurations of the Iberian-Biscay-Ireland model for the period 1993–2016 (product ref. 2.7.10) and for year 2017 (product ref. 2.7.12): both models have different spatial resolutions (1/12° vs. 1/36° respectively) and this is important for modelling the astronomical

tide in coastal regions with complex bathymetry and orography (Shum et al. 1997; Turner et al. 2013).

2.7.2. Extremes variability in North-West Shelf region

Sea Surface Temperature

The mean results (Figure 2.7.2(b)) show the latitudinal dependence of 99th percentile sea surface temperature, with values ranging from 22°C at 40°N to 9°C near Iceland. The shallower waters of the North Sea present warmer extreme values than those at equivalent latitudes in the Atlantic.

2017 (Figure 2.7.2(d)) show positive anomalies in north and south of the domain. There is an extensive area of positive anomaly in the north-east region, extending to the coast of Iceland. This warm anomaly extends onto the North-West Shelf around north-eastern Scotland and is possibly advected with the Fair Isle current into the North Sea. This is also visible around north-eastern Scotland, from Aberdeen to north of the Orkneys, and near the Hebrides. There is a positive anomaly extending from the English Channel into the Southern Bight of the southern North Sea, which is coincident in both the North-West Shelf and Iberian-Biscay-Ireland model domains. There is a narrow band of positive anomaly along the coast of the northern part of the Bay of Biscay, near Nantes, although the exact extent varies between the North-West Shelf and Iberian-Biscay-Ireland domains. Anomaly values are negative in the rest of the domain, especially near the Baltic Sea and south of the Scandinavian Peninsula.

In general, model and in-situ results are very consistent.

Sea Level

The annual mean of the 99th percentile sea level map (product ref. 2.7.18) for the North-West Shelf reflects the spatial distribution of tidal ranges (Figure 2.7.3(c)), consistent with the M_2 amplitude co-tidal chart (O'Dea et al. 2012, 2017). Mean 99th percentiles model reanalysis data (product ref. 2.7.18) are consistent (Figure 2.7.3(c)) with the tide gauge data (product ref. 2.7.2).

The 2017 99th percentile value is very similar to that of the reanalysis period over most of the domain, in both pattern and amplitude (not shown) and this is reflected by the anomaly map (Figure 2.7.3(d)) which has values ranging from −10 cm to +40 cm. The largest differences occur in the North Sea, with 2017 being up to 30 cm higher in 2017, than in the mean. This is particularly significant when looking at the percentage differences (not shown) as the mean tidal ranges are relatively low here (see Figure 2.7.3(c)) – 2017 was >60% higher than in

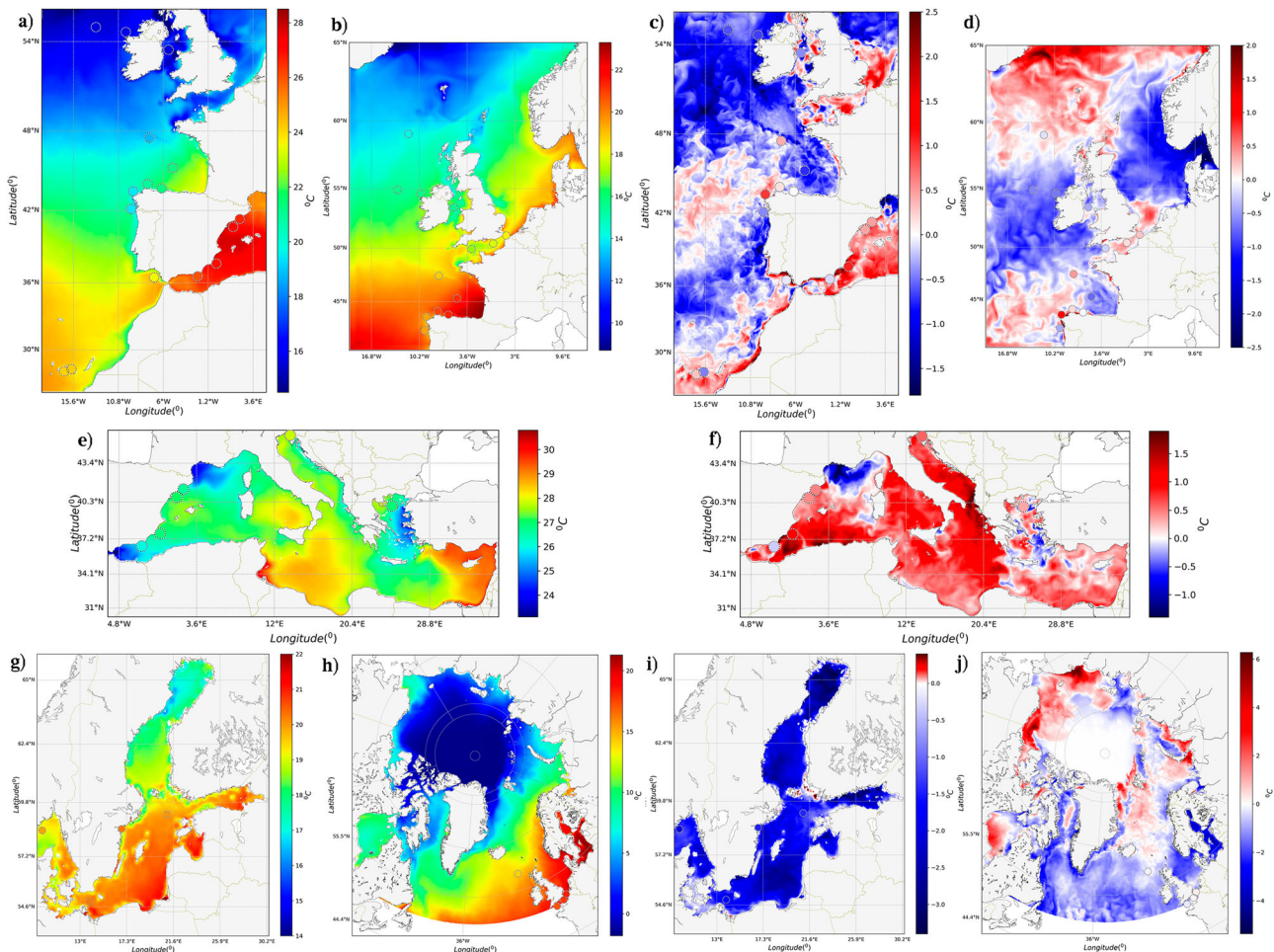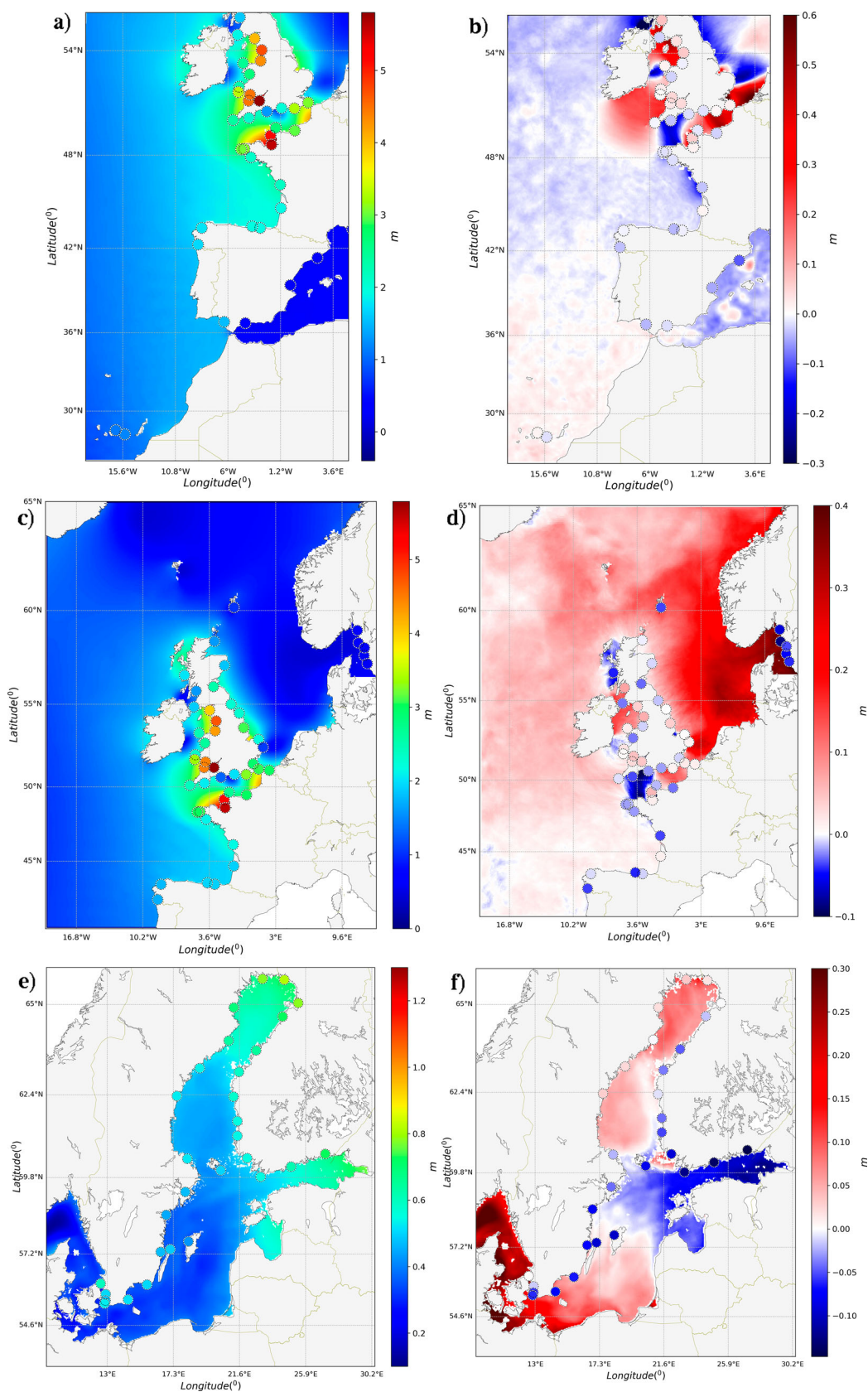**Figure 2.7.3.** Map of mean 99th percentile sea level computed from reanalysis model data and *in situ* measurements (inset circles) for the Iberian-Biscay-Ireland region (a) (product ref. 2.7.10 and 2.7.1), North-West Shelf region (c) (product ref. 2.7.18 and 2.7.2) and Baltic Sea (e) (product ref. 2.7.20 and 2.7.4). Map of 99th percentile anomaly in 2017 for the Iberian-Biscay-Ireland region (b) (product ref. 2.7.12, 2.7.5 and 2.7.9), North-West Shelf region (d) (product ref. 2.7.17, 2.7.6 and 2.7.9) and Baltic Sea (f) (product ref. 2.7.19 and 2.7.8).

the reanalysis period. This appears to be a large difference in the western English Channel, with the 2017 extreme sea levels being less than in the reanalysis period, by ∼10 cm, but given the large tidal range here, is ∼10% lower.

Interestingly, in the Skagerrak and Kattegat there is a disagreement between the model and *in situ* anomalies (up to 40 cm difference), with the tide gauges showing a negative anomaly, while the model shows a positive bias. This is likely a result of the Baltic boundary conditions used in the North-West Shelf reanalysis. There is a relatively good agreement between the model and tide gauges anomalies around the UK.

North-West Shelf and Iberian-Biscay-Ireland model generally a good spatial agreement. Both show the negative anomaly in the eastern English Channel, and across the centre of the Irish Sea, with adjacent positive anomaly in the western English Channel and Celtic Sea, and Irish Sea. To the west of the UK there is a large difference in the sea level anomaly, with the Iberian-Biscay-Ireland showing a negative anomaly in the central and northern North Sea. This difference could be related, as previously discussed, to the different Iberian-Biscay-Ireland tidal solutions in reanalysis and operational products.

2.7.3. Extremes variability in the Mediterranean region
Waves
Figure 2.7.1(c) shows that the highest values of the mean annual 99th percentile are located where high winds and long fetch are simultaneously present. Specifically, such values extend from the Gulf of Lion to southwestern Sardinia through the Balearic Sea. They result from northerly winds dominant in the western Mediterranean Sea (Mistral or Tramontana), that are accelerated by orography (Menendez et al. 2014) and act over a large area. In the Ionian Sea, the northerly Mistral wind is still the main cause of high waves whilst in the Aegean and Levantine Seas, high waves are caused by the northerly Bora winds, prevalent in winter, and the northerly Etesian winds, prevalent in summer (Lionello et al. 2006; Chronis et al. 2011; Menendez et al. 2014).

During the year 2017 (Figure 2.7.1(d)), the positive anomalies in the west (up to 1.25 m) and central-west Mediterranean and the negative anomalies in the east (up to −0.75 m) are in turn indicative of stronger than usual winds in the former case and weaker than usual in the latter. Model data and in-situ data show consistent results.

Sea Surface Temperature
The mean annual 99th percentile (Figure 2.7.2(e)) in the period 1993–2016 presents lower values in the Alborán

Sea, linked to the inflow of cold Atlantic waters through the Gibraltar Strait, in the Gulf of Lion, caused by the strong Mistral wind, and in the North Aegean Sea, which also can be explained by the action of local winds; while highest sea surface temperature values are mainly located in the Levantine Sea, which is the warmest area of the Mediterranean Sea, and in the Gulf of Gabes.

Results for the year 2017 (Figure 2.7.2(f)) are characterised by very large positive anomalies in most of the domain, with maximum value of around 1.8°C. Negative anomalies are located in limited areas (Gulf of Lion and Eastern Aegean Sea) with values down to −1.5°C.

2.7.4. Extremes variability in the Baltic region
Waves
The distribution of extreme significant wave heights during 2017 from product reference 2.7.21 corresponds to the fetch limited wind waves generated by prevailing westerly and south-westerly winds (Isemer et al. 2008). The highest significant wave heights up to 4.5 m were in the southeastern Baltic Proper remaining over 4 m until the entrance of the Gulf of Finland. In the Gulf of Finland wave growth is limited by the narrowness of the gulf (Tuomi et al. 2011) and therefore percentiles remain in range of 2–3 m. In the northern Baltic extreme significant wave heights reach up to 4 and 3.5 m in Bothnian Sea and Bothnian Bay respectively.

It is worth to mention, nevertheless, that results from the wave field for the year 2017 (not shown) are in good agreement with the data from the two buoys available at the region.

There is no multi-year CMEMS wave product available for the Baltic at this moment. Therefore the 2017 anomaly values can't be computed. However, the differences were evaluated using published results of extreme wave heights from long-term wave field simulations (Björkqvist et al. 2017). The wave conditions in the Bothnian Bay were more severe in 2017 exceeding long-term percentiles by approximately 0.50 m. In the rest of the Baltic the 2017 significant wave height extremes remained within the range of ±0.25 m to the reported long-term percentiles by Björkqvist et al. (2017). In the calculation of wave statistics for 99th percentiles Björkqvist et al. (2017) excluded wave data from the calculations during ice covered period, while in CMEMS zero significant wave height values were used.

Sea Surface Temperature
Mean sea surface temperature extremes (product reference 2.7.20) show latitudinal gradient with temperatures in range of 20–22°C in the southern and 17–19°C in the northern part (Figure 2.7.2(g)). Lower sea surface

temperature values along the western coast of the Baltic Sea represent the most frequent upwelling areas (Myrberg and Andrejev 2003; Lehmann et al. 2008, 2012) in response to the prevailing winds from the southwest (Isemer et al. 2008). In the Gulf of Finland, low temperature is obvious along both the northern and the southern coasts. These low value regions are due to coastal upwelling during different periods. The upwelling area along the northern coast is more extensive than along the southern coast, but the sea surface temperature values are slightly higher. The western part of the southern coast of the Gulf of Finland is described with lower sea surface temperature and wider offshore extent of the upwelling zone. The upwelling in the area is caused by strong wind events from the northeast. This peculiarity arises from shallower thermocline position and steeper slope on the southern coast of the Gulf of Finland (Kikas and Lips 2016). The eastern part of the southern Gulf of Finland is less affected by the upwellings, as there the sea surface temperature does not distinguish from the open sea area. Only long-lasting winds from the east or sequence of the storm from the east can cause intensive upwelling and drop of the sea surface temperature there (Suursaar and Aps 2007; Väli et al. 2011).

2017 presents a very clear negative anomaly over the whole domain (Figure 2.7.2(i)), both at the measuring stations (product ref. 2.7.8) and in the model data (product ref. 2.7.19). Sea surface temperature extremes show differences of −2 to −3°C from the mean. There are clear signals of upwelling events along the northern and eastern coasts of the Baltic Proper as well as on the northern coast of the Gulf of Finland. This corresponds to typical upwelling pattern with prevailing south-westerly winds. Especially distinctive is the upwelling zone extending along the northern coast of the Gulf of Finland, which is clearly visible on maps of sea surface temperature extremes for 2017 (not shown). There was no major upwellings on the southern coast of the Gulf of Finland, therefore the anomaly shows higher temperatures there compared to offshore/background differences.

Sea Level
Mean sea level 99th percentiles range from approximately 0.4–0.8 m (Figure 2.7.3(e)) in the Baltic (product reference 2.7.20). The extremes in the Baltic Sea are mainly caused by wind setup amplified by the seiches and remotely generated long waves (Hünicke et al. 2015). The extremes are underestimated by about 0.1 m in the model. The discrepancy increases towards the southern Baltic Sea, being largest in the Danish Sounds. This could be attributed to the possible mismatch between model and measurements in the transition zone between the North Sea and the Baltic Sea.

The sea level extremes are slightly lower in the open part of the sea compared to the coastal areas, affected by the wind setup.

The anomaly of the sea level extremes in 2017 (Figure 2.7.3(f)) is in the range of ±0.15 m and −0.15–0.05 m in the model (product reference 2.7.19) and in the measurements (product ref. 2.7.8), respectively, which are not significant differences from the long-term mean extremes. Within this small range of variation, the model and measurements tend to agree in the Gulf of Bothnia and in the Gulf of Finland. The most notable differences are for the southern part of the Baltic Proper, where model results/measurements show higher/lower sea level extremes than the long-term mean. At the local scale, the model shows high sea level around the Archipelago Sea, but the measurements have lower extremes there. Obviously, local positive sea level anomalies there are a model artefact, as measurements show continuous increase in sea level anomaly from the Gulf of Finland through the Archipelago Sea to the Bothnian Sea.

2.7.5. Extremes variability in the Black Sea region
Waves
Since there are no available wave observations in this region matching the requirements of this study, the analysis for this domain is based on model data only. Figure 2.7.1(e) shows a well-known pattern demonstrating that the highest values of the mean annual 99th percentile are in the areas where high winds and long fetch are simultaneously present (from multi-year wave product ref. 2.7.14). The mean extreme values in the region tend to be largest in the western Black Sea, with values as high as 3.5 m. Values in the eastern part of the basin are around 2.5 m (Behrens et al. 2019).

In 2017 (product reference 2.7.13), the highest values of the 99th percentile are in the central part of the basin (between 34 and 36 deg. E, not shown). In consequence, the anomaly values for 2017 show a strong longitudinal dependency, with negative anomalies in the western part of the Black Sea (up to 0.5 m) and positive ones in the central and eastern Black Sea (up to 0.7 m, Figure 2.7.1(f)). Results from wave fields for 2017 are in good agreement with satellite data (Jason-3 and Sentinel-3a) as well as with the Varna wave-buoy, showing values of mean SWH up to 1.8 m in the centre of the Black Sea. (Quality Information Document of 2.7.13 product).

2.7.6. Extremes variability in the Arctic region
Sea Surface Temperature
The distribution of the mean annual 99th percentile of sea surface temperature (Figure 2.7.2(h)) reflects the

dominant currents of the region. The warmest waters with the subarctic (10–20°C) occur within the region of the northern European continental shelf and the North Atlantic Current, as well as within its extension through the Nordic Seas (Wekerle et al. 2017) and into the Barents Sea (Skagseth 2008). Relatively warmer (5–10°C) waters also extend northward to the west of Svalbard (Seidov et al. 2015) carried by the western branch of the Norwegian Atlantic Current. The Bering Strait connects the Arctic to the Pacific and exhibits relatively warm surface waters (>5°C) which extend into the Chukchi Sea (Seidov et al. 2015). Cold Polar Surface Water (Rudels 2015) which exists throughout the Arctic basin extends southwards through the Canadian Arctic Archipelago and along the east coast of Greenland, due to presence of the Greenland boundary current.

Anomalies of SST within the Arctic region and its extended domain during 2017 show a complex regional pattern of positive and negative anomalies. Negative anomalies are found throughout the northern Atlantic and much of the Canadian archipelago and the Laptev Sea. Positive anomalies of up to 6°C are found in the East Siberian Sea, the Beaufort Sea and the coastal regions of the Kara Sea. Positive anomalies of up to 3°C are seen throughout the Greenland Sea and in the northern Barents Sea. Positive anomalies of up to 4°C occur in the Chukchi Sea and in Hudson Bay.

References

Section 2.1. Sea surface winds and Ekman pumping

Bakun A, Black BA, Bograd SJ, Garcia Reyes M, Miller AJ, Rykaczewski RR, Sydeman WJ. 2015. Anticipated effects of climate change on coastal upwelling ecosystems. Curr Clim Change Rep. 1:85. doi:10.1007/s40641-015-0008-4.

Belmonte Rivas M, Stoffelen A. 2019. Characterizing ERA-Interim and ERA5 surface wind biases using ASCAT. Ocean Sci. 15:831–852. doi:10.5194/os-15-831-2019.

Bograd SJ, Lynn RJ. 2001. Physical-biological coupling in the California current during the 1997–99 El Niño-La Niña cycle. Geophys Res Lett. 28(2):275–278. doi:10.1029/2000GL012047.

Chen G, Han W, Li Y, Wang D. 2016. Interannual variability of equatorial eastern Indian ocean upwelling: local versus remote forcing. J Phys Oceanogr. 46:789–807. doi:10.1175/JPO-D-15-0117.1.

de Kloe J, Stoffelen A, Verhoef A. 2017. Improved use of scatterometer measurements by using stress-equivalent reference winds. IEEE J Sel Topics Appl Earth Observ In Remote Sens. 10(5). doi:10.1109/JSTARS.2017.2685242.

Ekman VW. 1905. On the influence of the Earth's rotation on ocean-currents. Arkiv for Matematik, Astronomi och Fysik. 2(11):1–52.

Hall A, Visbeck M. 2002. Synchronous variability in the southern hemisphere atmosphere, sea ice, and ocean resulting from the annular mode. J Clim. 15:3043–3057. doi:10.1175/1520-0442(2002)015<3043:SVITSH>2.0.CO;2.

Holland PR, Kwok R. 2012. Wind-driven trends in Antarctic sea-ice drift. Nature Geosc. 5:872–875. doi:10.1038/ngeo1627.

Large WG, McWilliams JC, Doney SC. 1994. Oceanic vertical mixing: a review and a model with a nonlocal boundary layer parameterization. Rev Geophys. 32(4):363–403. doi:10.1029/94RG01872.

Lorenz EN. 1955. Available potential energy and the maintenance of the general circulation. Tellus. 7:157–167. doi:10.1111/j.2153-3490.1955.tb011148.x.

Pelegri JL, Marrero-Diaz A, Ratsimandresy AW. 2006. Nutrient irrigation in the North Atlantic. Prog in Oceanogr. 70:366–406. doi:10.1016/j.pocean.2006.03.018.

Raphael MN, Marshall GJ, Turner J, Fogt RL, Schneider D, Dixon DA, Hosking JS, Jones JM, Hobbs WR. 2016. The Amundsen sea low: variability, change, and impact on Antarctic climate. Bull Am Meteorol Soc. 97:111–121. doi:10.1175/BAMS-D-14-00018.1.

Risien CM, Chelton DB. 2008. A global climatology of surface wind and wind stress fields from eight years of Quikscat scatterometer data. J Phys Oceanogr. 38:2379–2413. doi:10.1175/2008JPO3881.1.

Spall MA, Pickart RS. 2003. Wind-driven recirculations and exchange in the Labrador and Irminger Seas. J Phys Oceanogr. 33:1829–1845. doi:10.1175/2384.1.

Thompson DWJ, Solomon S. 2002. Interpretation of recent Southern Hemisphere climate change. Science. 296:895–899. doi:10.1126/science.1069270.

Turner J, Phillips T, Hosking JS, Marshall GJ, Orr A. 2013. The Amundsen sea low. Int J Clim. 33(7):1818–1829. doi:10.1002/joc.3558.

Section 2.2. The seasonal intensification of the slope Iberian Poleward Current

Charria G, Lazure P, Le Cann B, Serpette A, Reverdin G, Louazel S, Batifoulier F, Dumas F, Pichon A, Morel Y. 2013. Surface layer circulation derived from Lagrangian drifters in the Bay of Biscay. J Mar Syst. 109–110:S60–S76.

Declerck A, Delpey M, Rubio A, Ferrer L, Basurko OC, Mader J, Louzao M. 2019. Transport of floating marine litter in the coastal area of the south-eastern Bay of Biscay: A Lagrangian approach using modelling and observations. J Oper Oceanogr. doi:10.1080/1755876X.2019.1611708.

González M, Uriarte A, Fontán A, Mader J, Gyssels P. 2004. Marine dynamics. In: Borja A, Collins M, editors. Oceanography and marine environment of the Basque Country. Vol. 70, Elsevier Oceanography Series. Amsterdam: Elsevier; p. 133–157.

Herbert G, Ayoub N, Marsaleix P, Lyard F. 2011. Signature of the coastal circulation variability in altimetric data in the southern Bay of Biscay during winter and fall 2004. J Mar Syst. 88(2):139–158. doi:10.1016/j.jmarsys.2011.03.004.

Kaplan DM, Lekien F. 2007. Spatial interpolation and filtering of surface current data based on open-boundary modal analysis. J Geophys Res Oceans. 112:C12007. doi:10.1029/2006JC003984.

Lazure P. 1997. La circulation des eaux dans le Golfe de Gascogne. In: 10émes rencontres interregionales de l'AGLIA. Saint Jean de Luz; p. 83–88.

Le Cann B, Serpette A. 2009. Intense warm and saline upper ocean inflow in the southern Bay of Biscay in autumn-winter 2006–2007. Cont Shelf Res. 29(8):1014–1025.

Pingree RD, Le Cann B. 1992. Three anticyclonic Slope Water Oceanic eDDIES (SWODDIES) in the southern Bay of Biscay in 1990. Deep-Sea Res. 39(7/8):1147–1175.

Rubio A, Caballero A, Orfila A, Hernández-Carrasco I, Ferrer L, González M, Solabarrieta L, Mader J. 2018. Eddy-induced cross-shelf export of high Chl-a coastal waters in the SE Bay of Biscay. Remote Sens Environ. 205. doi:10.1016/j.rse.2017.10.037.

Rubio A, Fontán A, Lazure P, González M, Valencia V, Ferrer L, Mader J, Hernández C. 2013. Seasonal to tidal variability of currents and temperature in waters of the continental slope, SE Bay of Biscay. J Mar Syst. 109–110:S121–S133.

Rubio A, Reverdin G, Fontán A, González M, Mader J. 2011. Mapping near-inertial variability in the SE Bay of Biscay from HF radar data and two offshore moored buoys. Geophys Res Lett. 38(19):L19607.

Solabarrieta L, Frolov S, Cook M, Paduan J, Rubio A, González M, Mader J, Charria G. 2016. Skill assessment of HF radar-derived products for Lagrangian simulations in the Bay of Biscay. J Atmos Ocean Technol. 33:2585–2597. doi:10.1175/JTECH-D-16-0045.1.

Solabarrieta L, Rubio A, Cárdenas M, Castanedo S, Esnaola G, Méndez FJ, Medina R, Ferrer L. 2015. Probabilistic relationships between wind and Surface water circulation patterns in the SE Bay of Biscay. Ocean Dyn. 65(9):1289–1303.

Solabarrieta L, Rubio A, Castanedo S, Medina R, Fontán A, González M, Fernández V, Charria G, Hernández C. 2014. Surface water circulation patterns in the southeastern Bay of Biscay: new evidences from HF radar data. Cont Shelf Res. 74:60–76.

Teles-Machado A, Peliz A, McWilliams J, Dubert J, Le Cann B. 2016. Circulation on the northwestern Iberian margin: swoddies. Prog Oceanogr. 140:116–133. doi:10.1016/j.pocean.2015.09.011.

Section 2.3. Mediterranean deep and intermediate water mass properties

Ben Ismail S, Schroeder K, Sammari C, Gasparini GP, Aleya L. 2014. Interannual variability of water mass properties in the Tunisia–Sicily channel. J Mar Syst. 135:14–28.

Bethoux JP, Gentili B. 1999. Functioning of the Mediterranean Sea: past and present changes related to fresh water input and climatic changes. J Mar Syst. 20:33–47.

Cook BI, Anchukaitis KJ, Touchan R, Meko DM, Cook ER. 2016. Spatiotemporal drought variability in the Mediterranean over the last 900 years. J Geophys Res Atmos. 121:2060–2074.

Gačić M, Schroeder K, Civitarese G, Cosoli S, Vetrano A, Eusebi Borzelli GL. 2013. Salinity in the Sicily channel corroborates the role of the Adriatic–Ionian Bimodal Oscillating System (BiOS) in shaping the decadal variability of the Mediterranean overturning circulation. Ocean Sci. 9:83–90.

Gasparini GP, Ortona A, Budillon G, Astraldi M, Sansone E. 2005. The effect of the eastern Mediterranean transient on the hydrographic characteristics in the Strait of Sicily and in the Tyrrhenian Sea. Deep-Sea Res. 52:915–935.

Giorgi F. 2006. Climate change Hot-spots. Geophys Res Lett. 33:L08707.

Josey SA, Somot S, Tsimplis M. 2011. Impacts of atmospheric modes of variability on Mediterranean Sea surface heat exchange. J Geophys Res. 116:C02032.

Naranjo C, García-Lafuente J, Sammartino S, Sánchez-Garrido JC, Sánchez-Leal R, Jesús Bellanco M. 2017. Recent changes (2004–2016) of temperature and salinity in the Mediterranean outflow. Geophys Res Lett. 44:5665–5672.

Rixen M, Beckers JM, Levitus S, Antonov J, Boyer T, Maillard C, Fichaut M, Balopoulos E, Iona S, Dooley H, et al. 2005. The western Mediterranean deep water: a proxy for climate change. Geophys Res Lett. 32:L12608.

von Schuckmann K, Le Traon P, Alvarez-Fanjul E, Axell L, Balmaseda M, Breivik L-A, Brewin RJW, Bricaud C, Drevillon M, Drillet Y, et al. 2018. The Copernicus marine service ocean state report issue 2. J Oper Oceanogr. 11 (sup1): s1–S142. doi:10.1080/1755876X.2018.14892808.

Schroeder K, Chiggiato J, Bryden HL, Borghini M, Ben Ismail S. 2016. Abrupt climate shift in the western Mediterranean Sea. Sci Rep. 6:23009.

Schroeder K, Chiggiato J, Josey SA, Borghini M, Aracri S, Sparnocchia S. 2017. Rapid response to climate change in a marginal sea. Sci Rep. 7:4065.

Schroeder K, Millot C, Bengara L, Ben Ismail S, Bensi M, Borghini M, Budillon G, Cardin V, Coppola L, Curtil C, et al. 2013. Long-term monitoring programme of the hydrological variability in the Mediterranean Sea: a first overview of the hydrochanges network. Ocean Sci. 9:1–24.

Vargas-Yáñez M, García-Martínez MC, Moya F, Balbín R, López-Jurado JL, Serra M, Zunino P, Pascual J, Salat J. 2017. Updating temperature and salinity mean values and trends in the western Mediterranean: THE RADMED project. Progr Ocean. 157:27–46.

Section 2.4. Phytoplankton blooms in the Baltic Sea

Brewin RJW, Sathyendranath S, Müller D, Brockmann C, Deschamps P-Y, Devred E, Doerffer R, Fomferra N, Franz B, Grant M, et al. 2015. The ocean colour climate change initiative: III. A round-robin comparison on in-water bio-optical algorithms. Remote Sens Environ. 162:271–294. doi:10.1016/j.rse.2013.09.016.

Fennel K. 1999. Convection and the timing of phytoplankton spring blooms in the western Baltic Sea. Estuar Coast Shelf Sci. 49(1):113–128. doi:10.1006/ecss.1999.0487.

Groetsch PMM, Simis SGH, Eleveld MA, Peters SWM. 2016. Spring blooms in the Baltic Sea have weakened but lengthened from 2000 to 2014. Biogeosciences. 13(17):4959–4973. doi:10.5194/bg-13-4959-2016.

Hansson M, Håkansson B. 2007. The Baltic algae watch system – a remote sensing application for monitoring cyanobacterial blooms in the Baltic Sea. J Appl Remote Sens. 1. doi:10.1117/1.2834769.

Hansson M, Pamberton P, Håkansson B, Reinart A, Alikas K. 2010. Operational nowcasting of algal blooms in the Baltic Sea using MERIS and MODIS. ESA Living Planet Symposium; Bergen, Norway. Vol. 686.

HELCOM. 2015. HELCOM eutrophication assessment manual. [accessed 2018 Jul 22]. http://www.helcom.fi/Documents/Eutrophication assessment manual.pdf.

Kahru M, Elmgren R, Di Lorenzo E, Savchuk O. 2018. Unexplained interannual oscillations of cyanobacterial

blooms in the Baltic Sea. Sci Rep. 8(1):6365. doi:10.1038/s41598-018-24829-7.

Kahru M, Nõmmann S. 1990. The phytoplankton spring bloom in the Baltic Sea in 1985, 1986: multitude of spatio-temporal scales. Cont Shelf Res. 10(4):329–354. doi:10.1016/0278-4343(90)90055-Q.

Mélin F, Vantrepotte V, Chuprin A, Grant M, Jackson T, Sathyendranath S. 2017. Assessing the fitness-for-purpose of satellite multi-mission ocean color climate data records: a protocol applied to OC-CCI chlorophyll-a data. Remote Sens Environ. 203:139–151. doi:10.1016/j.rse.2017.03.039.

O'Reilly JE, Maritorena S, Mitchell BG, Siegel DA, Carder KL, Garver SA, Kahru M, McClain C. 1998. Ocean color chlorophyll algorithms for SeaWiFS. J Geophys Res Ocean. 103(C11):24937–24953. doi:10.1029/98JC02160.

Pitarch J, Volpe G, Colella S, Krasemann H, Santoleri R. 2016. Remote sensing of chlorophyll in the Baltic Sea at basin scale from 1997 to 2012 using merged multi-sensor data. Ocean Sci. 12(2):379–389. doi:10.5194/os-12-379-2016.

Raudsepp U, She J, Brando VE, Kõuts M, Lagemaa P, Sammartino M, Santoleri R. 2018. Baltic inflows. In: von Schuckmann K, Le Traon P-Y, Smith N, Pascual A, Brasseur P, Fennel K, Djavidnia S, editors. Copernicus marine service ocean state report, issue 2. J Oper Oceanogr. 11(sup1):s13–s16. doi:10.1080/1755876X.2018.1489208.

Sathyendranath S, Brewin RJW, Jackson T, Mélin F, Platt T. 2017. Ocean-colour products for climate-change studies: what are their ideal characteristics? Remote Sens Environ. 203:125–138. doi:10.1016/j.rse.2017.04.017.

Siegel DA. 2002. The north Atlantic spring phytoplankton bloom and Sverdrup's critical depth hypothesis. Science. 296(5568):730–733. doi:10.1126/science.1069174.

Wan Z, Bi H, She J. 2013. Comparison of two light attenuation parameterization focusing on timing of spring bloom and primary production in the Baltic Sea. Ecol Modell. 259:40–49. doi:10.1016/j.ecolmodel.2013.03.010.

Wasmund N, Dutz J, Pollehne F, Siegel H, Zettler ML. 2017. Biological assessment of the Baltic Sea 2016. Warnemünde: Leibniz Institute for Baltic Sea Research. Mar Sci Rep. 105. doi:10.12754/msr-2017-0105.

Wasmund N, Dutz J, Pollehne F, Siegel H, Zettler ML. 2018. Biological assessment of the Baltic Sea 2017. Warnemünde: Leibniz Institute for Baltic Sea Research. Mar Sci Rep. 108. doi:10.12754/msr-2018-0108.

Section 2.5. Cod reproductive volume potential in the Baltic Sea

Cardinale M, Arrhenius F. 2000. The influence of stock structure and environmental conditions on the recruitment process of Baltic cod estimated using a generalized additive model. Can J Fish Aquat Sci. 57(12):2402–2409. doi:10.1139/f00-221.

Cardinale M, Modin J. 1999. Changes in size-at-maturity of Baltic cod (Gadus morhua) during a period of large variations in stock size and environmental conditions. Fish Res. 41(3):285–295. doi:10.1016/S0165-7836(99)00021-1.

EFSA Publication, Nielsen R. 1998. Mechanisms influencing long term trends in reproductive success and recruitment of Baltic cod: implication for fisheries management:

CORE program final report. EU Commission DGXIV, I–III. [s.l.]: European Commission. EU AIR2. CT94-1226.

Heikinheimo O. 2008. Average salinity as an index for environmental forcing on cod recruitment in the Baltic Sea. Boreal Environ Res. 13:457–464.

Hinrichsen H-H, von Dewitz B, Lehmann A, Bergström U, Hüssy K. 2017. Spatio-temporal dynamics of cod nursery areas in the Baltic Sea. Prog Oceanogr. 155:28–40. doi:10.1016/j.pocean.2017.05.007.

ICES. 2005. Report of the study group on multispecies assessment in the baltic (SGMAB); Jun 13–17; Riga, Latvia. ICES CM 2005/H:06.

ICES. 2016. Report of the Baltic fisheries assessment working group (WGBFAS); Apr 12–19; Copenhagen, Denmark. ICES HQ. ICES CM 2016/ACOM:11.

ICES. 2018. ICES advice on fishing opportunities, catch, and effort. https://doi.org/10.17895/ices.pub.4378.

Karaseva EM, Zezera AS. 2016. Causes of different impact of major Baltic inflows on cod reproduction in the Gotland basin of the Baltic Sea. Oceanology. 56(5):643–654. doi:10.1134/S0001437016040068.

Karasiova EM. 2011. Assessment of production of eggs of eastern Baltic cod (Gadus morhua callarias L.) on the basis of long-term ichthyoplankton data. Russ J Dev Biol. 42(3):168–172. doi:10.1134/S1062360411030076.

Karasiova EM, Voss R, Eero M. 2008. Long-term dynamics in eastern Baltic cod spawning time: from small scale reversible changes to a recent drastic shift. ICES CM 2008/J:03.

Köster FW, Möllmann C, Hinrichsen H-H, Wieland K, Tomkiewicz J, Kraus G, Voss R, Makarchouk A, MacKenzie BR, St John MA, et al. 2005. Baltic cod recruitment – the impact of climate variability on key processes. ICES J Mar Sci. 62(7):1408–1425. doi:10.1016/j.icesjms.2005.05.004.

MacKenzie B, St John M, Wieland K. 1996. Eastern Baltic cod: perspectives from existing data on processes affecting growth and survival of eggs and larvae. Mar Ecol Prog Ser. 134:265–281. doi:10.3354/meps134265.

Plikshs M, Hinrichsen H-H, Elferts D, Sics I, Kornilovs G, Köster FW. 2015. Reproduction of Baltic cod, Gadus morhua (Actinopterygii: Gadiformes: Gadidae), in the Gotland basin: causes of annual variability. Acta Ichthyol Piscat. 45(3):247–258. doi:10.3750/AIP2015.45.3.04.

Raudsepp U, Legeais J-F, She J, Maljutenko I, Jandt S. 2018. Baltic inflows. In: von Schuckmann K, Le Traon P-Y, Smith N, Pascual A, Brasseur P, Fennel K, Djavidnia S, editors. Copernicus marine service ocean state report, issue 2. J Oper Oceanogr. 11(sup1):s13–s16. doi:10.1080/1755876X.2018.1489208.

Section 2.6. The North Pacific Gyre Oscillation

Di Lorenzo E, Schneider N, Cobb KM, Chhak K, Franks PJS, Miller AJ, McWilliams JC, Bograd SJ, Arango H, Curchister E, et al. 2008. North Pacific gyre oscillation links ocean climate and ecosystem change. Geophysical Research Letters. 35:L08607.

Kalnay E, Kanamitsu M, Kistler R, Collins W, Deaven D, Gandin L, Iredell M, Saha S, White G, Woollen J, et al. 1996. The NCEP/NCAR 40-year reanalysis project. Bull Am Meteor Soc. 77:437–471.

Niiler P, Maximenko NA, McWilliams JC. 2003. Dynamically balanced absolute sea level of the global ocean derived from near-surface velocity observations. Geophys Res Lett. 30 (22):2164.

Walker GT, Bliss EW. 1932. World weather V. Mem R Meteorol Soc. 4:53–84.

Yi D, Gan L, Wu B, Miller AJ. 2018. The north Pacific gyre oscillation and mechanisms of its decadal variability in CMIP5 models. J Clim. 31(6):2487–2509.

Section 2.7. Sea level, sea surface temperature and SWH extreme percentiles from model results and *in situ observations in European Seas*

Ambar I, Días J. 2008. Remote sensing of coastal upwelling in the north-eastern Atlantic ocean. In: Barale V., Gade M, editors. Remote sensing of the European seas. Dordrecht: Springer. doi:10.1007/978-1-4020-6772-3_11.

Behrens A, Staneva J, Gayer G. 2019. Validation of wave model results in data sparse semi-enclosed areas like the Black Sea. J Oper Oceanogr.

Björkqvist J-V, Tuomi L, Fortelius C, Pettersson H, Tikka K, Kahma KK. 2017. Improved estimates of nearshore wave conditions in the Gulf of Finland. J Mar Syst. 71:43–53. doi:10.1016/j.jmarsys.2016.07.005.

Chronis T, Papadopoulos V, Nikolopoulos EI. 2011. QuickSCAT observations of extreme wind events over the Mediterranean and Black Seas during 2000–2008. Int J Climatol. 31:2068–2077.

Hünicke B, Zorita E, Soomere T, Madsen KS, Johansson M, Suursaar Ü. 2015. Recent change-sea level and wind waves. In: Bolle H-J, Menenti M, Rasool I, editors. Second assessment of climate change for the Baltic Sea basin. Cham: Springer; p. 155–185. doi:10.1007/978-3-319-16006-1_9.

Isemer H-J, Russak V, Tuomenvirta H. 2008. A.1.2 atmosphere. In: Bolle H-J, Menenti M, Rasool I, editors. Assessment of climate change for the Baltic Sea basin. Berlin: Springer; p. 386–392. doi:10.1007/978-3-540-72786-6.

Kikas V, Lips U. 2016. Upwelling characteristics in the Gulf of Finland (Baltic Sea) as revealed by Ferrybox measurements in 2007–2013. Ocean Sci. 12(3):843–859. doi:10.5194/os-12-843-2016.

Lehmann A, Myrberg K, Höflich K. 2012. A statistical approach to coastal upwelling in the Baltic Sea based on the analysis of satellite data for 1990–2009. Oceanologia. 54(3):369–393. doi:10.5697/oc.54-3.369.

Lehmann A, Raudsepp U, Szymelfenig M, Lips I, Matciak M, Kowalewski M, Krezel A, Burska D, Szymanek L, Ameryk A. 2008. Upwelling events, coastal offshore exchange, links to biogeochemical processes – highlights from the Baltic. Oceanologia. 50(1):95–113.

Lionello P, Rizzoli PM, Boscolo R, editors. 2006. Mediterranean climate variability. Amsterdam: Springer. (Developments in earth and environmental sciences. 4).

Locarnini RA, Mishonov AV, Antonov JI, Boyer TP, Garcia HE, Baranova OK, Zweng MM, Paver CR, Reagan JR, Johnson DR, et al. 2013. World ocean atlas 2013. In: Levitus S, Mishonov A, editors, technical editors. NOAA atlas NESDIS 73, 40 pp. (Volume 1: Temperature).

Menendez M, García-Díez M, Fita L, Fernández J, Méndez FJ, Gutiérrez JM. 2014. High-resolution sea wind hindcasts over the Mediterranean area. Clim Dyn. 42:1857–1872.

Myrberg K, Andrejev O. 2003. Main upwelling regions in the Baltic Sea – a statistical analysis based on three-dimensional modelling. Boreal Environ Res. 8(2):97–112.

O'Dea E, Arnold AK, Edwards KP, Furner R, Hyder P, Martin MJ, Siddorn J, Storkey D, While J, Holt J, Lui H. 2012. An operational ocean forecast system incorporating NEMO and SST data assimilation for the tidally driven European north-west shelf. J Oper Oceanogr. 5:3–17.

O'Dea E, Furner R, Wakelin S, Siddorn J, While J, Sykes P, King R, Holt J, Hewitt H. 2017. The CO5 configuration of the 7 km Atlantic margin model: large-scale biases and sensitivity to forcing, physics options and vertical resolution. Geosci Model Dev. 10:2947–2969.

Pontes MT. 1998. Assessing the European wave energy Resource. J Offshore Mech Arctic Eng. 120(4). doi:10.1115/1.2829544.

Pugh DT. 2004. Changing sea levels. Effects of tides, weather and climate. Cambridge University Press. ISBN 978-0-521-53218-1.

Rudels B. 2015. Arctic Ocean circulation, processes and water masses: A description of observations and ideas with focus on the period prior to the international polar year 2007–2009. Progr Oceanogr. 132:22–67.

Seidov D, Antonov JI, Arzayus KM, Baranova OK, Biddle M, Boyer TP, Johnson DR, Mishonov AV, Paver C, Zweng MM. 2015. Oceanography north of 60° N from World Ocean Database. Progr Oceanogr. 132:153–173.

Shum CK, Woodworth PL, Andersen OB, Egbert GD, Francis O, King C, Klosko SM, Le Provost C, Li X, Molines J-M, et al. 1997. Accuracy assessment of recent ocean tide models. J Geophys Res. 102(C11):25173–25194. doi:10.1029/97JC00445.

Simoncelli S, Fratianni C, Pinardi N, Grandi A, Drudi M, Oddo P, Dobricic S. 2014. Mediterranean Sea physical reanalysis (MEDREA 1987-2015) (Version 1) [dataset]. Copernicus Monitoring Environment Marine Service (CMEMS). doi:10.25423/medsea_reanalysis_phys_006_004.

Skagseth Ø. 2008. Recirculation of Atlantic water in the western Barents Sea. Geophys Res Lett. 35. doi:10.1029/2008GL033785.

Suursaar Ü, Aps R. 2007. Spatio-temporal variations in hydrophysical and chemical parameters during a major upwelling event off the southern coast of the Gulf of Finland in summer 2006. Oceanologia. 49(2):209–228.

Tuomi L, Kahma KK, Pettersson H. 2011. Wave hindcast statistics in the seasonally ice-covered Baltic Sea. Boreal Environ Res. 16:451–472.

Turner JF, Iliffe JC, Ziebart MK, Jones C. 2013. Global ocean tide models: assessment and use within a surface model of lowest astronomical tide. Marine Geodesy. 36(2):123–137. doi:10.1080/01490419.2013.771717.

Väli G, Zhurbas V, Laanemets J, Elken J. 2011. Simulation of nutrient transport from different depths during an upwelling event in the Gulf of Finland. Oceanologia. 53(1–TI):431–448. doi:10.5697/oc.53-1-TI.431.

Wekerle C, Wang Q, Danilov S, Schourup-Kristensen V, von Appen W-J, Jung T. (2017). Atlantic WATER in the Nordic Seas: locally eddy-permitting ocean simulation in a global setup. J Geophys Res Oceans. 122:914–940. doi:10.1002/ 2016JC012121.

Chapter 3: Case studies

3.1. The use of Copernicus Marine Service products to describe the State of the Tropical Western Pacific Ocean around the Islands: a case study

Authors: Elisabeth Holland, Karina von Schuckmann, Maeva Monier, Jean-François Legeais, Silvia Prado, Shubha Sathyendranath, Cecile Dupouy

Statement of main outcome: The Western Tropical Pacific Ocean remains one of the last frontiers for scientific research. This area of the ocean is exposed to strong variations at inter-annual to decadal scales forced by climate modes such as the El Niño Southern Oscillation, as well as long-term changes driven by global warming. These Pacific Island States lie in the main route of devastating storms and this area of the ocean lacks ocean observations. We have created a Copernicus Marine Atlas for the Pacific Ocean States, that delivers ocean data to address the needs of decision-makers and to meet climate directives. It responds directly to Fiji's requests at the 2017 United Nations Oceans Conference for the Sustainable Development Goal (SDG)14 (for life below water) and in the 2017 COP23 conference for SDG13 (on climate action). The Copernicus Marine Atlas for the Pacific Islands States shows sustained and drastic ocean warming, sea level rise, and a decrease in the base of the marine food chain (phytoplankton) in this area. The Pacific Big Ocean States are vulnerable to the changing marine environment and face unprecedented threats to the three pillars of sustainable development: economy, environment, and society.

Products used:

Ref. No.	Product name and type	Documentation
3.1.1	1.5.1 DUACS (Data Unification and Altimeter Combination System) delayed-time altimeter daily sea level products, Altimetry	http://climate.copernicus.eu/climate-data-store
3.1.2	GLOBAL_REANALYSIS_ PHY_001_026 Reanalysis	PUM: http://marine.copernicus.eu/documents/PUM/CMEMS-GLO-PUM-001-026.pdf QUID: http://marine.copernicus.eu/documents/QUID/CMEMS-GLO-QUID-001-026.pdf
3.1.3	INSITU_GLO_TS_OA_REP_ OBSERVATIONS_013_002_b *In situ* for the year 2017: INSITU_GLO_NRT_ OBSERVATIONS_013_030 *In situ*	PUM: http://marine.copernicus.eu/documents/PUM/CMEMS-INS-PUM-013-002-a.pdf; QUID: http://marine.copernicus.eu/documents/QUID/CMEMS-INS-QUID-013-002a.pdf) for the year 2016:

(Continued)

Continued.

Ref. No.	Product name and type	Documentation
		PUM: http://marine.copernicus.eu/documents/PUM/CMEMS-INS-PUM-013.pdf QUID: http://marine.copernicus.eu/documents/QUID/CMEMS-INS-QUID-013-030-036.pdf
3.1.4	GLOBAL_REP_PHY_001_021 *In situ*, remote sensing	PUM: http://marine.copernicus.eu/documents/QUID/CMEMS-GLO-QUID-001-021.pdf QUID: http://marine.copernicus.eu/documents/PUM/CMEMS-GLO-PUM-001-021.pdf
3.1.5	OCEANCOLOUR_GLO_ CHL_L3_REP_ OBSERVATIONS_009_065 Remote sensing	PUM: http://marine.copernicus.eu/documents/PUM/CMEMSOC-PUM-009-ALL.pdf QUID: http://cmemsresources.cls.fr/documents/QUID/CMEMS-OC-QUID-009-064-065-093.pdf

Fiji served as President of the UN General Assembly in 2017, linking climate (SDG13) and ocean (SDG14) as the foundation of blue economies for island and coastal states around the world. The resulting United Nations Oceans outcome statement stressed

> the importance of enhancing understanding of the health and role of our ocean and the stressors on its ecosystems, including through assessments on the state of the ocean, based on science and on traditional knowledge systems. We also stress the need to further increase marine scientific research to inform and support decision-making, and to promote knowledge hubs and networks to enhance the sharing of scientific data, best practices and 'know-how'. (UN 2017)

The Southern Pacific Ocean remains one of the last frontiers for scientific research. Few *in situ* monitoring systems exist to document the state of the Pacific Ocean. Indeed, accessing available fisheries data is compromised because of the competitive nature of the fishing industry (Transform Agorau, pers. comm.). The effective and growing Argo float network, with 3907 floats in February 2019 (http://www.argo.ucsd.edu/About_Argo.html), has truly revolutionised large-scale physical oceanography (Riser et al. 2016). The continuing limited capability of climate system models to adequately simulate ocean-climate coupling and dynamics, including the El Nino Southern Oscillation, underscores the importance of

integrating the available data sets (Bellenger et al. 2014).

The Pacific Islands Meteorological Services Directors have repeatedly emphasised the need to include ocean forecasting and services in the suite of the WMO Global Framework for Climate Services (SPREP 2012), and the third Pacific Meteorological Council Meeting (SPREP 2017). As president of COP23, Prime Minister Frank Bainimarama has emphasised the importance of the climate and ocean connection and the need to protect ocean health to protect the planet: 'We are all in the same canoe' (https://cop23.com.fj/fijian-prime-minister-cop23-president-remarks-assuming-presidency-cop23/). The Copernicus Marine Service Atlas for Pacific Ocean States compiled by the author team responds directly to Fiji's requests at the 2017 United Nation Oceans for SDG 14, life below water and the 2017 COP23 for SDG13, climate action which goes beyond the Pacific.

The Copernicus Marine Service Atlas for the Pacific Ocean States goes beyond the unique compilation of CMIP3 climate model projections and data tools compiled by the Pacific Climate Change Science Program (PCCSP 2011, 2014). A complete overview of tropical Pacific observing network is available in the WMO publication library (GCOS 2014a, 2014b). Our study focuses on the application of the available CMEMS products to the Pacific domain defined by PCCSP.

The data sets available through the Copernicus Marine Service provide a valuable window on the under-observed Pacific Ocean and help build a foundation for providing ocean services, including food security, essential biological variables and indicators of ocean health, data to inform early warning systems and climate adaptation. To begin, we address the following key ocean variables:

- sea surface temperature, a much-needed variable for assessing coral reef health and bleaching and tropical cyclone forecasting
- ocean heat content trends for the upper 700 m depth, to monitor ocean warming and thermal volume changes contributing to sea level rise; to track changes in stratification, ocean currents, as well as marine ecosystems and human livelihoods. Moreover, this indicator is linked to the ocean's role as a major heat source for the global atmospheric circulation and has important implications for regional and global climates, including severe events.
- sea level trends from 1993 to 2017 to better inform climate adaptation and coastal planning. Sea level trend values in the entire Pacific Islands domain (Box 3) range between -0.5 mm y^{-1} and $+7.2$ mm y^{-1}, illustrating the non-uniformity of the sea level rise in this region.

- near-surface chlorophyll concentrations – as linked to phytoplankton populations – to assess ocean productivity and health as their changes can imply major impacts on ecosystem processes and biogeochemical cycling, which in turn can have significant implications for economy productivity and food availability.

To develop the Pacific case study, the domain was defined to encompass the 15 P-ACP (African, Caribbean and Pacific) countries defined by the EU Cotonou agreement and served by the EU's ACP secretariat (http://www.acp.int/) including: Cook Islands, Federated States of Micronesia, Fiji, Kiribati, Nauru, Niue, Palau, PNG, RMI, Samoa, Solomon Islands, Timor-Leste, Tonga, Tuvalu, and Vanuatu. The domain corresponded to that used for the Pacific Islands in the Pacific Climate Changes Science Program (Australia Bureau of Meteorology and CSIRO 2011). To explore the dynamics inside and outside the Western Pacific Warm Pool, the domain was further subdivided.

Global mean sea surface temperature, upper ocean heat content and mean sea level all show pronounced increasing trends over the last decades and with strong evidence that the positive trend is related to the increase in greenhouse gas concentration (Rhein et al. 2013). Nevertheless, the global surface and subsurface warming and global mean sea level rise is not spatially uniform (Meyssignac et al. 2016). Long-term warming of the western Pacific is a well-documented consensus in literature (Cane et al. 1997; Cravatte et al. 2009; Deser et al. 2010). Accordingly, the Copernicus Marine Service Atlas for the Pacific Islands area shows a significant surface and subsurface warming trend and sea level rise (Figures 3.1.1 and 3.1.2) at values close to and even exceeding the global mean warming and sea level rise rates (see Table 3.1.1, see also Chapter 1). The Western Pacific Islands area shows strong variability over various time scales (Merrifield et al. 2012; Han et al. 2014 Sun et al. 2017;). At inter-annual time scales, western tropical Pacific surface and subsurface temperatures, and sea level vary in synchrony with the modes of the El Niño Southern Oscillation (Figure 3.1.2; e.g. Wang et al. 1999; Ablain et al. 2017). The near-surface layers warm in the easternmost Box 2 during the 1997/1998 and 2015/2017 El Niño phase (shown in red) and cool during the 1998–2000, 2007/2008 and 2010/2011 La Niña phase (shown in blue, Figure 3.1.2(a)). Moreover, year-to-year changes for western tropical Pacific sea level are thermosteric driven: sea level rises as ocean temperatures rise (Figure 3.1.2(b,c)).
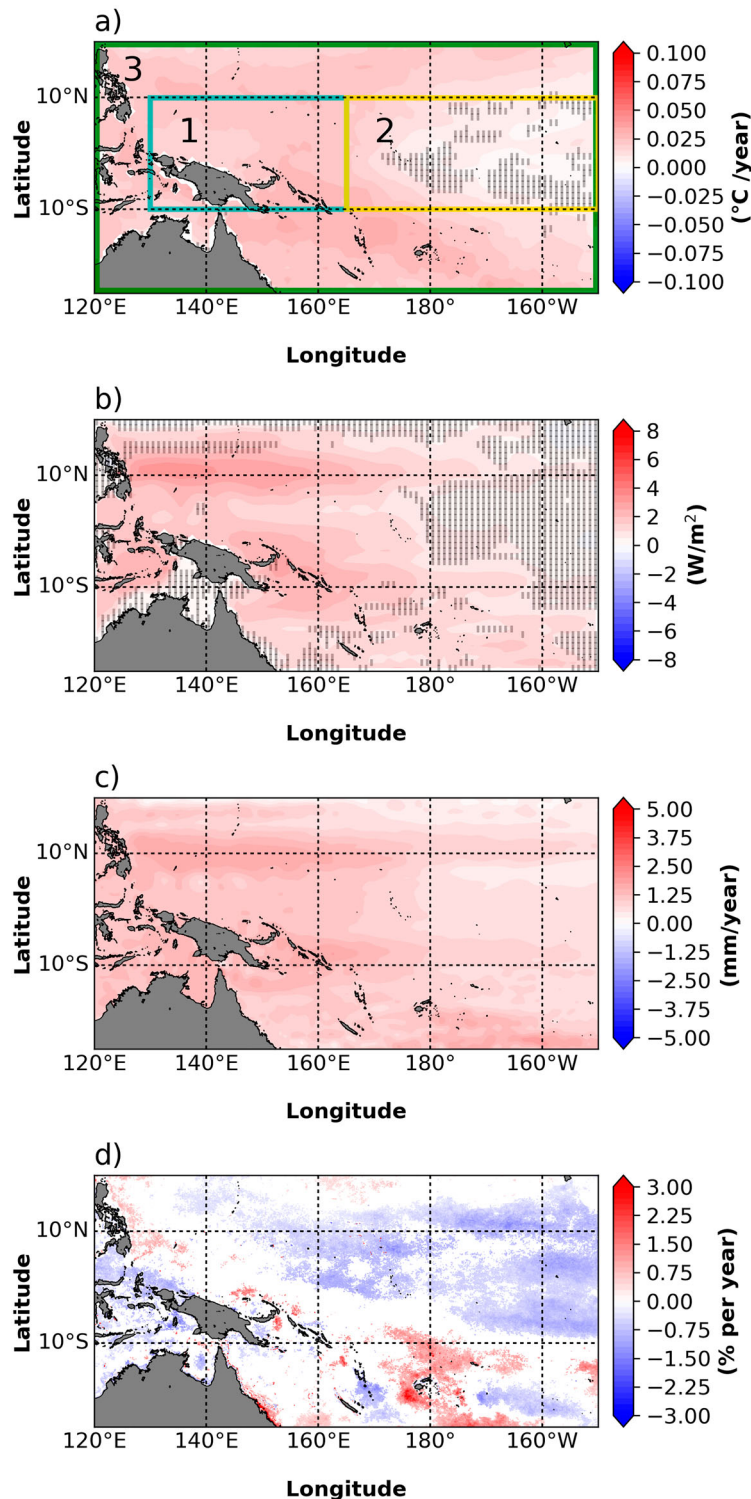
Figure 3.1.1. Regional trends of (a) sea surface temperature and (b) upper ocean (0–700 m) ocean heat content over the period 1993–2017 for the western tropical Pacific. The results are derived from a multiproduct approach (ensemble mean of product 3.1.2–3.1.4). Black dots indicate areas where the noise exceeds two times the signal. (c) Regional sea level trend (in mm y^{-1}) for the western tropical Pacific over the period January 1993–May 2017 (note to reviewer: will be up-dated until December 2017) as derived from re-processed satellite altimetry data (product reference 3.1.1). No Glacial Isostatic Adjustment correction is applied on the altimeter data. (d) Map of regional chlorophyll trend (September 1997–December 2017) in the western tropical Pacific as observed by remote sensing. Only statistically significant ($p < .05$) trends are shown, and are based on the CMEMS product 3.1.5. See Table 3.1.1 for the definition of the dataset, and access to related documentation. Regions for analysis are indicated in (a), i.e. Western Pacific Islands (blue, Box 1; 130° E–165°E; 10°S to 10°N to encompass the Western Pacific Warm Pool); Central Pacific Islands (yellow, Box 2: 165°E–150°W; 10°S to 10°N); and Entire Pacific Islands domain (green, Box 3 is consistent with domain used for the Pacific Climate Change Science Program).

Figure 3.1.2. Averaged time series over the full area (green line, Box 3, full map area of Figure 3.1.1(a)), and the western (dark blue line, Box 1) and eastern (yellow line, Box 2) tropical Pacific Ocean for (a) sea surface temperature, (b) ocean heat content, (c) sea level and (d) Chlorophyll-a. The seasonal cycle had been removed from all time series (1993–2014 for (a)–(c), 1997–2014 for (d)). Details on box areas and data use is given in the caption of Figure 3.1.1. The Multivariate El Niño So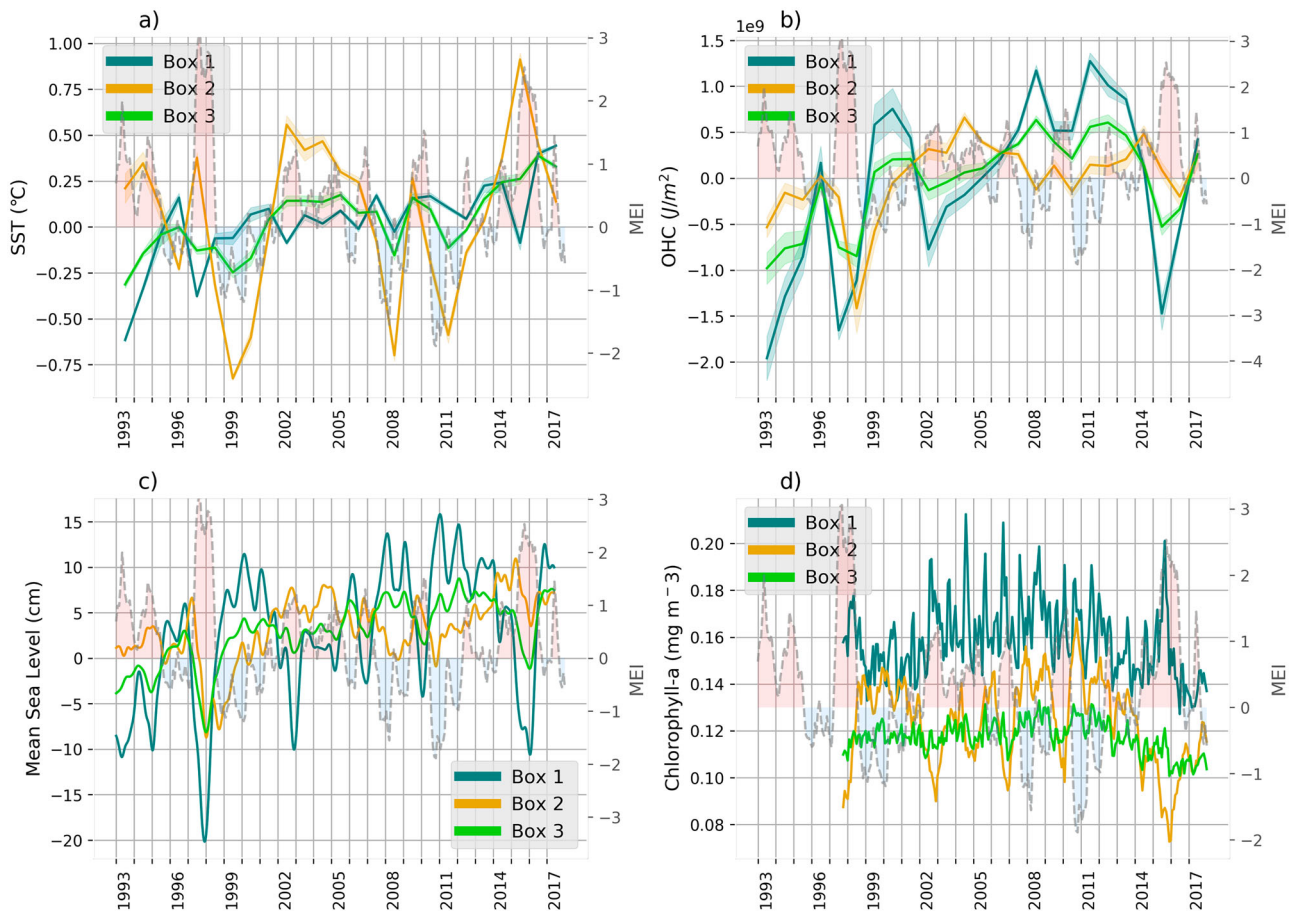uthern Oscillation Index is used to describe the ENSO phase with the El Niño phase shown as red (positive) shaded areas and La Niña shown as blue (negative) shaded areas (Wolter and Timlin 2011, downloaded: https://www.esrl.noaa.gov/psd/enso/mei/).

We introduce chlorophyll concentration (Figure 3.1.1 (d) and Figure 3.1.2(d)) to provide a measure of the amount of phytoplankton present with its corresponding marine productivity on which the entire marine ecosystem depends, directly or indirectly. Ocean chlorophyll could be used by decision-makers to assess the health and productivity of natural resources and marine life that depend on phytoplankton. Reduced chlorophyll

Table 3.1.1. Trend values and their uncertainties (90% confidence interval) of area mean Sea Surface Temperature (SST) and Ocean Heat Content (OHC) over the period 1993–2017 (ensemble approach from products 3.1.2–3.1.4), Sea Level over the period January 1993 to December 2017 (product ref. 3.5.1) and Chlorophyll concentration over the period September 1997–December 2017 (product ref. 3.5.5). Areas for Boxes 1 and 2 are given in Figure 3.1.1(a), and full domain covers the western tropical Pacific as shown in the maps of Figure 3.1.1. Note that the uncertainties related to the sea level internal variability are not included in the sea level trend uncertainties.

Variable	Western Pacific Islands Box 1 1993–2017 trend	Central Pacific Islands Box 2 1993–2017 trend	Entire Pacific Islands domain Box 3 1993–2017 trend
SST °C y^{-1}	+0.02 ± 0.01	+0.01 ± 0.02	+0.02 ± 0.01
OHC (0–700 m) W m^{-2}	+1.9 ± 1.5	+0.8 ± 0.7	+1.2 ± 0.7
Sea level mm y^{-1}	+4.8 ± 2.5	+2.8 ± 2.5	+3.5 ± 2.5
Chlorophyll % y^{-1}	-0.4 ± 0.02	−0.7 ± 0.001	−0.4 ± 0.001

concentration and associated decrease in primary production may negatively impact fish and marine life, important for food security and economic health of the Pacific Islands countries that dependent on fisheries.

Significant trends, both positive and negative, have been reported on a regional basis, for both chlorophyll concentration and primary production (Mélin et al. 2017; Racault et al. 2017), and some of the most pronounced trends have been reported for the eastern and western Pacific region. In the western Pacific area (Box 1 of Figure 3.1.2(d), blue line), large variations from year-to-year characterise the chlorophyll concentrations, highlighting the need for regular monitoring services. River run off coincident with ITCZ and SPCZ dynamics in the equatorial coastal areas like that of northern Papua New Guinea explains the greater high-frequency variability than open ocean regions. In the central Pacific (Box 2 of Figure 3.1.2(d), yellow line), a reduction of chlorophyll concentration since the year 1997 is recorded at a rate of ~−0.7%/year which is either linked to decadal or longer variability (as observed in the northern Pacific e.g. Sun et al. 2017) or the impact of climate change. Chla is strikingly well correlated with the Central Pacific El Niño signal with high Chla associated with the negative (La Niña) phase of ENSO as seen in 1998, 1999, 2007 and 2010, and a lower Chla associated with the positive (El Niño) phase of ENSO as seen in 2015. For the entire Pacific Islands (green line, Box 3, Figure 3.1.2(d)), Chla mimics that of the western Pacific (blue line, Box 1) with a lower amplitude due to the weaker correlation with Central Pacific ENSO events (yellow line, Box 2). In the Fijian Archipelago, with the inverse, Chla concentration is increasing between 0% and 2% per year (Figure 3.1.1(c)), indicating a high positive response of phytoplankton, or/and a shift in phytoplankton composition (Dupouy et al. 2018).

Given that time series from remote sensing used here is only 18 years long, and the dominant signature is decadal scale variability (Gregg et al. 2017), this time series is admittedly too short to disentangle the effect of inter-annual variability and longer-term climate change. Nevertheless, this series demonstrates (1) the correlation between Chla and ITCZ in the western Pacific due to coastal areas in large Pacific Islands in the Western Pacific (Box 1), (2) the strong correlation between Chla and La Niña phase due to the equatorial upwelling enrichment in the Central Pacific (Box 2) and (3) less correlation for the entire region due to smoothing of the ENSO or ITCZ effects as demonstrated by the reduced variability (Box 3). The variability around the long-term trend appears visually to be inversely related to the MEI (Figure 3.1.2(d), yellow line).

The State of the Pacific Ocean case study is a demonstration of how Copernicus Marine Service products might be used to inform decision-making in a region that regards itself as data poor, especially for ongoing monitoring of biological variables. The perception of data poverty results from limited capacity to access, display and analyse data (Holland 2018). The Copernicus Marine Services State of Pacific Ocean challenges those perceptions of data poverty by demonstrating the richness of the data available to inform decision-making in the Pacific Islands.

Our hope is that the State of the Pacific Ocean atlas serves as a springboard to begin stakeholder engagement and dialogue on how to use the available data to inform decision-making. In the 2018 Pacific Island Forum Leaders meeting, the Pacific leaders of the 16 Forum member countries prioritised climate change and blue economies. Optimising utilisation of the available data requires further dialogue at the science policy interface to generate the robust products required to inform decision-making.

The Pacific Islands Forum Marine Sector Working Group (MSWG) has prioritised the need to document data available for the Pacific Islands domain. A first step will be to show the products to the MSWG and other stakeholders to engage them in collaborative discussions about how the data might be used. The long-term goal is to produce data products that would inform decision-making for the blue economies of the Pacific. The data is available to inform decision-making on an annual basis through the World Ocean Atlas, and could become useful on more refined time scales, quarterly to weekly to inform climate and ocean outlooks. One step might be to transform the data products provided here into real time data available to the Forum Fisheries agency, Honiara, Solomon Islands for display in their fisheries monitoring facility. Another step for the MSWG would be developing real time data displays that provide the more than 20 years of context for physical ocean monitoring (GCOS 184)

Future needs for the Copernicus data include refining the approach to finer time scales with the eventual goal of providing real time data and information services and short-term two-week forecasts. The data products are available through CMEMS, but (i) regionalisation (e.g. downscaling) and (ii) cross-validation between products (e.g. link the consolidated products with the non-consolidated ones) are required. The data products shown are subset of the data available for the Pacific Islands to launch the much-needed dialogue with the key stakeholders and champions. With the successful launch of this Pacific Ocean Atlas, other ideas and innovations will emerge for research products and applications.

The Copernicus Marine Services State of Pacific Ocean analysis of available data demonstrates that the ocean surrounding the Pacific Islands is warmer, has higher heat content, with sea level rising at rates higher than the global mean and a decline in chlorophyll content.

3.2. Review of the use of ocean data in European fishery management and monitoring applications

Authors: Mark R. Payne, Patrick Lehodey

Statement of main outcome: Operational oceanographic data is potentially of great value for use in the monitoring and management of marine living resources due to the close coupling between the physiology of marine organisms and their environment. However, while oceanographic data is invaluable in understanding the processes governing the dynamics and behaviour of these organisms from a historical perspective, it has generally not been used in the day-to-day management of fisheries resources. We discuss the reasons for this situation and highlight emerging results, such as dynamic ocean management and marine ecological forecasting, that are starting to reverse this tendency. Finally, we discuss what can potentially be done to improve the uptake of this information.

Ref. No.	Product name and type	Documentation
3.2.1	SST_GLO_SST_L4_NRT_ OBSERVATIONS_010_001 SST_GLO_SST_L4_REP_ OBSERVATIONS_010_011	PUM: http://marine.copernicus.eu/ documents/PUM/CMEMS-OSI-PUM-010-001.pdf QUID: http://marine.copernicus.eu/ documents/QUID/CMEMS-OSI-QUID-010-001.pdf
3.2.2	GLOBAL_ANALYSIS_FORECAST_ PHY_001_024_MONTHLY Model	PUM: http://marine.copernicus.eu/ documents/PUM/CMEMS-GLO-PUM-001-024.pdf QUID: http://marine.copernicus.eu/ documents/QUID/CMEMS-GLO-QUID-001-024.pdf

Marine organisms are coupled to their physical environment in a way that, as terrestrial mammals, is hard for us to comprehend. Most marine organisms are ectotherms ('cold blooded'), meaning that their body is at the same temperature as the surrounding environment: as a consequence, their metabolisms, and therefore their food requirements, growth rates, reproductive development and activity rates are all directly modulated by the temperature of their surroundings (Pörtner 2002). In addition, the concentration of dissolved oxygen at the surface is strongly temperature-dependent (higher temperature waters contain less oxygen) while below the surface the consumption of oxygen by other organisms can lead to areas of critical oxygen depletion (Breitburg et al. 2018). Salinity can play an important role in limiting the fitness and distribution of organisms, particularly in and around regions of transition between fresher and saltier waters e.g. from the high salinity North Sea (surface salinity of approximately 33–35) to the low salinity Baltic Sea (surface salinity 2–15) (Pecuchet et al. 2016). Variations in seawater pH and its resulting impacts on carbonate concentration have also been shown to affect both shell-forming organisms (e.g. coccolithophores, shellfish) and higher organisms (e.g. fish) (Dupont and Pörtner 2013).

This tight linkage between the physical environment and marine organisms has long been recognised within both the science and management of living marine resources. Oceanographic data therefore can potentially play an important role in informing these activities (Tommasi et al. 2017). Here we review how operational oceanographic products are currently used in these fields, with a particular focus on the CMEMS product catalogue. We focus on three different applications of this information, according to the timescale in question, i.e. understanding the historical perspective, evaluating the current state of the system and looking towards the future. Finally, we examine potential future directions and how collaboration between these two fields can best be fostered.

Firstly, historical oceanographic data play a key role in developing our scientific understanding of marine organisms and ecosystems: indeed, an entire sub-discipline of oceanography ('fisheries oceanography') has evolved at the interface of fisheries science and physical/chemical/biological oceanography that focuses on resolving these questions. One of the most prominent applications of such historical data is in cataloguing and understanding changes in the context of climate change and climate variability: a review performed in the lead up to the last IPCC report (AR5) identified 1700 such examples of observed responses to climate change in marine systems, including around 800 in European waters (Poloczanska et al. 2013). Large-scale indices have been used to link climate variability to ecological consequences in the ocean, including the North Atlantic Oscillation, the Atlantic Multidecadal Oscillation (Nye et al. 2014), the North Atlantic Subpolar Gyre intensity (Hátún et al. 2009), the El Niño Southern Oscillation (Chavez et al. 2002) or the Indian Ocean Dipole (Saji et al. 1999). The oceanographic data sets underlying these studies are diverse in nature and often reflect what is available to the authors, rather than being selected from either the global marketplace or from a systematic catalogue such as the CMEMS portal. In particular, the most impactful and important results are those that are based on long time series of both biological and physical observations (e.g. Boyce

et al. 2010). Nevertheless, the satellite record is now starting to be of sufficient length to drive analyses on its own to, for example, link temperature to changes in fish distributions (e.g. MacKenzie et al. 2014) (Figure 3.2.1) or to study changes in lower trophic levels based on ocean colour (Racault et al. 2012).

Historical environmental data are also key inputs to develop empirical statistical (correlative) models with direct applications for marine management and conservation. Amongst the most common of these are the so-called species distributions models (also known as environmental niche models or bioclimatic envelope models) that link the distribution of a target species to environmental variables such as temperature, salinity, bathymetry, chlorophyll and primary productivity (e.g. Brunel et al. 2018, Raudsepp et al. 2019: Section 2.5 of this report). Other biological responses are also commonly correlated with environmental variables, in particular recruitment (the number of juveniles produced by a fish stock each year), growth and phenology (the timing of key biological events). Despite the limitations associated with correlative approaches these models have been used in two ways. Firstly, they help to understand the processes that are controlling the response of interest. Secondly they can be used to both project changes into the future under climate change e.g. Bruge et al. (2016), and, more recently, to drive near-term predictions (e.g. Figure 3.2.2). In all cases, long time series of synoptic oceanographic data, matching at least the temporal range of the biological observations, are critical to developing this work, and their lack can often represent a bottleneck in the analysis.

While oceanographic data is critical to scientific investigations of historical changes in marine populations and ecosystem, this data has seen little uptake on the near-term timescale and in the management of living marine resources. A review of the management practices of around 1250 fish populations globally (Skern-Mauritzen et al. 2016) showed that just 24 used ecosystem drivers to inform their short-term decision-making about setting fishing quotas: of these, 15 populations (1.2%) used oceanographic variables while 10 (0.8%) used the abundances of either the species' predators or prey. In essence, oceanographic information is simply not used in setting quota.

This result may seem surprising to the reader, given the prior discussion about the importance of the environment for the dynamics of biological systems. However, it reflects the current state of the art in this field. In spite of aspirations to move towards the more holistic 'ecosystem-approach to fisheries management' and 'ecosystem-based management' (Rice 2011), the majority of fisheries management systems today remain firmly rooted in the traditional single-stock paradigm that considers one population largely in isolation from both all other species and the environment (Skern-Mauritzen et al. 2016). Nevertheless, many fisheries are managed effectively today based on these simple approaches, supplemented with regular monitoring of changes in the populations and their productivity (Daan et al. 2011).

Why is this? An important factor limiting the uptake of oceanographic data is the paucity of quantitative, reliable and robust relationships between the environment and biological responses that can be used in a management context. This point is particularly well illustrated by a review paper from the late 1990s, that revisited published relationships between the environment and recruitment, to see whether they were still being used in a management context (Myers 1998). Of the 49 published relationships reviewed, the author found just one that was in use 10 years later: results that were, in his own words, 'dismal'. While many factors
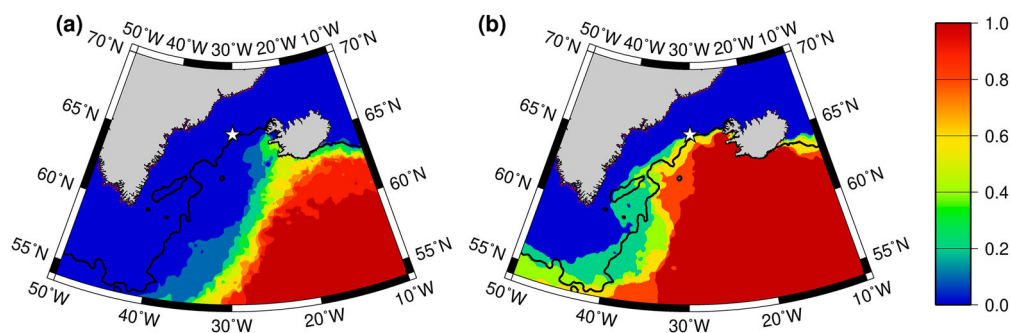
Figure 3.2.1. Using remote sensing data to understand changes in the distribution of Atlantic bluefin tuna (*Thunnus thynnus*). In August 2012 bluefin tuna were caught in Denmark strait (location marked by a star on both plots) for the first time in recorded human history. Bluefin tuna are generally restricted to waters warmer than 11 degrees. The plot here shows the proportion of years where August SST > 11°C for (a) 1985–1994 and (b) 2007–2011, while the contour line shows location of the 11°C isotherm for 2012. A clear expansion in the amount of thermally suitable habitat is seen in recent years, providing a corridor whereby tuna can access Denmark strait. From MacKenzie et al. (2014). Reprinted by permission of John Wiley & Sons, Inc. SST Data source is ref. 3.2.1.

Figure 3.2.2. Forecasts of the spawning distribution of blue whiting (Micromesistius poutassou) in March 2019, issued in January 2019. The forecast is based on a species distribution model (Miesner and Payne 2018) linking spawning distribution of this species to salinity at 300–600 m and a range of geographical covariates. Distribution is represented here as the probability of observing blue whiting larvae and is plotted as (a) the value and (b) the anomaly rela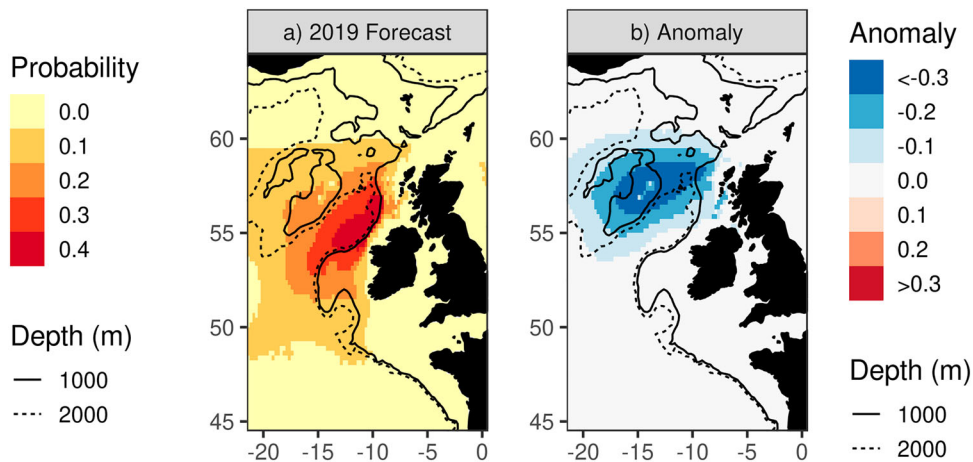tive to the climatological probability (1960–2010). Probabilities > 0.4 can be considered as the core spawning habitat. The 1000 and 2000 m isobaths are added for reference. The EN4 data product (Good et al. 2013) provides the basis for the historical development of the model, while the CMEMS PSY4 reanalysis provides the most recent estimates of the state of the system (product ref. 3.2.2). The original model of Miesner and Payne (2018) has been applied here to show the most recent estimates of spawning distribution.

contribute to this situation, the essence of the problem is the sheer complexity of marine biological dynamics together with a lack of appropriate data (e.g. predator and prey fields) that means that the majority of processes that impact recruitment are not and cannot be parameterised in models. This results in the phenomenon of 'non-stationarity', where the apparent relationships between the environment and the biological response appears to shift over time, leading to the abandonment of published correlations that Myers (1998) uncovered.

While this situation may appear bleak for the providers of operational oceanographic products, it is important to remember that there are other important uses of this information beyond setting quota. Both the commercial fishing industry and recreational fishers are acutely aware of the link between physics and biology, and have the flexibility and profit/enjoyment motive to take advantage of this information: indeed, commercial services have sprung up providing this information to end-users for a fee (e.g. 'Roffers Ocean Fishing Forecasting Service', www.roffs.com). Similarly, the scientific monitoring of the abundance and distribution of marine species also operates within a different framework to that of fisheries management, and can and at times does take advantage of oceanographic information to design their surveys. Changes in fish distribution and productivity, often associated with trends in the physical environment, have consequences for geographically linked fisheries management plans and international quota agreements. Furthermore, the new field of dynamic ocean management (Maxwell et al. 2015) places a high weight on

oceanographic data. Rather than fixing marine protected areas in time and space, this new paradigm makes them dynamic, following the movement and distribution of protected species. Oceanographic data is key to dynamically defining these habitats and regions of interest. The first such tools that implement this approach are now emerging e.g. EcoCast (Hazen et al. 2018) and have shown tremendous potential for improving the way that the ocean is managed.

The tendency of oceanographic data getting greater uptake away from the goal of setting fisheries quota can also be seen when looking into the future. Advances in the ability to observe and forecast the ocean over recent years have paved the way for the creation of marine ecological forecasts for use in the management of living resources. A recent review of these forecast systems globally (Payne et al. 2017) revealed around 10 operational forecast products (Figure 3.2.3). The majority of these forecasts were of the spatial distribution of species, while only one, for salmon on the US West Coast, was directly related to setting quota, highlighting again the point that there are valuable uses for oceanographic observations and forecasts beyond setting quota (Tommasi et al. 2017). A second key point from this review was that Australia and the USA are currently leading the world in the development of such products, while there were no such marine ecological forecast products available in Europe, even though European waters, and particularly the NE Atlantic, are amongst the most predictable waters in the world (Langehaug et al. 2017). However, since that review the first such
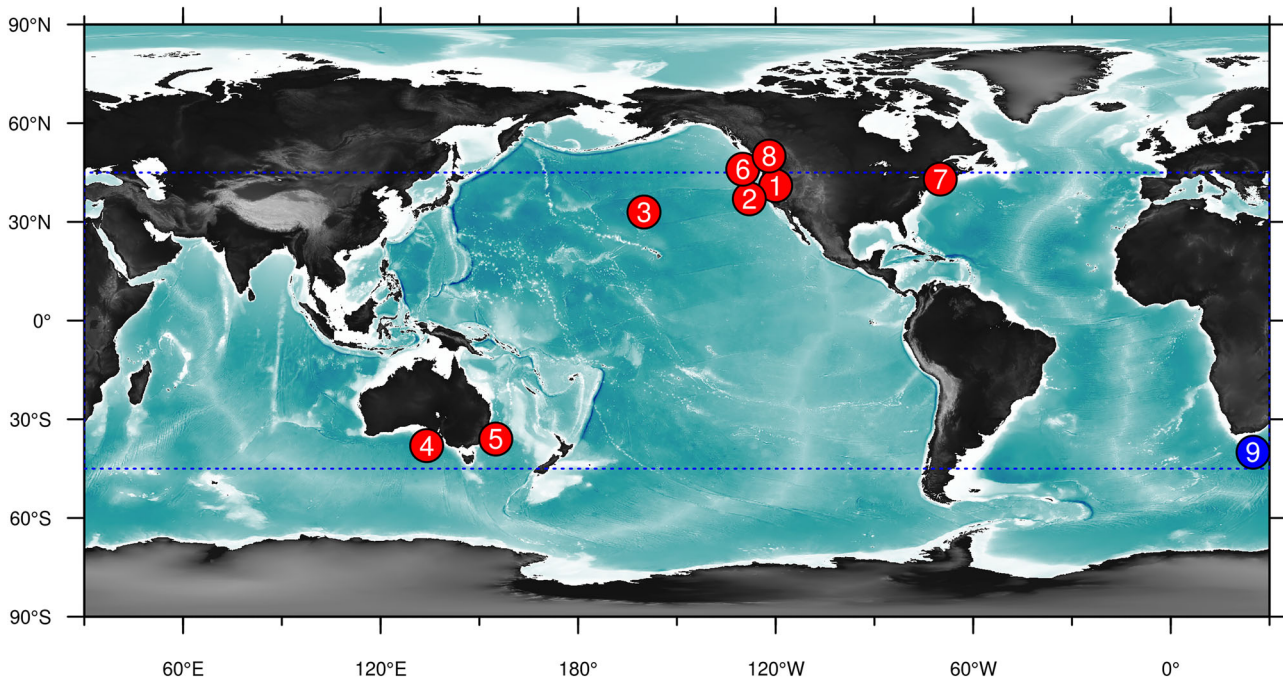
Figure 3.2.3. Distribution of marine ecological forecasts products globally. (1) Return rates of salmon along US West Coast. (2) Whale-watch – distribution and numbers of blue whales in California Current. (3) Turtlewatch – spatial areas where there is a high risk of loggerhead turtle bycatch. (4) Distribution of southern bluefin tuna in the Great Australian Bight. (5) Forecasts of areas closed to the SE Australian long-line tuna fishery. (6) Distribution of California Sardine. (7) Timing of Gulf of Maine lobster landings. (8) Timing of salmon run on the Columbia River. (9) Coral Reef Watch's Heat Stress Outlook. Reproduced from Payne et al. (2017).

European product has come online (Payne 2018) (Figure 3.2.2) and we can expect to see more of these types of products develop in the future.

The final time scale we consider is that of future climatic change. Here, oceanographic and climatic data clearly plays a critical role, as it forms the basis for future projections. Much of the work referred to above that is performed in a historical context can also be used to inform projections of future change (Drinkwater et al. 2010). As the focus of such work is primarily to develop scenarios about the impacts of climate change, rather than trying to make specific estimates or predictions for use in management, weak biological knowledge is only one of a number of other sources of uncertainty that need to be considered (Payne et al. 2016). Much debate exists around the usefulness and reliability of these biological projection models (e.g. Cheung et al. 2012; Brander et al. 2013) and this field is still maturing.

In spite of the poor historical uptake of operational data, the field is emerging rapidly. A particularly promising example of what can be done is provided by the recent implementation of a regional operational model for the Indonesian Ministry of Fisheries. The system couples ocean circulation model and primary production derived from satellite ocean colour data with a model of intermediate trophic levels on the top of which are simulated the spatial dynamics of three exploited tuna species

(Tranchant et al. 2016; Lehodey et al. 2018). Boundary conditions of the regional model are provided by the CMEMS global operational model. The biological component of the model is a complete population dynamics model allowing monitoring of the effects of environmental variability on the stocks (e.g., related to the Indian Ocean Dipole), and the estimation of the fishing impacts. The success of this application relies on the strong multidisciplinary approach adopted covering physical and biogeochemical oceanography, numerical modelling and engineering, marine biology, fisheries oceanography and fish population dynamics modelling. In addition, the low and mid trophic levels (zooplankton and micro nekton) simulated from realistic ocean physics and primary production directly derived from, or assimilating satellite data appear promising potential key explanatory variables to develop other applications, including recruitment indices or species habitat models.

In conclusion, the direct use of operational oceanographic data in the management of living marine resources is currently very limited. Nevertheless, oceanographic data have an important role to play in the science that currently supports management, particularly in understanding the changes that have taken place in the past, and in projecting the response to climate change in the future. Furthermore, emerging fields such as dynamic ocean management and marine ecological

forecasting lean heavily on oceanographic data as their foundation. There is also a clear desire to rectify the underutilisation of environmental information in the management of both fisheries and the entire ecosystem, with a move towards more integrated and environmentally informed management approaches. It therefore seems reasonable to expect significant increases in the uptake of operational oceanographic data in the future for use in the management of living marine resources.

Box:

What can operational oceanographers do to support fisheries management?

There is little doubt that operational oceanography can make an important contribution to fisheries management: as noted above, the relationship between physics and biology in the ocean is well recognised. However, there are numerous hurdles that need to be overcome to help these two closely related fields work together more effectively.

Perhaps the most important barriers are the simple differences between the practitioners of the two fields. It is easy to overlook the fact that the background, training, skill sets, tools and often the motivations and career paths of the people working in each of these fields can be wildly different (e.g. Berx et al. 2011). These differences in the way of working can limit both the uptake of data and the quality of science and decision-making: clear, effective and continued communication between the fields is therefore essential.

Re-evaluating the way oceanographic data are presented to the rest of the science community can help the communication. Data portals such as CMEMS have tremendous potential to both guide and educate end-users in making choices about the appropriate data product for their needs, but need to take the end-users perspective. For example, product descriptions are often primarily oriented towards the technically literate user and can therefore be difficult to penetrate for the non-specialists. Further developments in the guidance to finding and selecting the appropriate dataset (e.g. NCAR's Climate Data Guide (Schneider et al. 2013) could be highly beneficial for many end-users.

Providing tools and products that are compatible with the wide variety of end-users skills and requirements is also critical. For example, subsetting and online processing tools that allow the users to drive the data extraction and processing process themselves (e.g. by defining areas/polygons of interest, calculating averages and statistics on the server side and providing outputs in a variety of formats) are particularly useful for those not used to handling large datasets.

It is however important that these tools work well with the current toolsets of users: while fisheries scientists work primarily in Excel and R, the current script-based subsetting tools provided by CMEMS are based on Python and NetCDF. Fortunately, technological developments, such as the emergence of robust standards for metadata and web access services following the 'FAIR' principles of Findable, Accessible, Interoperable, and Reusable data (Wilkinson et al. 2016) are helping to pave the way and ease the challenge of moving data between scientific disciplines.

Finally, and most importantly, there is a need for greater understanding and collaboration between the fields. Education and outreach activities, including training courses, are critical but also need to work in both directions, not just to increase the skill-set of potential end-users, but also to educate operational oceanographers in the principles of marine science and fisheries management. Co-development of new products by oceanographers and marine biologists working together is a particularly important and productive approach that can help to bring the two fields closer. Indeed, much can be learnt from the newly developing climate services community, for example, where co-development and co-production of climate services helps to overcome the challenges associated with differences between the producers of climate data and the information needs of end-users (Bruno Soares and Dessai 2016). In the same way, it is hoped that a greater dialogue between operational oceanographers and fisheries scientists can lead to improvements in the state of the marine ecosystem and benefit those that depend on the ocean, whilst at the same time realising the tremendous potential offered by operational oceanographic products.

3.3. Synergy between CMEMS products and newly available data from SENTINEL

Authors: Joanna Staneva, Arno Behrens, Gerhard Gayer, Lotfi Aouf

Statement of main outcome: This study explores the synergy between the CMEMS Monitoring and Forecasting Centres model products and the newly available satellite data. Working with these complementary sources of reliable information is useful not only for validation and assimilation purposes but also to explore in depth both the temporal and spatial scales of variability in European seas. The quality of the newly available Sentinel-3A (S3) data is assessed in comparison with data from Jason-3 (J3) at regional scales. The general performance of the wave products is very good and fairly

similar compared to both satellite products. The assimilation of these satellite data in the global Monitoring and Forecasting Centres has indicated the skill of the system during storms generating high waves (Aouf 2018). The joined satellite and model analyses also demonstrates the capabilities of CMEMS as a whole, and the potential benefits of merging observational and modelled Copernicus products (Wiese et al. 2018 Behrens et al. 2019;).

Products used:

Ref. No.	Product name and type	Documentation
3.3.1	WAVE_GLO_WAV_L3_ SWH_NRT_OBSERVATIONS _014_001	PUM: http://marine.copernicus.eu/ documents/PUM/CMEMS-WAV-PUM-014-001-002.pdf QUID: http://marine.copernicus.eu/ documents/QUID/CMEMS-WAV-QUID-014-001.pdf
3.3.2	INSITU_GLO_NRT_ OBSERVATIONS_013_030	PUM: http://marine.copernicus.eu/ documents/PUM/CMEMS-INS-PUM-013.pdf QUID: http://marine.copernicus.eu/ documents/QUID/CMEMS-INS-QUID-013-030-036.pdf
3.3.3	GLOBAL_ANALYSIS_ FORECAST_WAV_001_027	PUM: http://marine.copernicus.eu/ documents/PUM/CMEMS-GLO-PUM-001-027.pdf QUID: http://marine.copernicus.eu/ documents/QUID/CMEMS-GLO-QUID-001-027.pdf
3.3.4	BLKSEA_ANALYSIS_ FORECAST_WAV_007_003	PUM: http://marine.copernicus.eu/ documents/PUM/CMEMS-BS-PUM-007-003.pdf QUID: http://marine.copernicus.eu/ documents/QUID/CMEMS-BS-QUID-007-003.pdf

3.3.1. Black Sea

The Black Sea Near Real Time (NRT) in-situ data, systematically maintained at regional level and quality controlled is considered as a drawback with respect to the other MFCs for improving data assimilation capabilities and for enforcing the validation of the CMEMS products (Staneva et al. 2015). The best way for systematic validations of wave model results in such a regional area is the use of satellite data. In the frame of COPERNICUS Marine Evolution System for the Black Sea that needs to provide improved wave predictions, the third-generation spectral wave model WAM is used. The quality of the wind and wave data provided by the new satellite Sentinel-3A is evaluated. The focus is brought to the regional scales where altimeter data are of lower quality than in the open ocean (Wiese et al. 2018; Behrens et al. 2019). Satellite data of Sentinel-3A and Jason-3 are assessed in a comparison with the WAM data. The comparison between the radar altimeter measurements and the model results have been done for all satellite tracks of Sentinel-3A and Jason-3 that are available for the considered two years' period. QQ-Scatterplots for the comparisons between model versus Jason-3 (top panels) and versus Sentinel-3A (bottom panel) are shown on Figure 3.3.1. On the left hand side the analysis with the new results with the improved wave growth, on the right hand side the old model results. The model simulations with the old MS-MFC version (right panels of Figure 3.3.1) converges to the satellite observations for wave heights below about 2 m, somewhat underestimates the observations for wave heights between 2 and 4 m, and tends to overestimate Hs for higher waves. Due to change in the parameterisation of the wave growth in the source term for the wind input on the quality of the wave NRT products has been improved (left panels of Figure 3.3.1). The statistical analysis of the comparisons between model results and measurements shows reduced bias for the considered time period. Especially for higher waves, the agreement between model and altimeter data is improved significantly for all satellites.

The wave heights in the Black Sea are usually moderate and the differences between measured and computed data are small several interesting situations of the period between 1 December 2015 and 30 November 2017 are discussed in Behrens et al. (2019). On the left side, it is the descending path on 20170210 00:12:52–00:14:20 UTC that touches the area of maximum wave height whereas the ascending path on 20170314 09:25:06–09:26:46 UTC on the right side of Figure 3.3.2 directly crosses the area of maximum wave height.

Additionally two examples for comparisons between wave model data and measured data recorded by the radar altimeter of Sentinel-3A are presented in Figure 3.3.3. The descending satellite track on 20170216 08:25:46–08:27:07 UTC (left) crosses in that case an area of moderate wave height up to 2 m and the corresponding time series along the satellite path show a very good agreement between measurements and model data. The ascending track on the right in Figure 3.3.3 (20170110 19:05:58–19:06:48 UTC) passes the area of maximum wave heights in the east with a good agreement of the wave heights up to 2.8 m as well.

Due to the way satellite altimeter data are processed, the data quality can deteriorate in the vicinity of coastlines, particularly for passes from land to ocean. To test how much the satellite measurements over the study area are affected by this problem, the flights are separated into onshore and offshore flights, with onshore flights passing from the ocean to the shore and offshore flights passing from the shore to the ocean and the statistics are compared to the ones by using the all data. Additional
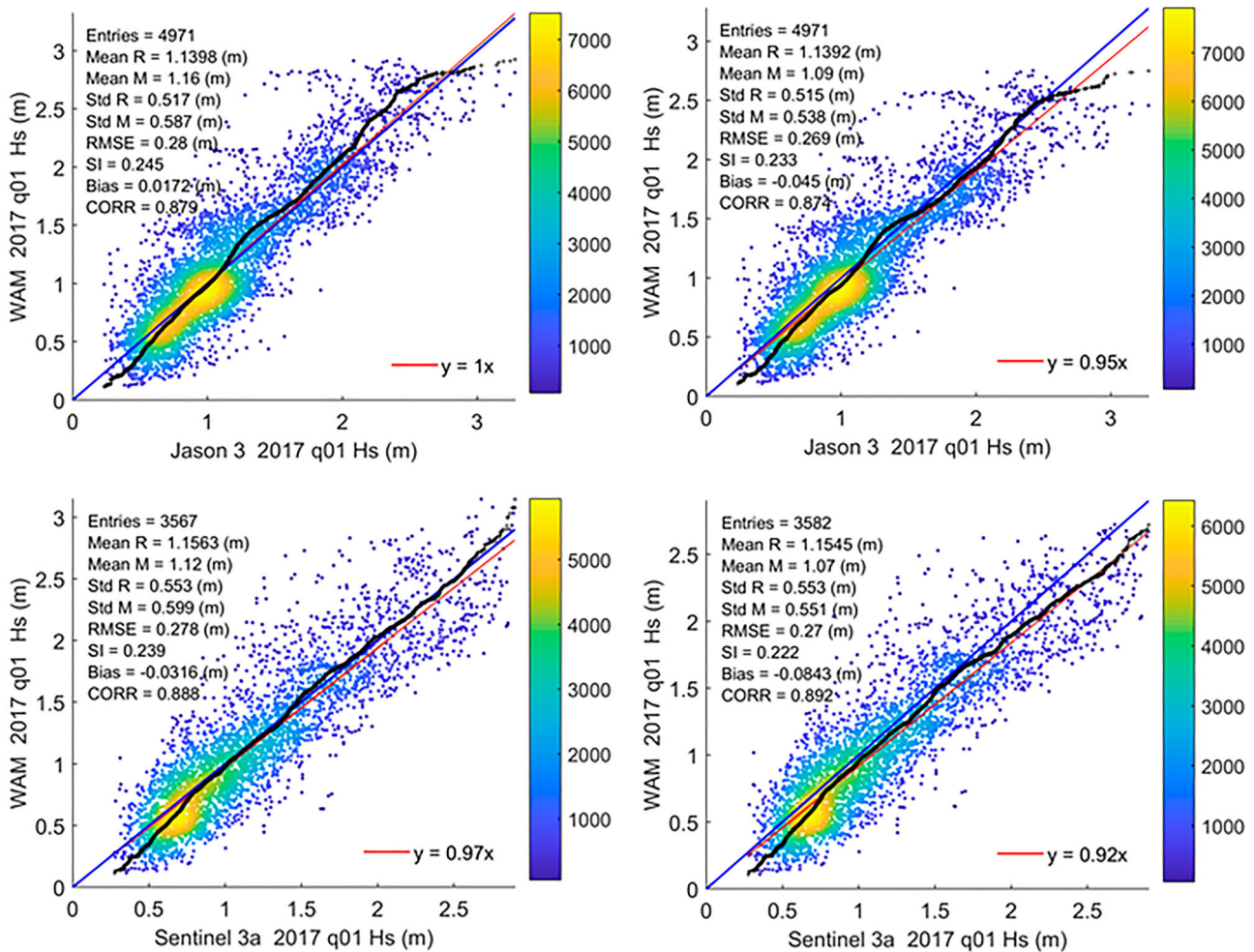
Figure 3.3.1. QQ-Scatterplots for the comparisons between model versus Jason-3 (top panels) and versus Sentinel-3A (bottom panel) data for the first quarter of 2017. On the left hand side the analysis with the new results with the improved wave growth, on the right hand side the old model results. QQ-plot (black line), 45° reference line (blue line), least-squares best fit line (red line). The colour bar shows number of entries. Data source are Ref. 331 and 3.3.4.

analyses are performed by subsampling the track data that are 15 km off the coast (off cost row). When comparing the all data with the off-coast ones, it can be concluded that the data quality by the significant wave from Sentinel-3A height is not affected by the coastline. The general performance of WAM for the Black Sea is very good and similar in comparison with S3 and J3 data; only in the bias differences are observed for J3 is 0.017 m and for S3 0.030 m (see Table 3.3.1). When comparing the statistical values for Sentinel-3A and Jason-3 for both onshore and offshore flights, no substantial differences are found, and the statistics are very similar (Wiese et al. 2018). Therefore, the transition from land to water does not influence the quality of the newly available CMEMS satellite observations over our study area.

3.3.2. Global Ocean

Satellite wave data play an important role to improve the wave products provided by the global Monitoring Forecasting Center (MFC) of the Copernicus Marine Environment and Monitoring Service (CMEMS). An upgraded level 2 processing of the Sentinel-3 Radar Altimeter (SRAL) has been implemented operationally by ESA and EUMETSAT in December 2017. This has improved significantly the quality of significant wave height (Aouf 2018). The assimilation of these data in the global CMEMS-MFC has indicated the skilfulness of the system during storms generating high waves. The North-Atlantic storm Carmen in early January 2018 induced a very strong winds of 140 km/h near the French north-western coast. High waves of more than 10 m have been recorded by the Brittany buoys during this event, as illustrated in Figure 3.3.4. Figure 3.3.5 shows a snapshot of difference of significant wave heights with and without assimilation of S3A wave data on 3 January 2018 at 0:00 UTC. This clearly reveals an impact of difference of more than 1.2 m near the Brittany coast, which corrects the overestimation induced by the wave model.
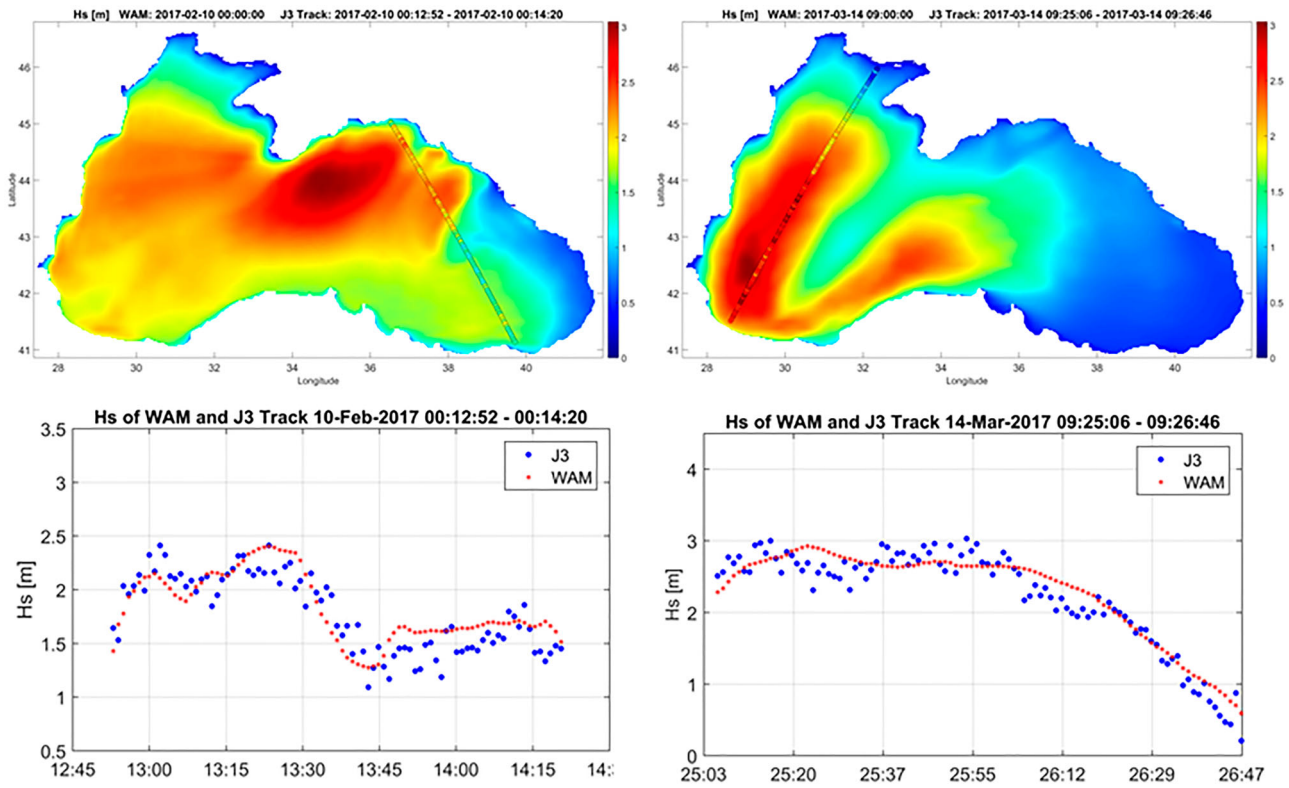
Figure 3.3.2. Left: distribution of Hs on 20170210 (00 UTC) and the ascending Jason-3 satellite track 20170210, 00:12:52–00:14:20. Right: distribution of Hs on 20170314 (09 UTC) and the descending Jason-3 satellite track 20170314, 09:25:06–09:26:46. Data source are Ref. 3.3.1 and 3.3.4.
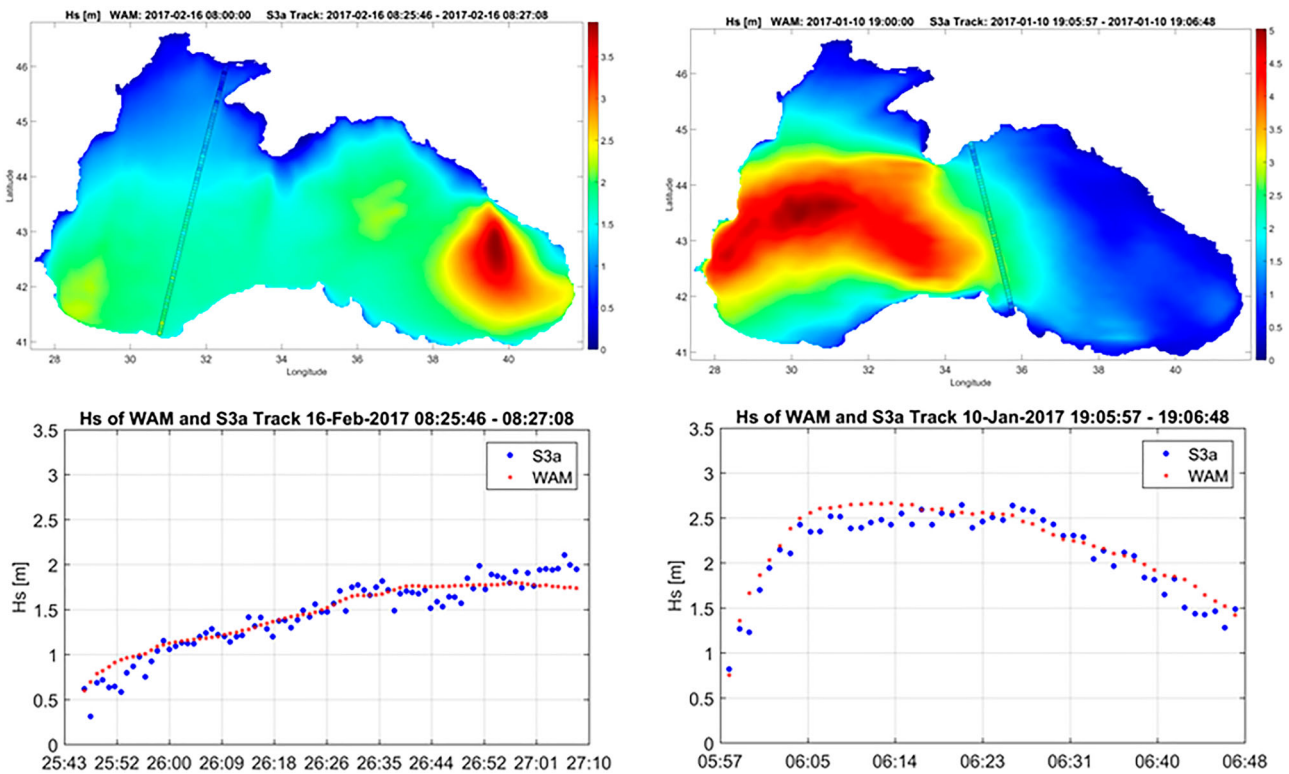

Figure 3.3.3. Left: distribution of Hs on 20170216 (08 UTC) and the descending Sentinel-3A satellite track 20170216, 08:25:46–08:27:07. Right: distribution of Hs on 20170110 (19 UTC) and the ascending Sentinel-3A satellite track 20170110, 19:05:48–19:06:48. Data source are Ref. 3.3.1 and 3.3.4.

Table 3.3.1. Comparison of the data quality during the first quarter of 2017 for all satellite data (All), outside the first 15 km off the coast (Non_coast), subsampling by onshore and offshore flights, for Sentinel-3A (S3) and Jason-3 (J3); for bias [in m], root mean square error [in m] (RMSE), Scatter Index (SI), Correlation coefficient (CORR).

|	All		Off coast		Oncoast		Onshore		Offshore	
	J3	S3	J3	S3	J3	S3	J3	S3	J3	S3
RMSE	0.280	0.278	0.280	0.277	0.279	0.301	0.271	0.299	0.283	0.303
BIAS	0.017	−0.032	0.017	0.030	0.028	−0.060	0.052	−0.077	0.016	0.044
SI	0.245	0.239	0.245	0.237	0.264	0.293	0.279	0.282	0.258	0.304
CORR	0.879	0.888	0.880	0.891	0.858	0.784	0.843	0.778	0.864	0.792
Slope	1.012	0.970	1.012	0.972	1.023	0.924	1.062	0.902	1.009	0.945
RV	0.706	0.748	0.708	0.754	0.634	0.518	0.464	0.530	0.673	0.504
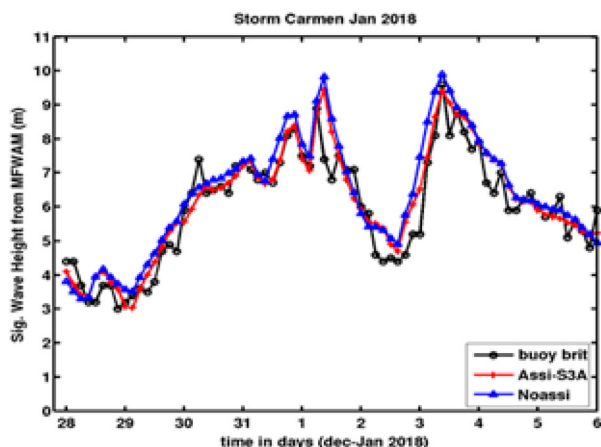
Figure 3.3.4. Time series of significant wave heights at Brittany buoy location during the storm Carmen in early January 2018. Black, red and blue lines indicate significant wave heights from the buoys, the model MFWAM with and without assimilation, respectively.
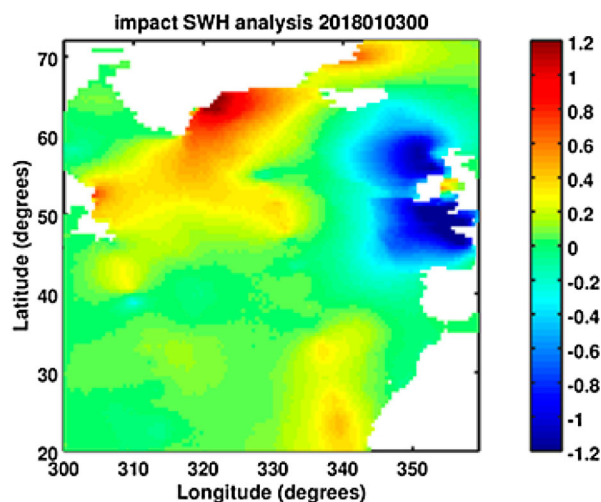

Figure 3.3.5. Difference of significant wave height (in metres) from the wave model MFWAM (Météo-France WAve Model) with and without assimilation on 3 January 2018 at 0:00 UTC. Positive and negative analysis increment stand for an overestimation and underestimation of SWH of the model, respectively. Data source is from 3.3.1.

The assimilation of S3A wave data corrects the misfit of the wave model mostly because of uncertainties related to the wind forcing provided by the atmospheric system. Figure 3.3.5 illustrates the time series of significant wave heights during Carmen at Brittany buoy which is located at 47.5°N and 8.7°W. The validation of the assimilation during the Carmen storm with Brittany buoy has showed an improvement of the normalised scatter index of significant wave height from 12.2% to 10.1%. The assimilation of five altimeters including S3A enhances the impact during storm Carmen and reduces the normalised scatter index of significant wave height to 9.7%. This indicates that such performance of global CMEMS-MFC will ensure better wave products for user applications in many ocean basins.

3.4. Joint Monitoring Programme of the EUtrophication of the NOrthSea with SATellite data user case

Authors: Dimitry Van der Zande, Marieke Eleveld, Heloise Lavigne, Francis Gohin, Silvia Pardo, Gavin Tilstone, Anouk Blauw, Stiig Markager, Lisette Enserink

Statement of main outcome: During the second cycle of the MSFD assessment, incomparability of monitoring methods for chlorophyll-a (CHL) was identified as a main issue hampering a coherent assessment of the eutrophication state of the North Sea. Operational satellite-based ocean colour products provide a solution as they are neutral, transparent and provide cross-boundary information on the CHL state of the North Sea. However, to this day, satellite-based CHL is generally not used in official MSFD reporting. We present the technical steps needed to generate a harmonised CHL indicator map from publicly available CHL products and bridge the gap between the ocean colour community and national monitoring teams/policy makers. This harmonised CHL indicator product enables the progression from point-by-point and country-by-country analyses, to basin-wide analysis of the eutrophication state. Finally, we evaluate the quality of the satellite-based CHL products by a comparison analysis with *in situ*

datasets for different assessment areas in the Greater North Sea.

Products used:

Ref. No.	Product name and type	Documentation
3.4.1	OCEANCOLOUR_ATL_ CHL_L3_REP_ OBSERVATIONS_009_067	PUM: http://marine.copernicus.eu/ documents/PUM/CMEMS-OC-PUM-009-ALL.pdf QUID: http://marine.copernicus.eu/ documents/QUID/CMEMS-OC-QUID-009-066-067-068-069-088-091.pdf
3.4.2	OCEANCOLOUR_ ATL_CHL_L3_REP_ OBSERVATIONS_009_098	PUM: http://marine.copernicus.eu/ documents/PUM/CMEMS-OC-PUM-009-ALL.pdf QUID: http://marine.copernicus.eu/ documents/QUID/CMEMS-OC-QUID-009-033-037-082-098.pdf
3.4.3	OCEANCOLOUR_ATL _OPTICS_L3_REP_ OBSERVATIONS_009_066	PUM: http://marine.copernicus.eu/ documents/PUM/CMEMS-OC-PUM-009-ALL.pdf QUID: http://marine.copernicus.eu/ documents/QUID/CMEMS-OC-QUID-009-066-067-068-069-088-091.pdf
3.4.4	OCEANCOLOUR_ATL _OPTICS_L3_NRT_ OBSERVATIONS_009_034	PUM: http://marine.copernicus.eu/ documents/PUM/CMEMS-OC-PUM-009-ALL.pdf QUID: http://marine.copernicus.eu/ documents/QUID/CMEMS-OC-QUID-009-034-036-046-047-087-089-090-092.pdf
3.4.5	OCEANCOLOUR_BAL _CHL_L3_REP_ OBSERVATIONS_009_080	PUM: http://marine.copernicus.eu/ documents/PUM/CMEMS-OC-PUM-009-ALL.pdf QUID: http://marine.copernicus.eu/ documents/QUID/CMEMS-OC-QUID-009-080-097.pdf
3.4.6	OCEANCOLOUR_BAL _CHL_L3_NRT_ OBSERVATIONS_009_049	PUM: http://marine.copernicus.eu/ documents/PUM/CMEMS-OC-PUM-009-ALL.pdf QUID: http://marine.copernicus.eu/ documents/QUID/CMEMS-OC-QUID-009-048-049.pdf
3.4.7	OCEANCOLOUR_BAL_ OPTICS_L3_NRT_ OBSERVATIONS_009_048	PUM: http://marine.copernicus.eu/ documents/PUM/CMEMS-OC-PUM-009-ALL.pdf QUID: http://marine.copernicus.eu/ documents/QUID/CMEMS-OC-QUID-009-048-049.pdf
3.4.8	OCEANCOLOUR_BAL _OPTICS_L3_REP_ OBSERVATIONS_009_097	PUM: http://marine.copernicus.eu/ documents/PUM/CMEMS-OC-PUM-009-ALL.pdf QUID: http://marine.copernicus.eu/ documents/QUID/CMEMS-OC-QUID-009-080-097.pdf

The Marine Strategy Framework Directive (MSFD) is currently one of the most important drivers for monitoring the coastal and offshore waters in Europe with the objective of reaching a 'good environmental status' (GES) by 2020 (Gohin et al. 2008). It is a crucial legal instrument of the European Commission to protect the marine environment including its ecosystems and biodiversity. Human-induced eutrophication is one of the criteria for assessing the extent to which GES is being achieved. Eutrophication can be defined as the enrichment of water by nutrients causing an accelerated growth of algae and higher forms of plant life to produce an undesirable disturbance to the balance of organisms present in the water and to the quality of the water concerned, and therefore refers to the undesirable effects resulting from anthropogenic enrichment by nutrients (OSPAR 2017).

The eutrophication status is established by monitoring of nutrients, and CHL concentration as a proxy of phytoplankton biomass. More specifically, the indicator of choice is the 90-percentile of the CHL concentrations (CHL-P90) over the phytoplankton growing season (i.e. March–September incl.) for a period of six years expressed in $\mu g\,l^{-1}$ or $mg\,m^{-3}$. CHL-P90 represents the CHL level such that 90% of the observations are equal to or less than this value. While *in situ* data acquisition is still considered as the main monitoring tool, the European Commission highlighted the need for greater coherence with related EU legislations (Water Framework Directive and Habitats and Birds Directive) and for more coherent and coordinated approaches within and between marine regions and sub-regions (European Commission 2014). While preparing for the second cycle of MSFD assessment, various OSPAR groups (Intersessional Correspondence Group on Eutrophication (ICG-EUT) and the Hazardous Substances and Eutrophication Committee (HASEC)) have identified incomparability of monitoring methods for CHL as a main issue hampering a coherent assessment of the common indicator CHL in the Greater North Sea. Moreover, the assessment levels for CHL, based on background concentrations, have been determined with different methods between member states. This results in different GES determinations across national borders that cannot be explained by differences in water quality (Figure 3.4.1). Additionally, the budgets for marine monitoring are decreasing in many European countries forcing them to efficiently use monitoring resources.

During recent years, there has been a growing tendency to use optical remote sensing as a supporting tool to achieve the monitoring requirements because of severe resource constraints of available ship time and personnel and the need for a coherent assessment of CHL between all OSPAR member states bordering the North Sea. Satellite data of CHL combine cheaper data
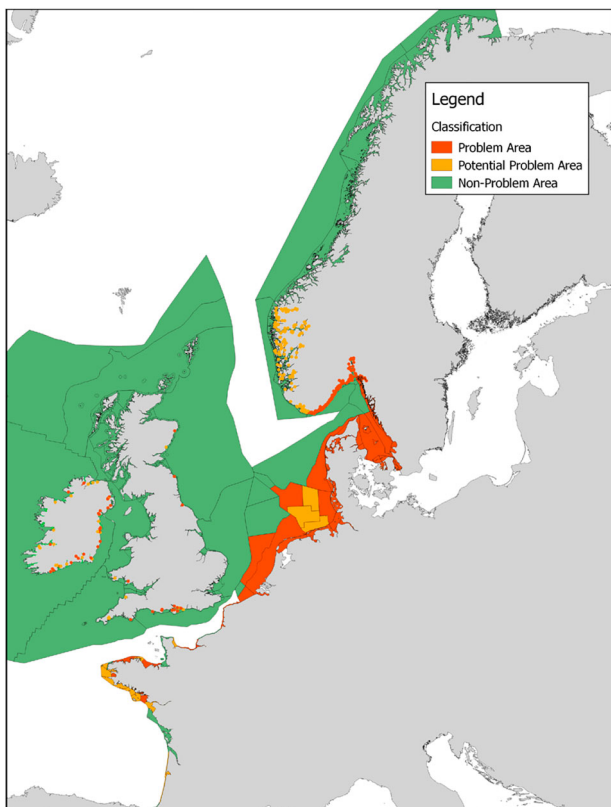
Figure 3.4.1. Map of problem areas for eutrophication for the North Sea region produced by the OSPAR Common Procedure by evaluating the primary indicators (nutrient concentrations, chlorophyll-a and dissolved oxygen) and one secondary criteria (Phaeocystis). For the problem areas measures need to be taken to reduce or eliminate the anthropogenic causes of eutrophication (OSPAR 2017).

collection with a much improved geographical and temporal coverage compared to traditional *in situ* data.

The two-year EU-project Joint Monitoring Programme of the EUtrophication of the NOrth-Sea with SATellite data (JMP-EUNOSAT, Feb. 2017-Feb. 2019) aims at developing a coherent set of assessment levels and a cost-effective GES assessment for eutrophication in the Greater North Sea. The consortium consists of 14 partners[1] from all countries bordering the North Sea.

Satellite data from ocean colour sensors (i.e. SeaWiFS, MODIS, MERIS, VIIRS, Sentinel-3) can provide spatially coherent data on CHL concentrations using CHL retrieval algorithms. There has been considerable success with blue/green-ratio algorithms such as OC4 (O'Reilly et al. 1998) and OC5 (Gohin et al. 2002) in case 1 waters where the variation of optical properties (absorption and scattering) is dominated by phytoplankton and associated material. In contrast, the optical complexity in coastal waters often poses many challenges to the accurate retrieval of biogeochemical parameters using satellite remote sensing (Sathyendranath 2000; Lee 2006). CHL

retrieval by blue/green-ratio algorithms tend to fail when applied to coastal waters whose optical properties are strongly influenced by non-covarying concentrations of suspended particulate matter (SPM) and coloured dissolved organic matter (CDOM). Such waters are defined as case 2 waters. Several constituent retrieval algorithms for use in case 2 waters have been developed: (1) red-edge algorithms (Gons et al. 2005) taking advantage of the CHL absorption peak near 670 nm and (2) artificial network approaches trained to varying parameter concentrations and optical property ranges specifically developed for use with MERIS data, such as the MERIS Ground Segment Processor (MEGS; Doerffer and Schiller 2007) and the FUB/WeW (Schroeder et al. 2007).

The technical objective of JMP EUNOSAT is to evaluate publicly accessible satellite-based CHL products available from CMEMS, ODESA and IFREMER, and determine their validity for different water types, e.g. clear, turbid or CDOM-rich waters, so that the choice of satellite product is determined by environmental conditions per (cross-border) assessment area, rather than national boundaries of the member states.

We started from a collection of well-validated operational satellite-based CHL products for the Greater North Sea: (1) CMEMS OC5-CI (product 3.4.1), (2) CMEMS GSM (product 3.4.2), (3) CMEMS OC4 adapted to Baltic waters (product 3.4.5 and 3.4.6), (4) OC4 applied to CMEMS remote sensing reflectance products (product 3.4.3 and 3.4.4) and (5) MEGS 7.5 applied to the MERIS archive obtained from ODESA online (http://www.odesa-info.eu/). For each of these products it was determined for which water types, described in terms of remote sensing reflectance (RRS) spectra (product 3.4.3, 3.4.4, 3.4.7 and 3.4.8), they provided the most accurate CHL estimations (i.e. relative error < 50%) based on a variety of reference datasets from the CoastColour Round Robin (CCRR) project[2] (Nechad et al. 2015). These reference data sets were specifically designed to test algorithms and assess their accuracy for retrieving water quality parameters and comprise 5000 matchups of CHL concentrations and hyperspectral RRS-spectra covering a wide range of water types in terms of CHL, SPM and CDOM concentrations. The RRS-spectra were used as input to the considered CHL algorithms and their resulting CHL estimates were compared to the reference values allowing the development of a pixel-based quality assessment.

Figure 3.4.2(A,B) shows the application of this approach on satellite observations for the 8th of April 2010 for the OC4 and OC5 products showing an algal bloom in the Belgian and Dutch coastal waters. Figure 3.4.2(C,D) shows a classification map indicating the water types where the OC4 and OC5 algorithms
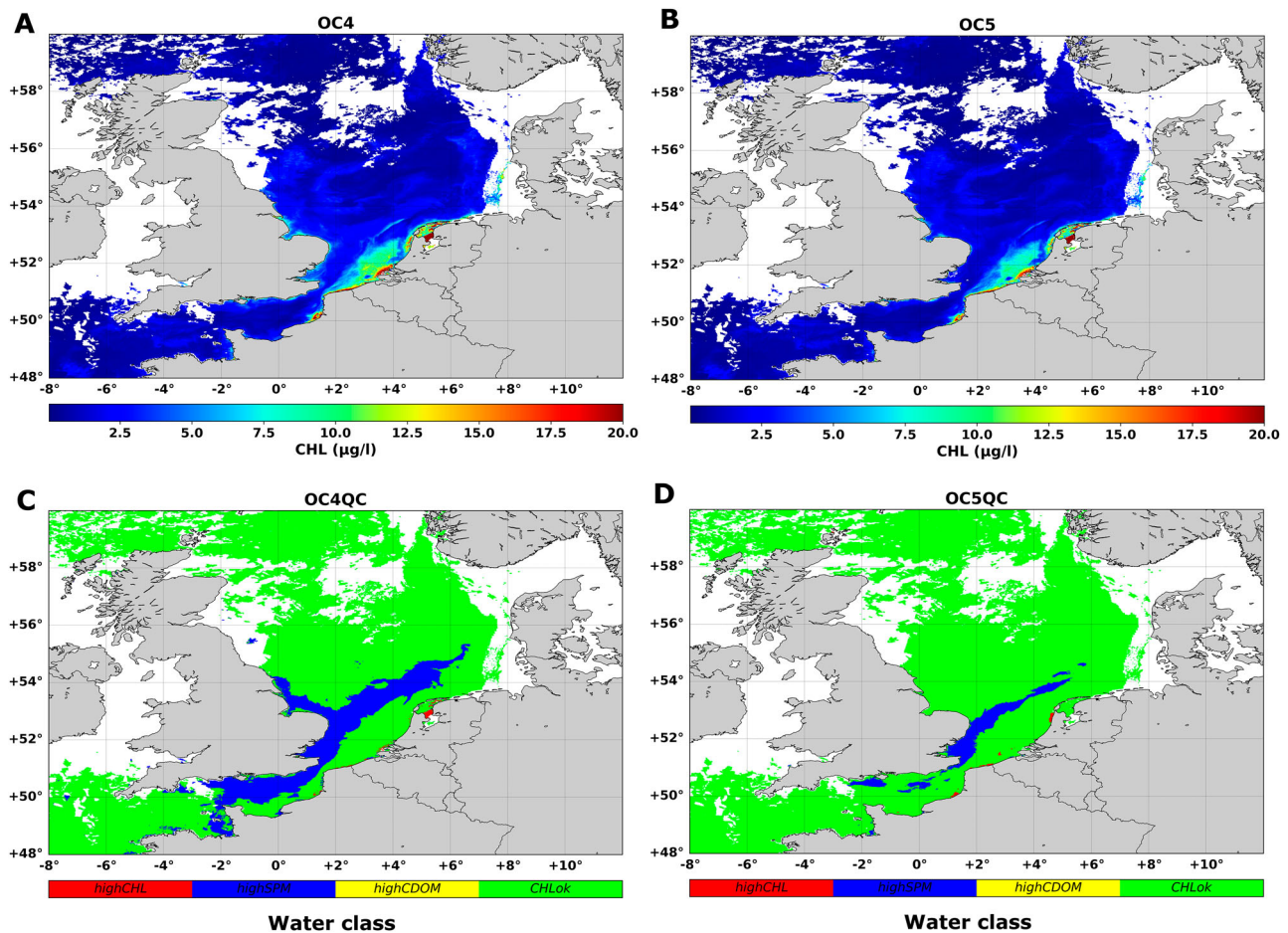
Figure 3.4.2. (A and B) CHL products generated using the OC4 and OC5 algorithms for the 8th of April 2010 showing an algal bloom in the Belgian and Dutch coastal waters. (C and D) Water type classification map indicating the water types where the OC4 (C) and OC5 (D) algorithms are applicable indicating that OC5 can be applied in more situations than OC4. These products are merged on a pixel by pixel basis with a priority rule given to OC4, then OC5 and finally MEGS 7.5 filling up the map with the most appropriate algorithms available for different water types (based on validation analysis, data not shown): clear waters with OC4, moderately turbid waters with OC5 and highly turbid waters with MEGS 7.5. OC4 is inaccurate in the English Channel and South-East UK due to high concentrations of suspended matter (SPM). Cloud cover is presented in white, i.e. no is data available. In case no clouds are present, but both OC4 and OC5 are not applicable, the MERIS MEGS 7.5 product is used. If that product is also not suitable we have no reliable data for that specific day. The main goal of this approach is to eliminate erroneous data from the process.

are applicable indicating that the OC5 algorithm can be applied in more situations than the OC4 algorithm. The OC4 algorithm is inaccurate in the English Channel and southeast UK due to high SPM concentrations.

In the next phase of the JMP-EUNOSAT project, a blending process was developed to join CHL datasets based on best suited algorithm/water type combination, with special attention to the transition zones between different water types to ensure a gradual merge. This step enabled the progress from point-by-point and country-by-country analyses, to basin-wide analysis with data that covers gradients in the ecosystem system. This enabled a definition of cross-border assessment areas based on ecosystem characteristics. The blended JMP-EUNOSAT CHL product was compared to available *in situ* datasets for all assessment areas (data not shown).

This regional intercomparison will quantify the suitability of used standard products and blending approach for eutrophication assessment. Figure 3.4.3 shows different quality-controlled CHL products (i.e. OC4, OC5, MEGS_7.5) for the 8th of April 2010. These products are merged on a pixel by pixel basis with a priority rule given to OC4, then OC5 and finally MEGS 7.5 filling up the map with the most appropriate algorithms available: clear waters with OC4, moderately turbid waters with OC5 and highly turbid waters with MEGS 7.5.

Intercomparison of satellite products with ship-based observations

The quality-controlled and merged satellite-based CHL observations are compared to *in situ* observations that have been collected in national monitoring programs.
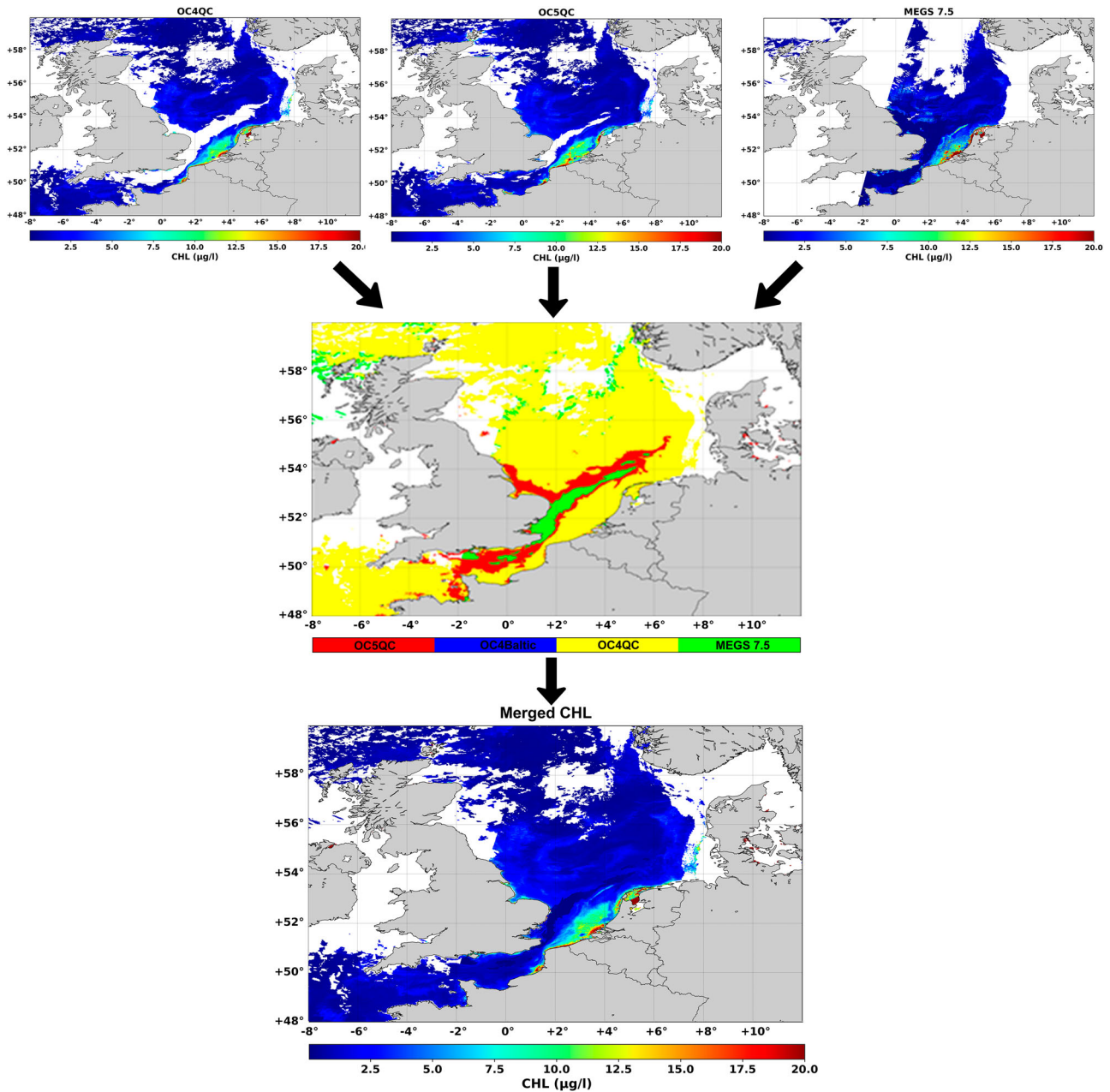
Figure 3.4.3. Blending process of different quality-controlled CHL products on a pixel per pixel basis. The different quality-controlled CHL products (i.e. OC4, OC5 and MEGS_7.5) for the 8th of April 2010 are presented in the top row.

Figure 3.4.4 shows 90-percentile map of CHL for the growing season (March-Sept incl.) of 2003 providing a spatial interpretation of the intensity of the algal blooms in the North Sea. Additionally, CHL time series are provided for the national monitoring stations Stonehaven (Scotland), Rottumerplaat 50 (The Netherlands), 330 (Belgium) and Boulogne (France) for the year 2003 showing the ability of the satellite data to capture the temporal CHL dynamics. The *in situ* measured CHL was analysed using the HPLC-method. For the time series of satellite data, we extracted a 3×3 macro-pixel and the 1×1 km centre pixel containing the monitoring station location. The resulting time series are presented in monthly bins as *in situ* data is mostly collected on a monthly basis in these stations. The satellite data is presented as boxplots to demonstrate the increased availability of satellite data compared to *in situ* sampling, i.e. 20–50 observations per growing season depending on the location, cloud cover and water conditions.
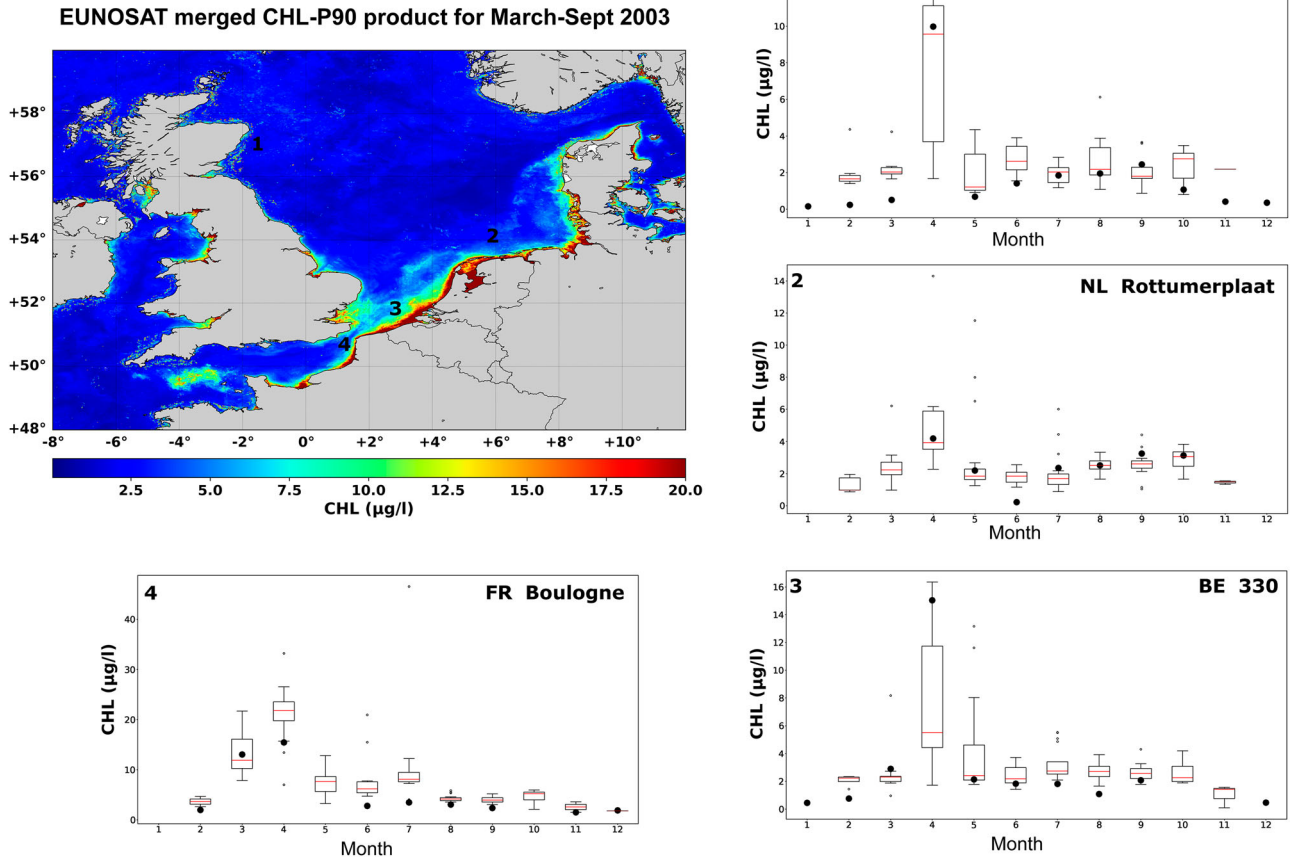
Figure 3.4.4. Map of the 90th percentile of the blended and quality-controlled CHL product for the growing season (March–September incl.) of 2003 providing a spatial interpretation of the intensity of the algal blooms in the North Sea. Additionally, a direct comparison of CHL time series, presented as boxplots, is provided for the national monitoring stations Stonehaven (Scotland), Rottumerplaat (The Netherlands), 330 (Belgium) and Boulogne (France) for the year 2003 showing the ability of the satellite data to capture the temporal CHL dynamics. Black dots represent the mean monthly in-situ CHL concentration, the boxplots show the monthly satellite-based CHL concentration with box extending from the lower to upper quartile values of the data, with a line at the median and the whiskers showing the 10- and 90-percentiles.

Towards operational collaboration between North Sea Countries

For efficient monitoring of eutrophication, it is advised to combine all available monitoring platforms, i.e. dedicated monitoring surveys taking water samples, Ferry-boxes mounted on 'ships of opportunity' and satellite observations. In this way, the strengths and weaknesses of one platform can be compensated by another in terms of spatial and temporal resolution, sampling depth, ability to measure different variables, analytical precision and costs. To enable such a combined use of different data sources, there is a need for a scientifically sound procedure to feed data collected with different methods into one common indicator for the assessment (e.g. CHL) describing both the state and the development of the pelagic environment. Data distribution centres such as CMEMS play a key role in this endeavour as they provide validated ocean colour products as input

for the JMP-EUNOSAT processing chain. With the Copernicus program guaranteeing a reliable source of data to at least 2036, special efforts are made to ensure future integration of Sentinel-3/OLCI data into the processing chain. Sentinel-3/OLCI has a similar spectral bandset as MERIS which is useful to provide more reliable results in turbid coastal waters. Additionally, the full resolution data (300 m spatial resolution) will provide more robust CHL estimates close to the coast.

3.5. Regional mean time series for the Northwest European Shelf Seas

Authors: Jonathan Tinker, Richard Renshaw, Rosa Barciela, Richard Wood

Statement of main outcome: We have developed a set of regional mean time series to aid Copernicus Marine Environmental Monitoring Service (CMEMS)

Northwest European Shelf Seas reanalysis product users (product number 3.5.1). Consultation with end-users has highlighted the appetite for pre-computed regional mean time series on a number of standardised regions masks, for variables such as Sea Surface and Near Bed Temperature (SST, NBT). We consider these regional mean time series to describe and summarise the behaviour of the CMEMS Northwest European Shelf Seas Reanalysis (which is extensively evaluated). We use the CMEMS Northwest European Shelf Seas Reanalysis evaluation from its Quality User Information Document (http://marine.copernicus.eu/documents/QUID/CMEMS-NWS-QUID-004-009-011.pdf) to suggests qualitative error bounds for the regional mean time series, of ±0.5°C and ±0.5 PSU. We also provide time series of the regional spatial variance for users who want an estimate of the distribution of values within a region. Regional summaries are used in many monitoring and management activities, and providing a ready-made integrated product that will aid utilisation for a wide range of end-users.

Products used:

Ref. No.	Product name and type	Documentation
3.5.1	NORTHWESTSHELF_ REANALYSIS_PHYS_004_009	PUM: http://marine.copernicus.eu/documents/PUM/CMEMS-NWS-PUM-004-009-011.pdf QUID: http://marine.copernicus.eu/documents/QUID/CMEMS-NWS-QUID-004-009-011.pdf

The Northwest European Shelf Seas face many overlapping pressures, and so are subject to significant statutory management, including the Marine Strategic Framework Directive (MSFD) and the Common Fisheries Policy (CFP). Both of these policies require an accurate knowledge of the current state of the sea to aid and inform decisions. However, *in situ* measurements are often underfunded and relatively sparse on the Northwest European Shelf Seas (relative to the local Rossby radius), and so there is scope to complement these with ocean model reanalyses. Reanalyses synthesise models and observations into a statistical 'best guess' of the ocean state – ocean reanalyses potentially provide more skill than either the model or observations alone (Balmaseda et al. 2015), with the model physics providing continuous 3-d fields, and the observations to anchor them in reality. The model reanalyses and near real time forecast analyses provided by the CMEMS are therefore an ideal dataset to help inform these management processes.

Regional summary statistics are used in a wide range of applications. Many monitoring and management processes report on such predefined standard regions. For example, International Council for the Exploration of the Sea (ICES) provides fisheries management advice to multiple governments and regional fisheries management organisations (according to ICES Advisory regions) advising on multiple aspected, including MSFD and CFP. The UK Marine Monitoring and Assessment Strategy (UKMMAS) gathers much of its evidence on the state of the UK waters in the Charting Progress 2 biogeographic regions (DEFRA 2010), which feeds into the MSFD. The UK's Marine Climate Change Impact Partnership reports observed and projected climate impacts on the Charting Progress 2 regions (e.g. MCCIP 2013).

Pre-computing regional means for useful regions may simplify the use of CMEMS data for some users, and allow for a wide range of new CMEMS users. As part of the Horizon 2020 funded AtlantOS project, work package 8.6 assessed user requirement for CMEMS Northwest European Shelf Seas data within three major European organisations, involved with the MSFD and CFP (Barciela et al. 2019). In-depth interviews were undertaken with scientists at the European Environment Agency (EEA, MSFD), ICES (CFP and fisheries management) and Cefas (the UK government agency responsible for the UK's MSFD and CFP reporting). Each organisation was asked a number of questions, including 'How would you like the products/service to evolve in the future?'. Both ICES and EEA asked for pre-computed time series of temperature, salinity and stratification in predefined regions – specifically in regions that they were already using (ICES Ecoregions). In response, we are therefore releasing the regional mean time series as a CMEMS product. In addition, there are many marine organisations with less technical resource than the EEA and ICES (and no expertise in working with spatial data in netCDF files) that may also benefit from such a simplified product.

The choice of appropriate region masks is important for uptake for the regional mean product. We initially built on the Northwest European Shelf Seas region mask of Wakelin et al. (2012). To identify region masks important to users, we undertook informal user engagement through the UK's Marine Climate Change Impact Partnership steering group, which is a partnership between scientists, the UK government and its agencies, and non-governmental organisations with wide engagement. For example, over 150 scientists from more than 50 leading science organisations contributed to the 2013 full report card

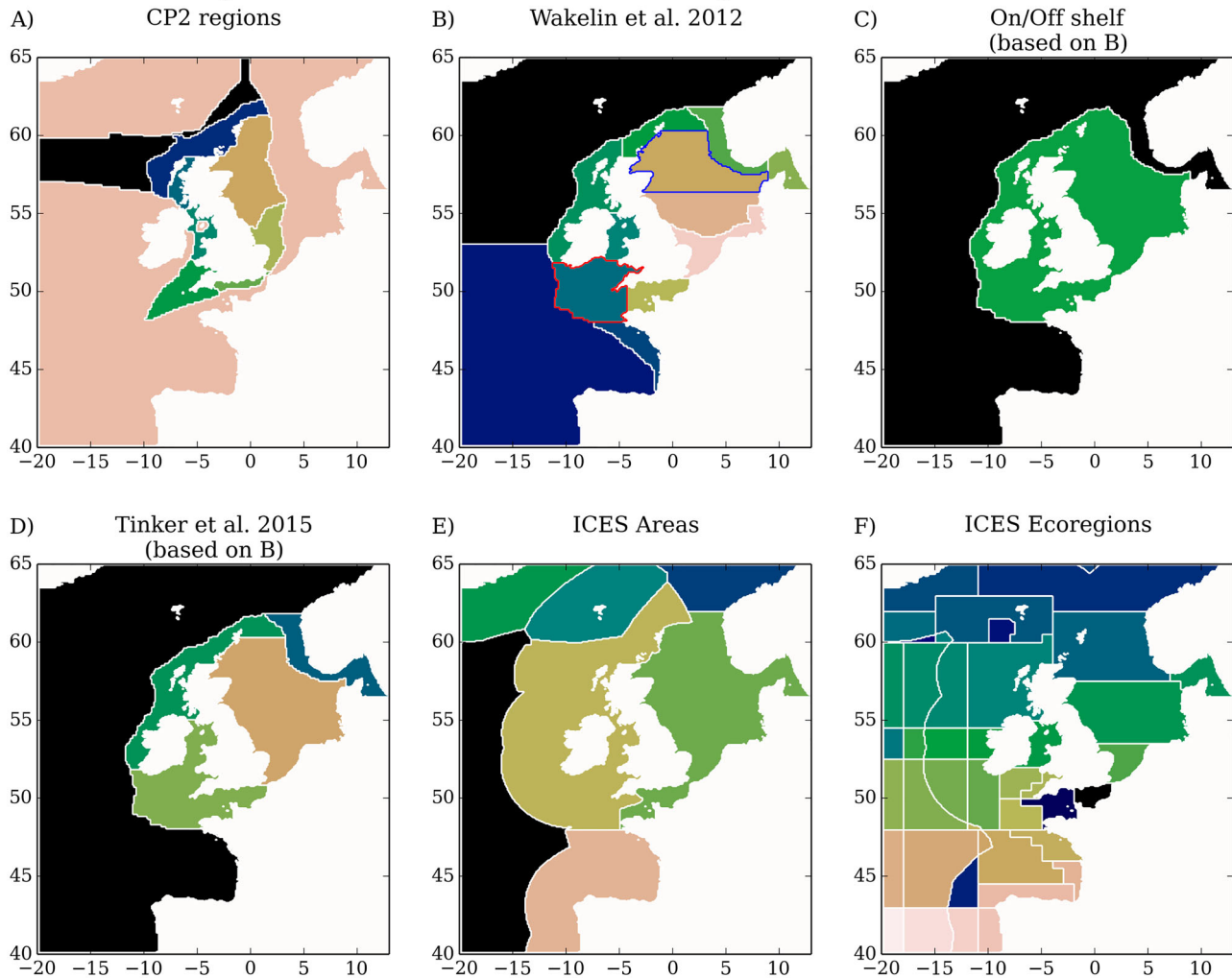# Region Masks for CMEMS NWS regional mean time series

Figure 3.5.1. Sets of standardised regions used for time series: (A) the UK Charting Progress 2 (CP2) regions; (B) regions based on Wakelin et al. (2012). The northern North Sea (blue) and Celtic Sea (red) region, which are used in Figure 3.5.2, are highlighted; (C) regions delimiting the shelf, by combining regions in (B); (D) combined regions in (B), used in model evaluation by Tinker et al. (2015); (E) ICES Advisory Areas (ICES 2004); and (F) ICES Ecoregions (ICES 2004).

(MCCIP 2013). These discussions supported the ICES Ecoregions and ICES Advisory Areas (ICES 2004), and advocated inclusion of the UK government Charting Progress 2 regions (DEFRA 2010). These region maps are presented in Figure 3.5.1. Wakelin et al. (2012) divided the NWS according to geographical region and characteristics (Figure 3.5.1(b)), and into shelf and oceanic regions (Figure 3.5.1(c)). Tinker et al. (2015) joins some of these to create larger regions for model evaluation (to increase the numbers of observations within each region Figure 3.5.1(d)). The UK government Charting Progress 2 divides the UK sea area into eight regions, principally based on physical and biological features such as tidal fronts and seabed flora and fauna (Figure 3.5.1(a)). The ICES regions (Figure 3.5.1(e)) and Ecoregions

(Figure 3.5.1(f)) are based on biogeographic and oceanographic features and existing political, social, economic, and management divisions. With sufficient user support, additional region masks may be included in future versions of the CMEMS Northwest European Shelf Seas reanalysis.

The regional means provide a simple overview of the conditions within the region. For example, the SST and SSS from the Celtic Sea and the northern North Sea (respectively) can be plotted with no, or little, processing as in Figure 3.5.2. Some regions may include different water masses (for example, coastal water and regions of freshwater influence) which can lead to a wide range of values within the region – for some applications this may be important, and should be considered when interpreting the regional
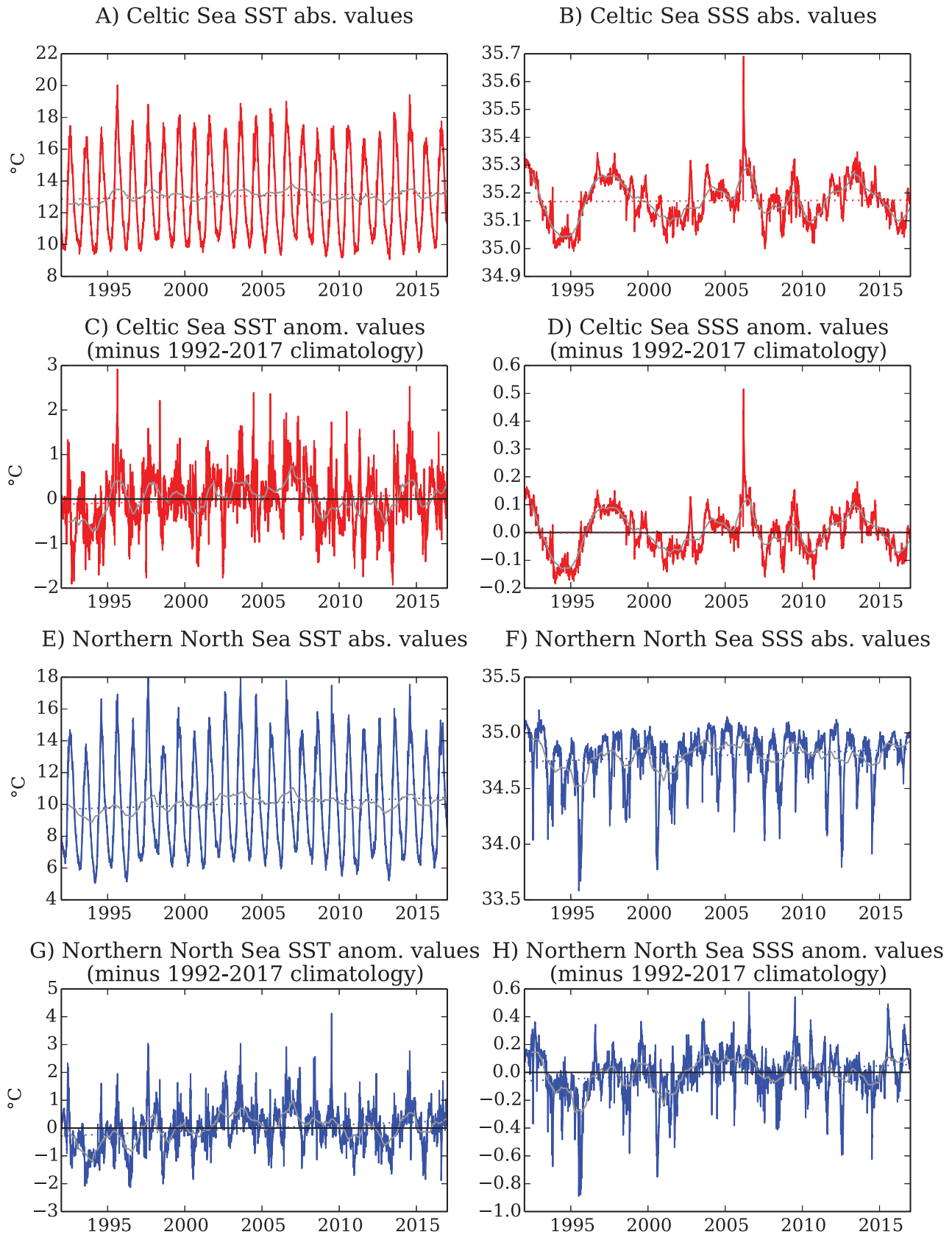
Figure 3.5.2. Example regional mean time series for the Celtic Sea ((A–D); red; upper two rows) and the northern North Sea ((E–H); blue; lower two rows) for SST ((A, C, E, G); left column) and SSS ((B, D, F, H); right column). Absolute daily mean SST/SSS (light shading) averaged over the regions (as defined in Figure 3.5.1(B), with colouring matching the region outline), with a 30-day running mean (dark line), a 365-day running mean (grey), and a linear trend line (dotted coloured line) are presented in the first and third rows (Celtic Sea SST and SSS (A, B) and northern North Sea SST and SSS (E, F)). Regional mean anomalies (relative to a climatological seasonal cycle calculated between 1992 and (end of) 2017 are presented in the second and fourth row (Celtic Sea SST and SSS (C, D) and northern North Sea SST and SSS (G, H)).

means. We also include the regional (spatial) variance, which, together with the mean, gives an estimate of the distribution of values within the region – this may be useful for users concerned about how representative the regional mean is.

There are only a few variables on the NWS that are sampled with complete spatial coverage (SST being the exception). Therefore it is difficult to robustly validate the regional mean product. For sea surface temperature, it is possible to evaluate the regional mean time series with a spatially complete data set, such as the (largely satellite based) OSTIA analysis (Operational Sea-surface Temperature and sea-Ice Analysis; Roberts-Jones et al. 2012), however, as the reanalysis assimilates SST, this is circular. Instead, the regional mean time series are considered descriptors of the behaviour of the NWS reanalysis, rather than describing reality. The NWS reanalysis has been extensively evaluated in the Quality Information Documents (QUID), and given the data assimilation of observations, provides the statistical 'best guess' of the state estimate for the Northwest European Shelf Seas (Tinker et al. 2018). Here we use the relevant parts of the QUID to inform the user of the scale of the model errors and biases that will be propagate into the regional mean time series product.

The reanalysis temperature biases are generally smaller than ±0.5°C at all depths over the shelf. Reanalysis salinity biases are generally of magnitude less than ±0.5 PSU. In the coastal regions of the Southern Bight of the North Sea and around the Norwegian Trench, the reanalysis is typically too fresh, and is typically too saline in the Irish Sea, and further offshore in the Norwegian Trench. These errors are captured within the regional mean time series, and so provide qualitative error bounds of ±0.5°C and ±0.5 PSU for regions on the Northwest European Shelf Seas.

As these regional mean time series have only just been produced they have not been available to end-users, and so no examples of their use can be cited. However, similar Northwest European Shelf Seas regional mean time series and summary statistics have been used in a number of recent studies. Tinker et al. (2018) used regional mean time series of the previous NWS reanalysis, calculated on the Wakelin et al. (2012) regions (Figure 3.5.1(B)) to investigate seasonal predictability on the Northwest European Shelf. Tinker et al. (2015, 2016) used regional mean time series calculated from their Northwest European Shelf Seas climate projection to aid model evaluation, and to summarise their findings. The CMEMS Northwest European Shelf Seas regional mean time series product

will be released by Autumn 2019, and will include surface and bed (and surface-minus-bed) temperature and salinity, for the regional mean and its associated spatial variance. Once the new regional mean time series (introduced here) are released, work will continue to help raise awareness with MCCIP partners, and other policy users.

3.6. Using CMEMS and the Mediterranean Marine Protected Areas sentinel network to track ocean warming effects in coastal areas

Authors: Nathaniel Bensoussan, Emma Cebrian, Jean-Marie Dominici, Diego Kurt Kersting, Silvija Kipson, Zafer Kizilkaya, Oscar Ocaña, Marion Peirache, Frédéric Zuberer, Jean-Baptiste Ledoux, Cristina Linares, Mikel Zabala, Bruno Buongiorno Nardelli, Andrea Pisano, Joaquim Garrabou

Statement of main outcomes: Systematic and sustained *in situ* sampling effort is being conducted in a growing number of Mediterranean Marine Protected Areas to track and assess climate change effects in marine coastal ecosystems. Considering the need for accurate observation at large geographical scale, we conducted joint analysis of CMEMS satellite derived high-resolution foundation sea surface temperature with T-MEDNet database of multi-year *in situ* temperature acquired nearshore in Mediterranean Marine Protected Areas. Statistical analysis of the match-up database (multi-year, 22 sites) demonstrated the applicability of the CMEMS satellite data to the nearshore areas and further documented associated uncertainties across temperature and variability gradients. Rapid and accelerated warming of sea surface temperature in the northwestern Mediterranean during the past decade is reported and compared to the 1982–2011 period (0.047 vs. 0.029°C/year respectively). Elevated and consistent warming rates were calculated at local scale from *in situ* and satellite observations. Combining CMEMS remote sensing and *in situ* monitoring systems, as shown in this study, is a pillar to enhance our understanding on climate change impacts in coastal areas.

Products used:

Ref. No.	Product name and type	Documentation
3.6.1	SST_MED_SST_L4_REP_OBSERVATIONS_010_021 Remote sensing	PUM: http://marine.copernicus.eu/documents/PUM/CMEMS-OSI-PUM-010-021-022.pdf QUID: http://marine.copernicus.eu/documents/QUID/CMEMS-OSI-QUID-010-021-022.pdf
3.6.2	T-MEDNet consolidated *in situ* temperature time series. www.t-mednet.org (DOI pending) *In situ*	www.t-mednet.org/T-Database

The coastal ocean is among the most dynamic and biologically diverse areas on Earth and supports a wide range of key marine ecosystems, which are providing goods and services to our societies. Climate change is one of the major threats for the conservation of marine coastal ecosystems through direct but also cumulative effects with other stressors (e.g. Coll et al. 2010; Hughes et al. 2017). Understanding how ocean warming is affecting the structure and functioning of marine ecosystems is crucial to support sound management and conservation policies and strategies. In the Mediterranean Sea, the occurrence of mass mortality events affecting the coastal macrobenthic biota and shifts in species distribution are the major effects of ongoing warming trend (e.g. Garrabou et al. 2009; Kersting et al. 2013, Bianchi et al. 2017). However, studies considering appropriate large-spatial and long-term scales on different climate change indicators are scarce. Representative data across biogeographic gradients are essential to enhance our capacity to evaluate current changes and impacts as well as to explore, through novel modelling approaches, future trajectories of ecosystems under different scenarios. Such information is required to establish vulnerability assessments and develop adaptation plans for the different management frameworks (from local to regional scales).

A systematic and sustained observation effort of Essential Climate and Ocean Variables (ECV/EOV), among which sea surface temperature and subsurface temperature, is essential to analyse changes and trends in marine ecosystems (IPCC, see Wong et al. 2014). Building sound knowledge of climate change impacts in the complex 3D marine realm might push requirements for sustained and accurate environmental data acquisition at relevant resolution both in time and space like never before (e.g. Bates et al. 2018).

Sea surface and subsurface temperature can be measured with different sensors and instrumental platforms, which have intrinsic differences, making it necessary to carefully assess errors and biases between them before merging data sets (Smale and Wernberg 2009). While satellites provide good spatial and temporal coverage of the surface layer of the ocean, the ability of gridded or operational satellite observations products in retrieving accurate sea surface temperature information in coastal areas has been repeatedly challenged (e.g. Smale and Wernberg 2009; Smit et al. 2013; Brewin et al. 2017, 2018). *In situ* measurements are needed to document the temperature variations beneath the surface, and they provide more reliable and accurate source of information on local conditions but show spatial and temporal limitations. In particular, one can note the scarcity of long-term series suited for climate change studies in the coastal zone. Indeed, long-term coastal observation is at the confluence of several challenges, among which are investment and maintenance costs, fieldwork constraints, data management, qualification and reporting.

Understanding the processes driving the ecological responses to climate change across different biological organisation levels (from the genes to ecosystems) is essential to address sound adaptation measures. High-resolution *in situ* measurements provide key information to characterise the variability of thermal regimes in which marine organisms thrive. In particular, these data have been key to characterise the thermal environment associated with the onset of mass mortality events that have affected the benthic biota during the past decades (e.g. Bensoussan et al. 2010; Crisci et al. 2011),
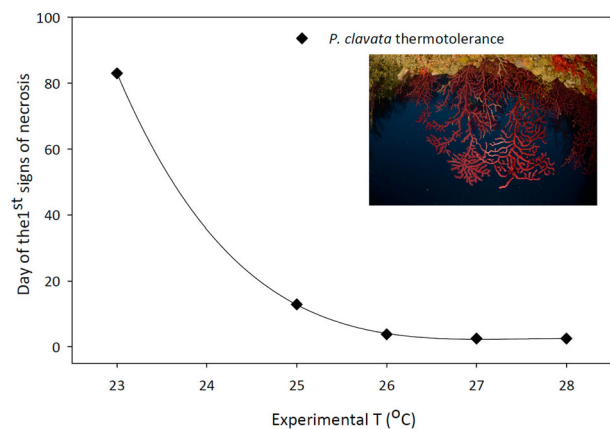
Figure 3.6.1. Thermotolerance response function of the red gorgonian *Paramuricea clavata*. The response curve shows the exposure duration to different temperature treatments (experimental T°C) leading to the first signs of tissue necrosis. Results were obtained from the compilation of different thermotolerance experiments and from *in situ* observations, combining local (at depth) information on thermal environment and necrosis. Figure modified from the data presented in Crisci et al. (2011, 2017) and Pairaud et al. (2014), integrating new experimental results.

and for the design of tailored field and laboratory experimental studies on the biological responses to warming of sensitive species (e.g. Ledoux et al. 2015; Crisci et al. 2017). For instance, comprehensive assessment of the thermotolerance response function of *Paramuricea clavata*, a habitat forming species, has been conducted from thermotolerance experiments and field observations (Figure 3.6.1). Non-linear response was evidenced, showing (sub-) lethal impacts across a range of temperature conditions, from sustained periods (months) of warm temperature to few days of extreme hot conditions. Such conditions might be detected using different and complementary approaches, like anomalies, extreme warm or hot conditions, and their integrative over different time scales, from event to season or year (see also sections 4.4 on Marine Heat Waves). This kind of information can provide empirical response functions to thermal stress that can be used to develop early warning systems and explore the risk of onset of mass mortality events under different climatic scenarios (e.g. Bensoussan et al. 2013; Pairaud et al. 2014; Galli et al. 2017).

In this study, we perform a joint analysis of multi-year to decadal high-resolution temperature time series acquired *in situ* from T-MEDNet network (www.t-mednet.org, product reference 3.6.2) with CMEMS remote sensing product of daily optimally interpolated foundation sea surface temperature at 4 km spatial resolution/smoothness (product reference 3.6.1) in the Mediterranean coastal zone. This joint analysis focuses on two main topics: characterisation of thermal regimes and warming trends. The results obtained advocate for the complementarity of these valuable date sets, from local to large scales in the coastal zone, by evaluating representativeness, uncertainties and limitations from which an improved framework on the assessment of climate change effects can be designed.

Instrumental development and a new generation of temperature data loggers now allow for deployment in multiple locations and depths over periods from months to years for high frequency (minutes to hours) characterisation of seawater temperature in a cost-effective manner. The origin of T-MEDNet network was set during the late nineties, when Mediterranean marine ecologists interested in climate change impacts on marine coastal ecosystems started to implement a standardised strategy to obtain *in situ* temperature data. This strategy consisted in temperature acquisition at high frequency (1 h) and high-resolution across the seasonal thermocline, using data loggers deployed every 5 m from surface to 40 m depth or more. Since then systematic and sustained sampling effort has been conducted in a growing number of sites, mainly Marine Protected Areas (Figure

3.6.2(a)). Same data loggers are being used at standard depth (Hobo U22, accuracy 0.21°C, resolution 0.02°C), are attached to rocky walls or moorings exposed to dominant winds and currents, and retrieved every 6–12 months by scuba divers. At present over 40 sites are being monitored, mainly in the north and central western Mediterranean but also in the Alboran Sea, southwestern Mediterranean, Tunisian, Adriatic and Aegean sub-basins (Figure 3.6.2(a)). T-MEDNet temperature monitoring sites span across a large range of Mediterranean Sea surface temperature (more than 7°C, from 2nd to 92th percentile of surface variability, Figure 3.6.2(b)). The monitoring strategy has proved its efficiency, with high return rates on observations (median return rate above 80%). Field surveys were complemented by the launch, in 2009, of a collaborative platform (www.t-mednet.org) for rigorous data management and quality check, allowing the building of unified consolidated database on *in situ* temperature in coastal waters consisting in more than 13×10^6 samples acquired at high frequency and standard depth levels. The development of this regional observation network was possible through sustained partnership between research institutions, Marine Protected Areas management bodies, Non-Governmental Organisations (e.g. IUCN, MEDPAN) and regional organisations (SPA/RAC). The ultimate goal is to contribute to a representative sentinel network on climate change effects in the Mediterranean Sea with the aim to maintain and enhance monitoring effort, also in terms of representativeness across the different sub-basins.

In Figure 3.6.2(c), we show an example of the time series acquired in the Marine Protected Area 'Reserve Naturelle de Scandola' (Corsica, France) over the period 2004–2018. From such long-term and high-resolution time series, robust baselines on coastal thermal regimes and seasonal stratification dynamics can be obtained (Figure 3.6.2(d)). The Marine climatology obtained from multi-year continuous monitoring shows some typical features of North Western Mediterranean thermal regimes. The annual cycle of the water column is governed by the seasonal cycle, which originate in seasonal vertical temperature stratification, and can display important variability depending on the area, due to the local wind regimes, bathymetry and topography (see for instance Bensoussan et al. 2010). The minimum temperature is observed in February–March (13.2°C) when the water column can become fully mixed. Spring and Summer surface warming induce seasonal vertical temperature stratification with the development and progressive deepening of the surface mixed layer. Maximum temperature occurs in August and generally, elevated daily temperatures are observed in the upper 15 m
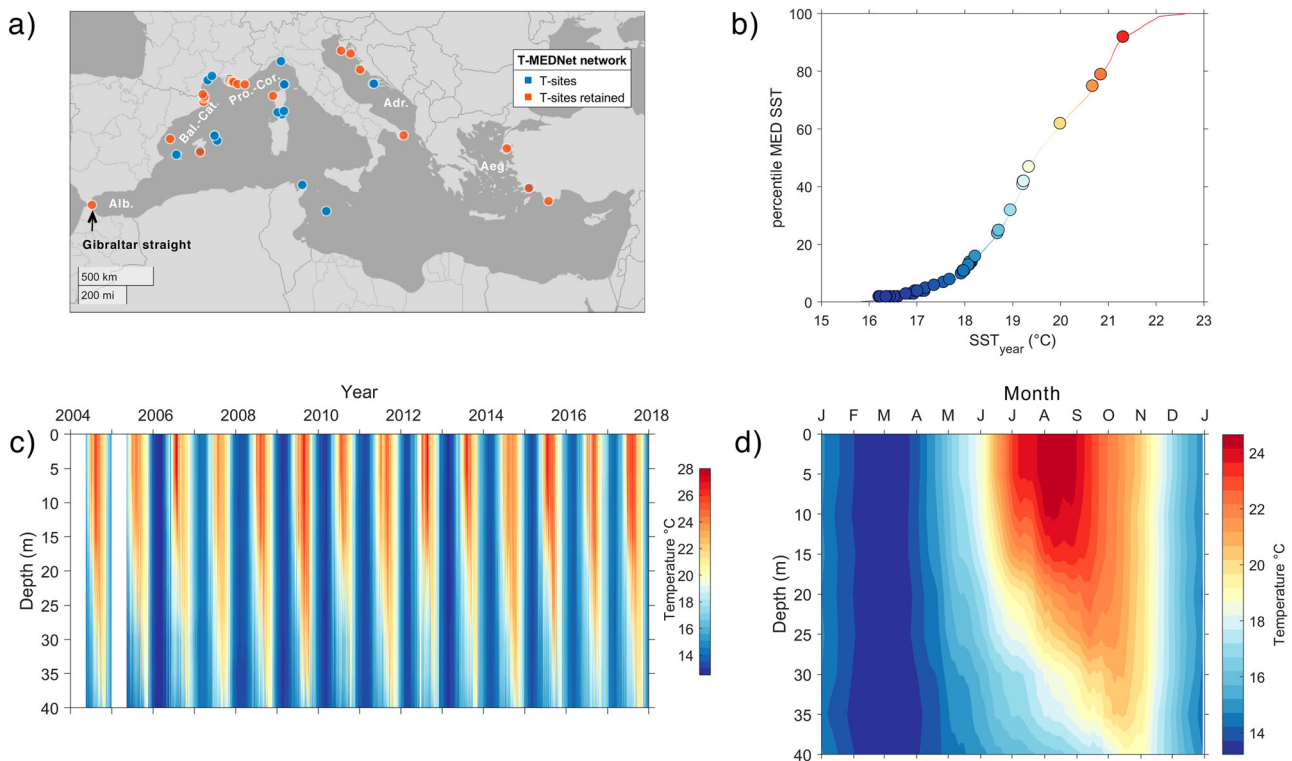
Figure 3.6.2. (a) Location map of T-MEDNet temperature monitoring sites in the Mediterranean Sea (Product reference 3.6.2). The sites retained for statistical comparison with satellite data are shown in orange, in the Alboran (Alb.), Balearic-Catalan (Bal.-Cat.), Provence-Corsica (Pro.-Cor.), Adriatic (Adr.) and Aegean (Aeg.) sub-regions. (b) Yearly mean sea surface temperature at the T-MEDNet sites and corresponding percentile relative to distribution over the entire Mediterranean Sea. Calculations were conducted over the period 1982–2011 from product reference 3.6.1. (c) Example of the high-resolution and long-term time series acquired *in situ* using data loggers set at standard depth levels (every 5 m from 5 to 40 m depth) in the Marine Protected Area of Scandola (Corsica, France) since 2004. (d) Climatological mean seawater temperature between the surface and 40 m depth at Scandola Marine Protected Area. The climatological mean was calculated over the period 2004–2017, for each depth and day of year using a 11-day moving window and additional smoothing on 31 days.

of the water column (mean maximum values ranging between 23°C and 26°C). The temperature difference between 5 and 40 m depth is 8°C on average in August. In late summer and fall, surface cooling and important (wind induced) vertical mixing occur, with subsequent deepening of the mixed layer depth to the bottom in late October or November. Benthic ecosystems dwelling between the surface and 40 m depth are thus exposed to contrasted environmental conditions, with strong differences in the magnitude and phasing of their hydrological cycle (e.g. mean amplitude of 12°C at the surface vs. 6°C at 40 m depth, maximum observed in August and October respectively). From the data series available, the different patterns of stratification and temporal variability were characterised across the network.

Regarding the *in situ* T-MEDNet network temperature database (product reference 3.6.2), a first subsample was obtained, retaining maximum depth of 5 m (*in situ$_{5m}$*) and more than one full year of measurements, for joint analysis with sea surface temperature from CMEMS (product reference 3.6.1). Out of these criteria,

22 time series were considered (median length 7.4 years), from the western and eastern Mediterranean basins where contrasted hydro-climatic conditions occur (Figure 3.6.2(a,b)). A matchup database of co-located satellite (nearest pixel) and *in situ$_{5m}$* multi-year daily time series was built for statistical analysis of the observed differences over the annual cycle. Comparisons between remote sensing and *in situ$_{5m}$* data were carried out using classical descriptors and analysis for bias, standard deviation, correlation and root mean square difference and results were synthesised in Taylor diagrams (Taylor 2001).

Important differences were evidenced from the 22 sites (Figure 3.6.3(a,b)). Overall, high correlation (>0.97) and low bias (<0.4°C) were shown for most sites (group A, N = 15) while lower agreement was evidenced for six sites distributed along 60 km of coastline in Provence (group B1) and on the southern coast of Gibraltar Straight (B2, Ceuta, Spain). From the observed variability in the correlation and standard deviation patterns, the 22 sites were clustered in six groups (groups A1
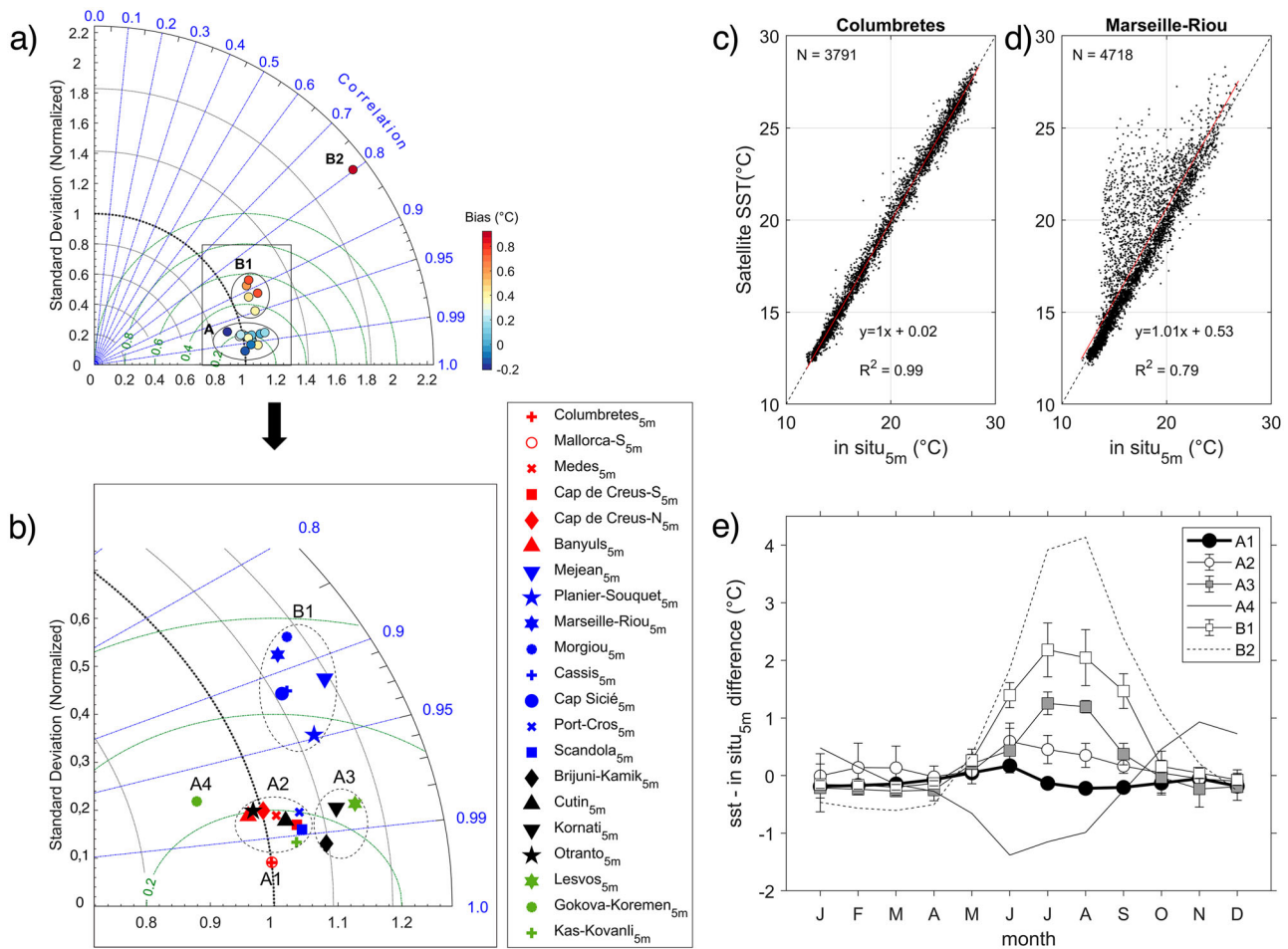
Figure 3.6.3. (a) Taylor diagram showing comparison between multi-year time series of satellite derived daily sea surface temperature from CMEMS (Product reference 3.6.1) and T-MEDNet *in situ* measurements at 5 m depth (product reference 3.6.2) considering all available samples over the 2004–2017 period. (b) Zoom on the box shown in panel a showing sites clustering along the standard deviation and correlation axes. Different symbol colours were used for sites from the Balearic-Catalan (red), Provence-Corsica (blue), Adriatic (black) and Aegean (green) sub-regions. (c–d) Linear regression analysis of daily temperature data in two sites from subgroups A1 and B1 (Columbretes Islands and Marseille-Riou respectively). (e) Average of the mean monthly bias for the different subgroups of stations show in the panels a–b.

to A4, B1 and B2). They were further analysed in order to quantify typical uncertainties and monthly bias during the annual cycle (Table 3.6.1, Figure 3.6.3(e)) and to better understand the determinants of the observed variability (e.g. Figure 3.6.3(c,d)).

Interestingly, highest and near perfect agreement in correlation ($R = 0.996$) and amplitude pattern (point lying on the unit standard deviation arc) was shown for two sites located off mainland coast, nearshore small islands in the Balearic Sea (group A1, Columbretes and Mallorca-S, distant by ca. 200 km, Figure 3.6.3(b,c)). The root mean square difference calculated over more than eight years of data was 0.44°C, i.e. comparable to typical accuracy of satellite measurement in non-nearshore area (0.5°C, Table 3.6.1, Pisano et al. 2016). These results demonstrate the high consistency and accuracy of multi-year local time series obtained from

the optimally interpolated satellite data in such near open sea conditions (product reference 3.6.1).

Comparatively, two to five-fold increase in root mean square difference was evidenced in typical coastal zone (mostly Marine Protected Areas, Table 3.6.1). Generally, low bias occurred in winter and fall but significant warm bias was shown in June (0.7°C for group A2) or during summer (Figure 3.6.3(e)). This pattern, consistent with the seasonal cycle, was amplified in sites within the clusters showing lower agreement, with summer bias >2°C to 4°C in groups B1 and B2 respectively (Figure 3.6.3(b,e), Table 3.6.1). However, a distinct seasonal pattern was shown in Gokova Koremen (A4, STD = 0.90, Figure 3.6.3(e), Table 3.6.1) where effect from the nearby Akyaka river is strongly suspected, which might explain the seasonal inversion in vertical temperature gradients in the top 5 m of the water column.

Table 3.6.1. Summary of the satellite – *in situ* matchup data over the Mediterranean Sea in the near-shore and off-shore as a function of sensor type.

Data Type	Depth (m)	Bias (°C)	RMSD (°C)	Correlation	Standard deviation (Normalized)	Number of samples (and sites)	Reference period (median duration in year)
Nearshore HF time series using benthic data loggers, coastal moorings - multi-year data sets from T-MEDNet - this study							
A1	5.0	-0.11	0.44	0.996	1.01	6 768 (2)	2007-2017 (9.7)
A2	5.0	0.16	0.75	0.984	1.04	23 960 (9)	2004-2017 (7.2)
A3	5.0	0.09	0.81	0.983	1.14	7 539 (3)	2012-2017 (3.7)
A4	5.0	-0.21	0.99	0.970	0.91	985 (1)	2015-2017 (2.7)
B1	5.0	0.59	1.64	0.910	1.14	16 232 (6)	2004-2017 (7.4)
B2	5.0	0.92	2.1	0.798	2.15	1 008 (1)	2014-2017 (2.8)
Total						56 222 (22)	
Source: Pisano et al. 2016							
Drifter	0.2	-0.23	0.52			102 164	2004-2012
TSG	4.0	-0.25	0.58			57 369	1990-2012
CTD	3.0	-0.29	0.58			6 649	1982-2012
XBT	3.0	-0.29	0.58			5 927	1990-2012
ARGO Float	3.0	-0.18	0.54			769	1999-2012
Total		-0.24	0.55	0.992		172 878	1982-2012

From group A2, a high agreement between the satellite and *in situ*$_{5m}$ data was achieved for nine sites from the different sub-basins, from cold to warm Mediterranean Sea surface temperature: in the Catalan, Provence-Corsica, Adriatic and S-Aegean Seas. The satellite data typically explained 96% of the variance observed *in situ*, with a root mean square difference $0.75 \pm 0.18°C$ (Figure 3.6.3(b), Table 3.6.1). Figure 3.6.4(a–d) shows how satellite and *in situ*$_{5m}$ data track each other during the entire annual cycle of year 2015 in Columbretes Islands (from group A1), and in three sites from group A2 accounting for large-spatial temperature gradients in the Mediterranean Sea (*in situ* data completeness index 99.6%). The high agreement allows fine analysis of the local subsurface annual temperature cycle and of such inter-site differences using satellite data. The highest bias between satellite and *in situ*$_{5m}$ daily temperatures occurred during periods of strong sea surface warming (e.g. in June and warm summer events) which might be a sign of vertical temperature gradients, or during cold episodic events that were smoothed in the satellite data (up to 1°C in Columbretes, 2–3°C in other sites).

To take into account how complex coastal hydrological dynamics can affect satellite data, we considered a group of six T-MEDNet *in situ* monitoring sites (group B1), from the Gulf of Marseille to the East, to Cap Sicié to the West (Figure 3.6.5(c,d)). These sites displayed comparatively lower agreement between *in situ*$_{5m}$ and satellite data than other sites from the A groups. Since the hydrology in the area is under the influence of coastal upwelling cells triggered by

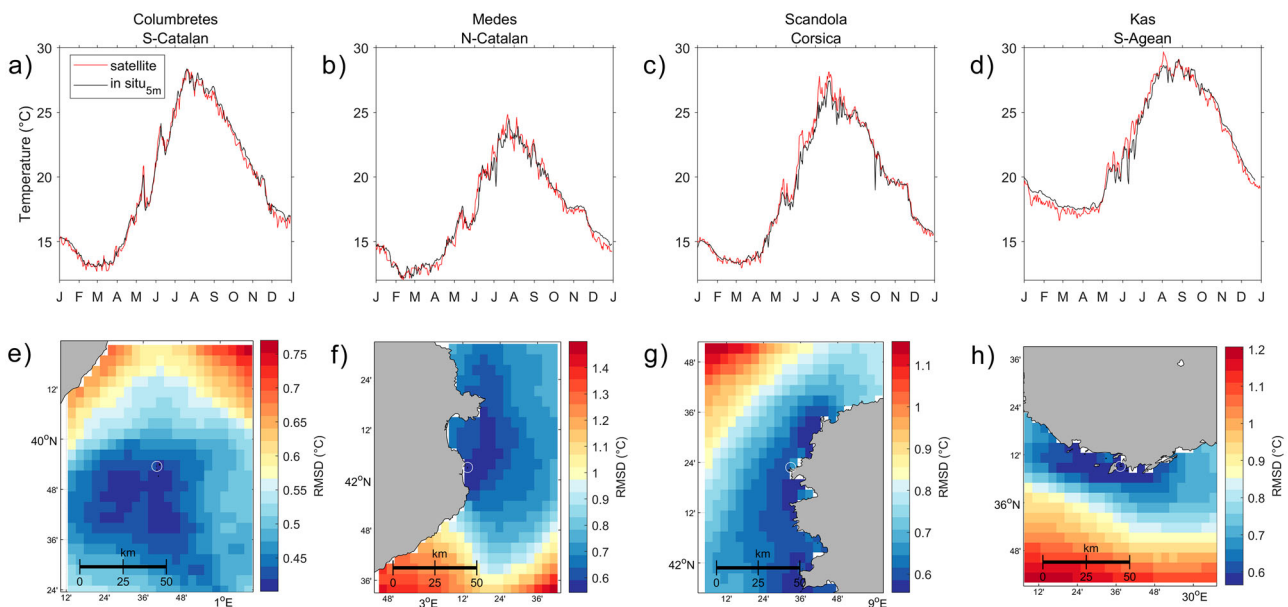**Figure 3.6.4.** (a–d) Satellite and *in situ* temperature time series for year 2015 for sites from the Western and Eastern basin (Columbretes from group A1 and Medes, Scandola and Kas, from group A2). (e–h) Spatial maps of RMSD for match-ups (same day) of *in situ*$_{5m}$ data for all satellite sea surface temperature data from pixels in $1 \times 1°$ box. Reference of the products used: 3.6.1 and 3.6.2.
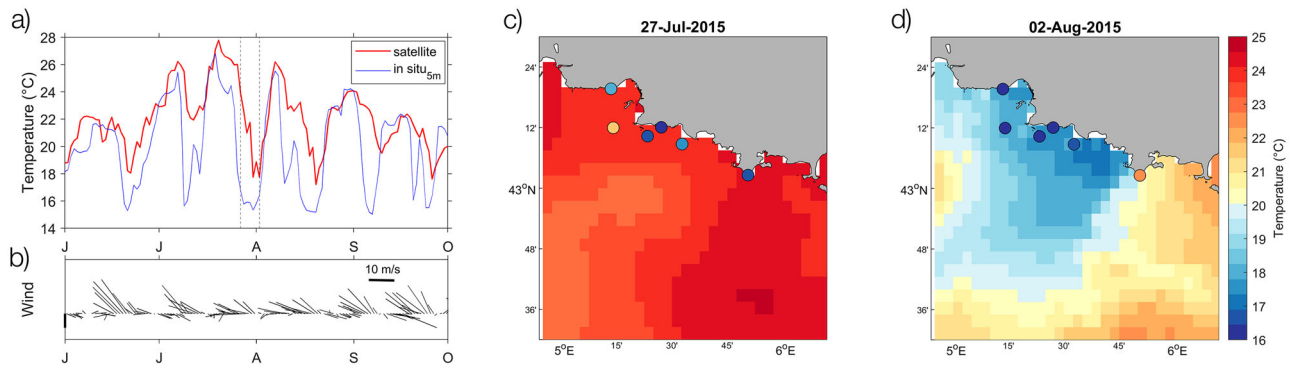
Figure 3.6.5. (a) Time series of satellite derived sea surface temperature and *in situ$_{5m}$* in Marseille Riou (Provence France). (b) Wind data from local observations at Cap Couronne (Source Météo France). (c–d) spatial maps of sea surface temperature and *in situ* measurement during the set up and relaxation phase of the upwelling event observed at the end of July 2015 (dashed vertical lines in panel A).

alongshore Mistral winds (Millot and Wald 1981; Bensoussan et al. 2010), we related the oceanographic time series with independent wind data (Meteo France). We found that the degradation of matching patterns of group B1 could be attributed to satellite data which did not accurately resolve the surface temperature during the frequent upwelling events (Figure 3.6.5(a,b)). In fact, from their setup, when temperature decreased at rates up to 7°C/day, to their relaxation. Although most upwelling events were captured by the satellite data, time lag of few days was observed for their set up and their intensity was systematically underestimated. This was also illustrated in the spatial maps of sea surface temperature for the strong upwelling event that occurred at the end of July 2015. Local bias up to 8°C occurred on 27th of July 2015 (Figure 3.6.5(c)), while higher spatial agreement between satellite and *in situ* data was shown during the relaxation phase of this specific event whose influence was not limited to the nearshore but concerned broader areas (Figure 3.6.5(d)). These discrepancies are likely due to the satellite data quality check and interpolation procedures, which result in smoothing of such cold events.

Similarly, satellite smoothing of the summer high frequency variability was evidenced for sites of group A3. These three sites from the N-Adriatic and N-Aegean Seas share common features such as complex topography on large and shallow continental shelves and important wind forcing which drive episodic cooling events (Bora and Meltem winds). Contrarily in Ceuta (B2) warm bias was consistently observed during summer and the satellite derived sea surface temperature over the pixel area was not representative of local nearshore conditions, which might be interpreted as sign of spatial variability due to complex hydrodynamics along the southern coast in the Gibraltar straight.

Finally, in order to analyse the spatial representativeness of the *in situ* point measurements, statistics were computed considering all satellite data from pixels within boxes of 1° longitude and 1° latitude centred on the monitoring sites shown in Figure 3.6.4(a–d). The spatial maps of root mean square difference for year 2015 (Figure 3.6.4(e–h)) indicate smooth gradients, with highest agreement between satellite and *in situ* data for closest and adjacent pixels, though not necessarily alongshore (Figure 3.6.4(f–h)). Coherent spatial patterns were observed, for instance for Capes vs. Gulfs that further illustrate the interest of combining satellite and *in situ* data to enhance analysis of the spatial variability over coastal areas. In Columbretes, owing to the near open sea conditions and low horizontal sea surface temperature gradients (0.6°C annual difference over the S-Catalan Sea map, data not shown), high agreement concerned vast areas (100's km^2), south and east of the nearshore monitoring site (Figure 3.6.4(e)).

Warming can vary regionally and locally, with potential impacts on ecosystems. In order to evaluate the applicability of satellite data for representing subsurface trends in the nearshore area, nine time series from sites in the northwestern Mediterranean were selected from T-MEDNet database. The sites selection was based on the availability of a minimum number of seven years covered by data over the 2007–2016 period (Figure 3.6.6). The monthly average temperature, climatology and anomalies at each site were computed, out of which few were excluded from analysis when based on less than 15 days of observation. Finally, the average completeness index on monthly anomalies was 84 ± 9% (mean ± std), ranging from 73% to 96%. Warming rates (in °C per year) were calculated using the Sen's method to estimate the slope of the monthly anomalies time series (Sen 1968) over the 2007–2016 period. Warming trends over the northwestern Mediterranean Sea were calculated from satellite data (product reference 3.6.1) over the past decade (2007–2016) and at
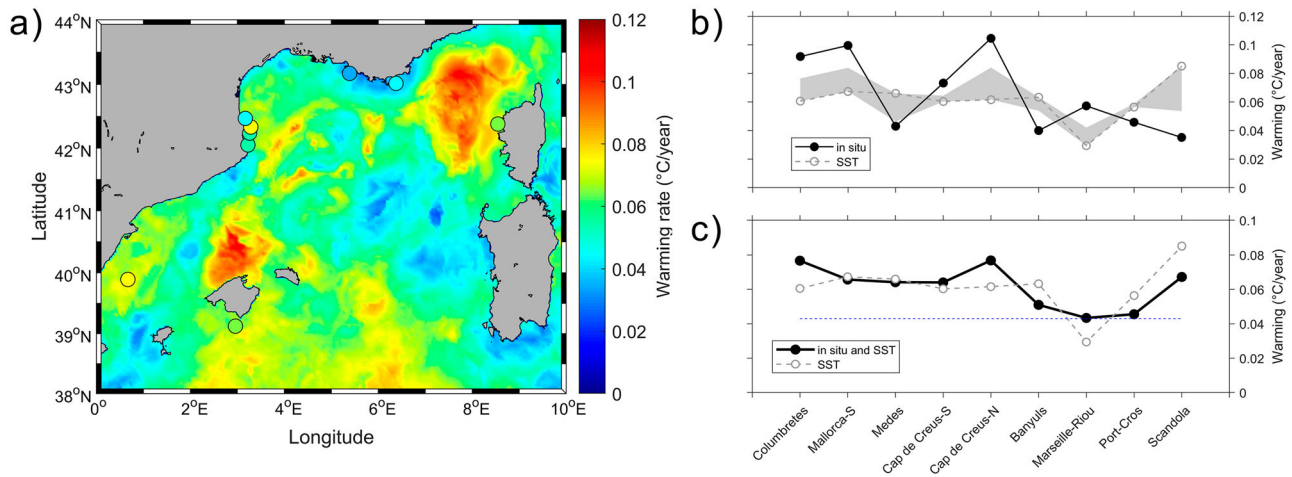
Figure 3.6.6. Sea surface warming trends over the past decade (period 2007–2016) in the northwestern Mediterranean Sea. (a) Trends over the north western Mediterranean Sea from high-resolution satellite data and combined *in situ* and satellite data from nine coastal sites (see panel (c)). Results show accelerated warming over the area compared to the 1982–2011 period (0.047 ± 0.031°C/year vs. 0.029 ± 0.003°C/year respectively) (b) Comparison of surface warming trends in the 9 coastal sites shown on map calculated from *in situ* or satellite sea surface temperature data. The effect of missing data on trends calculation is also shown (grey shaded area). (c) Best estimates of surface warming trends in the nine coastal sites obtained by combining *in situ* and satellite data (black curve). Trends from satellite data at the coastal sites and over the entire area are indicated by the grey curve and blue line respectively.

climatological time scale (1982–2011). For comparison at local scale, satellite data from nearest pixel to the nine T-MEDNet sites were considered, retaining the complete data sets over the 2007–2016 period, and also sub-samples by retaining only matching dates with *in situ*$_{5m}$ in order to evaluate the potential incidence of missing data.

Analysis conducted on satellite data from CMEMS (product reference 3.6.1) attest to rapid and accelerated warming of sea surface temperature in the northwestern Mediterranean during the past decade compared to the 1982–2011 period (0.047 ± 0.031°C/year vs. 0.029 ± 0.003°C/year respectively, Figure 3.6.6(a)). Strong spatial variability is obvious and elevated warming rates (>0.1°C per year) occurred in the Balearic Sea and the Provence-Corsica Sea, mostly offshore. Rapid warming was also evidenced from the analysis of the T-MEDNet *in situ* time series to the coast (Figure 3.6.6(b)). Local warming rates calculated from *in situ*$_{5m}$ and satellite data showed comparable values on average (0.065 vs. 0.061°C/year respectively), but important differences arose when comparing pair of values at each site (mean of absolute difference 0.024 ± 0.014°C/year). We must also note the stronger inter-site variability of warming rates, at the various spatial scales, from *in situ* time series when compared to satellite data (Figure 3.6.6(b)).

We further evaluated the effect of missing data which is a characteristic of most, if not all, *in situ* time series, on estimation of trends. Trend calculation is known to be highly sensitive to the length of the time window, as well as the start and end dates considered. Here we showed

that even minor change in the completeness index of the data set (e.g. for Columbretes, retaining 96% vs. 100% of the satellite data over the 2007–2016 period) can result in significant variability/uncertainty in warming trends estimates (grey shaded area, Figure 3.6.6(b)). Overall, we assume that missing data may account for a 50% or more of the observed differences in the warming rates obtained using satellite and *in situ*$_{5m}$ data. Considering the statistical analysis conducted above, *in situ*$_{5m}$ data gaps were filled by satellite data with high confidence for all sites (from group A1 and A2), except for Marseille-Riou (upwelling area as discussed above).

Interestingly, the new estimates combining *in situ* and satellite data showed fair agreement with trends derived from the complete satellite data (Figure 3.6.6(c)). These results showed overall elevated warming rates (0.043° C/year in Marseille to 0.077°C/year in the Catalan Sea) among which most are higher than the average warming at sub-regional scale (blue dotted line, Figure 3.6.5(c)). These results further demonstrate the interest of combining satellite and *in situ* observations to enhance and validate analysis on thermal regimes and warming trends in the vital coastal and nearshore area.

Climate change is expected to have significant impacts in the coastal areas. Integrated Coastal Zone Management and Ecosystem Based Approach strategies are being implemented to deal with current and long-term climate change as well as other drivers of change. Through these strategies, integrated and adaptive approach to coastal zone planning and management are developed in order to achieve Good Environmental

Status and sustainable development of coastal areas. Marine Protected Areas are one of the main instruments being implemented in this framework. Besides Marine Protected Areas are recognised as nature-based solutions to cope with climate change in many frameworks (e.g. Convention on Biological Diversity, Sustainable Development Goal 14). In this study we showed the relevance of joint effort with Marine Protected Areas in tracking and informing on ongoing changes associated to climate change in coastal areas.

The statistical analysis of the satellite and *in situ* matchup database (22 sites, multi-year) firstly determined that high agreement in terms of correlation (0.98), RMSD (0.5–0.8°C) and bias (year = 0.3°C, month < 0.8°C) was attained in most Marine Protected Areas in the different sub-basins, from cold to warm Mediterranean Sea surface temperature. Secondly the large variability in matching patterns, with higher uncertainty in the nearshore compared to offshore and significant warm bias during summer, largely reflects the underlying coastal oceanographic processes that determine the local seawater temperature variability. Our results, consistent with the literature (e.g. Smale and Wernberg 2009; Smit et al. 2013; Brewin et al. 2018), further document uncertainties associated to such approach in the Mediterranean Sea and highlight potential limitations, especially in upwelling areas, that may inform user uptake and future product improvement. These results also demonstrate the interest of considering multi-year time series acquired nearshore using benthic data loggers in complement to other sensors platforms/classically used for satellite data validation (surface drifter, thermosalinograph, CTD, XBT, Argo float, Table 3.6.1, Pisano et al. 2016). Future work could focus on the validation of different sea surface temperature products but also high-resolution models and reanalysis, by considering the hourly and high vertical resolution of T-MEDNet *in situ* measurements. This analysis also informed on the spatial representativeness of *in situ* point measurements from which adaptive and cost-effective sampling strategy could be designed across environmental gradients in the Mediterranean coastal regions and potentially offshore, considering small islands. We advocate that in coastal areas where poor knowledge on oceanographic features, systematic *in situ* measurements over a complete annual cycle should be considered in order to maximise the potential of use and interpretation of satellite derived sea surface temperature at local and broader spatial scales relevant for coastal management (e.g. Gulfs, Marine Protected Area and coastal networks). Indeed, the long-term remote sensing data series (since 1982) can be of particular relevance for broad scale ecological studies (e.g. for computation of climatological

means), analysis of extreme warm or hot events based on anomalies to the climatological mean (see for instance Sections 4.4 on Marine Heat Waves) and warming trends.

Combining remote sensing and *in situ* monitoring systems as shown in this study is a pillar to enhance our understanding of climate change impacts and improve 3D modelling approach in hydrologically complex coastal areas. Supporting the development of a representative coastal monitoring network at Mediterranean scale, e.g. across the network of Marine Protected Areas, while pursuing the enhancement and delivery of CMEMS products to provide accurate and high-resolution information offers a unique opportunity to address vulnerability and adaptation plans to climate change over broad ecological and economic settings.

3.7. Combined analysis of Cryosat-2/SMOS sea ice thickness data with model reanalysis fields over the Baltic Sea

Authors: Urmas Raudsepp, Rivo Uiboupin, Ilja Maljutenko, Stefan Hendricks, Robert Ricker, Ye Liu, Dorotea-ciro Iovino, K. Andrew Peterson, Hao Zuo, Thomas Lavergne, Signe Aaboe, Roshin P. Raj

Statement of outcome: The satellites Cryosat-2 and SMOS provide a new insight for accurate estimation of the sea ice thickness in the Baltic Sea, a heavily trafficked seasonally ice-covered boreal sea. In this study, we demonstrate that combined Cryosat-2/SMOS ice thickness product correlates with the high-resolution model ice thickness values with correlation coefficient of 0.41 and root mean square difference of 0.30 m. Model and Cryosat-2/SMOS data accuracy is good during the ice growth period when ice thickness is below 0.6 m. Cryosat-2/SMOS data captures inter-annual variations of ice thickness, volume and concentration as well as regional differences between Baltic Sea basins. Moreover, Cryosat-2/SMOS data provide added value to the ice thickness estimations based solely on the model during the ice melting period. Therefore, including Cryosat-2/

SMOS ice thickness product as a member in the existing product family (numerical model reanalysis product and operational ice charts) enables multiproduct ice thickness estimation with reduced uncertainties.

Products used:

Ref. No.	Product name and type	Documentation
3.7.1	BALTICSEA_REANALYSIS_ PHY_003_011 Reanalysis	PUM: http://marine.copernicus.eu/ documents/PUM/CMEMS-BAL-PUM-003-011.pdf QUID: http://marine.copernicus.eu/ documents/QUID/CMEMS-BAL-QUID-003-011.pdf
3.7.2	CS2SMOS Remote sensing	http://epic.awi.de/41602/ Ricker et al. (2017)
3.7.3	SEAICE_BAL_SEAICE_L4_NRT _OBSERVATIONS_011_011 Remote sensing	PUM: http://marine.copernicus.eu/ documents/PUM/CMEMS-OSI-PUM-011-004-011.pdf QUID: http://marine.copernicus.eu/ documents/QUID/CMEMS-OSI-QUID-011-001to007-009to012.pdf
3.7.4	C3S ERA5 Model reanalysis	ECMWF (2019)
3.7.5	BALTIC_OMI_SI_volume Observations	PUM: in production QUID: in production http://marine.copernicus.eu/ science-learning/ocean-monitoring-indicators/catalogue/
3.7.6	BALTIC_OMI_SI_extent Observations	PUM: in production QUID: in production http://marine.copernicus.eu/ science-learning/ocean-monitoring-indicators/catalogue/

Knowledge of accurate sea ice thickness has a vital role in the annual course of physical and ecological conditions in the Baltic Sea. Moreover, it is an important parameter for safe winter navigation facilitating planning of ice-breaking activity and operation of the icebreakers (Valdez Banda et al. 2015; Boström and Österman 2017). In the seasonally ice-covered Baltic Sea, *in situ* sea ice thickness measurements outside the fast ice zone (ice attached to the coastline, not drifting) are difficult to perform. Air- and shipborne electromagnetic soundings are considered to be the most accurate method to measure ice thickness in the drift ice zone where the contribution of the fractions of level and deformed ice thickness is included (Ronkainen et al. 2018). The shortcomings of electromagnetic measurements are limited spatio-temporal coverage and uncertainties related to snow on the ice and porous ridge keels. Operational sea ice charts (Karvonen et al. 2003; product reference 3.7.3), which have been produced by combining *in situ* measurements, visual observations and Synthetic Aperture Radar data, are considered as the standard method for spatial mapping of the sea ice thickness in the Baltic Sea. Still, production of these maps includes a high degree of expert knowledge and these maps represent the typical thickness of level ice (Ronkainen et al. 2018; Gegiuc et al. 2018). Moreover, numerical model simulations of ice

thickness, ice concentration and therefore ice volume have been improved over time, but have not reached sufficient accuracy at seasonal time scales (Vihma and Haapala 2009; Herman et al. 2011; Pemberton et al. 2017).

Copernicus Marine Environmental Monitoring Service provides ice thickness and volume estimates based on operational sea ice charts (product reference 3.7.3) and numerical model simulations (product reference 3.7.1).Considering the limited number of *in situ* ice thickness measurements and uncertainties in the existing estimates of the sea ice thickness and volume in the Baltic Sea, any new data source should be included in the estimation of seasonal and inter-annual sea ice thickness and volume variations with reduced uncertainties in the Baltic Sea, e.g. product reference 3.7.5.

Previous studies have shown that SMOS data could be used for estimating sea ice thickness in the Baltic Sea regional scale (Maaß et al. 2015; Kaleschke et al. 2016), while the merged Cryosat-2 and SMOS data product has proven to be valuable at global scale (Ricker et al. 2017). Thus, in principle, the combined ice thickness product of Cryosat-2 and SMOS (CS2SMOS) complemented with auxiliary ice concentration data from the Ocean and Sea Ice Satellite Application Facility (OSI-401-b) (Tonboe et al. 2018) could provide information about ice thickness in the open part of the Baltic Sea.

Therefore, a general purpose of the study is to assess the potential of CS2SMOS ice product for monitoring/forecasting the ice conditions (thickness, volume) in the Baltic Sea. Ice thickness values of two products are compared: sea ice thickness from CS2SMOS (product reference 3.7.2) and from a numerical ocean/sea ice model based on the NEMO-LIM3.6 modelling system for the Baltic Sea (product reference 3.7.1). No sea ice data of any kind has been assimilated into the NEMO-LIM3.6 modelling system for the Baltic Sea due to insufficient confidence on the ice thickness observations, which are derived from digitised hand-drawn ice charts based on ship observations and various other sources (Pemberton et al. 2017). Both products are considered to have errors which are difficult to quantify beforehand. The sources of the errors could be related to (1) dynamic/variable ice conditions, (2) relatively low ice thickness and (3) coarse resolution (25 km) of the CS2SMOS product (product reference 3.7.2) compared to the basin scale. Moreover, the ice thickness in the northern Baltic Sea is often in the range of 0.4–1 m which is the 'transition zone' in terms of sensitivity of the two sensors in the CS2SMOS product (Ricker et al. 2017). The comparison of ice thickness from the model and CS2SMOS product with operational ice charts (product reference 3.7.3) is limited to the year 2016, only,

because of the availability of the data from Copernicus Marine Environment Monitoring Service catalogue.

Spatial resolution of satellite data is 25×25 km and return period of the satellite is about one week. Model data has 2×2 nmi (3.7×3.7 km) grid resolution at hourly frequency. Operational ice charts have spatial resolution of 0.5×0.5 km data and updated daily (product reference 3.7.3). Satellite data covers open sea area only (Figure 3.7.1). To compare satellite data and model results the model values are transferred to the satellite data grid and comparison is made for the points where satellite data has ice concentration and thickness values higher than zero. Hence, ice concentration and ice thickness from model are averaged over the spatial domain of 25×25 km and time interval of one week. To retrieve the ice volume, the product of three components – (i) ice concentration, (ii) ice thickness and (iii) model grid area – is calculated for each model gridpoint and time
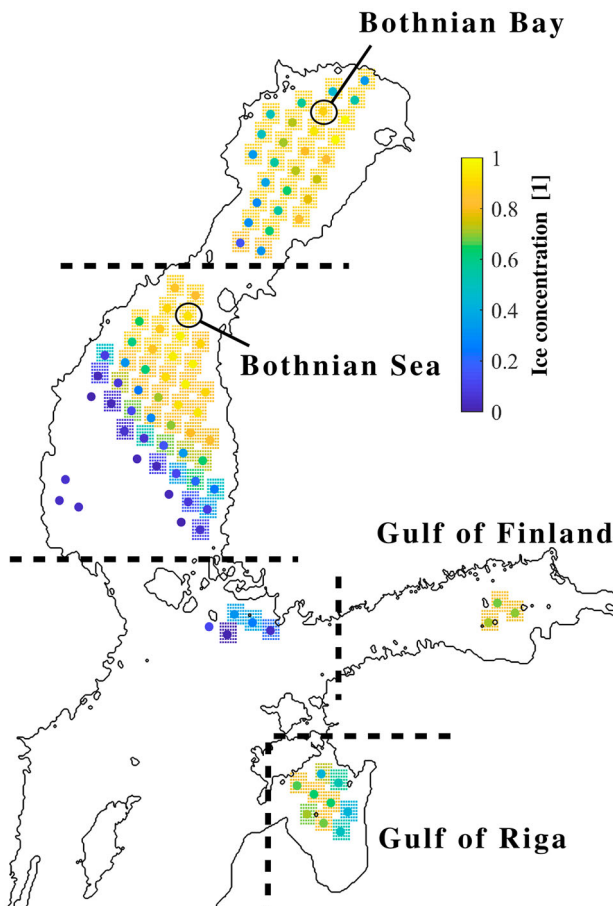

Figure 3.7.1. Example of overlaid ice concentration product (product reference 3.7.2) in the Baltic Sea indicating the resolution and coverage of the products on 24 January, 2011. Also, the borders of sub-basins and the stations for which the comparison between model and remote sensing product was carried out are shown. The dots show model and squares the CS2SMOS data points.

instant which fall into the spatial area and time interval of the satellite data resolution.

The Bothnian Bay represents the region with thicker ice (up to 1 m) and high ice concentration values (usually between 0.6 and 1.0). The Bothnian Sea, the Gulf of Finland and the Gulf of Riga represent regions with thinner and more dynamic ice conditions where ice thickness is usually below 0.5 m except for cold winters like 2011.

Correlation (R) and root mean square difference (RMSD) were calculated for assessing the overall agreement of the two ice thickness products in the gridpoints that are not contaminated by the coastline and the islands. In total we have $N = 6133$ comparison points over the six-year time span, 2011–2016. A general agreement between the model and remote sensing ice thickness ($R = 0.41$, RMSD $= 0.30$ m) is in the same range as in the satellite validation experiments in the Arctic (Ricker et al. 2017). Considerable difference is that Ricker et al. (2017) compare CS2SMOS ice thickness with airborne electromagnetic thickness measurements, but we compare CS2SMOS with numerical model ice thickness. The latter contains a high uncertainty itself. Due to peculiarities of each considered sub-basin of the Baltic Sea regional statistics for each sub-basin were calculated separately (Figure 3.7.2).

We have compared each satellite measurement with corresponding area and time averaged model value by calculating a mean and standard deviation of the model/satellite ice thickness relative to the predefined satellite/model ice thickness intervals. A general tendency of the means for each subregion is that for thicker ice from the model, the satellite ice thickness is lower. For instance, in the Bothnian Bay for each model ice thickness interval starting from 0.3–0.4 m to 1.4–1.5 m, interval mean satellite ice thicknesses vary between 0.3 and 0.5 m (Figure 3.7.2(a)). In the other basins, among the few model values with the ice thickness in excess of 0.6, corresponding satellite ice thickness values are mainly lower than the model values. The same tendency is true for the mean model ice thickness relative to predefined satellite ice thickness intervals. This is especially pronounced for the Bothnian Sea and the Gulf of Riga, where for the ice intervals from 0.4 m to 1.2 m, the mean ice thickness is between 0.2 and 0.4 m (Figure 3.7.2 (b,d)). The scatters around the means are large with STDs up to 0.35 m and without significant differences between model and satellite, or ice thickness intervals. In the Bothnian Bay (Figure 3.7.2(a)) and in the Gulf of Finland (Figure 3.7.2(c)), the satellite mean ice thickness is close to the mean ice thickness from the model for the predefined model ice thickness intervals up to 0.6 and 0.7 m, respectively, but the scatter is still large (STD is up to 0.25 m). The model mean ice thickness,
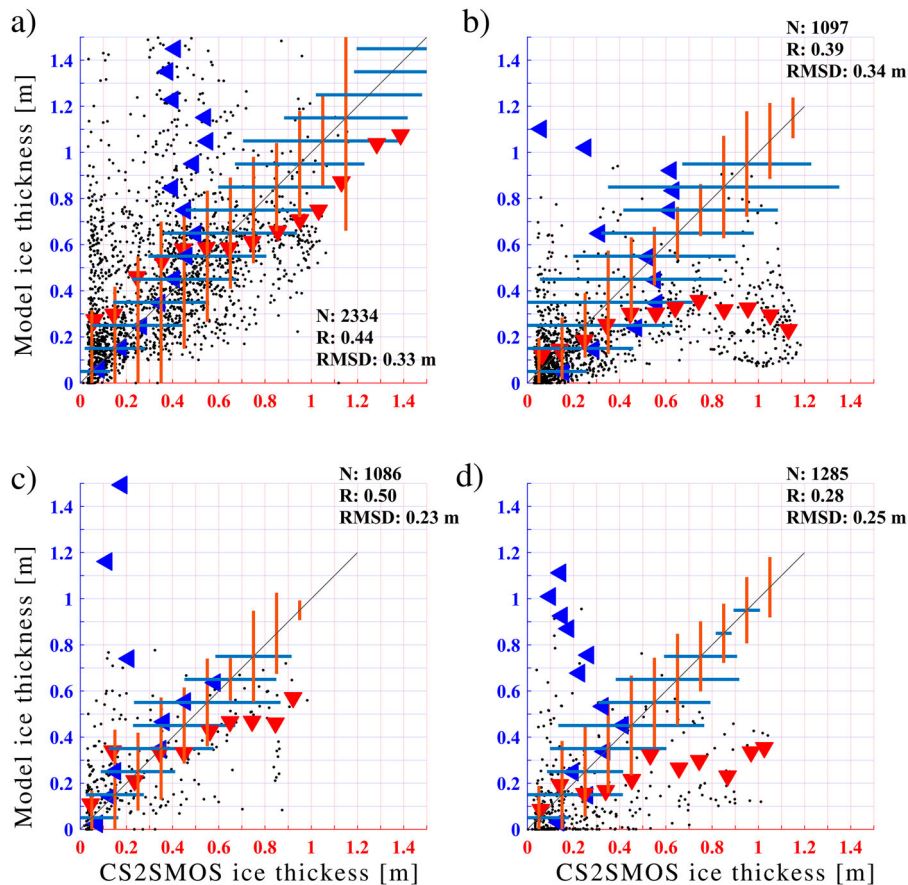
Figure 3.7.2. Scatter plots of CS2SMOS and model ice thickness in the Bothnian Bay (a), the Bothnian Sea (b), the Gulf of Finland (c) and the Gulf of Riga (d). Data from product references 3.7.1 and 3.7.2. Red triangles denote average model ice thickness for the ranges of CS2SMOS ice thicknesses with interval of 0.1 m. Vertical red lines denote the ±STD of corresponding model ice thicknesses relative to mean, but plotted on 1:1 line. Likewise, the blue triangles denote average CS2SMOS ice thickness for the ranges of model ice thickness with interval of 0.1 m. Horizontal blue lines denote the ±STD of corresponding CS2SMOS ice thicknesses relative to mean, but plotted on 1:1 line.

relative to the satellite, is overestimated by up to 0.15 m for the intervals up to 0.5–0.6 and by 0.3–0.4 for the Bothnian Bay and Gulf of Finland, respectively, but underestimated thereafter. In the Bothnian Sea and the Gulf of Riga the model mean ice thickness relative to the satellite is underestimated over the almost whole range of satellite ice thickness intervals.

In the Bothnian Bay and Bothnian Sea, the correlation coefficients ($R = 0.44$ and $R = 0.39$) and root mean square differences between CS2SMOS and model ice thickness values (RMSD = 0.33 m and RMSD = 0.34 m) are comparable. Relatively high RMSD values in comparison to the range of ice thickness values are caused by different reasons. In the Bothnian Bay, very low ice thickness in CS2SMOS which coincide with any of the ice thickness value in the model (Figure 3.7.2(a)). In the Bothnian Sea, unusual discrepancy is observed in the range of CS2SMOS ice thickness from 0.7 to 1.2 m where model values start to decline and correlation is even negative.

The correlation between CS2SMOS and model ice thickness is the strongest ($R = 0.5$) and the difference is the lowest (RMSD = 0.23 m) in the Gulf of Finland (Figure 3.7.2(c)). However, there are too few comparison points with ice thickness in excess of 0.5 m. Gulf of Finland is a narrow gulf perpendicular with the satellite track and has a staggered coastline with a number of small islands some of which are in the middle of the gulf. Because of the geometry of the Gulf of Finland there is a limited number of CS2SMOS data points that could be used for comparison (see Figure 3.7.1). The correlation between CS2SMOS and model ice thickness is the weakest in the Gulf of Riga (Figure 3.7.2(d)).

In addition, a time series analysis has been performed at a selected location in the Bothnian Bay and Bothnian Sea (see Figure 3.7.1) aiming to compare the seasonal course and inter-annual variations of model and remote sensing-based ice concentration, thickness and volume.
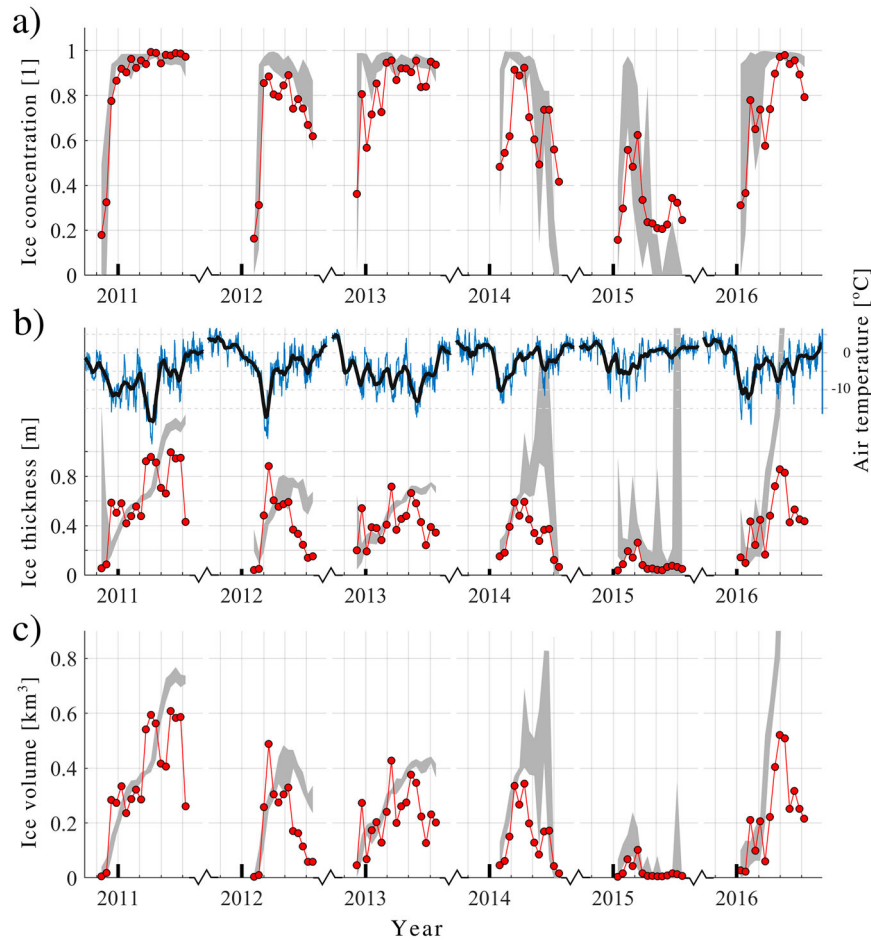
Figure 3.7.3. Time series of ice concentration (a), ice thickness (b) and ice volume (c) in the Bothnia Bay. Red dots show the CS2SMOS values. Shaded area represents the range of model values over the week centred at the CS2SMOS data derived time instant. Data from product references 3.7.1 and 3.7.2. Local (65.05°N, 23.23°E) air temperature time series are plotted on panel (b) (product reference 3.7.4). Blue line corresponds to 3-hourly data, thick black line corresponds to temperature time series smoothed using 30-day moving average filter.

In the Bothnian Bay, ice concentrations of both products (remote sensing and model) follow the same general seasonal pattern (Figure 3.7.3(a)). Bias is around 0.1 with model values usually higher (Table 3.7.1), and RMSD is about 10% of the maximum possible value, except for 2014 and 2015. In case of ice thickness, bias is negative (i.e. model values are higher) and RMSD is about 50% of maximum ice thickness of CS2SMOS product in 2011–2014 (Figure 3.7.3(b)). In 2015 and 2016, RMSD is about 100% of maximum ice thickness of CS2SMOS product. Visual comparison of model and CS2SMOS data indicates that model ice thickness follows the CS2SMOS ice thickness during the ice formation period, and continues to increase during the ice melting period as detected from CS2SMOS data and air temperature (Figure 3.7.3(b)). Statistically, bias and RMSD are slightly higher during the ice growth period than during ice melting period: bias is −0.18 and −0.14 m, RMSD is

0.40 and 0.46 m, respectively. In the ice volume comparison (Figure 3.7.3(c) and Table 3.7.1), the large discrepancy between model and CS2SMOS values is slightly suppressed, RMSD remains around 30% of maximum CS2SMOS ice volume values, except for the year 2016.

Inter-annual changes of the ice parameters are more pronounced in the Bothnian Sea (Figure 3.7.4), than in the Bothnian Bay (Figure 3.7.3). At the selected location in the Bothnian Sea, durable ice is formed in 2011 and 2013. In 2015, ice is completely absent. The results are consistent with the inter-annual changes of air temperature. Maximum ice extent and ice volume for the entire Baltic Sea calculated from operational ice charts by SMHI (Samuelsen et al. 2018; product references 3.7.5 and 3.7.6) and mean ice thickness for the Bothnian Bay (Ronkainen et al. 2018) confirm the results of inter-annual variations of ice thickness and ice volume which are calculated from CS2SMOS product at selected

Table 3.7.1. Yearly root mean square difference (RMSD) and bias between CS2SMOS and model values (CS2SMOS minus Model): ice thickness, ice concentration and ice volume for the selected locations in Bothnian Bay and Bothnian Sea (see Figure 3.7.1 for locations). Data from product references 3.7.1 and 3.7.2.

	Year	2011	2012	2013	2014	2015	2016
Bothnian Bay							
Ice concentration [1]	RMSD	0.05	0.11	0.11	0.28	0.24	0.11
	BIAS	−0.01	−0.11	−0.08	−0.05	0.05	−0.14
Ice thickness [m]	RMSD	0.35	0.27	0.20	0.36	0.17	1.01
	BIAS	−0.12	−0.16	−0.10	−0.29	−0.11	−0.87
Ice volume [km³]	RMSD	0.17	0.14	0.11	0.15	0.04	0.60
	BIAS	−0.04	−0.10	−0.07	−0.15	−0.02	−0.55
Bothnian Sea							
Ice concentration [1]	RMSD	0.14	0.19	0.17	0.35	n/a	0.33
	BIAS	−0.06	0.05	−0.08	−0.11	n/a	−0.28
Ice thickness [m]	RMSD	0.28	0.11	0.20	0.07	n/a	0.09
	BIAS	0.21	−0.01	−0.06	−0.11	n/a	−0.11
Ice volume [km³]	RMSD	0.15	0.01	0.07	0.03	n/a	0.04
	BIAS	0.11	0.00	0.00	−0.02	n/a	−0.04

locations in the Bothnian Bay and Bothnian Sea. No conclusive differences between the bias and RMSD in the Bothnian Sea and Bothnian Bay could be derived (Table 3.7.1), although ice conditions in the Bothnian Sea are more dynamic due to larger and variable open water area.
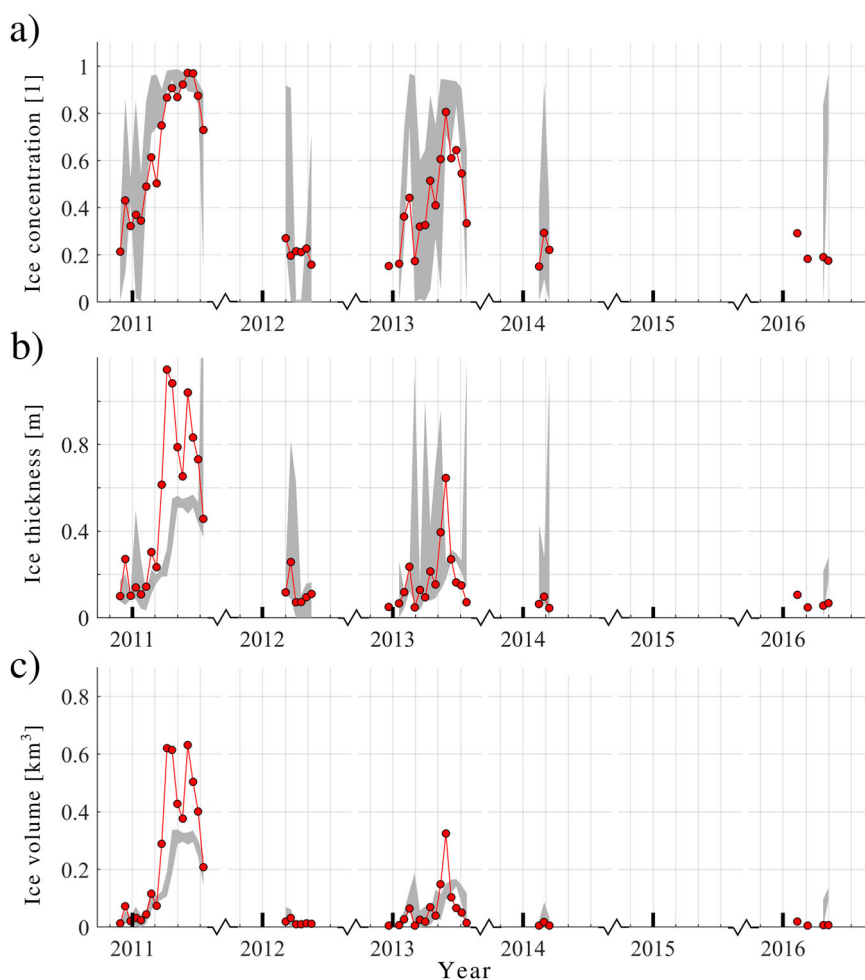

Figure 3.7.4. Time series of ice concentration (a), ice thickness (b) and ice volume (c) in the Bothnia Sea. Red dots show the CS2SMOS values. Shaded area represents the range of model values over the week centred at the CS2SMOS data derived time instant. Data from product references 3.7.1 and 3.7.2.
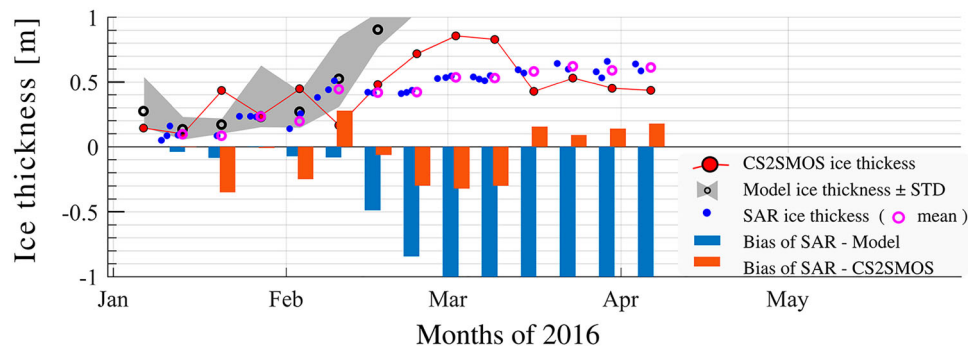
Figure 3.7.5. Ice thickness time series from CS2SMOS (product reference 3.7.2), Model (product reference 3.7.1) and ice charts (product reference 3.7.3) data sources in the Bothnian Bay (location shown on Figure 3.7.1) in 2016. Shaded area represents the range of model values over the week centred at the CS2SMOS data derived time instant. The difference between the ice charts and Model/CS2SMOS ice thicknesses is shown with blue/red bars.

A comparison of multiple ice thickness products CS2SMOS (product reference 3.7.2), model (product reference 3.7.1) and operational sea ice charts (product reference 3.7.3) in the Bothnian Bay for 2016 (Figure 3.7.5) shows that during the ice formation period in January and the first half of February ice thickness from the model and ice charts compare better than between the CS2SMOS and ice charts. Thereafter, model ice thickness increases beyond reasonable values (see Figure 3.7.3(b)). The ice thickness from the ice charts show a slow monotonic increase until the beginning of April, while sea ice thickness from CS2SMOS increases to a maximum value in the first 10 days of March, then drops below the ice thickness values from the ice charts and remains 0.1–0.15 m lower until the beginning of April. Based on the air temperature data (Figure 3.7.3(b)) only, we can not conclude whether the sea ice thickness from ice charts or from CS2SMOS is more accurate, but the model results are erroneous during this time.

In the Baltic Sea, sea ice thickness estimates include model data with 3.7×3.7 km grid resolution at hourly frequency and Synthetic Aperture Radar based operational ice charts with spatial resolution of 0.5×0.5 km updated daily. The validation of these estimates is fragmented due to sparse in-situ measurements and the accuracy has high uncertainties. Therefore, all new datasets that become available for the estimation of sea ice thickness in the offshore area of the Baltic Sea are valuable contributors for the improvement of the sea ice monitoring. The assessment of CS2SMOS ice thickness product shows that it can be used for the Baltic Sea. Indeed, spatial resolution of CS2SMOS data is 25×25 km, return period of the satellite is about one week and CS2SMOS data are usable for open sea area only. Still, we suggest that CS2SMOS data could be used within Copernicus Marine Environmental Monitoring Service for increasing the accuracy of sea ice thickness estimates either by assimilating the data into a model or by including the data in multiproduct ice thickness estimations.

3.8. Chlorophyll-a evolution during the last 21 years and its relation with mussel growth and optimal repartition for aquaculture and fishery

Authors: Philippe Bryère, Antoine Mangin and Philippe Garnesson

Statement of main outcome: The aim of this study is to estimate the chlorophyll-a evolution effect over the past 21 years on mussel growth and optimal distribution for aquaculture and fishery. The results showed in this paper identify a decrease of chlorophyll-a concentration in the English Channel, the North Sea and the Irish Sea. This decrease in chlorophyll-a concentration begins around 2003. It is clearly observed in 2018 and is affecting mainly the higher concentrations (>10 mg m^{-3}). This might have an impact on the living organisms feeding on phytoplankton such as bivalves. Our results show that the chlorophyll-a decrease doesn't affect significantly the mussel growth seeing that they need less than 2 mg m^{-3} (annual mean) for optimal growth. However we observed that the most impacted areas for mussel farming are off Only the Normando Breton gulf is an important are for mussel farming. Fortunately, the impacted areas are offshore the farming sites. So even if the chlorophyll-a concentration has a tendency to decrease, it doesn't appear to impact the coastal mussel farms during the studied period. Offshore mussel farming and fishery areas, where the chlorophyll-a concentration is lower than in coastal areas, could be more affected in the future and should be further studied.
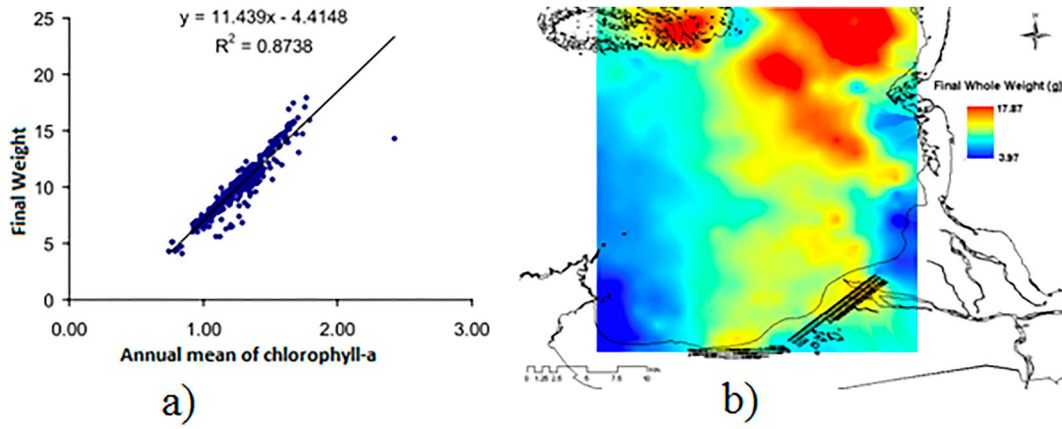
a)   b)

Figure 3.8.1. a) Relationship between the annual average of chlorophyll-a and the weight reached by mussels after 19 months of growth. Vertical axis: mean final weight (grams), Horizontal axis: annual mean chlorophyll-a concentration (mg m^{-3}). b) Mean final weight (grams) of mussels estimated applying the relationship for the period of 2003–2004 in the Bay of Mont Saint-Michel, using the annual averages of satellite estimated chlorophyll-a (Thomas et al. 2011).
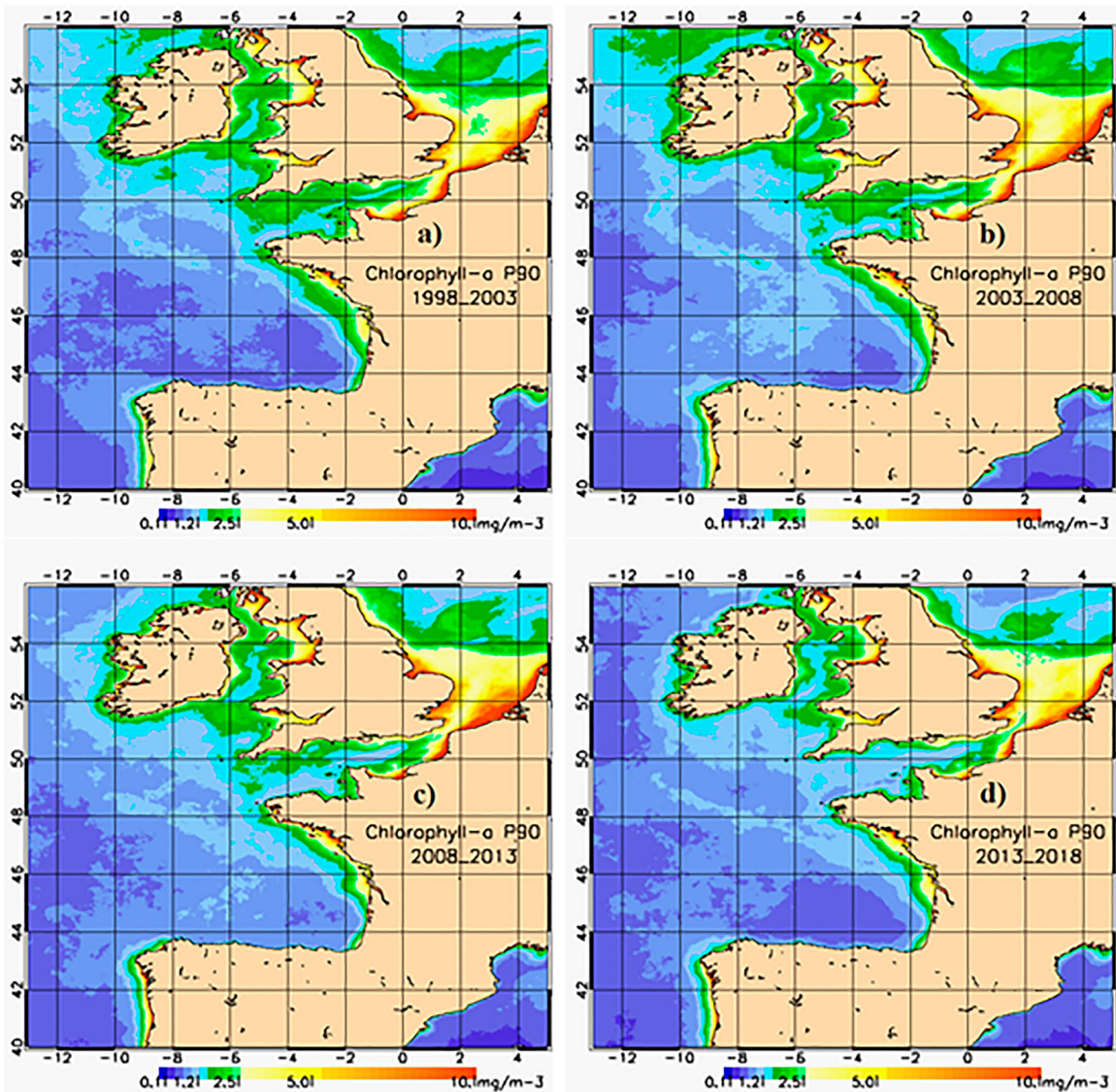

Figure 3.8.2. P90 of chlorophyll-a calculated over the productive period (March to October) on four periods of six years (a) 1998–2003, (b) 2003–2008, (c) 2008–2013 and (d) 2013–2018. The most impacted regions by the decrease are the English Channel and the Irish Sea.

Products used:

Ref. No	Product Name and Type	Documentation
3.8.1	OCEANCOLOUR_ATL_CHL_ L4_REP_OBSERVATIONS _009_098 Plankton Remote sensing	PUM: http://marine.copernicus. eu/documents/PUM/CMEMS-OC-PUM-009-ALL.pdf QUID: http://marine.copernicus. eu/documents/QUID/CMEMS-OC-QUID-009-030-032-033-037-081-082-083-085-086-098.pdf
3.8.2	OCEANCOLOUR_ATL_CHL_L4_ NRT_OBSERVATIONS_009_037 Plankton Remote sensing	PUM: http://marine.copernicus. eu/documents/PUM/CMEMS-OC-PUM-009-ALL.pdf QUID: http://marine.copernicus. eu/documents/QUID/CMEMS-OC-QUID-009-030-032-033-037-081-082-083-085-086-098.pdf
3.8.3	IBI_REANALYSIS_WAV_005_006 Wave Hindcast	PUM: http://marine.copernicus. eu/documents/PUM/CMEMS-IBI-PUM-005-006.pdf QUID: http://marine.copernicus. eu/documents/QUID/CMEMS-IBI-QUID-005-006.pdf
3.8.4	IBI_ANALYSIS_FORECAST_ WAV_005_005 Wave Forecast	PUM: http://marine.copernicus. eu/documents/PUM/CMEMS-IBI-PUM-005-006.pdf QUID: http://marine.copernicus. eu/documents/QUID/CMEMS-IBI-QUID-005-006.pdf

For many years the decrease of the riverine nutrient influx into the North-East Atlantic Basin, (mainly into the North Sea, the English Channel and the Bay of Biscay), has impacted the annual concentration of chlorophyll-a. Recently, Capuzzo et al. (2018), using *in situ* data, identified the sea surface warming and reduced nutrient riverine inputs as the major cause for the North-Sea primary productivity decline over the period 1998–2013. Using satellite data in the frame of the JMP EUNOSAT project (Joint Monitoring Program of the Eutrophication of NOrth Sea with SATellite data, founded by European commission, https://www. informatiehuismarien.nl/uk/projects/algae-evaluated-from/, see also chapter 3.4), Gohin et al. (2019) show an evolution of chlorophyll-a since 1997 with a negative trend in the English Channel. The estimation chlorophyll-a concentration by remote sensing has been successfully used for more than 20 years (SeaWiFs/NASA, Modis/NASA, Meris/ESA, Viirs/NASA) for global (Maritorena and Siegel 2005; Morel et al. 2007) and coastal applications (Gohin et al. 2002; Gohin 2011; Lapucci et al. 2012; Novoa et al. 2012; Loisel et al. 2017). In the Bay of Mont-Saint-Michel, Thomas et al. (2011) established a relationship between the annual averages of satellite estimated chlorophyll-a and the weight reached by mussels caught after 19 months of growth (Figure 3.8.1). For this reason, over the 2003–2004 period, they used the chlorophyll-a estimated with the OC5 algorithm from IFREMER (Gohin et al. 2002; Gohin 2011) as input in a dynamic energy budget (DEB) model.

This decrease of chlorophyll-a concentration might thus have an impact on the living organisms feeding on phytoplankton such as the bivalves. The estimation of chlorophyll-a concentration by remote sensing with satellite imagery has been used to obtain a spatial analysis of this impact. The goal of this study is to
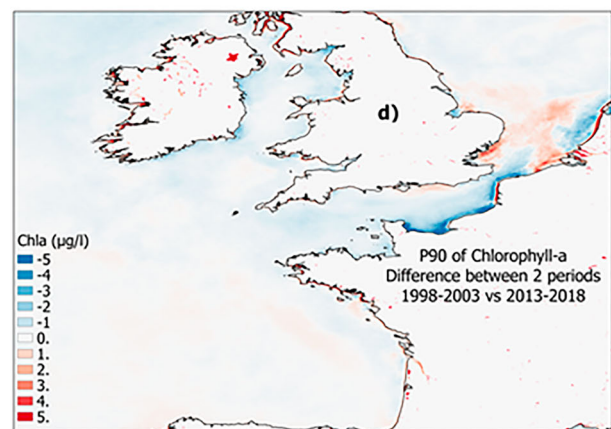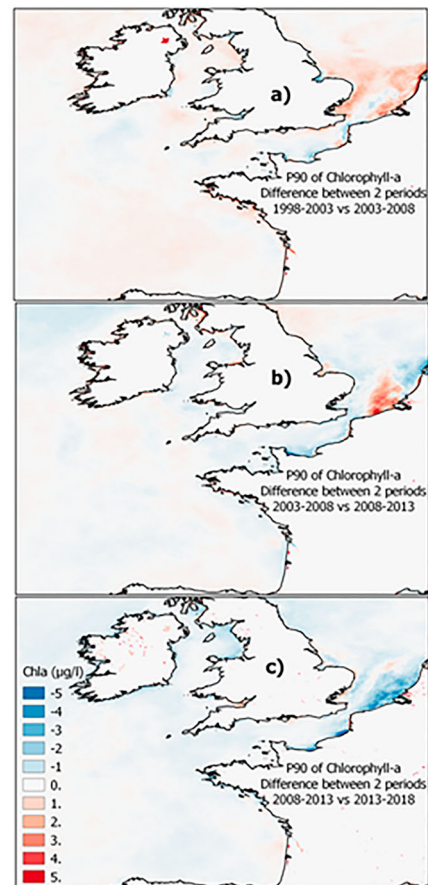

Figure 3.8.3. Differences of P90 of chlorophyll-a calculated over the productive period (March to October) on four periods of six years (a) 1998–2003 vs. 2003–2008, (b) 2003–2008 vs. 2008–2013, (c) 2008–2013 vs. 2013–2018. (d) 1998–2003 vs. 2013–2018. The results confirm that the most impacted regions by the decrease are the English Channel, the Irish Sea and the North Sea.

show the potential impact that the chlorophyll-a decrease might have on Atlantic Mussel (*Mytilus edulis*) growth and spatial repartition in the North-East Atlantic Basin using CMEMS products: satellite chlorophyll-a estimation for growth and farming (products 3.8.1 and 3.8.2), and modelled wave height for farming operations (products 3.8.3 and 3.8.4). In order to study the spatial and temporal evolution of chlorophyll-a, images of the 90-percentile (P90) calculated over the productive period (March to October) and over a period of six years (i.e. period used for reporting for European Framework Directives, Belin et al. 2014) have been generated for 4 periods (i.e. 1998–2003, 2003–2008, 2008–2013 and 2013–2018). The results show that the decrease of chlorophyll-a concentration is observed in the last 2 periods (Figure 3.8.2(c,d)) and impact mainly the Irish Sea and the English Channel (i.e. Bay of Seine, Bay of Mont-Saint-Michel). The southern regions like the Bay of Biscay, the Portuguese and Spanish coasts don't seem to be significantly impacted by the chlorophyll-a decrease and remain stable.

Using the difference of P90 of chlorophyll-a between the four periods (Figure 3.8.2(a–c)) we can observe its spatio-temporal evolution. During the first two periods (1998–2003 vs. 2003–2008, Figure 3.8.3(a)) we observe an increase in the North Sea in coastal areas and a slight decrease in the East English Channel except off the Bay of Somme. A slight increase is also observed in the coastal area of the Bay of Biscay. Over the second and third periods (2003–2008 vs. 2008–2013, Figure 3.8.3 (b)) the decrease is observed in the North Sea except off the Rhine/Scheldt mouth where there is a high increase. Moreover, a decrease is observed in the Eastern part of the English Channel, the Bay of Mont-Saint-Michel and in the North of Ireland. Finally, during the last two periods (2008–2013 vs. 2013–2018, Figure 3.8.3
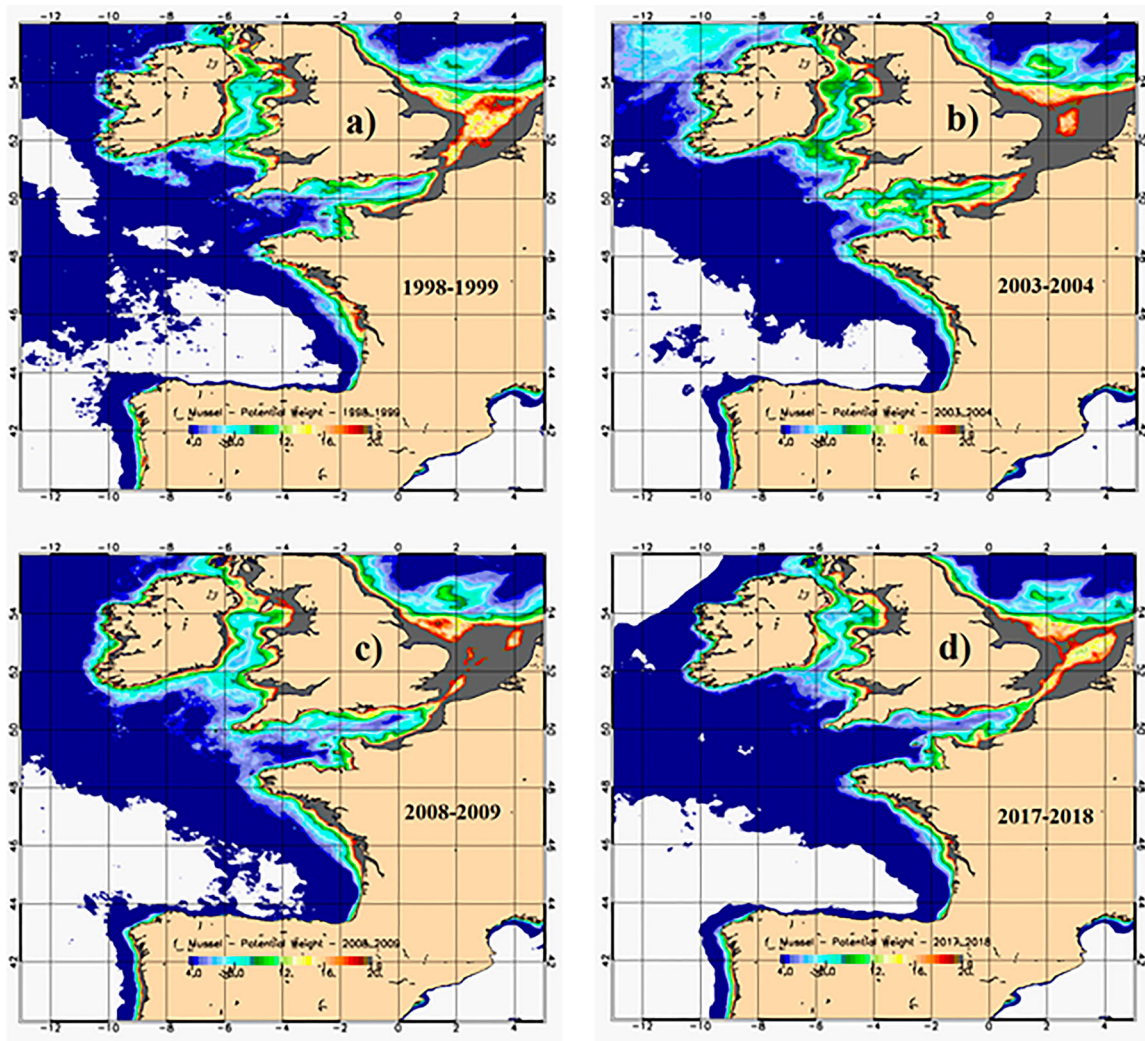

Figure 3.8.4. Mussel Final weight expected after two years (from 4 to 20 g), estimated from the mean of chlorophyll-a concentration calculated on a period of two years: (a) 1998–1999, (b) 2003–2004, (c) 2008–2009, (d) 2017–2018. Deep blue for mussels < 4 g and deep brown for mussels > 20 g. The grey shaded areas indicate the regions with not enough chlorophyll-a for mussel growth.

(c)) a high decrease is observed in the coastal areas of Belgium and Netherlands and in the French coasts of the East English Channel. The decrease is also observed all around Ireland and in the English coast of the Irish Sea. The difference between the first and the last period (1998–2003 vs. 2013–2018, Figure 3.8.2(d)) confirm a chlorophyll-a P90 decrease during the last 21 years that mostly impacted the English Channel (mainly French coasts), the Irish Sea and an area of the North Sea (off the North Coasts of the Netherlands).

These results confirm the observations of Gohin et al. (2019), i.e. the evolution of chlorophyll-a since 1997 with a negative trend in the English Channel while the Bay of Biscay was not impacted by this decrease. Moreover, these results are obtained using two different sources of chlorophyll-a data: products 3.8.1 and 3.8.2 were used for this study while Gohin et al. (2019) used the level 4 IFREMER products (Saulquin et al. 2011). Now that the decrease of chlorophyll-a is confirmed in the North of the IBIROOS region (Ireland-Biscay-Iberia Regional Operational Oceanographic System), we can study the impact on the mussel growth and then define the optimal farming locations in this area.

Initially, we applied, on the studied area, the relationship between chlorophyll-a concentration and mussel growth established by Thomas et al. (2011) as described

above. In summary, mussel growth is strongly correlated with the mean concentration of chlorophyll-a during its two years of growth. Biannual means of chlorophyll-a were computed from 1998 to 2018 using the satellite products 3.8.1 and 3.8.2. The relationship was applied to each pixel of the area to determine the mean final weight of the mussel after two years of growth. The resulting maps are shown below (Figure 3.8.4). Between the periods 1998–1999 and 2003–2004 (Figure 3.8.4(a,b)) an increase of the high growth areas can be observed in the English Channel, North Sea and the Irish Sea while others regions do not differ significantly. Then, from 2003–2004 to 2017–2018 (Figure 3.8.4(b–d)) we observe a significant decrease of the high growth areas in the North part of the studied regions. The results show that the main impacted areas are the North Sea, the English Channel (including the Bay of Seine and the Bay of Mont Saint-Michel) and the Irish Sea. In these regions, the decrease of chlorophyll-a concentration can be linked to the decrease of nutrients influx from rivers, mainly the Phosphorus (Romero et al. 2013).

Comparing the difference of expected weight between the periods 2003–2004 vs. 2017–2018 (Figure 3.8.5) we can observe that the coastal areas most impacted by the decrease of chlorophyll-a (deep blue) are the English Channel and the Irish Sea (Irish Coasts). The coastal
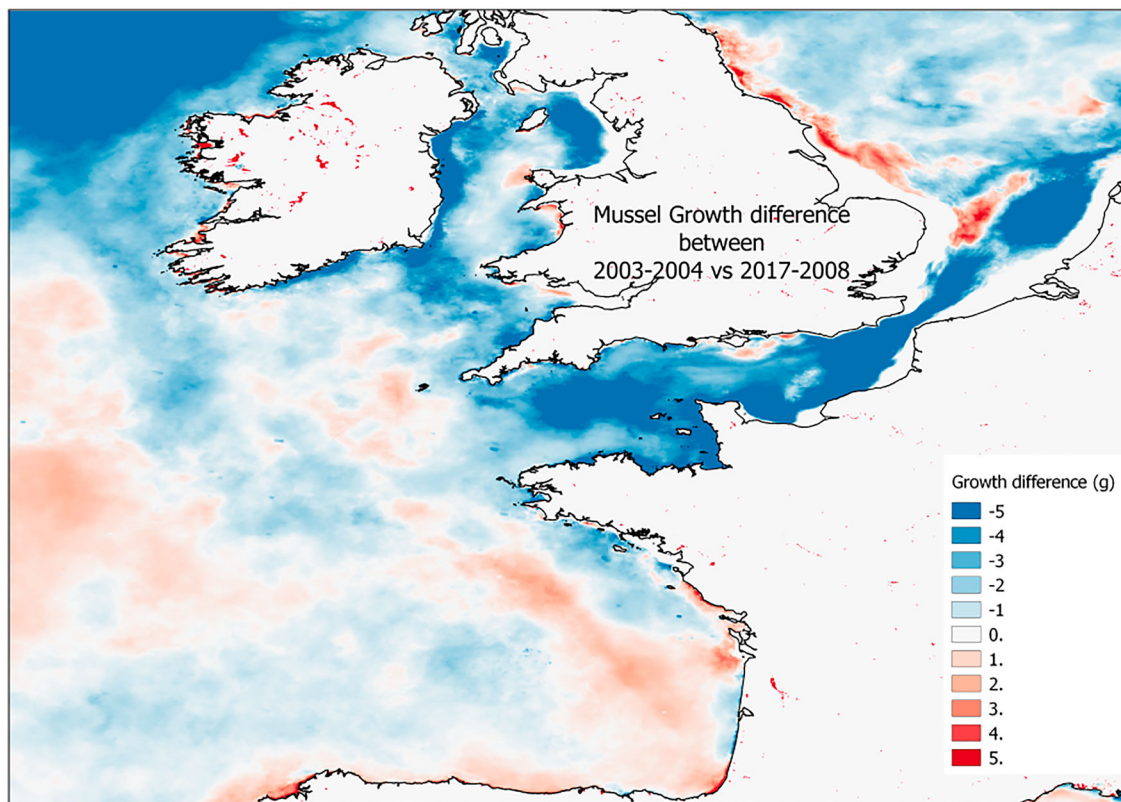

Figure 3.8.5. Mussel growth difference between 2003–2004 vs. 2017–2018. The most impacted zones by the decrease of chlorophyll-a (deep blue) are the central part at the south of the North Sea, the English Channel the Irish Sea and off the north-west of Ireland.

areas with a very high chlorophyll-a concentration are not impacted (North Sea, French Eastern part of the English Channel, Western English coast, Bay of Biscay). The north East of England and the south of the Bay of Biscay are the two regions that show a higher growth potential.

To finalise this case study we will analyse the delimitation of optimal sites for mussel farming using chlorophyll-a (product ref. 3.8.1 and 3.8.2) as well as wave product (product ref. 3.8.3 and 3.8.4). The chlorophyll-a concentration directly impacts the mussel growth while the wave height impacts the farming operation conditions. In prospecting sites for mussel culture, well-protected or sheltered coves and bays are preferred over unprotected open areas. Sites affected by heavy wind conditions and big waves could damage the stock and farming materials and, therefore, must be avoided. Thus, protected areas rich in plankton should be selected.

For this purpose, we have used the mean of chlorophyll-a concentration for two-year periods from 1998 to 2018 and the P90 of the maximum significant wave height (HSMAX) calculated from 1998–2018. Then, thresholds are applied to each parameter to exclude the areas that do not correspond to the suitability criteria (that could be adjusted depending on the studied area). The data combination, based on the environmental conditions, has been used to exclude the areas which do not comply with the following criteria (used in the EU FP7 SAFI project: http://www.copernicus.eu/projects/safi – SAFI Consortium (2016)):

- To avoid the areas too exposed to high waves: P90 of HSMAX < 3 m
- To select areas with enough chlorophyll-a for optimal mussel growth, but without eutrophication risks $1.2 <$ Mean chlorophyll-a < 25 mg m^{-3}
- Coastal distance < 10 km to optimise the exploitation costs

The results show (Figure 3.8.6) that between 1998–1999 and 2017–2018 there is an increase of optimal sites for
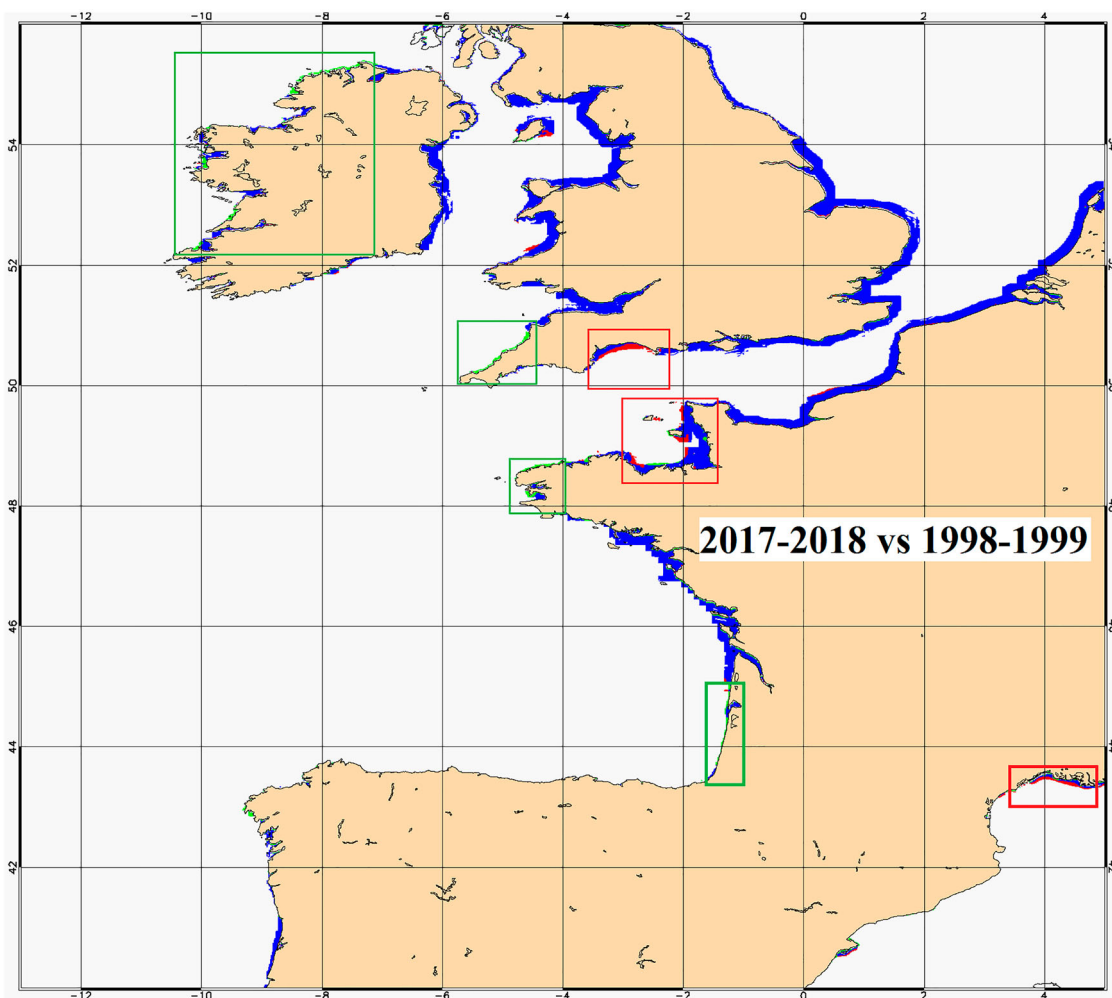

Figure 3.8.6. The differences between optimal sites (in red): (a) from 2017–2018 comparing to 1998–1999. Stable areas in blue, new sites in green, disappeared sites in red.

mussel farming in the North-West coasts of Ireland, the North Coast of Cornwall, the West Coast of Brittany and the Southern Coast of the French part of the Bay of Biscay. However during the same time there is a decrease of optimal sites for mussel farming in the Bay of Exeter, the Normano-Breton Gulf and off the Rhone river mouth.

In conclusion, these results confirm the observation of Gohin et al. (2019), showing a decrease of chlorophyll-a concentration in the English Channel and the North Sea. Moreover, we observe a similar negative trend in the Irish Sea. This decrease in chlorophyll-a concentration begins around 2003 and is clearly observed in 2018. This phenomenon concerns mainly the higher concentrations (>10 mg m^{-3}). The main cause seems to be the nutrients influx decrease from rivers over the last years, and the decline in phosphorus is certainly the major factor driving the evolution of the phytoplankton biomass (Romero et al. 2013).

As mentioned above, this negative trend might have an impact on the living organisms feeding on phytoplankton, as for instance the bivalves. Hence, it could impact the farming and fishery of commercial bivalves such as mussels in which growth is strongly correlated with chlorophyll-a concentration (Thomas et al. 2011). Our results show that the chlorophyll-a decrease impacts mainly the higher concentrations (>10 mg m^{-3}) and does not appear to significantly impact the mussel growth since they need less than 2 mg m^{-3} (annual mean) to achieve an optimal growth. However, we observed that the most impacted areas for mussel farming are the Bay of Exeter, the Rhone mouth and the Normano-Breton Gulf. Although the Normano-Breton Gulf is a high spot for mussel farming, fortunately, until now, the actual farms have not been affected

Although chlorophyll-a concentration has a tendency to decrease, the coastal mussel farms are not yet affected. However, the most impacted areas must be monitored to follow the evolution of the chlorophyll-a over the next years. Mussel offshore farming and fishery may be affected in the near future, therefore additional studies will be needed. It should be noted however that other external parameters, such as harmful algal blooms, fishing pressure, human pressure, have not been taken into account in this study, and may have a significant impact on local ecosystem.

Notes

1. The JMP-EUNOSAT project consortium consists of: RWS (co-ordinator), Deltares (NL), RBINS (BE), IFREMER (FR), PML, Cefas, MSS (UK), IMR, NIVA (NO), SMHI (SE), AU (DK), UBA, NLWKN, BSH (DE, all self-funded).

2. Coast Colour Round Robin (CCRR) data set published by Nechad et al. (2015). The CCRR project (http://www.coastcolour.org) funded by the European Space Agency (ESA) was designed to bring together a variety of reference datasets and to use these to test algorithms and assess their accuracy for retrieving water quality parameters. This information was developed to help end users of remote sensing products to select the most accurate algorithms for their coastal region.

References
Section 3.1. The use of Copernicus Marine Service products to describe the State of the Tropical Western Pacific Ocean around the Islands: A case study

Ablain M, Legeais JF, Prandi P, Marcos M, Fenoglio-Marc L, Dieng HB, Benveniste J, Cazenave A. 2017. Satellite altimetry-based sea level at global and regional scales. Surv Geophys. 38:7–31. doi:10.1007/s10712-016-9389-8.

Australia Bureau of Meteorology and CSIRO. 2011. Climate change in the Pacific: scientific assessment and new research. Vol. 1: regional overview. Vol. 2: country reports.

Bellenger H, Guilyardi E, Leloup J, Lengaigne M, Vialard J. 2014. ENSO representation in climate models: from CMIP3 to CMIP5. Clim Dyn. 42:1999–2018. doi:10.1007/s00382-013-1783-z.

Cane MA, Clement AC, Kaplan A, Kushnir Y, Pozdnyakov D, Seager R, Zebiak SE, Murtugudde R. 1997. Twentieth-century sea surface temperature trends. Science. 275:957–960.

Cravatte S, Delcroix T, Zhang DX, McPhaden M, Leloup J. 2009. Observed freshening and warming of the western Pacific warm pool. Clim Dyn. 33:565–589.

Dupouy C, Frouin R, Tedetti M, Maillard M, Rodier M, Duhamel S, Guidi L, Lombard F, Picheral M, Neveux J, et al. 2018. Diazotrophic *Trichodesmium* impact on UV VIS radiance and pigment composition in the South west tropical Pacific. Biogeosciences. 15:5249–5269.

Deser C, Phillips AS, Alexander MA. 2010. Twentieth century tropical sea surface temperature trends revisited. Geophys Res Lett. 37:L10701.

GCOS 184 tropical Pacific observing system, 2020 workshop (TPOS 2020) – Vol. I: workshop report and Recommendations (2014) & Vol. II: white papers. WMO

GCOS. 2014a. The global climate observing system report #184 volume 1, http://library.wmo.int/pmb_ged/gcos_184-v1_en.pdf.

GCOS. 2014b. The global climate observing system report #184 volume 2, http://library.wmo.int/pmb_ged/gcos_184-v2_en.pdf.

Gregg WW, Rousseaux CS, Franz BA. 2017. Global trends in ocean phytoplankton: a new assessment using revised ocean colour data. Remote Sens Lett. 8:1102–1111. doi:10.1080/2150704X.2017.1354263.

Han W, Meehl GA, Hu A, Alexander MA, Yamagata T, Yuan D, Ishii M, Pegion P, Zheng J, Hamlington BD, et al. 2014. Intensification of decadal and multi-decadal sea level variability in the western tropical Pacific during recent decades. Clim Dyn. 43:1357–1379.

Holland EA. 2018. Connecting the dots, oceans, climate and policy for big ocean states (BOSS). Pacific Ocean: Pacific

Climate, Pacific Climate Change Conference; University of Victoria, Wellington, New Zealand.

Mélin F, Vantrepotte V, Chuprin A, Grant M, Jackson T, Sathyendranath S. 2017. Assessing the fitness-for-purpose of satellite multi-mission ocean color climate data records: a protocol applied to OC-CCI chlorophyll-a data. Remote Sens Environ. 203:139–151. doi:10.1016/j.rse.2017.03.039.

Merrifield MA, Thompson PR, Lander M. 2012. Multidecadal sea level anomalies and trends in the western tropical Pacific. Geophys Res Lett. 39:L13602.

Meyssignac B, Piecuch CG, Merchant CJ, Racault M-F, Palanisamy H, MacIntosh C, Sathyendranath S, Brewin R. 2016. Causes of the regional variability in observed sea level, sea surface temperature and ocean colour over the period 1993–2011. Surv Geophys. doi:10.1007/s10712-016-9383-1.

PCCSP. 2011. Climate change in the Pacific volumes 1 & 2. https://www.pacificclimatechangescience.org/publications/reports/report-climate-change-in-the-pacific-scientific-assessment-and-new-research/.

PCCSP. 2014. Variability, extremes and change in the western tropical Pacific: new science and updated country reports 2014. https://www.pacificclimatechangescience.org/publications/reports/climate-variability-extremes-and-change-in-the-western-tropical-pacific-2014/.

Racault M-F, Sathyendranath S, Brewin RJW, Raitsos DE, Jackson T, Platt T. 2017. Impact of El Niño variability on oceanic phytoplankton. Front Mar Sci. 4:133. doi:10.3389/fmars.2017.00133.

Riser SC, Freeland HJ, Roemmich D, Wijffels S, Troisi A, Belbéoch M, Gilbert D, Xu J, Pouliquen S, Thresher A, et al. 2016. Fifteen years of ocean observations with the global Argo array. Nat Clim Chang. doi:10.1038/NCLIMATE2872.

Rhein M, Rintoul SR, Aoki S, Campos E, Chambers D, Feely RA, Gulev S, Johnson GC, Josey SA, Kostianoy A, et al. 2013. Observations: ocean. In: Stocker TF, Qin D, Plattner G-K, Tignor M, Allen SK, Boschung J, Nauels A, Xia Y, Bex V, Midgley PM, editors. Climate change 2013: the physical science basis. Contribution of Working Group I to the Fifth Assessment Report of the Intergovernmental Panel On Climate Change. Cambridge: Cambridge University Press.

SPREP. 2012. Pacific Islands meteorological strategy 2012–2021: sustaining weather and climate services in Pacific island countries and territories. ISBN: 978-982-04-447-2. https://www.sprep.org/attachments/Publications/PacificIslandsMeteorologicalStrategy.pdf.

SPREP. 2017. The First Pacific Ministerial Meeting on Meteorology and Third Meeting of the Pacific Meteorological Council – report of proceedings and outcomes. ISBN: 978-982-04-0669-8. https://www.sprep.org/attachments/Publications/CC/pmmm-pmc3.pdf.

Sun C, Kucharski F, Li J, Jin F-F, Kang I-S, Ding R. 2017. Western tropical Pacific multidecadal variability forced by the Atlantic multidecadal oscillation. Nat Commun. 8:15998. doi:10.1038/ncomms15998.

UN. 2017. Report of the United Nations Conference to support the implementation of Sustainable Development Goal 14: conserve and sustainably use the oceans, seas and marine resources for sustainable development (advance unedited version). https://sustainabledevelopment.un.org/content/documents/15662FINAL_15_June_2017_RepoRe_Goal_14.pdf.

Wang CZ, Weisberg RH, Virmani JI. 1999. Western Pacific interannual variability associated with the El Nino southern oscillation. J Geophys Res. 104:5131–5149.

Wolter K, Timlin MS. 2011. El Niño/southern oscillation behaviour since 1871 as diagnosed in an extended multivariate ENSO index (MEI.ext). Intl J Climatol. 31:1074–1087.

Section 3.2. Review of the use of ocean data in European fishery management and monitoring applications

Berx B, Dickey-Collas M, Skogen M, De Roeck Y-H, Klein H, Barciela R, Forster R, Dombrowsky E, Huret M, Payne M, et al. 2011. Does operational oceanography address the needs of fisheries and applied environmental scientists. Oceanography. 24:166–171.

Boyce DG, Lewis MR, Worm B. 2010. Global phytoplankton decline over the past century. Nature. 466:591–596. [accessed 2010 Jul 28]. http://www.nature.com/doifinder/10.1038/nature09268.

Brander KM, Neuheimer AB, Andersen KH, Hartvig M. 2013. Overconfidence in model projections. ICES J Mar Sci. 70:1065–1068. doi:10.1093/icesjms/fst055.

Breitburg D, Levin LA, Oschlies A, Grégoire M, Chavez FP, Conley DJ, Garçon V, Gilbert D, Gutiérrez D, Isensee K, et al. 2018. Declining oxygen in the global ocean and coastal waters. Science. 359:eaam7240.

Bruge A, Alvarez P, Fontán A, Cotano U, Chust G. 2016. Thermal niche tracking and future distribution of Atlantic mackerel spawning in response to ocean warming. Front Mar Sci. 3:1–13. http://journal.frontiersin.org/article/10.3389/fmars.2016.00086.

Brunel T, van Damme CJG, Samson M, Dickey-Collas M. 2018. Quantifying the influence of geography and environment on the northeast Atlantic mackerel spawning distribution. Fisher Oceanogr. 27:159–173.

Bruno Soares M, Dessai S. 2016. Barriers and enablers to the use of seasonal climate forecasts amongst organisations in Europe. Clim Chang. 137:89–103. doi:10.1007/s10584-016-1671-8.

Chavez F, Pennington J, Castro C, Ryan J, Michisaki R, Schlining B, Walz P, Buck K, McFadyen A, Collins C. 2002. Biological and chemical consequences of the 1997–1998 El Niño in central California waters. Prog Oceanogr. 54:205–232. http://linkinghub.elsevier.com/retrieve/pii/S0079661102000502.

Cheung WWL, Sarmiento JL, Dunne J, Frölicher TL, Lam VWY, Deng Palomares ML, Watson R, Pauly D. 2012. Shrinking of fishes exacerbates impacts of global ocean changes on marine ecosystems. Nat Clim Chang. 3:254–258. doi:10.1038/nclimate1691.

Daan N, Gislason H, Pope JG, Rice JC. 2011. Apocalypse in world fisheries? The reports of their death are greatly exaggerated. ICES J Mar Sci. doi:10.1093/icesjms/fsr069.

Drinkwater KF, Beaugrand G, Kaeriyama M, Kim S, Ottersen G, Perry RI, Pörtner H-O, Polovina JJ, Takasuka A. 2010. On the processes linking climate to ecosystem changes. J Mar Syst. 79:374–388. [accessed 2010 Jul 18]. http://linkinghub.elsevier.com/retrieve/pii/S092479630900092X.

Dupont S, Pörtner H-O. 2013. Marine science: get ready for ocean acidification. Nature. 498:429–429. doi:10.1038/498429a.

Good SA, Martin MJ, Rayner NA. 2013. EN4: Quality controlled ocean temperature and salinity profiles and monthly objective analyses with uncertainty estimates. J Geophys Res Oceans. 118:6704–6716. doi:10.1002/2013JC009067.

Hátún H, Payne MR, Beaugrand G, Reid PC, Sandø AB, Drange H, Hansen B, Jacobsen JA, Bloch D. 2009. Large bio-geographical shifts in the north-eastern Atlantic Ocean: from the subpolar gyre, via plankton, to blue whiting and pilot whales. Prog Oceanogr. 80:149–162. [accessed 2010 Jul 13]. http://linkinghub.elsevier.com/retrieve/pii/S0079661109000135.

Hazen EL, Scales KL, Maxwell SM, Briscoe DK, Welch H, Bograd SJ, Bailey H, Benson SR, Eguchi T, Dewar H, et al. 2018. A dynamic ocean management tool to reduce bycatch and support sustainable fisheries. Sci Adv. 4:eaar3001. doi:10.1126/sciadv.aar3001.

Langehaug HR, Matei D, Eldevik T, Lohmann K, Gao Y. 2017. On model differences and skill in predicting sea surface temperature in the Nordic and Barents Seas. Clim Dyn. 48:913–933.

Lehodey P, Senina I, Wibawa TA, Titaud O, Calmettes B, Conchon A, Tranchant B, Gaspar P. 2018. Operational modelling of bigeye tuna (Thunnus obesus) spatial dynamics in the Indonesian region. Mar Pollut Bull. 131:19–32. [accessed 2018 Jul 23]. https://www.sciencedirect.com/science/article/pii/S0025326X17306902.

MacKenzie BR, Payne MR, Boje J, Høyer JL, Siegstad H. 2014. A cascade of warming impacts brings bluefin tuna to Greenland waters. Glob Chang Biol. 20:2484–2491. [accessed 2014 Jun 3]. http://onlinelibrary.wiley.com/doi/10.1111/gcb.12597/full.

Maxwell SM, Hazen EL, Lewison RL, Dunn DC, Bailey H, Bograd SJ, Briscoe DK, Fossette S, Hobday AJ, Bennett M, et al. 2015. Dynamic ocean management: defining and conceptualizing real-time management of the ocean. Mar Pol. 58:42–50. http://linkinghub.elsevier.com/retrieve/pii/S0308597X15000639.

Miesner AK, Payne MR. 2018. Oceanographic variability shapes the spawning distribution of blue whiting (Micromesistius poutassou). Fisher Oceanogr. 27:623–638. doi:10.1111/fog.12382.

Myers RA. 1998. When do environment–recruitment correlations work? Rev Fish Biol Fisher. 8:285–305. [accessed 2011 Mar 29]. http://www.springerlink.com/index/P76366G6716KN272.pdf.

Nye JA, Baker MR, Bell R, Kenny A, Kilbourne KH, Friedland KD, Martino E, Stachura MM, Van Houtan KS, Wood R. 2014. Ecosystem effects of the Atlantic multidecadal oscillation. J Mar Syst. 133:103–116. [accessed 2013 Feb 24]. http://linkinghub.elsevier.com/retrieve/pii/S0924796313000316.

Payne MR. 2018. Blue whiting spawning habitat forecast. http://www.fishforecasts.aqua.dtu.dk/forecasts/01-blue-whiting-spatial-distribution.

Payne MR, Barange M, Cheung WWL, MacKenzie BR, Batchelder HP, Cormon X, Eddy TD, Fernandes JA, Hollowed AB, Jones MC, et al. 2016. Uncertainties in projecting climate-change impacts in marine ecosystems. ICES J Mar Sci: Journal du Conseil. 73:1272–1282. doi:10.1093/icesjms/fsv231.

Payne M, Hobday AJ, MacKenzie B, Tommasi D, Dempsey DP, Fässler SMM, Haynie AC, Ji R, Liu G, Lynch PD, et al. 2017. Lessons from the first generation of marine ecological forecast products. Front Mar Sci. 4. doi:10.3389/fmars.2017.00289/full.

Pecuchet L, Törnroos A, Lindegren M. 2016. Patterns and drivers of fish community assembly in a large marine ecosystem. Mar Ecol Prog Ser. 546:239–248.

Poloczanska ES, Brown CJ, Sydeman WJ, Kiessling W, Schoeman DS, Moore PJ, Brander KM, Bruno JF, Buckley LB, Burrows MT, et al. 2013. Global imprint of climate change on marine life. Nat Clim Chang. 3:919–925. doi:10.1038/nclimate1958.

Pörtner H-O. 2002. Climate variations and the physiological basis of temperature dependent biogeography : systemic to molecular hierarchy of thermal tolerance in animals. Comp Biochem Phys A. 132:739–761.

Racault M-F, Le Quéré C, Buitenhuis E, Sathyendranath S, Platt T. 2012. Phytoplankton phenology in the global ocean. Ecol Indicat. 14:152–163. doi:10.1016/j.ecolind.2011.07.010.

Rice J. 2011. Managing fisheries well: delivering the promises of an ecosystem approach. Fish Fisher. 12:209–231.

Saji NH, Goswami BN, Vinayachandran PN, Yamagata T. 1999. A dipole mode in the tropical Indian Ocean. Nature. 401:360. doi:10.1038/43854.

Schneider DP, Deser C, Fasullo J, Trenberth KE. 2013. Climate data guide spurs discovery and understanding. Eos, Trans Am Geophys Union. 94:121–122. doi:10.1126/science.1197869.

Skern-Mauritzen M, Ottersen G, Handegard NO, Huse G, Dingsør GE, Stenseth NC, Kjesbu OS. 2016. Ecosystem processes are rarely included in tactical fisheries management. Fish Fisher. 17:165–175. doi:10.1111/faf.12111.

Tommasi D, Stock CA, Hobday AJ, Methot R, Kaplan IC, Eveson JP, Holsman K, Miller TJ, Gaichas S, Gehlen M, et al. 2017. Managing living marine resources in a dynamic environment: the role of seasonal to decadal climate forecasts. Prog Oceanogr. 152:15–49. http://linkinghub.elsevier.com/retrieve/pii/S0079661116301586.

Tranchant B, Reffray G, Greiner E, Nugroho D, Koch-Larrouy A, Gaspar P. 2016. Evaluation of an operational ocean model configuration at 1/12° spatial resolution for the Indonesian seas (NEMO2.3/INDO12) – part 1: Ocean physics. Geosci Model Develop. 9:1037–1064. https://www.geosci-model-dev.net/9/1037/2016/.

Wilkinson MD, Dumontier M, Aalbersberg IJ, Appleton G, Axton M, Baak A, Blomberg N, Boiten J-W, da Silva Santos LB, Bourne PE, et al. 2016. The FAIR guiding principles for scientific data management and stewardship. Scient Data. 3:160018. http://www.pubmedcentral.nih.gov/articlerender.fcgi?artid=4792175&tool=pmcentrez&rendertype=abstract.

Section 3.3. Synergy between CMEMS products and newly available data from SENTINEL

Aouf L. 2018. The impact of the upgraded L2 S3A wave products on the wave forecast at Météo-France, Workshop of Sentinel-3 Validation Team (S3VT); Darmstadt, Germany; 13–15 Mar.

Behrens A, Gayer G, Staneva J. 2019. Verification of a high resolution operational wave model in the data sparse. Black Sea J Operation Oceanogr.

Cavaleri L, Abdalla S, Benetazzo A, Bertotti L, Bidlot J-R, Breivik Ø, Carniel S, Jensen RE, Portilla-Yandun J, Rogers WE, et al. 2018. Wave modelling in coastal and inner seas. Prog Oceanogr. doi:10.1016/j.pocean.2018.03.010.

Staneva J, Behrens A, Wahle K. 2015. Wave modelling for the coastal-ocean predicting system. J Phys: Conf Series. 633:233–254. ISBN: 978-3-939230-28-1.

Wiese A, Staneva J, Schultz-Stellenfleth J, Behrens A, Fenoglio-Marc L, Bidlot JR. 2018. Synergy between satellite observations and model simulations during extreme events. Ocean Sci. doi:10.5194/os-2018-87.

Section 3.4. Joint Monitoring Programme of the EUtrophication of the NOrthSea with SATellite data user case

Doerffer R, Schiller H. 2007. The MERIS case 2 water algorithm. Int J Remote Sens. 28(3-4):517–535.

European Commission. 2014. The European Commissions assessment and guidance (COM/2014/097_final). Luxembourg: Office for Official Publications of the European Communities.

Gohin F, Druon J, Lampert L. 2002. A five channel chlorophyll concentration algorithm applied to SeaWiFS data processed by SeaDAS in coastal waters. Int J Remote Sens. 23(8):1639–1661.

Gohin F, Saulquin B, Oger-Jeanneret H, Lozac'h L, Lampert L, Lefebvre A, Riou P, Bruchon F. 2008. Towards a better assessment of the ecological status of coastal waters using satellite-derived chlorophyll-a concentrations. Remote Sens Environ. 112(8):3329–3340.

Gons HJ, Rijkeboer M, Ruddick KG. 2005. Effect of a waveband shift on chlorophyll retrieval from meris imagery of inland and coastal waters. J Plankton Res. 27(1):125–127.

Lee Z. 2006. Reports of the international ocean-colour coordinating group, No. 5. IOCCG, Dartmouth, Canada.

Nechad B, Ruddick K, Schroeder T, Oubelkheir K, Blondeau-Patissier D, Cherukuru N, Brando V, Dekker A, Clementson L, Banks AC. 2015. Coastcolour round robin data sets: a database to evaluate the performance of algorithms for the retrieval of water quality parameters in coastal waters. Earth Syst Sci Data. 7(2):319.

O'Reilly JE, Maritorena S, Mitchell BG, Siegel DA, Carder KL, Garver SA, Kahru M, McClain C. 1998. Ocean color chlorophyll algorithms for SeaWiFS. J Geophys Res. 103 (C11):24937–24953.

OSPAR. 2017. Third OSPAR integrated report on the eutrophication status OF the OSPAR maritime area. ISBN: 978-1-911458-34-0.

Sathyendranath S. 2000. Reports of the international ocean-colour coordinating group, No. 3. IOCCG, Dartmouth, Canada.

Schroeder T, Schaale M, Fischer J. 2007. Retrieval of atmospheric and oceanic properties from MERIS measurements: a new Case 2 water processor for BEAM. Int J Remote Sens. 28:5627–5632.

Section 3.5. Regional mean time series for the Northwest European Shelf Seas

Balmaseda MA, Hernandez F, Storto A, Palmer MD, Alves O, Shi L, Smith GC, Toyoda T, Valdivieso M, Barnier B, et al. 2015. The ocean reanalyses intercomparison project (ORA-IP). J Oper Oceanogr. 8(sup1):s80–s97. doi:10.1080/1755876X.2015.1022329.

Barciela R, Tinker J, Wood R. 2019. Report on AtlantOS fitness to MSFD needs: assessment of impact of AtlantOS on North West Shelf state reanalyses. AtlantOS 633211. doi:10.3289/atlantos_d8.16.

DEFRA. 2010. Charting progress 2: the state of UK Seas. Department for Environment, Food and Rural Affairs, UK Government. http://chartingprogress.defra.gov.uk/.

ICES. 2004. Ecoregions and advisory areas. International Council for the Exploration of the Sea http://www.ices.dk/community/advisory-process/Pages/ICES-ecosystems-and-advisory-areas.aspx).

MCCIP. 2013. Marine climate change impacts report card 2013. In: Frost M, Baxter JM, Bayliss-Brown GA, Buckley PJ, Cox M, Withers Harvey N, editors. Summary report, MCCIP, Lowestoft, 12pp.

Roberts-Jones J, Fiedler E, Martin MJ. 2012. Daily, global, high-resolution SST and Sea ice reanalysis for 1985–2007 using the OSTIA system. J Clim. 25:6215–6232.

Tinker J, Krijnen J, Wood R, Barciela R, Dye S. 2018. What are the prospects for seasonal prediction of the marine environment of the NW European shelf? Ocean Sci. 14:887–909.

Tinker J, Lowe J, Holt J, Pardaens A, Wiltshire A. 2015. Validation of an ensemble modelling system for climate projections for the northwest European shelf seas. Prog Oceanogr. 138:211–237.

Tinker J, Lowe J, Pardaens A, Holt J, Barciela R. 2016. Uncertainty in climate projections for the 21st century northwest European shelf seas. Prog Oceanogr. 148:56–73.

Wakelin SL, Holt JT, Blackford JC, Allen JI, Butenschön M, Artioli Y. 2012. Modeling the carbon fluxes of the northwest European continental shelf: Validation and budgets. J Geophys Res. 117:C05020. doi:10.1029/2011JC007402.

Section 3.6. Using CMEMS and the Mediterranean Marine Protected Areas sentinel network to track ocean warming effects in coastal areas

Bates AE, Helmuth B, Burrows MT, Duncan MI, Garrabou J, Guy-Haim T, Lima F, Queiros AM, Seabra R, Marsh R, et al. 2018. Biologists ignore ocean weather at their peril. Nature. 560:299–301. doi:10.1038/d41586-018-05869-5.

Bensoussan N, Garreau P, Pairaud I, Somot S, Garrabou J. 2013. Multidisciplinary approach to assess potential risk of mortality of benthic ecosystems facing climate change in the NW Mediterranean Sea. OCEANS'13 MTS/IEEE Technical Program; San Diego, USA; 23–26 Sep. 6 pp.

Bensoussan N, Harmelin JG, Romano JC, Garrabou J. 2010. High resolution characterization of northwest Mediterranean coastal waters thermal regimes: to better

understand responses of benthic communities to climate change. Estuar Coast Shelf Sci. 87:431–441.

Bianchi CN, Francesco C, Guidetti P, Morri C. 2017. Seawater waring at the northern reach for southern species: gulf of Genoa, NW Mediterranean. J Mar Biol Assoc UK. doi:10.1017/S0025315417000819.

Brewin RJW, de Mora L, Billson O, Jackson T, Russell P, Brewin TG, Shutler J, Miller PI, Taylor BH, Smyth TJ, et al. 2017. Evaluating operational AVHRR sea surface temperature data at the coastline using surfers. Estuar Coast Shelf Sci. 196:276–289. doi:10.1016/j.ecss.2017.07.011.

Brewin RJW, Smale DA, Moore PJ, Dall'Olmo G, Miller PI, Taylor BH, Smyth TJ, Fishwick JR, Yang M. 2018. Evaluating operational AVHRR sea surface temperature data at the coastline using benthic temperature loggers. Remote Sens. 10:925.

Coll M, Piroddi C, Steenbeek J, Kaschner K, Ben Rais Lasram F, Aguzzi J, Ballesteros E, Bianchi CN, Corbera J, Dailianis T, et al. 2010. The biodiversity of the Mediterranean Sea: estimates, patterns, and threats. PLoS One. 5(8):e11842. doi:10.1371/journal.pone.0011842.

Crisci C, Bensoussan N, Romano JC, Garrabou J. 2011. Temperature anomalies and mortality events in marine communities: insights on factors behind differential mortality impacts in the NW Mediterranean. PLoS One. 6(9): e23814. doi:10.1371/journal.pone.0023814.

Crisci C, Ledoux JB, Mokhtar-Jamaï K, Bally M, Bensoussan N, Aurelle D, Cebrian E, Coma R, Féral JP, La Rivière M, et al. 2017. Regional and local environmental conditions do not shape the response to warming of a marine habitat-forming species. Sci Rep. doi:10.1038/s41598-017-05220-4.

Galli G, Solidoro C, Lovato T. 2017. Marine heat waves hazard 3D maps and the risk for low motility organisms in a warming Mediterranean Sea. Front Mar Sci. doi:10.3389/fmars.2017.00136.

Garrabou J, Coma R, Bensoussan N, Bally M, Chevaldonné P, Cigliano M, Diaz D, Harmelin JG, Gambi MC, Kersting DK, et al. 2009. Mass mortality in NW Mediterranean rocky benthic communities: effects of the 2003 heat wave. Global Change Biol. doi:10.1111/j.1365-2486.2008.01823.x.

Hughes TP, Barnes ML, Bellwood DR, Cinner JE, Cumming GS, Jackson JBC, Kleypas J, van de Leemput IA, Lough JM, Morrison TH, et al. 2017. Coral reefs in the anthropocene. Nature. 546(7656). doi:10.1038/nature22901.

Kersting DK, Bensoussan N, Linares C. 2013. Long-term responses of the endemic reef-builder Cladocora caespitosa to Mediterranean warming. PLoS One. 8(8):e70820. doi:10.1371/journal.pone.0070820.

Ledoux JB, Aurelle D, Bensoussan N, Marschal C, Feral JP, Garrabou J. 2015. Potential for adaptive evolution at species range margins: contrasting interactions between red coral populations and their environment in a changing ocean. Ecol Evol. doi:10.1002/ece3.1324.

Millot C, Wald L. 1981. Upwelling in the Gulf of Lions. In: Richards FA, editor. Coastal upwelling. United States. American Geophysical Union, 1; p.160–166, Coastal and Estuarine Science Series.

Pairaud I, Bensoussan N, Garreau P, Faure V, Garrabou J. 2014. Impacts of climate change on coastal benthic ecosystems: assessing current risk of mortality outbreaks associated with thermal stress in the NW Mediterranean coastal areas. Ocean Dyn. 64(1):103–115. doi:10.1007/s10236-013-0661-x.

Pisano A, Buogiorno Nardelli B, Tronconi C, Santoleri R. 2016. The new Mediterranean optimally interpolated pathfinder AVHRR SST Dataset (1982–2012). Remote Sens Environ. 176:10–116.

Sen PK. 1968. Robustness of some nonparametric procedures in linear models. Ann Math Stat. 39(6):1913–1922.

Smale DA, Wernberg T. 2009. Satellite-derived SST data as a proxy for water temperature in nearshore benthic ecology. Mar Ecol Prog Ser. 387:27–37. doi:10.3354/meps08132.

Smit AJ, Roberts M, Anderson RJ, Dufois F, Dudley SFJ, Bornman TG, Olbers J, Bolton JJ. 2013. A coastal seawater temperature dataset for biogeographical studies: large biases between in situ and remotely-sensed data sets around the coast of South Africa. PLoS One. 8(12):e81944. doi:10.1371/journal.pone.0081944.

Taylor KE. 2001. Summarizing multiple aspects of model performance in a single diagram. J Geophys Res. 106:7183–7192.

Wong PP, Losada IJ, Gattuso JP, Hinkel J, Khattabi A, McInnes KL, Saito Y, Sallenger A. 2014. Climate change 2014: impacts, adaptation, and vulnerability. Part A: global and sectoral aspects. In: Contribution of Working Group II to the Fifth Assessment Report of the Intergovernmental Panel of Climate Change. Cambridge: Cambridge University Press; p. 361–409.

Section 3.7. Combined analysis of Cryosat-2/ SMOS sea ice thickness data with model reanalysis fields over the Baltic Sea

Boström M, Österman C. 2017. Improving operational safety during icebreaker operations. WMU J Marit Affair. 16:73–88. doi:10.1007/s13437-016-0105-9.

Gegiuc A, Similä M, Karvonen J, Lensu M, Mäkynen M, Vainio J. 2018. Estimation of degree of sea ice ridging based on dual-polarized C-band SAR data. Cryosphere. 12:343–364.

Herman A, Jedrasik J, Kowalewski M. 2011. Numerical modelling of thermodynamics and dynamics of sea ice in the Baltic Sea. Ocean Sci. 7(2):257–276. doi:10.5194/os-7-257-2011.

Kaleschke L, Tian-kunze X, Maaß N, Beitsch A, Wernecke A, Miernecki M, Müller G, Fock BH, Gierisch AMU, Schlünzen KH, et al. 2016. SMOS sea ice product: operational application and validation in the Barents Sea marginal ice zone. Remote Sens Environ. 180:264–73. doi:10.1016/j.rse.2016.03.009.

Karvonen J, Simila M, Heiler I. 2003. Ice thickness estimation using SAR data and ice thickness history. IGARSS 2013 IEEE International Geoscience and Remote Sensing Symposium Proceedings (IEEE Cat No03CH37477). doi:10.1109/IGARSS.2003.1293683.

Maaß N, Kaleschke L, Tian-kunze X, Mäkynen M, Drusch M, Krumpen T, Hendricks S, Lensu M, Haapala J, Haas C. 2015. Validation of SMOS sea ice thickness retrieval in the

northern Baltic Sea. Tellus A. 67:24617. doi:10.3402/tellusa.v67.24617.

Pemberton P, Löptien U, Hordoir R, Höglund A, Schimanke S, Axell L, Haapala J. 2017. Sea-ice evaluation of NEMO-Nordic 1.0: a NEMO–LIM3.6-based ocean–sea-ice model setup for the North Sea and Baltic Sea. Geosci Model Dev. 10:3105–3123. doi:10.5194/gmd-10-3105-2017.

Ricker R, Hendricks S, Kaleschke L, Tian-Kunze X, King J, Haas C. 2017. A weekly Arctic sea-ice thickness data record from merged CryoSat-2 and SMOS satellite data. The Cryosphere. 11:1607–1623. doi:10.5194/tc-11-1607-2017.

Ronkainen I, Lehtiranta J, Lensu M, Rinne E, Haapala J, Haas C. 2018. Interannual sea ice thickness variability in the Bay of Bothnia. The Cryosphere. 12(11):3459–3476. doi:10.5194/tc-12-3459-2018.

Samuelsen A, Garric G, Raj RP, Axell L, Zuo H, Peterson KA, Aaboe S, Storto A, Lavergne T, Breivik L-A. 2018. Sea ice. In: von Schuckmann K, Le Traon P-Y, Smith N, Pascual A, Brasseur P, Fennel K, Djavidnia S, editors. Copernicus marine service ocean state report, issue 2. J Oper Oceanogr. 11(sup10:s13–s16. doi:10.1080/1755876X.2018.1489208.

Tonboe R, Lavelle J, Pfeiffer RH, Howe E. 2018. Product user manual for OSI SAF global sea ice concentration (Product OSI-401-b). Danish Meteorological Institute.

Valdez Banda OA, Goerlandt F, Montewka J, Kujala P. 2015. A risk analysis of winter navigation in Finnish sea areas. Accid Anal Prev. 79:100–116. doi:10.1016/j.aap.2015.03.024.

Vihma T, Haapala J. 2009. Geophysics of sea ice in the Baltic Sea: a review. Prog Oceanogr. 80:129–148. doi:10.1016/j.pocean.2009.02.002.

Section 3.8. Chlorophyll-a evolution during the last 21 years and its relation with mussel growth and optimal repartition for aquaculture and fishery

Belin C, Lamoureux A, Soudant D. 2014. Evaluation de la qualité des eaux littorales de la France métropolitaine pour l'élément de qualité Phytoplancton dans le cadre de la DCE. Etat des lieux des règles d'évaluations et résultats pour la période 2007–2012 [Evaluation of quality of the French metropolitan coastal water for the quality indicator Phytoplankton in the framework of European Directive. State of the art of evaluation rules and results for the period of 2007–2012]. Rapport DYNECO/VIGIES/14-05 – Tome 1. French.

Capuzzo E, Lynam CP, Barry J, Stephens D, Forster RM, Greenwood N, Mc Quatters-Gollop A, Silva T, van Leeuwen SM, Engelhard GH. 2018. A decline in primary production in the North Sea over 25 years, associated with reductions in zooplankton abundance and fish stock recruitment. Glob Change Biol. 24:e352–e364. doi:10.1111/gcb.13916.

Gohin F. 2011. Annual cycles of chlorophyll-a, non-algal suspended particulate matter, and turbidity observed from space and in-situ in coastal waters. Ocean Sci. 7:705–732. doi:10.5194/os-7-705-2011.

Gohin F, Druon JN, Lampert L. 2002. A five channel chlorophyll concentration algorithm applied to SeaWiFS data processed by SeaDAS in coastal waters. Int J Remote Sens. 23:1639–1661.

Gohin F, Van Der Zande D, Tilstone G, Eleveld MA, Lefebvre A, Andrieux-Loyer F, Blauw AN, Bryère P, Devreker D, Garnesson P, et al. 2019. Twenty years of satellite and in situ observation of surface chlorophyll-a from the northern Bay of Biscay to the eastern English Channel. Is the water quality improving? Remote Sens Environ.

Lapucci C, Ampolo Rella M, Brandini C, Ganzin N, Gozzini B, Maselli F, Massi L, Nuccio C, Ortolani A, Trees C. 2012. Evaluation of empirical and semi-analytical chlorophyll algorithms in the Liguran and North Tyrrhenian seas. J Appl Remote Sens. 6(1):063565. doi:10.1117/1.JRS.6.063565.

Loisel H, Vantrepotte V, Ouillon S, Ngoc DD, Herrmann M, Tran V, Mériaux X, Dessailly D, Jamet C, Duhaut T, et al. 2017. Assessment and analysis of the chlorophyll-a concentration variability over the Vietnamese coastal waters from the MERIS ocean color sensor (2002–2012). Remote Sens Environ. 190:217–232. doi:10.1016/j.rse.2016.12.016.

Maritorena S, Siegel DA. 2005. Consistent merging of satellite ocean colour data sets using a bio-optical model. Remote Sens Environ. 94(4):429–440.

Morel A, Huot Y, Gentili B, Werdell PJ, Hooker SB, Franz BA. 2007. Examining the consistency of products derived from various ocean color sensors in open ocean (case 1) waters in the perspective of a multi-sensor approach. Remote Sens Environ. 111:69–88.

Novoa S, Chust G, Sagarminaga Y, Revilla M, Borja A, Franco J. 2012. Water quality assessment using satellite-derived chlorophyll-a within the European directives, in the southeastern Bay of Biscay. Marine Poll Bull. 64:739–750.

Romero E, Garnier J, Lassaletta L, Billen G, Le Gendre R, Riou P, Cugier P. 2013. Large-scale patterns of river inputs in southwestern Europe: seasonal and interannual variations and potential eutrophication effects at the coastal zone. Biogeochemistry. 113:481. doi:10.1007/s10533-012-9778-0.

SAFI Consortium. 2016. SAFI final review 2-SAFI-PR2_ProjectOutcomes_v1.0.

Saulquin B, Gohin F, Garrello R. 2011. Regional objective analysis for merging high-resolution meris, modis/aqua, and SeaWiFS chlorophyll-a data from 1998 to 2008 on the European atlantic shelf. IEEE Trans Geosci Remote Sens. 49:143–154. doi:10.1109/tgrs.2010.2052813.

Thomas Y, Mazurié J, Alunno-Bruscia M, Bacher C, Bouget JF, Gohin F, Pouvreau S, Struski C. 2011. Modelling spatio-temporal variability of *Mytilus edulis* (L.) growth by forcing a dynamic energy budget model with satellite-derived environmental data. J Sea Res. 66:308–317.

Chapter 4: Specific events 2017

4.1. The Weddell Sea Polynya

Authors: Céline Heuzé, Gilles Garric, Thomas Lavergne

Statement of main outcome: During the year 2017 a large hole in the winter sea ice cover (polynya) appeared in the Weddell Sea, a region of the Antarctic Ocean. It stayed open for almost three months and was the first reappearance of such an event since 1976. Deep vertical oceanic mixing started after the polynya opened but was stopped after just two months, probably as sun-induced sea ice melting released enough freshwater to stabilise the water column. Such deep mixing is crucial for the global ocean circulation, deep ocean ventilation, and carbon and heat storage. The Weddell Polynya must therefore be actively monitored to understand why this deep mixing starts and stops.

Products used:

Ref. No.	Product name and type	Documentation
4.1.1	SEAICE_GLO_SEAICE_L4_REP_ OBSERVATIONS_011_009 Global Ocean Sea Ice Concentration Time Series Reprocessed from EUMETSAT OSI SAF	PUM: http://marine. copernicus.eu/ documents/PUM/ CMEMS-OSI-PUM-011-009.pdf QUID: http://marine. copernicus.eu/ documents/QUID/ CMEMS-OSI-QUID-011-001to007-009to012.pdf
4.1.2.	GLOBAL_REANALYSIS_PHY_001_026 Global ocean ensemble physics reanalysis	PUM: http://marine.copernicus. eu/documents/PUM/ CMEMS-GLO-PUM-001-026.pdf QUID: http://marine.copernicus. eu/documents/QUID/ CMEMS-GLO-QUID-001-026.pdf

Every winter at both poles, strong winds push the sea ice away from the coast (Smith and Barber 2007), opening small holes in the sea ice or so-called 'coastal polynyas'. Via these holes, the comparatively warm ocean is in direct contact with the cold atmosphere, which results in strong oceanic heat loss, sea ice formation and dense water production (e.g. Cavalieri and Martin 1994; Kusahara et al. 2010). In stark contrast with these small coastal polynyas, in austral winter 2017 a very large hole opened unexpectedly in the sea ice in the open ocean in the Weddell Sea – the Atlantic sector of the Southern Ocean. That hole, the Weddell Polynya, has been a modelling mystery for the last decades, occurring regularly in climate projections (e.g. Heuzé et al. 2013) yet only twice to date in the observational record. It is hence crucial to study this second occurrence, not only

to help improve global climate models but also due to the potential large role of the Weddell Polynya on the global oceanic circulation (Orsi et al. 2001) and on local ecosystems (Smith and Barber 2007).

The first satellites to routinely observe the Antarctic sea ice detected the Weddell Sea polynya, a huge hole that opened three winters in a row, from 1974 to 1976 and reached up to 350,000 km^2 (Carsey 1980). Then, nothing happened for forty years. A small 'halo' with sea ice concentrations never exceeding 90% (Lindsay et al. 2004) was regularly observed, but the polynya itself did not re-open until 27 July 2016 and closed shortly after on 17 August 2016. In 2017 however, the Weddell Polynya stayed open continuously from mid-September until the seasonal retreat of sea ice early December, and at its maximum reached approximately 300,000 km^2 (Figure 4.1.1).

There have been too few observed events to determine the exact reasons why the Weddell Polynya only opens occasionally. The Weddell Polynya is a latent heat polynya, meaning that it opens because sea ice is melted locally from below by upwelled warm waters (Morales-Maqueda et al. 2004). The sea ice halo indicates that this upwelling happens often, most likely because of the presence of the underwater seamount Maud Rise (Holland 2001). However, additional processes are required to trigger a full polynya opening but there is no consensus as to which they are, owing notably to a lack of in-situ measurements. The trigger could be an event in the atmosphere, e.g. persistent anomalous winds (Gordon et al. 2007; Cheon et al. 2014); or a weakening of the oceanic stratification (Comiso and Gordon 1987; Heuzé et al. 2015; Kjellsson et al. 2015); or even low frequency variations in the Weddell Sea heat content (Martin et al. 2013; Dufour et al. 2017).

The Weddell Sea and the other seas surrounding Antarctica are vast and cannot be sampled effectively with conventional automated in-situ observations (drifters, profilers, etc), and ship-based campaigns are too seldom to allow for the monitoring of such rapidly evolving phenomena as the polynya. The main direct observation of the polar ocean and its sea ice cover is thus made using satellite-based products. Figure 4.1.1 shows the temporal evolution of the Weddell Sea polynya in austral spring 2017 (15 September, 25 October, 15 November, and 1 December). Daily maps of sea-ice concentration are computed from passive microwave radiometer observations from the Special Sensor Microwave Imager/ Sounder (SSMIS). Raw brightness temperature measurements are converted to sea-ice concentration by the EUMETSAT Ocean and Satellite Application Facility (OSI SAF, http://www.osi-saf.org/) and redistributed by CMEMS as SEAICE_GLO_SEAICE_L4_NRT_OBSERVATIONS_011_001 (product reference 4.1.1).
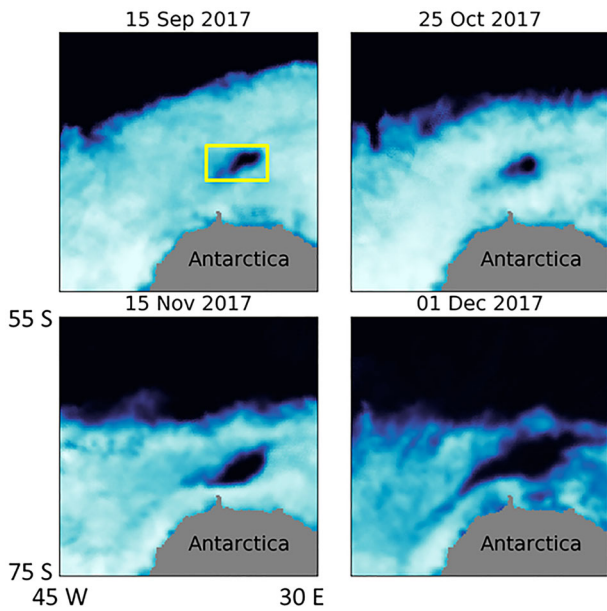
Figure 4.1.1. Evolution of the Weddell Sea Polynya in austral spring (15 September, 25 October, 15 November, and 1 December) 2017 as monitored by product 4.1.1. Yellow box highlights the area used for the output averaging of GREP (product 4.1.2) shown on Figures 4.1.2 and 4.1.3.

Figure 4.1.2. Monthly mixed layer depth over Maud Rise (yellow box, Figure 4.1.1) from product 4.1.2. Black line indicates the mean of 1993–2016 (individual dotted lines). Red line is 2017, with the polynya opening in September. Based on product 4.1.2 (GREP).

In the following section, we use the ensemble mean global reanalysis product GREP (product reference 4.1.2). GREP consists of GLORYS2V4 from Mercator Ocean (Fr), ORAS5 from ECMWF, FOAM/GloSea from the UK Met Office (UK) and C-GLORS from CMCC (It). All these reanalyses assimilate sea ice concentration from passive microwave observation data and the vertical mixing is parameterised according to a turbulent closure model adapted by Blanke and Delecluse (1993).

Observations (Martinson et al. 1981) and coupled models (e.g. Heuzé et al. 2013) both show a deepening of the mixed layer during a polynya event. The GREP product correctly reproduces this phenomenon (Figure 4.1.2): in 2017, the monthly mixed layer depth (MLD) departs from an average value in August to peak at 470 m in October 2017, 350 m deeper than the mean value of 1993–2016, and returns to a normal value in December. The deep mixed layers, by bringing warm water up, are thought to keep the polynya open. GREP in contrast shows that in November, as the polynya grew exponentially, the MLD had decreased again (Figure 4.1.2), suggesting that from November onwards the polynya continued growing because of melting of sea ice by the atmosphere, not by further upwelling of warm oceanic water.

The evolution of both temperature and salinity with time and depth in the polynya region (Figure 4.1.3) confirms these findings. After the opening of the polynya,
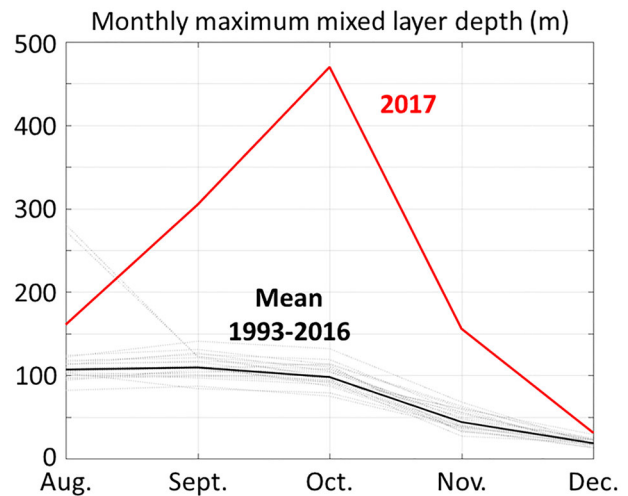
notably in September 2017, the surface waters are warmer and saltier than previously (resp. 0.05°C and 0.01, thick black line on Figure 4.1.3(b,d)) whereas from 70 m depth onwards they are colder and slightly fresher than before the polynya opened. This pattern of warming of the surface waters in winter coincident with a cooling of the subsurface, all while the MLD deepens, is indicative of convection. From November 2017 onwards however, the surface signal is dominated by the large freshening induced by the growth of the polynya (Figure 4.1.1) while at subsurface temperatures around 100 m increase again as the mixed layer shoals, further suggesting that the convection was limited to September–October 2017. It is worth noting that the hydrography from GREP is remarkably similar to that measured by the autonomous SOCCOM floats that accidentally sampled the 2017 polynya (see Figure SB6.2 of Swart et al. (2018) compared to Figure 4.1.3(a,c) here). Since modelling approaches are routinely used in the ice-covered Southern Ocean where observations are lacking, it is crucial that reanalysis such as the four members of the GREP product remain as accurate as possible, even when having to react to an unexpected polynya event.

In summary, although the opening of the Weddell Polynya in winter 2017 was unexpected, it was accurately detected by the passive microwave observations (product 4.1.1), which were then assimilated by GREP (product 4.1.2) resulting in GREP's hydrography matching that opportunistically observed (Swart et al. 2018). The GREP results presented here suggest that the 2017 Weddell Polynya had two different stages of development: first, in September and October, the mixed layer
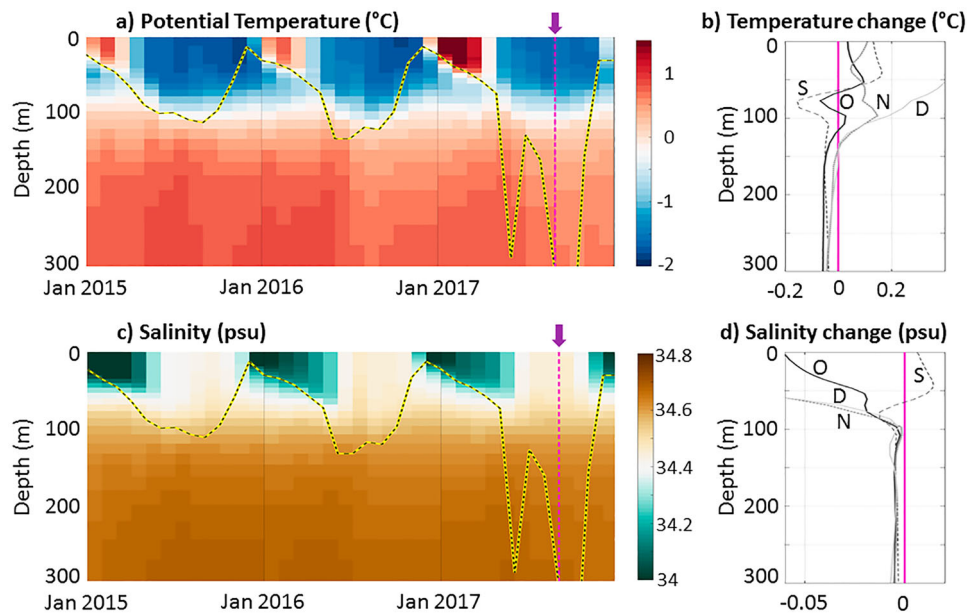
Figure 4.1.3. Evolution of the monthly hydrographic properties in GREP (product 4.1.2) with depth and time over Weddell Polynya region (yellow box, Figure 4.1.1): (a) Potential Temperature from January 2015 to December 2017; (b) change in that temperature after the opening of the polynya in September (S, dashed black), October (O, plain dark grey), November (N, dashed grey) and December (D, plain light grey) 2017 when compared with August 2017; (c) and (d) same as (a) and (b) respectively for the salinity. On (a) and (c), yellow dashed line is the monthly MLD from product 4.1.2; vertical purple dashed line and associated arrow, the opening of the polynya in September 2017; vertical dashed black lines, the turn of the year.

deepened and heat was redistributed through the water column, indicative of convection bringing warm water to the surface to further melt the sea ice from below; then, in November, the water column was stabilised, convection stopped, and the polynya grew only because of seasonal surface melting from above, hence producing even more freshwater to stabilise the water column. It is however too early to say whether the dynamics in the model are correct. Longer observational time series with more openings of the large Weddell Polynya than just the 1970s and 2017 are needed, along with measurements of its effect on the rest of the climate system in terms of heat and carbon fluxes and volumes of deep water formation. Since sea ice has been struggling to close over the polynya region in May and June 2018, we may be able to extend our analysis by one year soon.

4.2. Temperature and salinity anomalies in the North Atlantic subpolar gyre

Authors: Jérôme Gourrion, Julie Deshayes, Mélanie Juza, Tanguy Szekely

Statement of outcome: A regional cold and fresh anomaly appeared in the North Atlantic in 2014. It is associated with the onset of a positive North Atlantic Oscillation phase and intense deep convection in the Labrador Sea. The previous Ocean State Report indicates

that in 2016, this cold and fresh anomaly was located to the south of Iceland and primarily associated with an eastward migration of the eastern boundary of the subpolar gyre. In 2017, a similar cold and fresh anomaly is detected further to the north-east with temperature anomalies of smaller amplitude and salinity anomalies of similar amplitude as observed previously.

Products used:

Ref. No.	Product name and type	Documentation
4.2.1	INSITU_GLO_TS_OA_REP_ OBSERVATIONS_013_002_B INSITU_GLO_TS_OA_NRT_ OBSERVATIONS_013_002_A **In situ TS data**	PUM: http://marine. copernicus.eu/documents/ PUM/CMEMS-INS-PUM-013-002-ab.pdf QUID: http://marine. copernicus.eu/documents/ QUID/CMEMS-INS-QUID-013-002b.pdf http://marine.copernicus.eu/ documents/QUID/CMEMS-INS-QUID-013-002a.pdf
4.2.2	GLOBAL_REANALYSIS_PHY_001_030 **Reanalysis**	PUM: http://marine. copernicus.eu/documents/ PUM/CMEMS-GLO-PUM-001-030.pdf QUID: http://marine. copernicus.eu/documents/ QUID/CMEMS-GLO-QUID-001-030.pdf

The North Atlantic subpolar gyre is a region characterised by substantial variability on interannual to decadal

timescale, with cold and fresh anomalies, such as in the 1970s (Dickson et al. 1988; Belkin et al. 1998) but also in the 1980s and early 1990s, alternating with warm and salty anomalies, e.g. in the late 1990s (Robson et al. 2012). It is crucial to understand better the drivers of this regional variability, because (i) the presence of cold and fresh anomalies may conceal the long-term increase in ocean heat uptake (Levitus et al. 2009), (ii) sea surface temperature anomalies in the North Atlantic have a direct impact on European climate (e.g. Czaja and Frankignoul 2002) and (iii) it is expected to have consequences on the regional to global ocean and climate system through their potential impact on dense water formation (Hátún et al. 2005). In 2016, Gourrion et al. (2018) reported that cold and fresh anomalies are observed in the subpolar gyre, to the south of Iceland, from the surface down to 1000 m. The authors suggest that these anomalies were associated with an eastward migration of the eastern boundary of the subpolar gyre, and resulted from a regional adjustment of the basin-scale dynamical structures subsequent to dense water formation in the Labrador Sea. As these cold anomalies coincide with general warming trends elsewhere, there has been numerous studies focussing on those and other hypotheses have

been advanced, for example anomalous air-sea fluxes (e.g. Grist et al. 2016; Zunino et al. 2017), large scale changes in horizontal (Piecuch et al. 2017) and/or overturning (Robson et al. 2016) circulations, among others (see review of Josey et al. 2018). In this section, we analyse the temperature and salinity anomalies observed in the subpolar North Atlantic in 2017 and discuss their relationship with those observed previously.

In 2017, the global CMEMS *in situ* observation reprocessed dataset (product reference 4.2.1, hereafter designed as the CORA dataset) suggests that upper ocean anomalies in the subpolar North Atlantic are cold and fresh compared to the mean over the period 2003–2014 (Figure 4.2.1, left), similarly to 2016. Anomalies of maximum amplitude (around −1°C and −0.2 psu when integrated over 100–400 m depth) are located more to the north east (approximately at 21°W, 59°N) than previous year. To the south of the subpolar gyre and offshore Grand Banks (40°W, 48°N), as well as to the north of the Labrador Sea, upper ocean anomalies are warm and salty during 2017. In order to determine which upper ocean anomalies are robust, similar diagnostics from the GLO-MFC reanalysis product (product reference 4.2.2, hereafter designed as GLORYS12V1) are also produced
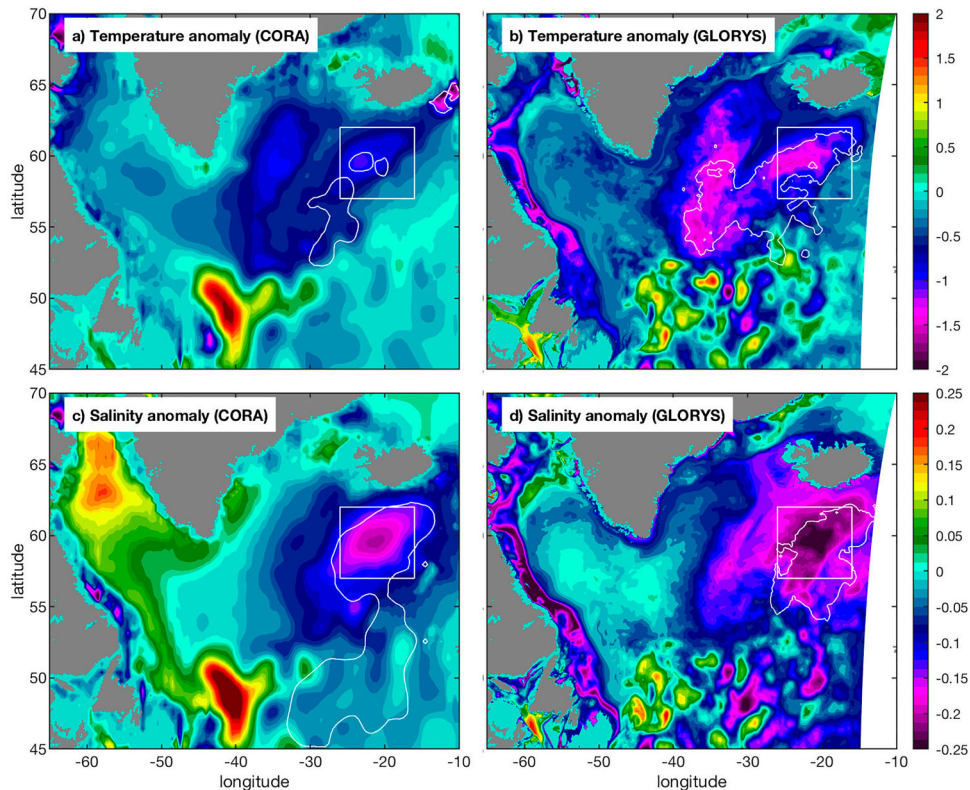

Figure 4.2.1. Temperature (in °C, top) and salinity (in psu, bottom) anomaly fields integrated within the 100–400 m depth layer in 2017 from the CORA observational dataset (product reference 4.2.1) and the GLORYS12V1 model (product reference 4.2.2). The reference period for anomaly computation is the mean over 2003–2014. The white box corresponds to the control box used in Figure 4.2.2 to compute the depth-time diagram. The white contours correspond to the patterns of temperature and salinity anomaly maxima in 2016 (delimited by the values of −1.3°C and 0.17 psu, respectively).

(Figure 4.2.1, right). The latter also offers the unique opportunity to examine coincident ocean circulation anomalies, as will be done later. In GLORYS12V1, upper ocean anomalies are cold and fresh to the south of Iceland, and warm and salty (although they are more patchy) to the south of the subpolar gyre, as obtained from CORA (product reference 4.2.1).

The CORA dataset is used to determine the extent at depth of upper ocean cold and fresh anomalies (Figure 4.2.2). By averaging those anomalies over a box centred on the anomalies of maximum amplitude (displayed in Figure 4.2.1), we notice that they have a signature reaching 1000 m depth, similar to what was already observed in 2016. Notwithstanding, temperature
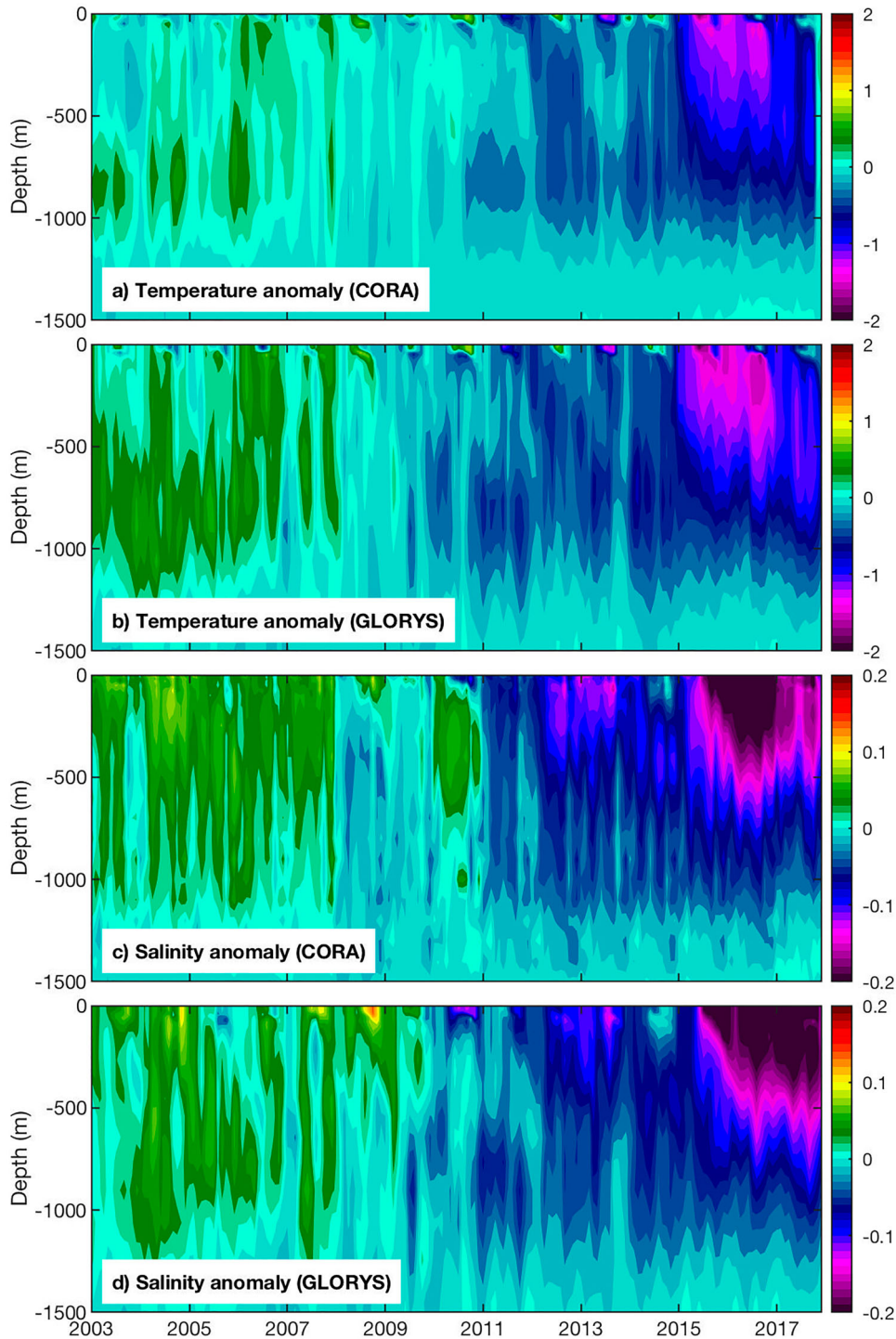

Figure 4.2.2. Depth-time diagram of temperature (in °C) and salinity (in psu₎) anomalies averaged over the control box (defined in Figure 4.2.1) from CORA (product reference 4.2.1) and GLORYS12V1 (product reference 4.2.2). The reference period for anomaly computation is the mean over 2003–2014.

anomalies in 2017 have weaker amplitude compared to those in 2016, while salinity anomalies have similar amplitude. This is also visible in depth-time diagram computed from GLORYS12V1 (Figure 4.2.2). As a consequence, cold and fresh anomalies detected in 2017 share similarities with those observed in 2016, except that they are located further to the north east, and that temperature signal has been attenuated.

Local anomalies in air-sea fluxes have the potential to drive upper-ocean anomalies, and we investigate their role in our region of interest in 2017, by computing net heat and freshwater fluxes from GLORYS12V1 over the white box displayed in Figure 4.2.1 (Figure 4.2.3, plain lines). As for previous variables, monthly anomalies are computed from the corresponding climatological seasonal cycles calculated over the period 2003–2014. In 2016 and 2017, heat flux anomalies are positive over the region of maximum cold anomalies, which suggests that 2017 upper ocean temperature anomalies have not been generated locally by anomalous atmospheric heat fluxes during 2017 winter. In addition, the fact that heat flux anomalies are positive in 2017 is consistent with a weakening of the negative ocean temperature anomalies, and suggests that air-sea interactions have had a damping influence on the cold anomalies of 2016. Freshwater flux anomalies

are weak on average in 2017, as they are negative in the first part of the year, and positive later. Figure 4.2.3 also suggests that those flux anomalies are very similar when averaged over a slightly bigger spatial box (dashed lines), which then includes the area of maximum amplitude cold and fresh anomalies in 2016. As a result, cold and fresh anomalies in 2017 have not been generated locally by anomalous air-sea fluxes, but result from pre-existing anomalies created elsewhere and advected into the area of interest (see Gourrion et al. 2018).

GLORYS12V1 also provides useful information about the ocean circulation. The region of maximum amplitude anomalies in 2017 lies in the north-eastern part of the cyclonic subpolar gyre, where the barotropic currents are oriented to the north-east (Figure 4.2.4). This is compatible with the north-east migration of the maximum amplitude anomalies from 2016 to 2017, as advected by the mean barotropic currents, and so confirms that the cold and fresh anomalies observed in 2017 are the continuation of those previously described in 2014, 2015 and 2016 (see Gourrion et al. 2018). Besides, anomalies in the barotropic streamfunction calculated every year as deviations from the 2003–2014 climatology. Results from Figure 4.2.5 suggest that the cyclonic subpolar gyre circulation is more intense over the last four years.
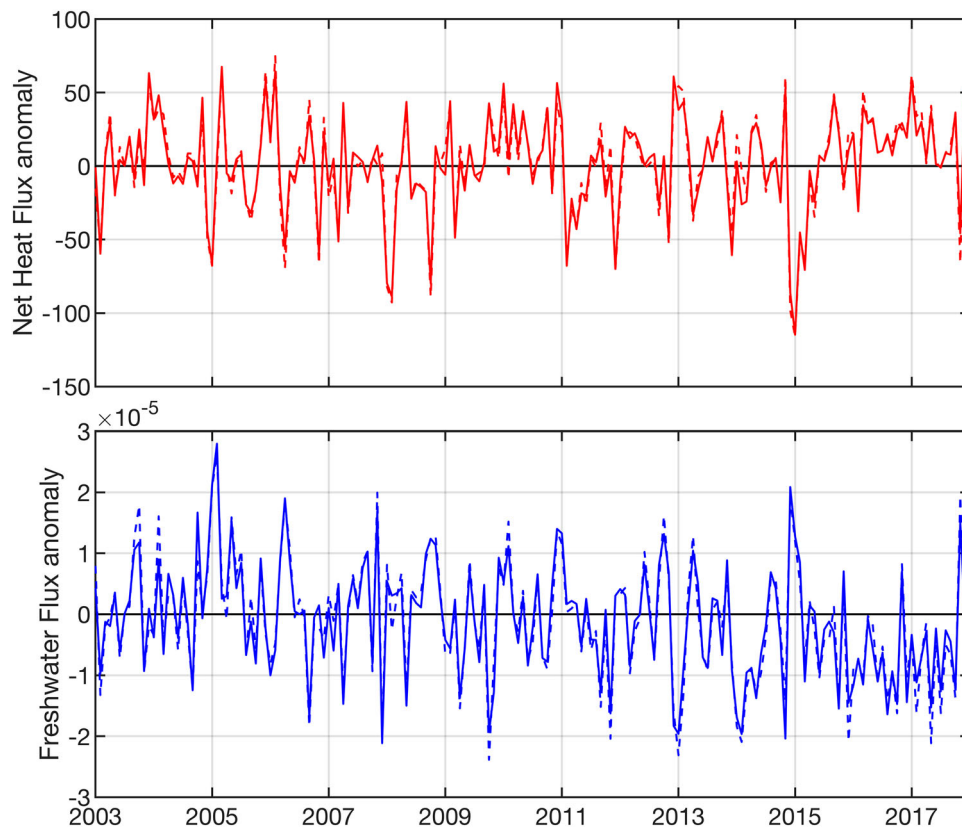

Figure 4.2.3. Net heat fluxes (in W/m^2) and freshwater fluxes (in kg/m^2/s) anomalies averaged over the control box (defined in Figure 4.2.1) from the GLORYS12V1 model (product reference 4.2.2). The fluxes are defined positive from the atmosphere to the ocean. The reference period for anomaly computation is the mean over 2003–2014.
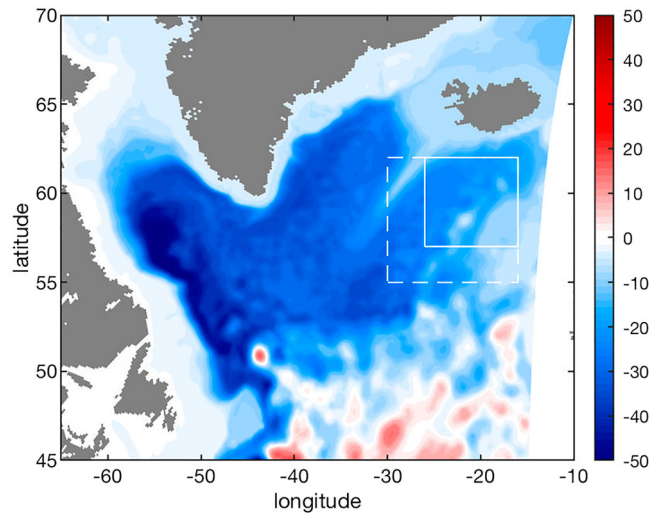
Figure 4.2.4. Mean barotropic streamfunction in 2017 from GLORYS12V1 (product reference 4.2.2). The white box with plain lines corresponds to the area used to compute depth-time anomalies in Figure 4.2.2. The white box with dashed lines represents the area of maximum amplitude cold and fresh anomalies in 2016 (see Gourrion et al. 2018).
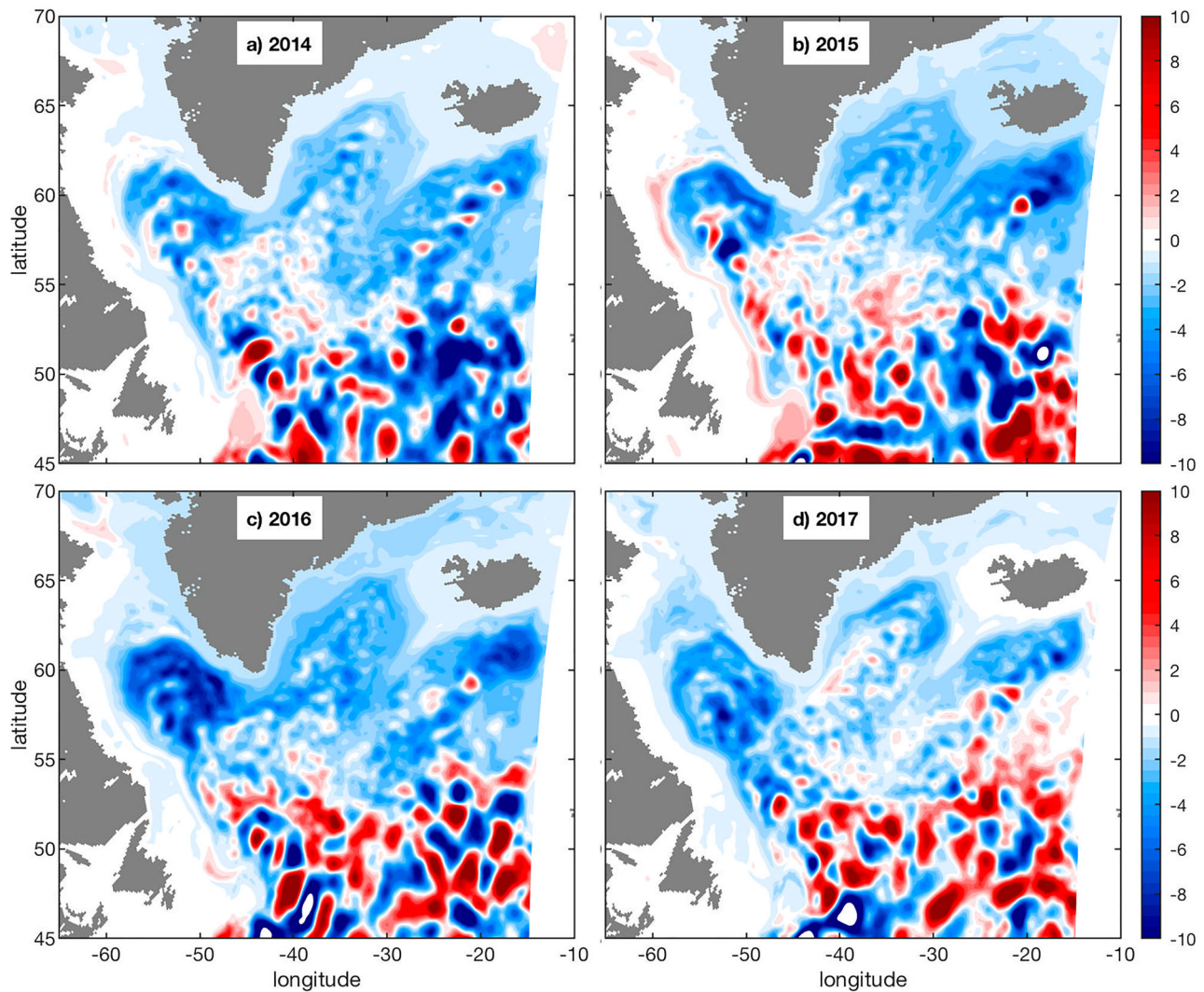

Figure 4.2.5. Barotropic streamfunction anomalies in 2014 (a), 2015 (b), 2016 (c) and 2017 (d) from GLORYS12V1 (product reference 4.2.2). The reference period for anomaly computation is the mean over 2003–2014.

Indeed, although anomalies in batrotropic circulation are very patchy to the south of 54N, which corresponds to the highly turbulent North Atlantic Current (this region is discussed below), they are overall negative to the north of 56N from 2014 to 2017. Previous studies underlined that intensifications of the subpolar gyre in the last 40 years have been associated with eastward migrations of the eastern boundary of the gyre (Flatau et al. 2003; Hátún et al. 2005; Deshayes and Frankignoul 2008), and that has actually been observed in 2016 through an eastward migration of 35.1 isohaline (Figure 4.2.3 in Gourrion et al. 2018). Hence, this suggests that the cold and fresh anomalies observed from 2014 to 2017 are the result of dynamical changes in the subpolar gyre, which drivers are discussed at length in Gourrion et al. (2018). Note that this is actually in agreement with the conclusions of Piecuch et al. (2017) although they only investigate anomalies in ocean heat content.

Figure 4.2.1 also highlights warm and salty anomalies observed to the south of the subpolar gyre during 2017. The yearly anomalies in barotropic streamfunction (Figure 4.2.5) are instrumental in speculating about their origin. Those anomalies are very patchy with alternating positive and negative patterns, which is not surprising as this is a highly turbulent region with intense mesoscale activity. Yet, there seems to be an overall intensification in the amplitude and occurrence of positive patterns from 2014 until 2017, which could reflect the interannual adjustment of the ocean to the positive North Atlantic Oscillation phase that began in 2014 (Barrier et al. 2014). Ultimately, this dynamic adjustment is expected to favour the northward penetration of warm and salty subtropical water masses, which could explain the observed warm and salty anomalies to the south of the subpolar gyre in 2017.

4.3. Anticyclonic Eddy Anomaly: impact on the boundary current and circulation in the western Mediterranean Sea

Authors: Eva Aguiar, Mélanie Juza, Baptiste Mourre, Ananda Pascual, Evan Mason, Aida Alvera-Azcárate, Joaquín Tintoré
Statement of main outcome: An intense anticyclonic eddy anomaly event was observed in fall-winter 2017 north of the island of Mallorca in the western Mediterranean Sea. Similar long-lived eddies were reported during 1998 and 2010. The eddy alters the general cyclonic circulation of the Balearic Sea and the regional water mass properties. In particular, glider data in 2017 showed an anomalous strong inflow through the Ibiza Channel of recent Atlantic Water. These changes significantly affect the heat, salt and nutrient distributions in the

area with implications for climate and primary production. The monitoring of these events is thus essential for both science and society in this area.

Products used:

Ref. No.	Product name and type	Documentation
4.3.1	SEALEVEL_MED_PHY_L4_REP_OBSERVATIONS_008_051 SEALEVEL_MED_PHY_L4_NRT_OBSERVATIONS_008_050 Sea level	PUM: http://marine.copernicus.eu/documents/PUM/CMEMS-SL-PUM-008-032-051.pdf QUID: http://marine.copernicus.eu/documents/QUID/CMEMS-SL-QUID-008-032-051.pdf
4.3.2	INSITU_MED_TS_REP_OBSERVATIONS_031_041 INSITU_MED_NRT_OBSERVATIONS_031_035 *In situ* TS data	PUM: http://marine.copernicus.eu/documents/PUM/CMEMS-INS-PUM-013.pdf QUID: http://marine.copernicus.eu/documents/QUID/CMEMS-INS-QUID-013-041.pdf http://marine.copernicus.eu/documents/QUID/CMEMS-INS-QUID-013-030-036.pdf

Mean flows, as part of the general circulation, are responsible for heat, salt and nutrient redistribution along our coasts, affecting climate and primary production. Their interactions with eddies produces exchanges of energy and momentum that can induce changes in the general ocean circulation (e.g. Kang and Curchitser 2015). Hence, it is essential to better understand the processes that favour eddy generation and their interaction with the mean flow. Previous theoretical studies have shown that instability processes associated with mean flows can lead to eddy generation and that these eddies, in turn, play an important role driving changes in the large-scale circulation (Holland and Lin 1975; Holland 1978; Hogg and Stommel 1985; Greatbatch 1987; Dengler et al. 2004; Marshall 2006).

In the southern part of the western Mediterranean Sea (Figure 4.3.1), the circulation in the Alboran Sea is mainly driven by the Atlantic Jet entering the basin at the Strait of Gibraltar (Parrilla and Kinder 1987; Viúdez and Haney 1997) bringing fresh Atlantic Water with salinity values around 36.5. In the northern part of the western Mediterranean, the circulation is characterised by a strong boundary current (the so-called Northern Current), which flows south-westward through the Balearic Sea, before splitting into two branches (Font et al. 1988): one deviating along the northern slope of the Balearic Islands forming the Balearic Current (Ruiz et al. 2009; Mason and Pascual 2013) and the other flowing southward through the Ibiza Channel (Pinot et al. 2002). This channel is often considered to be a choke point of meridional exchanges between the northern and southern basins (Heslop et al. 2012; Juza et al. 2013). The intense meso-scale activity
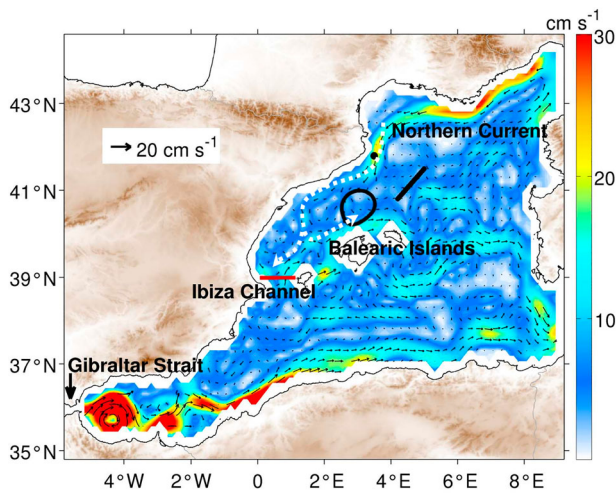
Figure 4.3.1. Mean geostrophic velocities from the product reference 4.3.1 over the period 1993–2012 in the western Mediterranean Sea. White arrows represent the main regional circulation pattern in the Balearic Sea. The black contour delimits the anticyclonic eddy anomaly influence-area where the climatological index is calculated (see text for more details). The black point denotes the deflection location of the Northern Current, the black line is the section where the transports are extracted to monitor that deviation, and the red line corresponds to the glider transect in the Ibiza Channel.

observed in the western Mediterranean Sea is associated with a small Rossby radius (approximately 10 km; Robinson et al. 2001). Moreover, the high number of available observations (Tintoré et al. 2013) converts this oceanic sub-basin into a small ocean laboratory where eddy-mean flow interactions can be monitored, detected, and studied.

In this study, we use sea level anomalies from the product reference 4.3.1 over the period 1993–2017. First, the eddy anomaly is characterised based on monthly mean sea surface height maps (adding the sea level anomaly maps to the mean dynamic topography; Rio et al. 2014) (Figure 4.3.2(a)). Then, the influence area of the anticyclonic eddy anomaly is defined (Figure 4.3.1) by calculating the mean contour of all the anticyclonic eddies detected by an eddy identification and tracking algorithm (Mason et al. 2014) north of Mallorca in 2017. A climatological index is derived from the spatially-averaged sea level over the influence area. This index is seasonal and low-pass filtered using a 30-day moving average to detect only long-lived eddy anomalies (Escudier et al. 2016) which are our focus in this study. The index enables us to define the anomalous character of the reported events (Figure 4.3.2(b)). Finally, the Northern Current is monitored at two locations as displayed in Figure 4.3.1 (Figure 4.3.2(c,d)). Geostrophic velocity time series have been computed from sea level anomalies using the equation for geostrophic equilibrium. Associated transport time

series have been calculated from the perpendicular component of the velocities projected onto the defined section. High-resolution glider data in the Ibiza Channel as part of the product reference 4.3.2 are also used over their available period 2011–2017 to indicate the presence or not of anomalous Atlantic Water of recent origin south of the position of the eddy anomaly.

The anticyclonic eddy anomaly first occurs during September 2017 and persists until February 2018, with a radius varying between 32 and 90 km (Figure 4.3.2 (a)). The climatological index (Figure 4.3.2(b)) confirms the formation and persistence of this eddy, and also highlights the two previous events in 1998 and 2010 (Pascual et al. 2002; Mason and Pascual 2013). The maxima of the index typically occur in the fall-winter months. They are higher in 1998 and 2017 (16 and 20 cm, respectively) compared to 2010 (12 cm), and correspond to long-lived anticyclonic eddies with durations of four to five months in 1998 and 2017, and two months in 2010. Other anticyclonic eddies in the same area as reported in the literature were not persistent enough (shorter than 30 days) to be detected by the index. These include for example, the eddies in fall 2001 (Rubio et al. 2009) and in April 2008 (Bouffard et al. 2010). The anticyclonic eddy analysed by Amores et al. (2013) in 2010 occurred in a different area further south. The 2007 anticyclonic eddy studied by Garreau et al. (2011) in this area was not stationary, and was migrating along the Catalan continental slope into the Balearic Sea during a period of two months and a half.

The time series of the zonal geostrophic component of the Northern Current off Cap de Begur from 1993 to 2017 clearly indicates the eastward deviation of the current downstream from Creus Cape (black point, Figure 4.3.1) during the years associated with the anticyclonic eddy anomaly (Figure 4.3.2(c)): 1998, 2010 and 2017. During these three events, the lags between the maxima of the northern current zonal component and of the climatological index suggest that the Northern Current deviates first. The anticyclonic eddy anomaly reaches its maximum two months later in 1998 and 2017 and one month later in 2010. The maximum transport monitored further south east is produced one week after the maximum of northern current deviation in 1998, and around two months later in the case of the 2010 and 2017 events (Figure 4.3.2(d)). These delays are associated with slightly different evolutions of the eddy anomaly.

Water mass transports are computed using data from gliders in the Ibiza Channel (as in Heslop et al. 2012) (section shown in Figure 4.3.1) starting from January 2011 (product reference 4.3.2). The time series of meridional geostrophic transports show an intensification of the northward flow associated with the entrance of
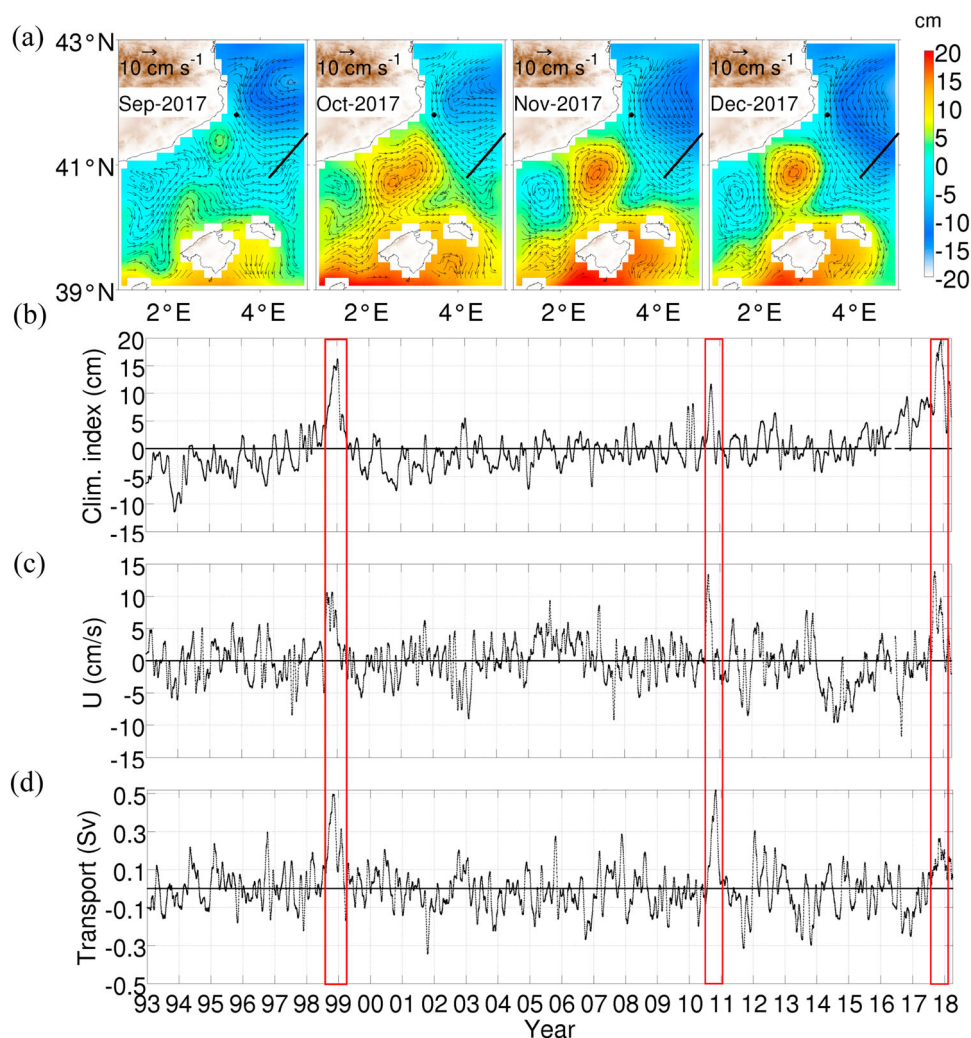
Figure 4.3.2. (a) Monthly sea surface height maps and associated geostrophic currents in September, October, November and December 2017 from the product reference 4.3.1, (b) Anticyclonic eddy anomaly climatological index, (c) Northern Current zonal component extracted at the point displayed in Figure 4.3.2(a), and (d) Geostrophic transport through the black section shown in Figure 4.3.2(a).

recent Atlantic Water into the Balearic Sea since the end of 2015 (Figure 4.3.3). Strong northward transports of this water mass are captured by the gliders, in particular in October 2016 (with values higher than 0.5 Sv) and in October 2017 when the maxima are reached (1 Sv). During these two autumnal glider missions, the inflow of recent Atlantic Water represents a large amount of the total transport (41–56% in 2016 and 48–59% in 2017) leading to an unusual and strong positive net inflow. During the anticyclonic eddy anomaly event of 1998, Pascual et al. (2002) also reported the anomalous presence of recent Atlantic Water in the Balearic Sea, which was explained by the possible weakening of the Northern Current that leads to the entrance of this water mass from the Alboran Sea through the Balearic channels.

The mechanisms involved in the process of the eddy generation are related to barotropic instabilities, due to horizontal shear perturbations of the ocean currents, and/or to baroclinic instabilities, induced by major changes in the stratification. Concretely, in this area, Pascual et al. (2002) argue that that the presence of warm water in the Balearic Sea interfered with the negative curl from the northwesterly Mistral wind shear downstream of the Pyrenees (Herbaut et al. 1997) could generate the strong eddy in fall 1998. Rubio et al. (2009) related the generation of the anticyclonic eddy in September 2001 to the separation of the coastal current downstream of Cape Creus that was induced by strong Mistral wind events. However, our empirical orthogonal function analysis of the winds in the northwestern Mediterranean Sea indicate that the zero curl-isoline on the northern edge of the eddy is a necessary but not a sufficient condition to produce the strong and long-term eddy (not shown). Consequently, we suggest a combination of several factors are responsible
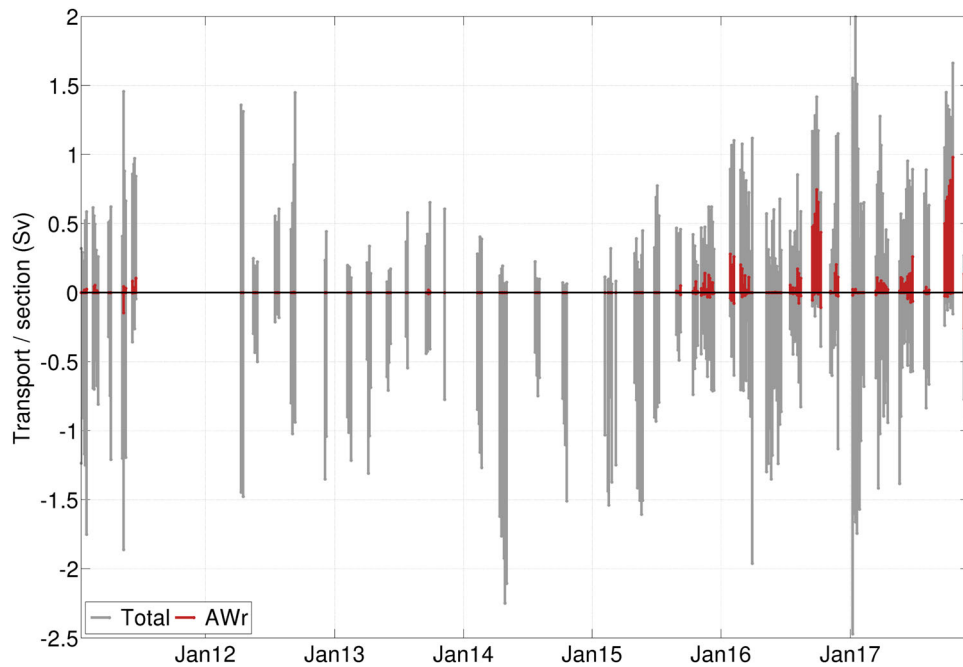
Figure 4.3.3. Northward (positive) and southward (negative) geostrophic transports in the Ibiza Channel integrated over the full water column (grey) and only considering recent Atlantic Water (red) obtained from product reference 4.3.2 during the glider missions from 2011 to 2017.

for the formation of the eddy event in 2017. These include the intense Mistral wind jets which could be responsible for the coastal detachment of the Northern Current. This in turn would favour the recent Atlantic Water coastal intrusion, and which would then gain negative vorticity due to the negative curl caused by wind in this area. High-resolution numerical model simulations will be used in the future to analyse this hypothesis and to improve our knowledge of the generation and permanence of these mesoscale eddies and their interaction with the mean flow.

Acknowledgements

4.4. Insights on 2017 Marine Heat Waves in the Mediterranean Sea

Authors: Nathaniel Bensoussan, Jacopo Chiggiato, Bruno Buongiorno Nardelli, Andrea Pisano, Joaquim Garrabou

Statement of main outcomes: Overall, 99.6% of Mediterranean Sea surface experienced at least one Marine Heat Wave event during year 2017. Strong Marine Heat Wave events occurred at regional scale, in June, July and August. Analysis of sea surface temperature from CMEMS revealed unprecedented Marine Heat Wave total duration in the north-western sub-region (up to 225 days locally in the north Catalan Sea) and exceptionally long single event (entire summer) in the Eastern Levantine Sea. In all sub-regions examined, a long-term increasing trend in annual Marine Heat Wave duration is obvious over the 1982–2017 period. As for previous significant Marine Heat Wave events (e.g. summer 2003), mass mortality events affected the benthic biota in the north-western Mediterranean Sea in 2017. Unprecedented large-scale and long-lasting benthic mucilaginous bloom also occurred in the north Catalan Sea. Analysis of *in situ* temperature time series in Scandola Marine Protected Area showed sub-surface intensification of Marine Heat Wave events (both in intensity and duration) which could not be inferred from surface data only. Enhancing the monitoring framework on physical and biological indicators is thus required for good evaluation of Marine Heat Wave and their impacts on Marine Coastal Biodiversity at local and regional scale.

Products used:

Ref. No.	Product name and type	Documentation
4.4.1	SST_MED_SST_L4_REP_ OBSERVATIONS_010_021 Sea surface temperature data	PUM: http://marine.copernicus. eu/documents/PUM/CMEMS-OSI-PUM-010-021-022.pdf QUID: http://marine.copernicus. eu/documents/QUID/

(Continued)

Ref. No.	Product name and type	Documentation
	Continued.	
4.4.2	T-MEDNet consolidated *in situ* temperature time series. www.t-mednet.org *In situ* temperature data	CMEMS-OSI-QUID-010-021-022.pdf www.t-mednet.org/T-Database

Ocean warming is associated to large changes in daily temperature distribution with increase in the occurrence of conditions presently perceived as extreme (known as climate intensification, see for instance section 2.2). Extreme warm sea temperature events observed around the world have been termed Marine Heat Waves. The interest in the characterisation of Marine Heat Waves has increased in the recent years (Hobday et al. 2016, 2018; Frölicher and Laufkötter 2018). For this study we applied the approach proposed by Hobday et al. (2016) in which Marine Heat Waves can be qualitatively defined as prolonged periods (five consecutive days or more) of anomalously warm water conditions when compared to the climatological mean (Hobday et al. 2016, 2018; see below for more information). Their mean duration and frequency have increased significantly over the past century, resulting in a 54% increase in sea surface annual Marine Heat Wave days globally (Oliver et al. 2018).

Increasing thermal stress is already having a range of important impacts on marine ecosystems and the goods and services they provide (Frölicher and Laufkötter 2018). Increasingly, mass mortality events on the benthic biota are reported in both tropical and temperate ecosystems (e.g. Garrabou et al. 2009; Wernberg et al. 2016; Hughes et al. 2017). In the north-western Mediterranean Sea, anomalously warm conditions during summers 1999, 2003 and 2006 have been associated to unprecedented mass mortality events, which have affected macrobenthic engineer species along tens to thousands of km of the coastline of Spain, France and Italy (Garrabou et al. 2009; Crisci et al. 2011; Marbà et al. 2015). Since 1999, several Marine Heat Waves and new mass mortality events occurred, particularly during recent years, as was the case during year 2017. However, the linkage between surface Marine Heat Wave metrics and biological impacts in subsurface marine habitats is not straightforward, firstly due to seasonal stratification and the influence of wind on coastal hydrodynamics (Bensoussan et al. 2010; Schaeffer and Roughan 2017). Furthermore, relating the thermal anomalies to biological observations might be seen as a highly context-dependent issue (e.g. species depth distribution, life cycle, differential response to thermal stress) and overall relies on biological responses to temperature (among other climatic and non-climatic stressors) which

are most often poorly constrained due to the lack of observation at the appropriate spatial and temporal scales.

In this context, we must note the importance of (i) a remote-sensing observing system to track the evolution of Marine Heat Wave events, (ii) sustained *in situ* observation over the long-term in marine coastal habitats, on both physical (temperature) and biological indicators, and (iii) a common analysis framework for comparison across temporal and geographic scales. Here, we analyse how such framework, when available, can allow good evaluation of Marine Heat Wave and better assessment of their ecological impacts. We provide insights on the 2017 Mediterranean marine heatwave, first with a view from the surface at regional and sub-regional scale in the Mediterranean Sea, considering CMEMS high resolution (4 km) satellite sea surface temperature (product reference 4.4.1). Then an inside view at local scale combining satellite and multi-year *in situ* data retrieved from T-MEDNet temperature series (product reference 4.4.2, see Section 3.6) recorded in a Marine Protected Area where biological impacts have been observed.

Identification and classification of MHW events
Marine heat waves have mostly been studied from the analysis of long-term satellite data sets over climatic time scale (30 years). Two different approaches can be conducted for their identification with respect to the long-term climatological mean for each location and day of year (Hobday et al. 2016) or with respect to an elevated temperature threshold (e.g. species specific thermotolerance threshold or upper percentiles of site temperatures, Marbà et al. 2015; Galli et al. 2017). While the later approach focus on extreme hot events, the former allows identification of strong anomalies (extreme warm events) throughout the entire annual cycle, which can prove relevant for a range of biological impacts, considering different biological processes and life stages of life cycle of marine organisms.

Relying on the definition of Hobday et al. (2016), Marine Heat Wave events, are identified as discrete and prolonged period of time (at least five consecutive days) with temperature above the site/day climatological 90th percentile. The method allows comparison of events duration and intensity across time and space from sites with different thermal regimes and we first analysed satellite sea surface temperature daily data from CMEMS (product reference 4.4.1). For each pixel, climatological mean and 90th percentiles were calculated over the 1982–2011 period, using a 11-day centred window and additional smoothing on the climatology with a 30-day running mean (Hobday et al. 2016). The following primary metrics were used to

describe the events: duration, maximum daily temperature (T_{max}), maximum intensity ($i_{max} = T_{max} - $ climatological mean), mean intensity and cumulative intensity ($i_{cum} = $ mean intensity $\times$ duration, in C° day). Total duration and total cumulative intensity were also calculated at different time scales, by aggregating duration or i_{cum} by month, season or year. The spatial extent of Marine Heat Wave events was computed at monthly and seasonal time scale from the satellite data of year 2017. In order to analyse the long-term trends at sub-regional scale, average daily temperature time series were calculated over three boxes shown in Figure 4.4.1(a). The Marine Heat Wave analysis was conducted over these spatially averaged time-series.

Classification of Marine Heat Wave events can be conducted by scaling their maximum intensity with respect to the degree to which temperature exceed the local climatology (Hobday et al. 2018). Categories of Marine Heat Waves are based on multiples of the value represented by the local difference between the climatological mean and the climatological 90th percentile. Multiples of this local difference describe different categories of Marine Heat Waves: defined as moderate (1–2×, Category I), strong (2–3×, Category II), severe (3–4×, Category III), and extreme (>4×, Category IV), based on their maximum intensity (i_{max}) at each point in space (Hobday et al. 2018).

The method is also suited for *in situ* time series (Hobday et al. 2016). Long-term (14 years) continuous (hourly) temperature time series has been acquired using vertical array of data loggers set at standard depth levels (every 5 m, between 5 and 40 m depth) in the no take zone of the Réserve Naturelle de Scandola (Parc Régional de Corse, France). Such oceanographic time series was obtained in the frame of sustained T-MEDNet network monitoring effort conducted jointly with Mediterranean Marine Protected Areas (see Section 3.6). The climatological mean and 90th percentile, were calculated for each depth over all daily averaged data available over the 2004–2016 period.

The 2017 Mediterranean MHW over the satellite record
Statistics computed from the CMEMS sea surface temperature data over the Mediterranean Sea show that 2017 was the sixth warmest year (mean SST = 19.86°C, anomaly + 0.65°C), and warmest spring on average since 1982 (Figure 4.4.1). During this warm year, significant Marine Heat Wave events occurred at regional scale in June, July and August (Figure 4.4.2) and at local to sub-regional scale across all four seasons, resulting in elevated total number of Marine Heat Wave days (Figure 4.4.2(a)). Overall, 99.6% of Mediterranean Sea surface experienced at least one Marine Heat Wave event and significant variability was evidenced at the various space scales (Figure 4.4.2). Marine Heat Wave days
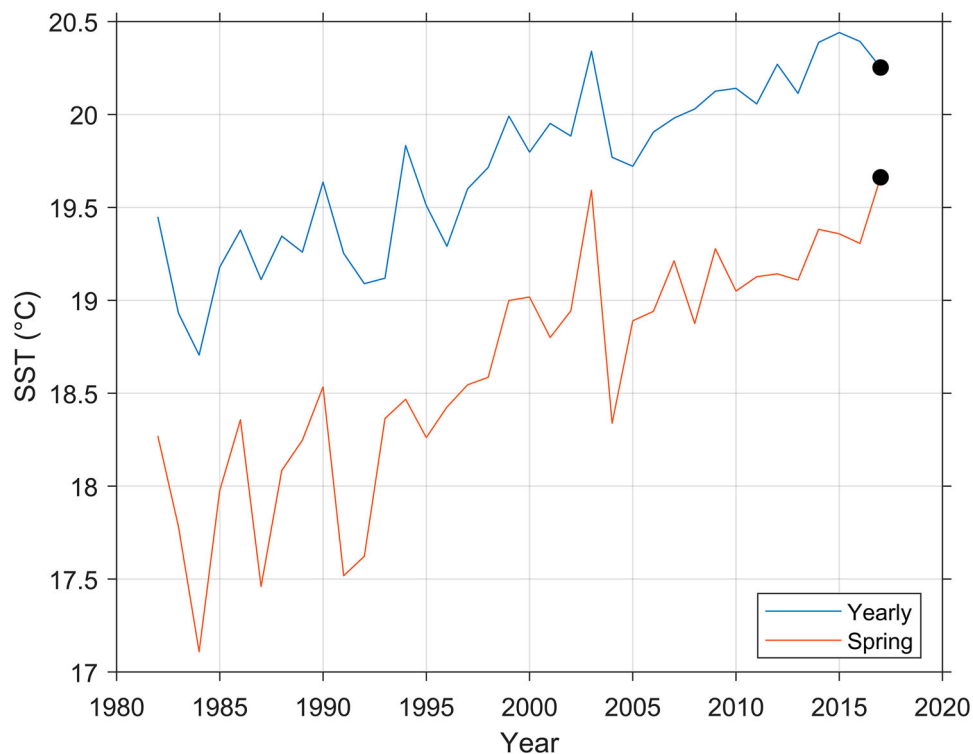

Figure 4.4.1. Time series of yearly and Spring (April, May and June) Mediterranean Sea surface temperature (SST) over the period 1982–2017. The black dots show results for year 2017. Reference number of the product used: 4.4.1.
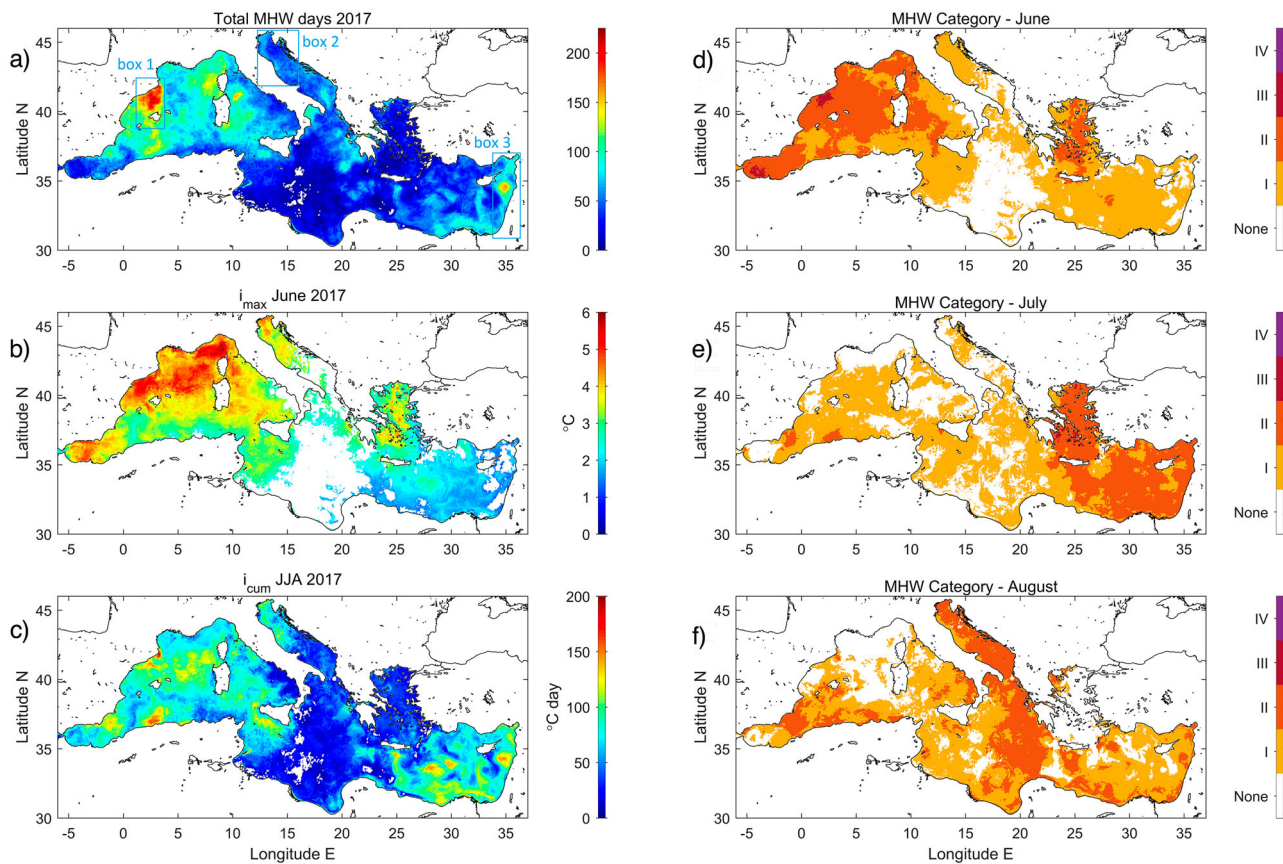
Figure 4.4.2. Maps showing different MHW metrics (left) and categorisation of MHW events by month (right). (a) Annual number of Marine Heat wave days in 2017, (b) MHW maximum intensity (i_{max}) during June 2017, (c) June to August 2017 MHW cumulative intensity (i_{cum}). (d, e, f) Highest MHW category by month, during the regional MHW events of June, July and August. Locations with no heatwave days are blanked out. Reference number of the product used: 4.4.1. Location of the three boxes considered for sub-regional analysis and of the Scandola Marine protected Area are shown in panel a.

were on average twice higher in the western than in the eastern basin (88 ± 31 vs. 43 ± 25 days, mean $\pm$ std). Total duration exceeded 6 months (max 225 days) in the northern Catalan-Balearic Sea and 4 months over 13% of the western basin surface, mainly from Algerian to Catalan Sea and from Sardinia to Ligurian Sea (Figure 4.4.2(a)). Similar amount of Marine Heat Wave days were not observed in the eastern basin, except locally in the eastern Levantine Sea.

A significant event at regional scale took place in June 2017, with a single long-lasting Marine Heat Wave (depending on the location, up to 20–25 days) in the western Mediterranean Sea. Figure 4.4.2(b) shows the very large spatial extent and elevated peak anomaly during this event. Maximum daily sea surface temperature anomalies up to 6°C were detected north of the Balearic-Corsica front but, in general, 4°C anomaly was reached in most part of the sub-basin and in the northernmost part of the eastern Mediterranean. We also analyse the cumulative intensity at the seasonal scale (here grouping June, July and August in order to account for different timing of observed events in the basin during

the warm season). Combining both duration and intensity, Figure 4.4.2(c) shows overall elevated thermal stress in the western basin and adjacent Sicily channel, in the Levantine and northern Adriatic sub-basins. Significant spatial variability was observed with local extremes along the North Catalan coast, in the Algerian and Levantine seas which could be associated to seasonal or permanent circulation features, like eddy intensification in the Balearic-Catalan Sea (see Section 4.3) and permanent gyres (e.g. Ierapetra and Cyprus gyres), locally exacerbating the regional warm signal. It should be noted, on the other hand, that elevated i_{max} in the Aegean Sea (Figure 4.4.2(b)), when combined with locally short duration of the Marine Heat Wave, leads to a low cumulated intensity (Figure 4.4.2(c)). This example is suggestive of the relevance of considering both scores together with maximal temperature when interpreting Marine Heat Wave intensity. Adoption of a Marine Heat Wave scale was also found useful to communicate and raise scientific and public awareness on these extreme warm events (Hobday et al. 2018). Under this scheme, peak intensity of category II (strong)

took place over most of the western Mediterranean in June, the Aegean-Levantine basin in July and the Adriatic-Ionian in August (Figure 4.4.2(d,e,f)).

Spatial and temporal variability of MHW events
We further focus our analysis to the Catalan-Balearic, northern Adriatic and eastern Levantine Sea, where relatively long event of category II occurred (Figure 4.4.3). In the north Catalan-Balearic area (Box 1, Figure 4.4.3(a)), sea surface temperature was overall warmer than average except in September. A sequence of eight Marine Heat Wave events took place between January and December, among which, the strong events of April and June (T_{max} 15 vs. 25°C) and the moderate but notably long fall event (78 days by the end of year, $i_{cum} = 113$°C day). This long event can be related to the intense anticyclonic eddy anomaly detected in fall-winter 2017 north of Mallorca Island, which blocked the general cyclonic circulation and enhanced the prevalence of Marine Heat Wave over the area (see Section 4.3).

In the warmer eastern Levantine Sea (Box 2, Figure 4.4.3 (b)), positive sea surface temperature anomaly prevailed from March to December and a notably long summer single event (97 days) occurred from 27 June to 1 October ($T_{max} = 29$°C in July, $i_{cum} = 133$ C°day). In the northern

Adriatic, six Marine Heat Wave events took place between late March and August (Figure 4.4.3(c)), out of which four were synchronous with events in the western Mediterranean (Box 1). Elevated T_{max} (28°C) was observed during the strong Marine Heat Wave event from 2 to 10 August.

Further analysis of the 36 years of satellite data attest of the unprecedented duration of the 2017 events (Figure 4.4.3(d,e,f)). In the western Mediterranean Sea (Box 1, Figure 4.4.3(d)), 2017 was the year with the highest annual number of Marine Heat Wave days since 1982. They were observed throughout the four seasons, as in 2015, but with only few days in summer compared to the years 2003, 2006 and 2015 (7 vs. 36–60 days respectively). Also, summer long event was evidenced in the eastern Levantine Sea for the second time since 1982 (as in 2012, Figure 4.4.3(e)). Interestingly in all areas, long-term increasing trend in Marine Heat Wave total duration (yearly) is obvious and longest total duration (>170 days per year) occurred during the past decade (2010 in the Levantine, 2014 in the Adriatic and 2017 in the Western). Splitting the observation period in two highlights contrasted Marine Heat Wave regimes. Since late nineties, Marine Heat Wave events have occurred every year in at least one season (except in 2005 in the N-Adriatic) and they last longer. This regime shift attest of the
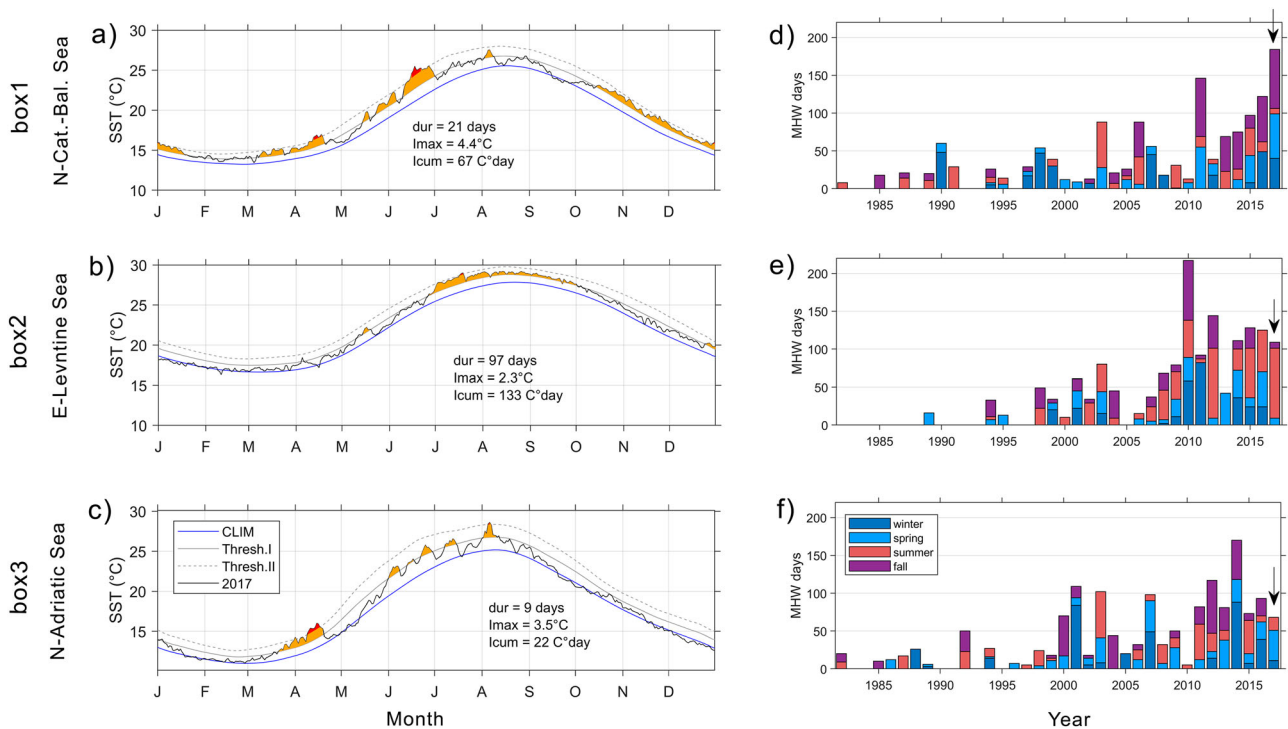

Figure 4.4.3. (a–c) Spatially averaged time series of daily sea surface temperature for the three boxes shown in Figure 4.4.2(a). The climatological mean (blue curve) and thresholds used to define MHW categories from moderate (dotted grey line) to strong (grey line) were calculated over the 1982–2011 period. MHW events are identified and filled with colours by categories (orange = moderate, red = strong). (d–f) Time series of the total number of marine heatwave days by year and by season since 1982, the arrow indicates the 2017 data. Reference number of the product used: 4.4.1.

important increase in the prevalence of extreme warm (upper decile) daily temperature under current warming trends (see Figure 4.4.1). Our results are in agreement with analysis conducted at global scale, which have been related to the acceleration of warming trends (Oliver et al. 2018).

Observed biological impacts
In 2017, concomitant with the thermal context, a range of biological impacts were observed. Firstly an unprecedented large-scale and long-lasting mucilaginous benthic algal bloom occurred along the French and Spanish coast of the northern Catalan Sea from spring till early fall (Figure 4.4.4). The mucilaginous algal blooms, mainly the Ectocarpal *Acinetospora crinita*, could cover all benthic habitats from 10 m down to 30 m depth. The cover of thick layers of mucilaginous algae dramatically affected even gorgonians which grow arborescent colonies up to 1 m in height depending on the species (Figure 4.4.4(b)). Subsequently, mass mortality on gorgonian species occurred in late Summer and Fall 2017 (mainly the red and white gorgonian *Paramuricea clavata* and *Eunicella singularis*, respectively). While in other areas of the north-western Mediterranean Sea mortality of gorgonians as well as other macrobenthic biota was observed, also in late summer. For instance, at the

Réserve Naturelle de Scandola (Corsica) the yellow gorgonian *Eunicella cavolini* and several sponges species (*Spongia* spp. *Petrosia ficiformis*, *Ircina* spp.) dwelling between 10 and 25 m depth suffered from moderate to severe mortality impacts.

Surface and subsurface MHW in nearshore coastal waters (Scandola Marine Protected Area)
Proper knowledge on changes in environmental conditions, including marine heat waves, is needed to better assess potential impacts on ecosystem structure and function. Owing to the limited availability of long *in situ* data sets, it is not clear how accurate information can be obtained in the near-shore using satellite data (but see section 3.6). As satellite are restricted to the surface, *in situ* observations are required to cope with the important depth variability occurring during the seasonal stratification period, typically from April–May to Fall convective events. For instance the summer 2003 mega atmospheric heatwave over Europe was associated to extreme sea surface temperature in the central Ligurian Sea in August while cold anomaly prevailed below 10 m depth (Sparnocchia et al. 2006). Here we conduct further analysis from satellite data retrieved at local scale and *in situ* measurements conducted along the depth gradient from 5 to 40 m depth.
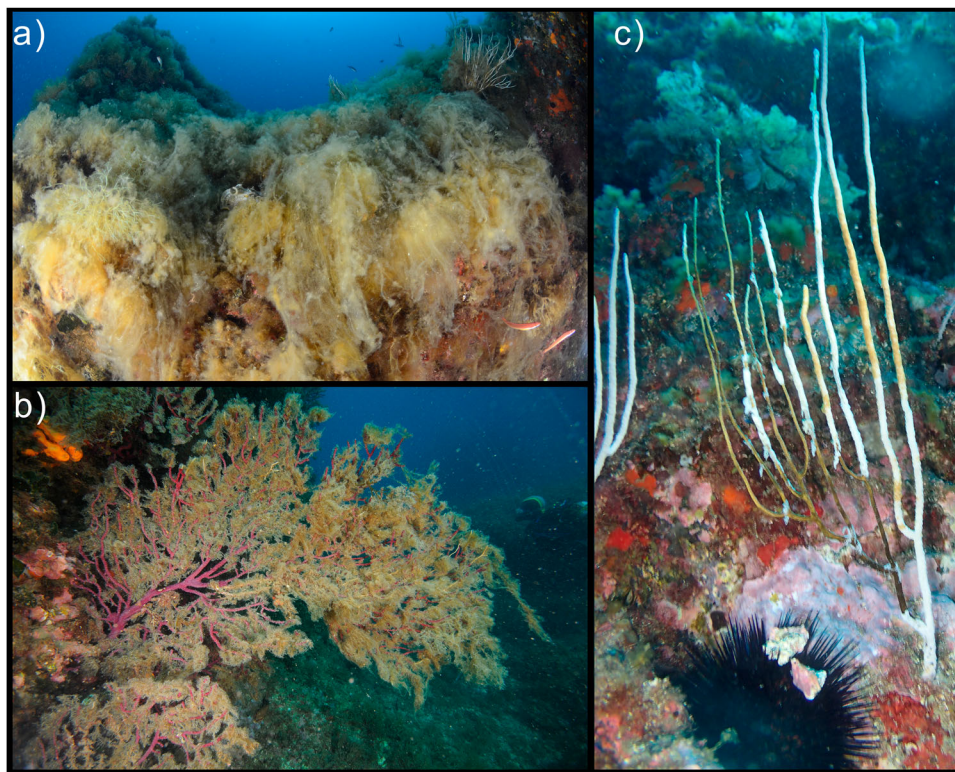

Figure 4.4.4. (a–b) Mucilaginous blooms covering different benthic assemblages (rocky infralittoral habitats and coralligenous) and species (the red gorgonian *Paramuricea clavata*) along the Catalan coast between Spring and Fall 2017, and (c) white gorgonian *Eunicella singularis* displaying signs of very recent necrosis (white tissue peeling off from the axis leaving denuded axis).

Local satellite data were retrieved from the closest pixel to the monitoring site considering the common years of data available (2004–2017). From the statistical analysis of the local satellite and *in situ$_{5m}$* multi-year matchup database, high agreement was evidenced for Scandola, both in terms of correlation (0.988), bias (0.17°C) and round

mean square difference (0.7°C). These results are in agreement with results shown in section 3.6 from analysis conducted in several Marine Protected Areas member of the T-MEDNet monitoring network. Figure 4.4.5(a,b) shows results from the Marine Heat Wave analysis conducted from June to October 2017 on the satellite and *in situ$_{5m}$*
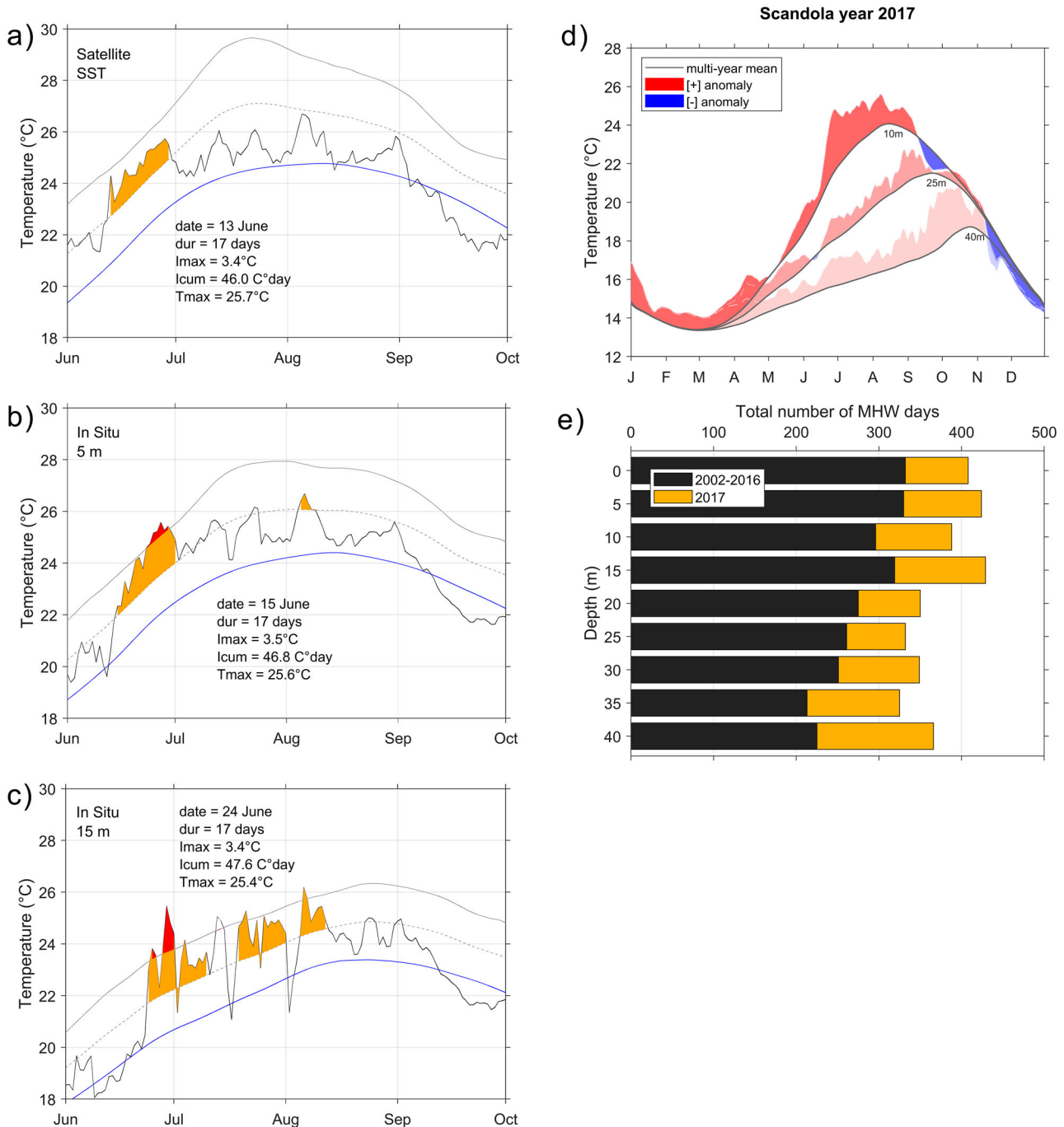

Figure 4.4.5. Information on MHW events in Scandola Marine Protected Area nearshore waters (Parc Régional de Corse, France). (a–c) Time series of daily satellite sea surface temperature and *in situ* temperature measured at 5 and 15 m depth. Climatology (blue line) and MHW thresholds (grey lines) calculated over the period 2004–2016 are also shown. MHW events are identified and filled with colours by categories (orange = moderate, red = strong). (d) *In situ* temperature anomalies relative to the multi-year mean at 10, 25 and 40 m depth. (e) Total number of MHW days from satellite (0 m) and *in situ* data (5–40 m depth). Reference number of the products used: 4.4.1 and 4.4.2.

data. The climatological mean and 90th percentile were slightly higher for the surface when compared to *in situ$_{5m}$* (by typically <1°C). Also some differences arose regarding the number and category of detected events. Considering the strong June event however, high agreement was evidenced with negligible differences in terms of duration (17 days), i_{max} (3.5°C) and i_{cum} (46 C°day). This event reached deeper marine habitats, in fact, down to 15 m depth, with a time lag of ca. 10 days (Figure 4.4.5 (c)) while warm pulses occurred deeper (shorter than five days, not shown). Overall, over these 4 months, total number of Marine Heat Wave days was higher at 15 m (38 days) depth compared to 5 m (22 days) and surface (17 days), which can be seen as subsurface intensification of Marine Heat Wave, and largely depends on the seasonal stratification dynamics (Bensoussan et al. 2010; Schaeffer and Roughan 2017). Such anomalies were observed in late September and October at 40 m depth, as vertical mixing occurred and propagated the warm signal to depth (Figure 4.4.5(d)). Meanwhile, one might notice that cold to neutral anomaly prevailed at the surface.

Considering the 2004–2017 period (Figure 4.4.5(e)), elevate total number of Marine Heat Wave days was calculated over the depth range examined (325–429 days, maximum in the upper 15 m) from which a significant fraction occurred in year 2017. Interestingly, we can note the fair agreement between Marine Heat Wave days calculated from the local satellite and *in situ$_{5m}$* data (0 vs. 5 m depth difference < 10%). Together with the high agreement evidenced for the June 2017 event, these results open new and interesting perspectives for satellite based analysis of Marine Heat Waves over climatic time scales (back to 1982) in the coastal zone.

Understanding the biological responses to warming and how changes in the thermal environment are driving changes in the marine biota is an active research field (see for instance Section 3.2 for fishes and Section 3.6 for the benthic biota). As introduced earlier in the section, different approaches might be used complementarily in order to assess such responses/impacts. In fact, metrics used to characterise Marine Heat Wave events (duration, i_{max}, i_{cum}) could usefully be adapted to quantify more largely the positive anomalies (Figure 4.4.5(d)) occurring over given periods of interest, from days to month(s) and thus integrate the strong dynamics and variability modes of subsurface conditions (e.g. inertial oscillations, Bensoussan et al. 2010).

Mass mortality events are particularly strong disturbances affecting benthic habitats since they affect a wide range of macrobenthic species over large geographical scales (tens to thousands of kilometres of coastlines) as was the case in the 2017. However, mass mortality is only one of the impacts of climate change in the benthic coastal habitats. Overall climate change is severely modifying the structure and functions of marine coastal ecosystems to new configurations, which might no longer support the goods and services to people. In this context, we must note the importance of sustained observation effort on sub-surface temperature and biological indicators for comparison across temporal and geographic scales to enhance our understanding of ongoing changes and our forecasting abilities.

Acknowledgements

4.5. Reversal of the Northern Ionian circulation in 2017

Authors: Giulio Notarstefano**,** Milena Menna, Jean-François Legeais

Statement of main outcome: A reversal of the surface circulation in the Northern Ionian Sea was observed in 2017. This changing of the circulation pattern seems to be periodic and it is critical for the redistribution of salt between the Eastern Mediterranean and the Northern Ionian – Southern Adriatic Seas. The periodicity of this reversal occurs on a quasi-decadal scale and, when it happens, it constitutes a special event because this phenomenon can deeply impact on the deep water formation sites and hence can affect the water masses distribution between the different Mediterranean sub-basins. Moreover, the shift of circulation mode can contribute to trigger abrupt events like the Eastern Mediterranean Transient that impacted the Mediterranean regional oceanography, shifting the deep water formation site from the South Adriatic to the Aegean/Cretan Sea.

Products used:

Ref. No.	Product name and type	Documentation
4.5.1	SEALEVEL_MED_PHY_L4_NRT_ OBSERVATIONS_008_050 SEALEVEL_MED_PHY_L4_REP_ OBSERVATIONS_008_051 Remote sensing	PUM: http://marine.copernicus. eu/documents/PUM/CMEMS-SL-PUM-008-032-051.pdf QUID: http://marine.copernicus. eu/documents/QUID/CMEMS-SL-QUID-008-032-051.pdf

The surface circulation in the Northern Ionian Sea is mainly influenced by quasi-decadal reversal of the Northern Ionian Gyre over the last 40 years even though a real periodicity is still not clear (Pinardi et al. 2015). This circulation system (Gačić et al. 2011; Pinardi et al. 2015; Simoncelli et al. 2016) is evident also at intermediate depth and strongly impacts on the distribution of salinity in the South Adriatic Sea (Gačić et al. 2010, 2011; Kokkini et al. 2017). Thermohaline changes in the South Adriatic Sea are of considerable importance for the Mediterranean Sea climate due to the deep water convection and dense water formation that takes place in this area (Gačić et al. 2014; Simoncelli et al. 2017). The anticyclonic circulation mode is associated with the northward deflection of the Atlantic Ionian Stream that brings fresh Atlantic water in the Northern Ionian and South Adriatic seas; consequently, the intrusion of the Levantine salty water in the South Adriatic is reduced (Figure 4.5.1, left panel). During the cyclonic circulation mode this water mass exchange is strongly modified (Figure 4.5.1, right panel): the eastward intense flow of the Atlantic Ionian Stream brings fresh Atlantic water in the Cretan Passage and, at the same time, more saline waters at the intermediate level from the Levantine basin flow into the Northern Ionian and South Adriatic seas. Currently, four reversals are documented by numerical and experimental studies: two of them, from cyclonic to anticyclonic mode, took place around 1987–1988 (Demirov and Pinardi 2002) and in 2006 (Gačić et al.

2010; Bessiéres et al. 2013); other two, from anticyclonic to cyclonic mode, occurred in 1997 (Pujol and Larnicol 2005) and in 2011 (Bessiéres et al. 2013; Gačić et al. 2014), respectively.

Satellite altimetry, available since 1993, is a powerful product to observe the ocean variability at global and regional level (Legeais et al. 2016, 2017), since it provides sea level anomaly measurements continuously in time. In particular, the absolute dynamic topography, obtained by adding the mean dynamic topography (Rio et al. 2014) to the sea level anomaly, and the related absolute geostrophic velocities, were used to define the temporal phases of cyclonic/anticyclonic Northern Ionian Gyre. The relative vorticity field (ζ) of the absolute geostrophic velocities was evaluated as the vertical component of the velocity field curl:

$$\zeta = \frac{\partial vg}{\partial x} - \frac{\partial ug}{\partial y}$$

where ug and vg are the components of the absolute geostrophic velocities.

Monthly means of the geostrophic current vorticity fields were spatially averaged in the region of northern Ionian Sea (white rectangles in Figure 4.5.1) and the time series of this parameter (blue line in Figure 4.5.2) was filtered using a 13-month moving average (red line in Figure 4.5.2), in order to remove the seasonal and intra-annual variations and focus on the interannual fluctuations. The geographical area of the spatial vorticity
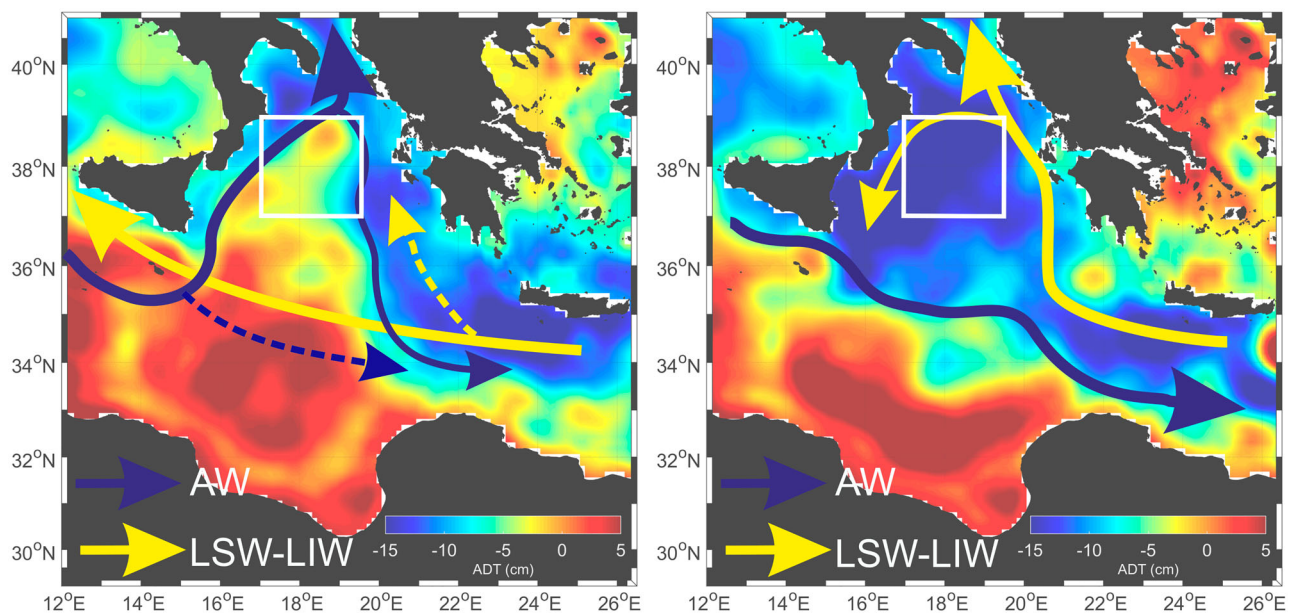

Figure 4.5.1. Summary of the water masses distribution in the Ionian Sea during the anticyclonic (left) and cyclonic (right) modes of the Northern Ionian Gyre (adapted from Lavigne et al. 2018), superimposed with the yearly maps of absolute dynamic topography (colours) in 1996 and 1999, respectively. The acronyms in the figure are: Atlantic Water (AW); Levantine Surface Water (LSW); Levantine intermediate water (LIW). White squares show the area used to estimate the time series of Figure 4.5.2. The reference number of the products used is 4.5.1: SEALEVEL_MED_PHY_L4_NRT_OBSERVATIONS_008_050, SEALEVEL_MED_PHY_L4_REP_OBSERVATIONS_008_051.
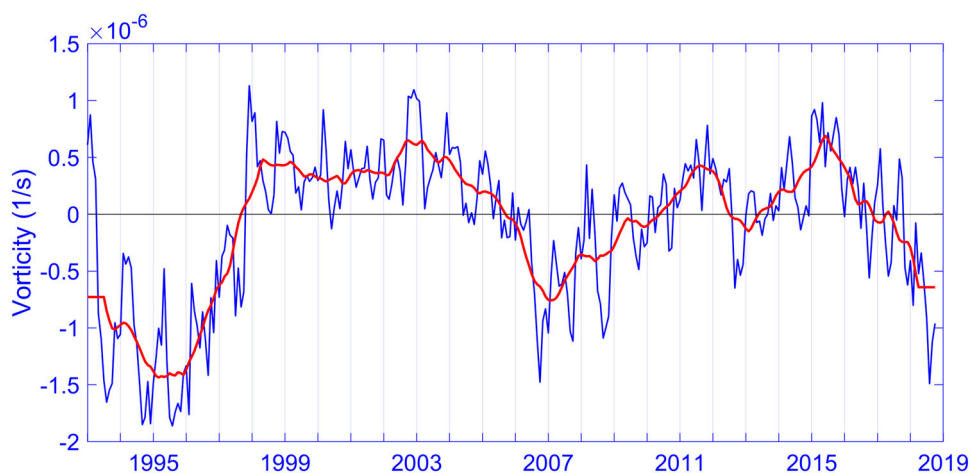
Figure 4.5.2. Time series of the spatially averaged current vorticity (blue line) and low-pass filtered (13 months) current vorticity (red line) computed in the Northern Ionian Sea (37–39°N; 17–19.5°E), during the period January 1993–November 2018. The temporal phases of the Northern Ionian Gyre are defined cyclonic when the vorticity field is positive and anticyclonic when the vorticity field is negative. Reference number of the product used: 4.5.1.

mean (37–39°N and 17–19.5°E: white rectangles in Figure 4.5.1) was selected according to the shape of the Northern Ionian Gyre (a similar choice was made in Shabrang et al. 2016). During the anticyclonic mode (Figure 4.5.1(a)) the Northern Ionian Gyre is located in the centre of the basin and is surrounded by recurrent mesoscale cyclonic eddies (e.g. along the eastern coast of Sicily, at the entrance of the Gulf of Taranto, along the eastern Ionian flanks), whereas during the cyclonic mode the whole northern Ionian Sea is involved in the counterclockwise circulation (Figure 4.5.1(b)) and the northern Ionian meander moves very close to the coasts. In order to identify the interannual variability of the Northern Ionian Gyre vorticity field, avoiding contaminations by the mesoscale structures located along the edges of the basin-scale meander, we focus on the area statistically less influenced by the mesoscale activity.

The vorticity field associated with the surface geostrophic circulation in the Northern Ionian Gyre is positive/negative during cyclonic/anticyclonic phases (Figure 4.5.2). Time series of the current vorticity shows that seasonal oscillations (blue line) do not influence the decadal variability and the reversals of Northern Ionian Gyre. Even Poulain et al. (2012) shows that the basin wide circulation in the Northern Ionian Sea remains invariant with the seasons, whereas a significant seasonality is evident in the central Ionian related to the Atlantic-Ionian Stream variations.

The inversion to Northern Ionian Gyre cyclonic mode in 1997 (Figure 4.5.2) is widely shared in literature (Pujol and Larnicol 2005; Bessiéres et al. 2013; Gačić et al. 2014; Pinardi et al. 2015). On the other hand, the inversion to anticyclonic mode in 2006 is still a controversial aspect.

It is supported by altimetry data (Gačić et al. 2014; see also Figure 4.5.2) and ocean state indices (Bessiéres et al. 2013; Reale et al. 2017), but not sustained by the MEDREA reanalysis products that document only a weakening of the cyclonic circulation in the period 2006–2016 (Simoncelli et al. 2014; Simoncelli et al. 2017). As pointed out by Bessiéres et al. (2013), there are many intermediate states between the two main circulation modes, during which transition phases exist and strengthening or weakening of the main modes can be observed. However, they also argue that the weak anticyclonic phase between 2006 and 2011 cannot be considered a temporary inversion or a weakening of the cyclonic circulation mode, since it lasted almost five years. In 2011, altimetry data show another reversal of Northern Ionian Gyre to cyclonic mode, prematurely and temporary interrupted between May 2012 and March 2013 due to the climatic variability induced by the severe winter 2012 which caused the formation of very dense Adriatic waters, flooding Ionian flanks in May and inverting the bottom pressure gradient (Gačić et al. 2014).

The mean maps of absolute dynamic topography and absolute geostrophic velocities show a new weakening of the Northern Ionian Gyre cyclonic mode in 2016 (Figure 4.5.2; Figure 4.5.3(a,b)). The anticyclonic meander located in the Southern Ionian Sea (south of 36°N; Figure 4.5.3(a)) protrudes northward (Figure 4.5.3(b)), promoting the gradual break-up of the sub-basin scale cyclone. Then, in the first part of 2017, the sea level in the centre of the northern Ionian becomes slightly higher than the flanks (Figure 4.5.3(c)) and finally, in the second part of 2017, the anticyclonic circulation is
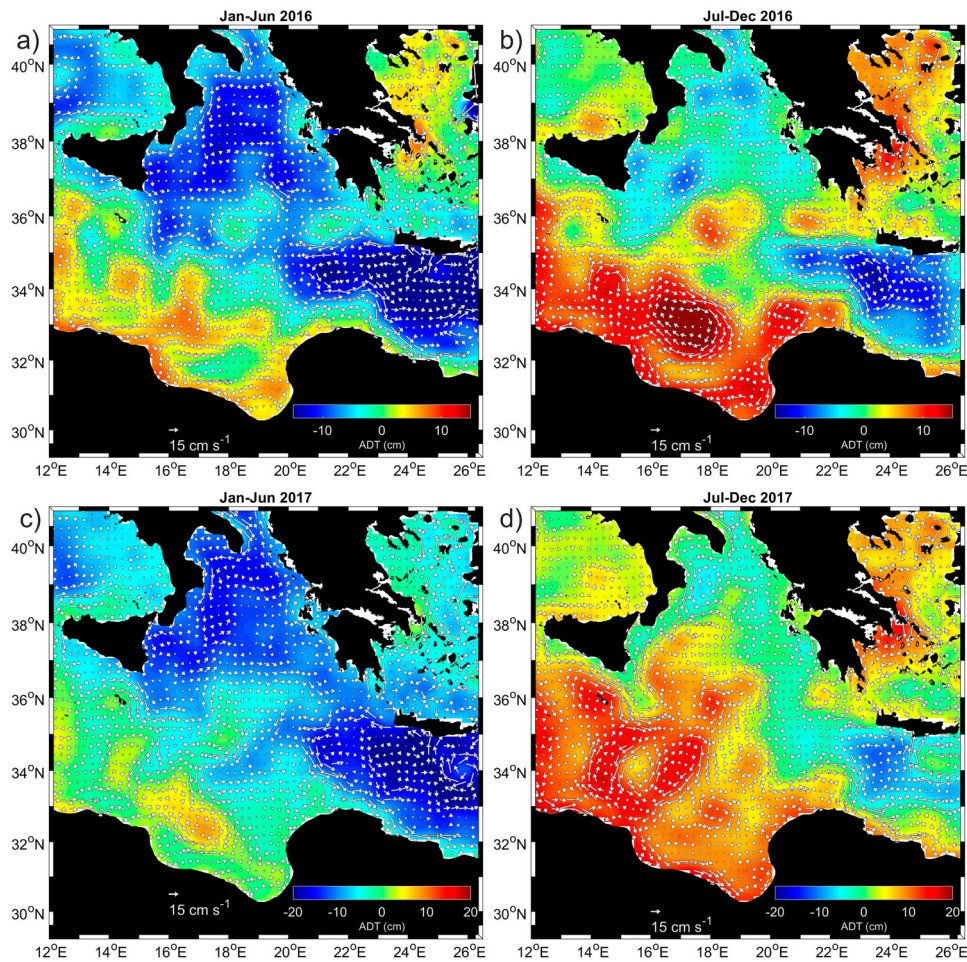
Figure 4.5.3. Mean maps of absolute dynamic topography (colour-coded in the figures, where warm colours/red means relative highs and cold colours/blue means relative lows) and absolute geostrophic velocities (white arrows) for the periods January–June 2016 (a), July–December 2016 (b), January–June 2017 (c) and July–December 2017 (d). Reference number of the product used: 4.5.1

established (Figure 4.5.3(d)). This change of the circulation mode should not be attributed to seasonal variability that rarely impacts the basin wide circulation (Gačić et al. 2014). Moreover, the low-pass filtered (13 months) current vorticity spatially averaged in the Northern Ionian Sea indicates that a shift of the surface circulation from cyclonic to anticyclonic has occurred in 2017, irrespective of the seasonal signal. Further studies, additional datasets and the support of numerical models are needed for a better comprehension, a robust description and a deeper analysis of the Ionian reversal phenomenon, not only for the year 2017 but also for the future years. It is of fundamental importance to keep on monitoring this circulation pattern that deeply impacts on the surface and intermediate water masses distribution and water masses formation. Indeed, the anticyclonic circulation mode is one of the main catalyst for abrupt events like the Eastern Mediterranean Transient (Gačić et al. 2011; Pinardi et al. 2015; Simoncelli et al. 2016) in which the South Adriatic deep water

formation site was substitute by the Aegean/Cretan Sea (Roether et al. 1996).

4.6. 'Silent' storm surge extremes in the western Baltic Sea on 4 January 2017

Authors: Jun She and Jacob Woge Nielsen

Statement of main outcome: Most storm surge events in the western Baltic Sea are caused by local gale winds. On 4 January 2017, sea level in the western Baltic Sea reached a 50 to 100 year high. However, the local wind speed over sea did not exceed 7 Beaufort (17.1 m/s). This is far from sufficient to generate such a rare surge event. By combining in-situ sea level and wind measurements, satellite observed wind speed, modelled sea level and water transport, mechanisms of the event are analysed. We find that wind conditions during two weeks prior to the event generated a 'U-shaped' sea level pattern, with high sea level in Kattegat and the central Baltic,

and low sea level in the western Baltic. A large scale, prevailing strong northeasterly on 4 January over the central Baltic Sea, shifted the water mass southwestward. It was found that, during the event, the Baltic surge propagated westwards with a speed of around 8.5 m/s. The southward flow from the Kattegat through the Danish Straits contributed 42% of the sea level rise, with 58% due to westward transport from the open Baltic Sea.

Products used:

Ref. No.	Product name and type	Documentation
4.6.1	WIND_GLO_WIND_L4_NRT_ OBSERVATIONS_012_004 Remote sensing	PUM: http://marine.copernicus.eu/ documents/PUM/CMEMS-OSI-PUM-012-004.pdf QUID: http://marine.copernicus.eu/ documents/QUID/CMEMS-OSI-QUID-012-004.pdf
4.6.2	BALTICSEA_ANALYSIS _FORECAST _PHY_003_006 Model	PUM: http://marine.copernicus.eu/ documents/PUM/CMEMS-BAL-PUM-003-006.pdf QUID: http://marine.copernicus.eu/ documents/QUID/CMEMS-BAL-QUID-003-006.pdf
4.6.3	INSITU_BS_TS_REP_ OBSERVATIONS_013_042 In-situ product	PUM: http://marine.copernicus.eu/ documents/PUM/CMEMS-INS-PUM-013-042.pdf QUID: http://marine.copernicus.eu/ documents/QUID/CMEMS-INS-QUID-013-042.pdf

Storm surges in the Baltic Sea may cause substantial loss of lives and property. To implement efficient safety measures, both accurate real time forecast and estimates of the coastal sea level 50, 100 and 1000 year return periods are required. Due to gaps in existing sea level observations in the coastal area, such estimates have to rely on both long-term observations and calibrated ocean models. It is therefore very important to understand the mechanisms forming the extreme sea level events. Many existing studies have focused on the long-term change and return periods of extreme sea level in the western Baltic Sea (Sztobryn et al. 2005; Gräwe and Burchard 2011; Wolski et al. 2014; Madsen et al. 2017). A comprehensive study was done by Sztobryn et al. (2005) on extreme storm surge events in the southern and western Baltic Sea during 1976–2000. It was found that all of the surges studied were caused by gale-force onshore winds of short or long duration, with a prevailing northerly component in the wind direction. However, occasionally an alternative mechanism may generate an extreme storm surge event. For example, in November 1993, a sea level high of 1.52 m was recorded at Korsør, located in the Great Belt. The return period exceeded 50 years. However, no local high winds were observed during the event. The calm weather conditions led to the event being referred to as a 'silent' storm surge. On 4 January 2017, a similar event was recorded in the western Baltic Sea. Although these 'silent' surges do not happen often, they significantly contribute to the history of sea level extremes in the western Baltic Sea (Madsen et al. 2017; Kystdirektoratet 2018). As there is still a lack of mechanism study and documentation on such kind of events, in this paper we will use comprehensive model and observation data from CMEMS to study the mechanisms of the event.

During 4 January 2017, sea level in a large part of the western Baltic Sea rose by 1.2–1.8 m during a relatively short period of 14–16 h. At Gedser, maximum sea level reached 1.67 m, which is the second highest recorded during the past hundred years (the highest being 1.68 m, recorded in 1954). At Bagenkop Havn sea level peaked at 1.77 m, which is 7 cm higher than the estimated 100 year event (Kystdirektoratet 2018). Table 4.6.1 shows the maximum sea level and corresponding UTC time, recorded at Danish and German

Table 4.6.1. Sea level peaks and corresponding UTC time, recorded at western Baltic Sea stations (see Figure 4.6.1), based on the product ref. 4.6.3.

| Danish stations	Longitude (deg.)	Latitude (deg.)	Max. Sea level (m)	Peak time (2017.1.4)
Køge	12.20	55.45	1.57	17:00
Rødvig	12.3728	55.2542	1.66	17:10
Hesnæs	12.1333	54.8167	1.70	17:50
Gedser	11.9256	54.5728	1.67	19:30
Rødby	11.35	54.55	1.68	20:20
Fåborg	10.25	55.10	1.68	22:30
Bagenkop	10.7528	54.7778	1.77	22:50
Fynshav	9.9869	54.995	1.66	23:10
Sønderborg	9.7833	54.9167	1.72	23:40
German stations				
Warnemünde	12.1033	54.1697	1.46	19:30
Wismar	11.4581	53.8989	1.68	20:15
Travemünde	10.8722	53.9581	1.73	21:00
Heiligenhafen	11.0056	54.3731	1.6	21:15
Kiel	10.2733	54.4997	1.64	22:45
Kalkgrund	9.8881	54.8247	1.67	23:45
Eckernförde	9.8361	54.4747	1.69	00:15 + 1day
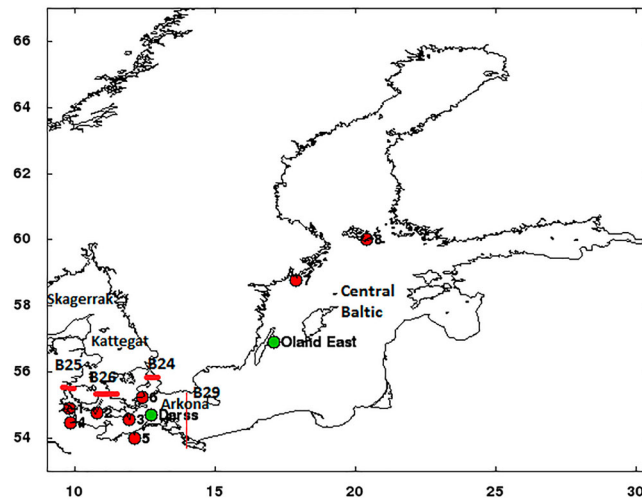
Figure 4.6.1. Subareas of the Baltic Sea and location of sea level stations. Tide gauge stations are marked with red dots and numbers – 1: Sønderborg; 2: Bagenkop Havn; 3: Gedser; 4: Eckernförde; 5: Warnemünde; 6: Rødvig; 7: Landsort Norra; 8: Degerby. Moorings are marked with green dots. Transects for transport calculation are indicated by red lines.

coastal stations in the western Baltic Sea (see Figure 4.6.1 for locations). The Danish stations cover an area from 12.37°E (Rødvig) to 9.78°E (Sønderborg) around 55.0° N while German stations cover 12.10°E (Warnemuende) to 9.84°E (Eckernfoerde) around 54.5°N. The maximum sea level was first reached at the easternmost stations, and then propagated westward.

The observed sea level time series are displayed in Figure 4.6.2 for the four Danish stations Rødvig, Gedser, Bagenkop Havn and Sønderborg. Sea level at those stations begins to drop around noon 2 January and reaches a low early 4 January. From then on, sea level increases during the next 16 h by about 2 m. It is noticed that there is a phase shift both in sea level highs and lows. Sønderborg is the first one to start dropping on 2 January, but the last one to reach its later minimum and maximum both on 4 January. Conversely, Rødvig is

the last one to start dropping, but the first one to reach its minimum and later maximum sea level. This phenomenon will be analysed in detail in the subsection 'propagation of surge'.

Wind and sea level conditions. The initial sea level before the surge event has a 'U-shaped' pattern, i.e., high sea level in the Kattegat and open Baltic Sea, and low sea level in the western Baltic Sea, as shown in Figure 4.6.3 (left). This creates a favourable condition both for southward water movement from the Kattegat and westward movement from the southern Baltic Sea to the western Baltic Sea on 4 January. By the late evening on 4 January, the sea level has changed dramatically (Figure 4.6.3 right). The western Baltic sea level increased by up to 1.8 m while sea level decreased in the Kattegat and the open Baltic.

The building up of the Baltic Sea high mean sea level is illustrated by the 17-day sea level time series in the
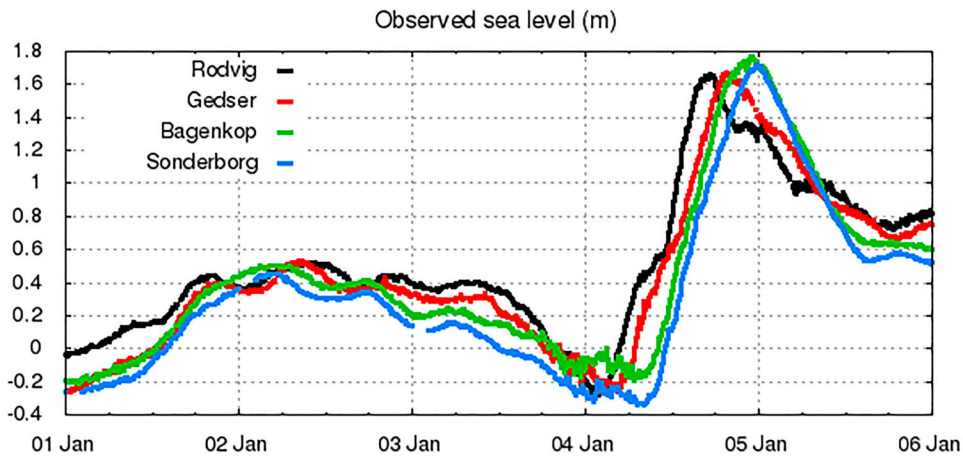

Figure 4.6.2. Hourly sea level before and during the 4 January 2017 storm surge observed at Rødvig, Gedser, Bagenkop Havn and Sønderborg, based on the product ref. 4.6.3.
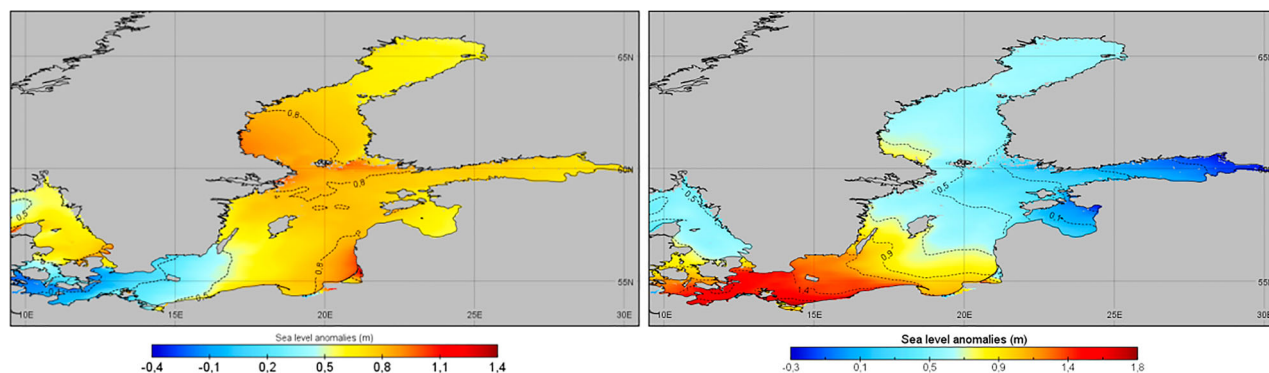
Figure 4.6.3. Modelled sea level at 2300 3 January 2017 (left) and 20-h sea level change, between 2300 3 January 2017 and 1900 4 January 2017 (right) (product ref. 4.6.2).

central Baltic Sea stations Landsort and Degerby, as shown in Figure 4.6.4. A gradual sea level rise in the central Baltic Sea is observed during 24 December 2016–3 January 2017. Then a sudden drop is recorded during 4 January, as the event takes place.

Wind conditions before the surge event are important for establishing the 'U-shaped' pattern of the sea level. The buoy measurements (Figure 4.6.5) show that, at Darss Sill, the winds are westerly and northwesterly during 02/01 to mid-04/01 with speeds increasing up to 18 m/s; at ÖlandÖst, the temporal pattern of winds are similar except for that the northwesterlies last 6 h less than Darss. The westerlies move water from Skagerrak to the Kattegat and also from the western to the open Baltic, which is important for building up the 'U-shaped' pattern of the sea level. Further analysis indicates that the persistent westerlies prevail during two weeks before the event and are responsible for building up the rising sea level in the central Baltic Sea, as shown in Figure 4.6.4.

Wind conditions change dramatically during the surge event. At the Darss Sill buoy, the wind shifts from westerly to northeasterly, accompanied by a wind speed decrease from 15 to 10 m/s during the second half of 4 January. At Öland Öst, the wind shift from westerly to northeasterly occurs 6 h earlier, and wind speed is much stronger (20–35 m/s). The strong northeasterly in the central Baltic Sea during the surge event is essential for piling up water in the western Baltic Sea. This analysis is further supported by the six-hourly wind fields from CMEMS (product ref. 4.6.1). In the morning of 4 January, the strong northeasterly wind (up to 23 m/s) in the central Baltic Sea and the northwesterly wind in southern Baltic Sea trigger a convergence of water in the southern Baltic Sea (Figure 4.6.6 left). Later the same day, northeasterly winds prevail in large parts of the Baltic Sea (Figure 4.6.6 right). This displaces water mass to the western Baltic Sea from the southern Baltic Sea.

Propagation of surge. The sea level peaks propagate westwards in the western Baltic Sea (Table 1 and
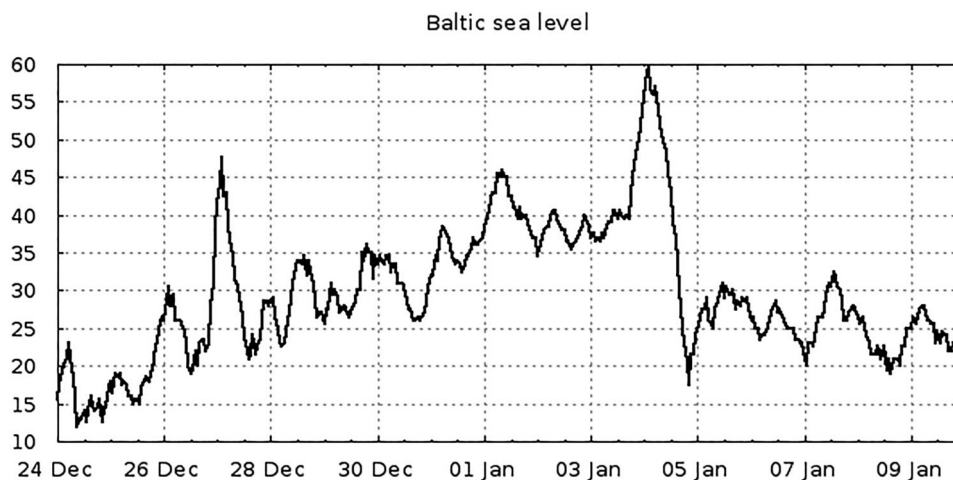

Figure 4.6.4. Observed sea level in the central Baltic Sea, calculated as an average of sea level at two central Baltic stations (Landsort Norra and Degerby) as derived from product ref. 4.6.3.
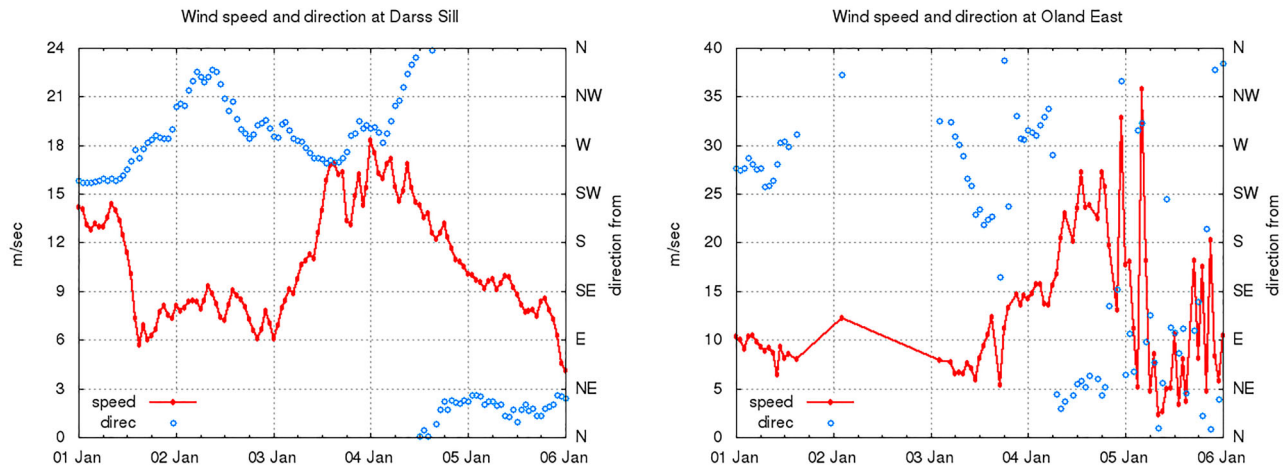
Figure 4.6.5. Hourly winds during the storm surge period at Darss Sill (54.7°N, 12.7°E, left) in the western Baltic Sea and Öland Öst station in the Oland East (56.92°N, 17.08°E, right). Note: the wind speed scale is different on the two graphs (product ref. 4.6.3).

Figure 2). This is further illustrated in Figure 4.6.7 using a sea level peak time vs. longitude plot. The Danish and German station pairs coincide well in their phases: Gedser and Warnemünde (at 12°E), Rødby and Wismar (at 11.4°E), Fåborg and Kiel (at 10.25°E) reach the peaks at the same or similar time (Table 4.6.1), which means that the propagation of the surge is westward.

Assuming a homogeneous wind impact in the area, the temporal lag of the maximum sea level is mainly caused by the propagation of a surface gravity wave. With shallow water assumption in the western Baltic Sea, the phase speed of free surface gravity wave and energy propagating speed should be the same, therefore referring as 'propagation speed' hereafter. The actual propagation speed of the sea level peaks can be estimated. For the German stations, a linear regression between the longitude distance between a station and Warnemünde (L_g, in metres) and corresponding sea level peak time difference T_g (in seconds) gives:

$$L_g = 8.5354 T_g + 6.1204$$

with square of correlation coefficient $R^2 = 0.9537$. Hence the speed of the sea level peak phase propagation is about 8.5 m/s. Similarly, a linear regression can be obtained for the Danish stations west of Gedser, resulting in a propagation speed of the sea level peak of 8.4 m/s.

The main part of the water body west of Gedser-Warnemünde transect has a depth of 15–20 m, suggesting a propagation speed of 12–14 m/s for free surface gravity waves. This means that the actual propagating speed is just 54–61% of the free surface gravity wave velocity. The difference is mainly attributed to bottom friction in the shallow waters.

Transport through the Danish Straits and the Arkona Basin. The analysis above shows the importance of the initial sea level condition (the 'U-shaped' pattern) in generating the high sea level in the western Baltic Sea. However, there is a lack of explanation on how this sea level was formed. Furthermore, prevailing wind conditions during 4 January suggest that flow from Kattegat to the western Baltic Sea through the Danish Straits (sections B24, B25 and B26) also
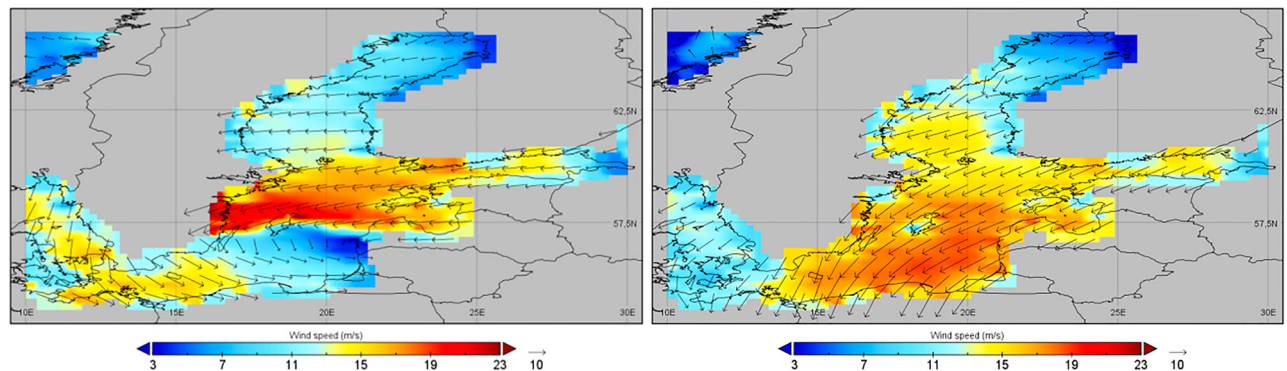

Figure 4.6.6. Sea surface wind conditions at 0600 4 January 2017 (left) and 1800 4 January 2017 (right). (product ref. 4.6.1)
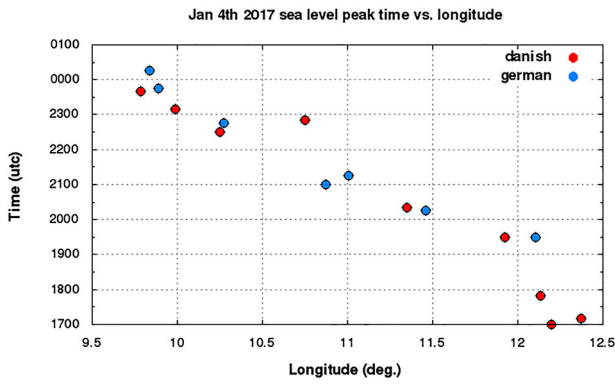
Figure 4.6.7. The longitude and sea level peak time at the western Baltic Sea stations (as shown in Table 1) (product ref. 4.6.3)

contributes to the high sea level. However, the amount and relevant importance of this transport has not been quantitatively assessed. This subsection will address these issues.

Accurate estimation of the transport through given transects requires high frequency and full model resolution data. Since the BAL MFC ocean forecast product only provides 25 out of 122 vertical layers of the forecast, the product is not suitable for transport calculation. Instead, we use an operational BOOS (Baltic Sea Operational Oceanography System) water transport product. The water transport values for 35 Baltic Sea transects are calculated daily, and results are shown on the BOOS website http://www.boos.org in near real time. For transports between Kattegat and western Baltic Sea, transects B24 (Øresund), B25 (Little Belt) and B26 (Great Belt) are added and used. For transport between the southern and western Baltic Sea, transect B29 (north-southward across the Arkona Basin) is used (Figure 4.6.1).

Time series of daily net transport was calculated from DMI (Danish Meteorological Institute) operational forecast product for the period 15 December 2016–6 January 2017 (Figure 4.6.8). Most of the time, transports through transect B29 (red line) are negatively correlated with transports through the Danish Straits (green line), which means that when water flows into the western Baltic Sea from the Kattegat, there is also water flowing out from the western Baltic Sea to the open Baltic Sea, and vice versa. Before 22 December, the transport features a net outflow from the Baltic to the Kattegat, with little or no impact on the Western Baltic (black line in Figure 4.6.8). During 22 December 2016–3 January 2017, the flow pattern reverses, with significant inflow through the Danish Straits, together with outflow from the Arkona Basin to the open Baltic Sea. As a result the sea level in the open Baltic Sea increased during 22 December 2016–3 January 2017 (cf. Figure 4.6.4). The simultaneous outflow from the western Baltic through both transects 2–3 January is essential in generating the low sea level in the western Baltic Sea. At the same time, North Sea westerlies transport water into the Kattegat from the Skagerrak. This forms the 'U-shaped' pattern of sea level on 3 January, as shown in Figure 4.6.3 (left).

The 'U-shaped' pattern of sea level is a necessary preface for the storm surge event on 4 January 2017. Generated by large scale wind forcing conditions, flow finally convergences in the western Baltic Sea on 4 January, by inflow not only from the Arkona Basin side but also from the Danish Straits. The westward transport from the open Baltic Sea through transect B29 amounts to about 58%, while the remaining 42% stem from southward transport through the Danish Straits.
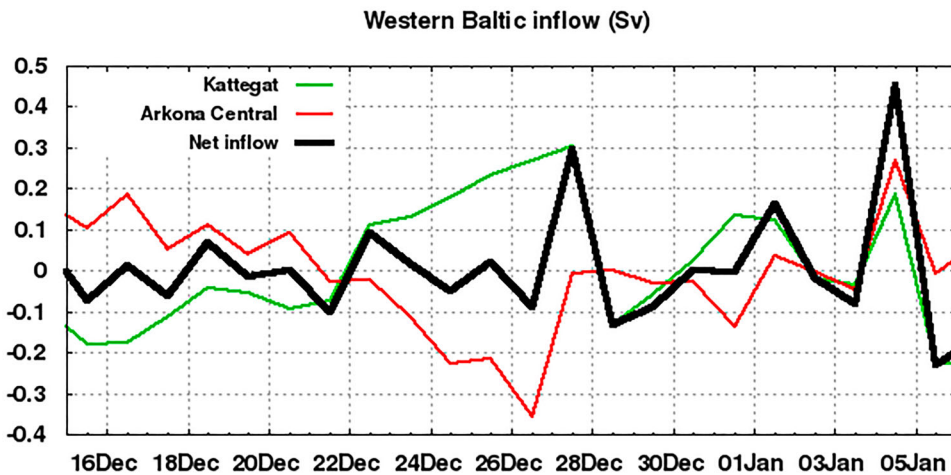

Figure 4.6.8. Daily net transport during 15 December 2016–6 January 2017, positive value means flow into the western Baltic Sea. Green: transport across transects B24–B26; red: transport across transect B29 and black: total net transport into the western Baltic Sea.

4.7. The 2017 coastal El Niño

Authors: Florent Gasparin, Vincent Echevin, Alexandre Mignot, Coralie Perruche, Marie Drévillon

Statement of main outcome: While the Tropical Pacific was rather in neutral El Niño-Southern Oscillation conditions during 2017, a significant surface warming with similar amplitude to typical eastern Pacific El Niños was found locally along the coast of Peru and Ecuador at the beginning of the year. Triggered by an anomalously low along-shore wind, the surface warming stopped the coastal upwelling and generated strong interannual precipitation over the coastal land in the north of Peru. This warm event, named 'coastal El Niño', was not anticipated by climate forecasting centres and left local authorities totally unprepared, regarding floods and landslides generated by persistent heavy rains from January to March.Given the strong consequences for the local populations, these very rare coastal El Niños (only two previously reported) therefore require further investigations.

Products used:

| Ref. no.	Product name and type	Documentation
4.7.1.	GLOBAL_REANALYSIS_ PHY_001_025	PUM: http://marine.copernicus.eu/ documents/PUM/CMEMS-GLO-PUM-001-025.pdf QUID: http://marine.copernicus.eu/ documents/QUID/CMEMS-GLO-QUID-001-025.pdf
4.7.2.	ECMWF Era-Interim reanalysis wind product Reanalysis (atmosphere)	Dee et al. (2011), downloaded from the website http://data.ecmwf. int/data/
4.7.3	OCEANCOLOUR_GLO_ CHL_L4_REP_ OBSERVATIONS_009_082 OCEANCOLOUR_GLO_CHL_ L4_NRT_OBSERVATIONS_ 009_033	PUM: http://marine.copernicus.eu/ documents/PUM/CMEMS-OC-PUM-009-ALL.pdf QUID: http://marine.copernicus.eu/ documents/QUID/CMEMS-OC-QUID-009-033-037-082-098.pdf http://marine.copernicus.eu/ documents/QUID/CMEMS-OC-QUID-009-030-032-033-081-082-083-085-086.pdf
4.7.4	GLOBAL_REANALYSIS_ BIO_001_018	PUM: http://marine.copernicus.eu/ documents/PUM/CMEMS-GLO-PUM-001-018.pdf QUID : http://marine.copernicus. eu/documents/QUID/CMEMS-GLO-QUID-001-018.pdf
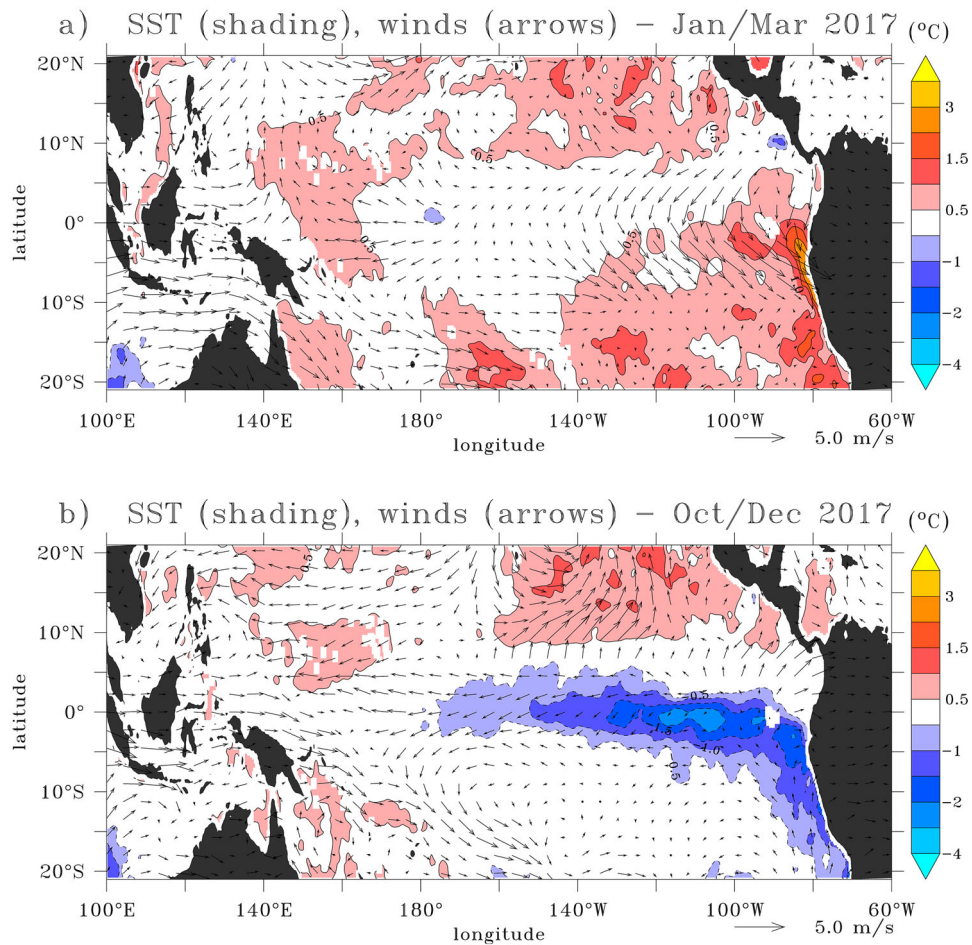
Figure 4.7.1. Temperature (shading, in °C) and winds (arrows, in m/s) anomalies, from the 1993–2014 climatology, time-averaged for the periods (b) January–March 2016 and (c) October–December 2016 (products reference 4.7.1, 4.7.2).

As the dominant interannual climate signal on Earth, the El Niño-Southern Oscillation includes a wide variety of local and large-scale atmospheric and oceanic phenomena, but is typically characterised by two anomalous basin-wide patterns in the tropical Pacific (e.g., Guilyardi et al. 2009; Wang et al. 2017 for a review). At the beginning of 2017, while the tropical Pacific conditions in 2017 were not marked by significant anomalous basin-wide El Niño-Southern Oscillation conditions such as during the 2015/2016 El Niño (Gasparin et al. 2017), a localised warm event, associated with anomalously strong precipitation, occurs in the southeastern Pacific along the northwestern coast of South America. This type of event, named 'coastal El Niño', is very rare and the mechanisms are not well known, as only two coastal El Niños were previously reported in 1891 and 1925 (Takahashi and Martínez 2017).

As seen in Figure 4.7.1, the January/March 2017 sea surface temperature is characterised by a strong warm anomaly of more than 4°C in the eastern equatorial Pacific off the coasts of Peru and Ecuador. This anomaly was similar in shape and intensity to anomalies typical of eastern Pacific El Niño conditions, with the major difference being the absence of El Niño conditions in the central-eastern Pacific during this period. Although a relatively weak downwelling equatorial Kelvin wave may have contributed to the warm sea surface temperature anomaly along the Peru coasts in February–March 2017 (through the deepening of the thermocline), the main forcing triggering the 2017 event was potentially a strong large-scale relaxation of the southeasterly trades in the eastern south Pacific (Figure 4.7.1). The large-scale mechanism which generated the wind decrease could be an enhanced deep convection over north Australia, triggering an atmospheric teleconnection between the western equatorial Pacific and the eastern South Pacific, as evidenced by Garreaud (2018).

The intense local ocean warming, which peaked during March 2017, resulted in enhanced local precipitation rate in the northern Peru and Ecuador. In Figure 4.7.2, the precipitation rate time series, area-averaged off the coasts of Peru (red box in Figure 4.7.2 (a)), shows that the March 2017 precipitation rate was more than 4 times higher than normal, exhibiting larger amplitude as for the 1997/1998 El Niño. This impacted on the surface ocean in favouring the development of a negative sea surface salinity anomaly along the coast of Peru (Figure 4.7.2(a)). In addition to the coastal area, this strong event caused high inland precipitation over the nearby desert land inducing devastating floods and 'huacos' (rivers of mud) in northern Peru and Ecuador (Fraser 2017). Further investigations would require to

quantify the dominant terms of the freshwater balance in the surface layer, including both atmospheric inputs and oceanic dynamics.

To further investigate how this event impacted on the phytoplankton biomass and the production of organic carbon through photosynthesis, the surface chlorophyll concentration (used as a proxy of phytoplankton biomass) is shown from independent estimates deduced from satellite observations and from a numerical model (Figure 4.7.3). A strong negative anomaly (<2.2 mg/m^3) clearly appears along the coast of Peru on both estimates. The model estimate suggests that this negative anomaly is extended down to about 30 m depth. The coastal upwelling system off Peru is a place of enhanced level of primary production due to high nutrient supply by wind-driven upwelling (Pennington et al. 2006). In March 2017, a decrease of the nearshore wind-driven upwelling along the coast of Peru (Figure 4.7.3(c)), associated with Ekman pumping changes (Echevin et al. 2018), probably reduced the inputs of nutrients to the surface layer, therefore decreasing the production of organic carbon and phytoplankton biomass.
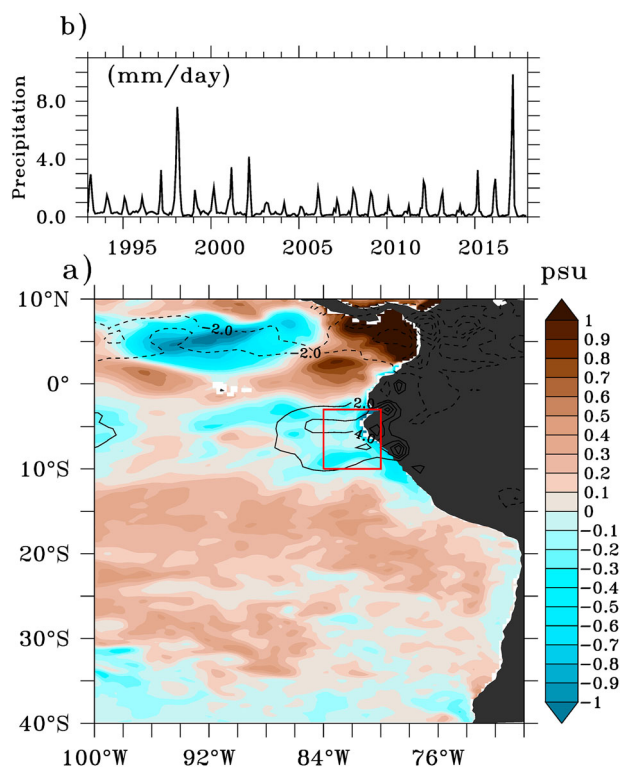

Figure 4.7.2. (a) Salinity anomaly (shading) and precipitation rate (contour, in mm/day), for the month of March 2017 (products reference 4.7.1, 4.7.2). (b) Precipitation rate is area-averaged in the red box of (a) (84°W–80°W, 3°S–10°S). Anomaly is calculated from the 1993–2014 climatology.
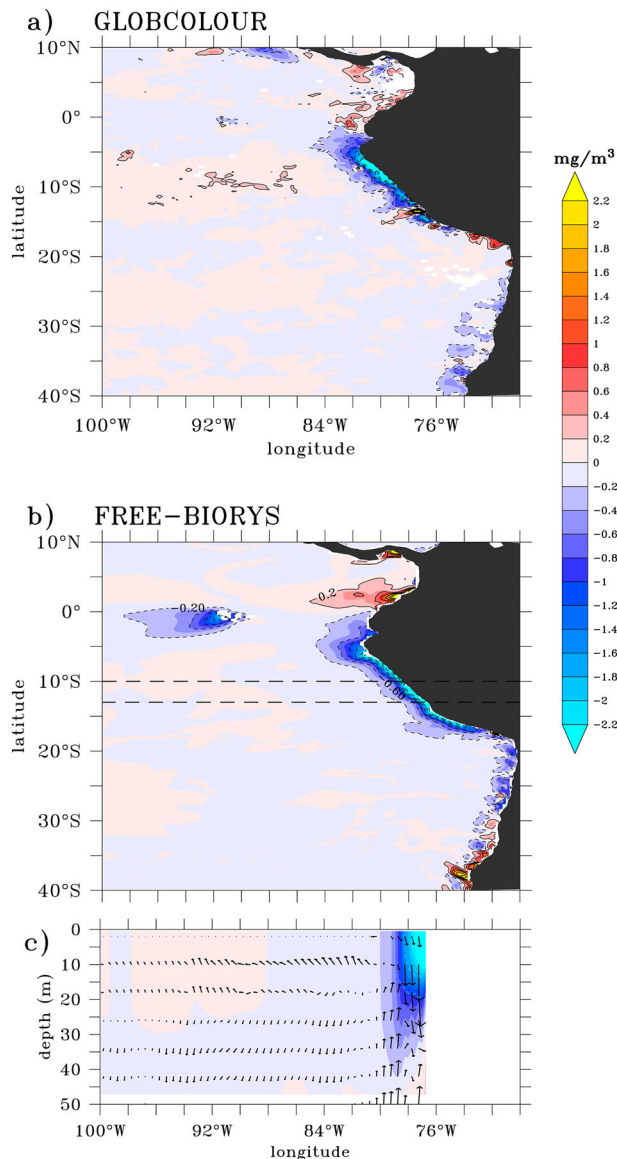
Figure 4.7.3. (a, b) Surface chlorophyll concentration anomalies (in mg/m^3), from the 2007–2017 climatology, for the month of March 2017 from (a) GLOBCOLOUR, and (b) the FREE-BIORYS product (products reference 4.7.3, 4.7.4). (c) Vertical section of chlorophyll concentration anomaly (shading) and current velocity anomaly (arrows), latitude-averaged over 10°S–13°S (dashed lines in b) in the upper 50 m. Anomalies are calculated from the climatological cycle. The current velocity has been vertically interpolated every 8 m.

Thus, the large-scale atmospheric variability in the eastern Pacific has led to significant modification of the local oceanic/land conditions (i) by warming coastal surface waters and (ii) by enhancing precipitation in the northern Peru and Ecuador, and (iii) by decreasing the upwelling-driven primary production in the coastal ocean. Unlike the very strong 2015/2016 El Niño, the 2017 coastal El Niño was not anticipated by climate forecasting centres and left local authorities totally

unprepared (Ramírez and Briones 2017; Garreaud 2018). Although the combination of oceanic/atmospheric observation and model products allows a detailed description of the 2017 coastal El Niño event, the rare occurrence of these coastal El Niños can make difficult the understanding and the prediction of these extreme events, which thus require further investigation.

References
Section 4.1. Weddell Sea Polynya

Blanke B, Delecluse P. 1993. Variability of the tropical Atlantic-Ocean simulated by a general-circulation model with 2 different mixed-layer physics. J Phys Oceanogr. 23:1363–1388.

Carsey FD. 1980. Microwave observation of the Weddell polynya. Month Weath Rev. 108:2032–2044.

Cavalieri DJ, Martin S. 1994. The contribution of Alaskan, Siberian, and Canadian coastal polynyas to the cold halocline layer of the Arctic Ocean. J Geophys Res Oceans. 99:18343–18362.

Cheon WG, Park YG, Toggweiler JR, Lee SK. 2014. The relationship of Weddell polynya and open-ocean deep convection to the southern hemisphere westerlies. J Phys Oceanogr. 44:694–713.

Comiso JC, Gordon AL. 1987. Recurring polynyas over the Cosmonaut Sea and the Maud Rise. J Geophys Res Oceans. 92:2819–2833.

Dufour CO, Morrison AK, Griffies SM, Frenger I, Zanowski H, Winton M. 2017. Preconditioning of the Weddell Sea polynya by the ocean mesoscale and dense water overflows. J Clim. 30:7719–7737.

Gordon AL, Visbeck M, Comiso JC. 2007. A possible link between the Weddell polynya and the southern annular mode. J Clim. 20:2558–2571.

Heuzé C, Heywood KJ, Stevens DP, Ridley JK. 2013. Southern ocean bottom water characteristics in CMIP5 models. Geophys Res Lett. 40:1409–1414.

Heuzé C, Ridley JK, Calvert D, Stevens DP, Heywood KJ. 2015. Increasing vertical mixing to reduce southern ocean deep convection in NEMO3.4. Geosci Model Dev. 8:3119.

Holland DM. 2001. Explaining the Weddell polynya – a large ocean eddy shed at Maud Rise. Science. 292:1697–1700.

Kjellsson J, Holland PR, Marshall GJ, Mathiot P, Aksenov Y, Coward AC, Bacon S, Megann AP, Ridley JK. 2015. Model sensitivity of the Weddell and Ross seas, Antarctica, to vertical mixing and freshwater forcing. Ocean Model. 94:141–152.

Kusahara K, Hasumi H, Tamura T. 2010. Modeling sea ice production and dense shelf water formation in coastal polynyas around East Antarctica. J Geophys Res Oceans. 115:C10006.

Lindsay RW, Holland DM, Woodgate RA. 2004. Halo of low ice concentration observed over the Maud Rise seamount. Geophys Res Lett. 31:L13302.

Martin T, Park W, Latif M. 2013. Multi-centennial variability controlled by Southern Ocean convection in the Kiel climate model. Clim Dynam. 40:2005–2022.

Martinson DG, Killworth PD, Gordon AL. 1981. A convective model for the Weddell polynya. J Phys Oceanogr. 11:466–488.

Morales-Maqueda MA, Willmott AJ, Biggs NRT. 2004. Polynya dynamics: a review of observations and modeling. Rev Geophys. 42:RG1004.

Orsi AH, Jacobs SS, Gordon AL, Visbeck M. 2001. Cooling and ventilating the abyssal ocean. Geophys Res Lett. 28:2923–2926.

Smith WO Jr, Barber D. 2007. Polynyas: windows to the world. Amsterdam: Elsevier.

Swart S, Campbell EC, Heuzé C, Johnson K, Lieser JL, Massom M, Mazloff M, Meredith M, Reid P, Sallée J-B, Stammerjohn S. 2018. Return of the Maud Rise polynya: climate litmus or sea ice anomaly? State of the Climate in 2017. BAMS. 48.

Piecuch CG, Ponte RM, Little CM, Buckley MW, Fukumori I. 2017. Mechanisms underlying recent decadal changes in subpolar North Atlantic Ocean heat content. J Geophys Res Oceans. 122(9):7181–7197.

Robson J, Ortega P, Sutton R. 2016. A reversal of climatic trends in the North Atlantic since 2005. Nat Geosci. 9 (7):513.

Robson J, Sutton R, Lohmann K, Smith D, Palmer MD. 2012. Causes of the rapid warming of the North Atlantic Ocean in the mid-1990s. J Clim. 25(12):4116–4134.

Zunino P, Lherminier P, Mercier H, Daniault N, García-Ibáñez MI, Pérez FF. 2017. The GEOVIDE cruise in May–June 2014 reveals an intense meridional overturning circulation over a cold and fresh subpolar North Atlantic. Biogeosciences. 14:5323–5342. doi:10.5194/bg-14-5323-2017.

Section 4.2. T/S anomalies in the North Atlantic subpolar gyre

Barrier N, Cassou C, Deshayes J, Treguier AM. 2014. Response of North Atlantic Ocean circulation to atmospheric weather regimes. J Phys Oceanogr. 44:179–201. doi:10.1175/JPO-D-12-0217.1.

Belkin IM, Levitus S, Antonov J, Malmberg SA. 1998. 'Great salinity anomalies' in the North Atlantic. Prog Oceanogr. 41(1):1–68.

Czaja A, Frankignoul C. 2002. Observed impact of Atlantic SST anomalies on the North Atlantic oscillation. J Clim. 15:606–623.

Deshayes J, Frankignoul C. 2008. Simulated variability of the circulation in the North Atlantic from 1953 to 2003. J Clim. 21:4919–4933. doi:10.1175/2008JCLI1882.1.

Dickson RR, Meincke J, Malmberg SA, Lee AJ. 1988. The 'great salinity anomaly' in the northern North Atlantic 1968–1982. Prog Oceanogr. 20(2):103–151.

Flatau MK, Talley L, Niiler PP. 2003. The North Atlantic oscillation, surface current velocities, and SST changes in the subpolar North Atlantic. J Clim. 16(14):2355–2369.

Gourrion J, Deshayes J, Juza M, Szekely T, Tintoré J. 2018. A persisting regional cold and fresh water anomaly in the Northern Atlantic. In: Copernicus marine service ocean state report, issue 2. J Oper Oceanogr. 11(sup1):s125–s129. doi:10.180/1755876X.2018.1489208.

Grist JP, Josey SA, Jacobs ZL, Marsh R, Sinha B, Van Sebille E. 2016. Extreme air–sea interaction over the North Atlantic subpolar gyre during the winter of 2013–2014 and its sub-surface legacy. Clim dyn. 46(11–12):4027–4045.

Hátún H, Sandø AB, Drange H, Hansen B, Valdimarsson H. 2005. Influence of the Atlantic subpolar gyre on the thermohaline circulation. Science. 309(5742):1841–1844.

Josey SA, Hirschi JJM, Sinha B, Duchez A, Grist JP, Marsh R. 2018. The recent Atlantic cold anomaly: causes, consequences, and related phenomena. Ann Rev Mar Sci. 10:475–501.

Levitus S, Antonov JI, Boyer TP, Locarnini RA, Garcia HE, Mishonov AV. 2009. Global ocean heat content 1955–2008 in light of recently revealed instrumentation problems. Geophys Res Lett. 36:L07608. doi:10.1029/2008GL037155.

Section 4.3. Anticyclonic Eddy Anomaly: impact on the boundary current and circulation in the western Mediterranean Sea

Amores A, Monserrat S, Marcos M. 2013. Vertical structure and temporal evolution of an anticyclonic eddy in the Balearic Sea (western Mediterranean). J Geophys Res Oceans. 118:2097–2106.

Bouffard J, Pascual A, Ruiz S, Faugère Y, Tintoré J. 2010. Coastal and mesoscale dynamics characterization using altimetry and gliders: A case study in the Balearic Sea. J Geophys Res Oceans. 115:C10029.

Dengler M, Schott FA, Eden C, Brandt P, Fischer J, Zantopp RJ. 2004. Break-up of the Atlantic deep western boundary current into eddies at 8° S. Nature. 432:1018–1020.

Escudier R, Renault L, Pascual A, Brasseur P, Chelton D, Beuvier J. 2016. Eddy properties in the western Mediterranean Sea from satellite altimetry and a numerical simulation. J Geophys Res Oceans. 121:3990–4006.

Font J, Salat J, Tintoré J. 1988. Permanent features of the circulation in the Catalan Sea. Oceanol Acta Spec issue.

Garreau P, Garnier V, Schaeffer A. 2011. Eddy resolving modelling of the Gulf of Lions and Catalan Sea. Ocean Dyn. 61 (7):991–1003.

Greatbatch RJ. 1987. A model for the inertial recirculation of a gyre. J Mar Res. 45:601–634.

Herbaut C, Martel F, Crépon M. 1997. A sensitivity study of the general circulation of the western Mediterranean Sea. Part II: the response to atmospheric forcing. J Phys Oceanogr. 27:2126–2145.

Heslop EE, Ruiz S, Allen J, López-Jurado JL, Renault L, Tintoré J. 2012. Autonomous underwater gliders monitoring variability at 'choke points' in our ocean system: a case study in the western Mediterranean Sea. Geophys Res Lett. 39:L20604.

Hogg NG, Stommel H. 1985. On the relation between the deep circulation and the Gulf Stream. Deep Sea Res Part Oceanogr Res Pap. 32:1181–1193.

Holland WR. 1978. The role of mesoscale eddies in the general circulation of the ocean—numerical experiments using a wind-driven quasi-geostrophic model. J Phys Oceanogr. 8:363–392.

Holland WR, Lin LB. 1975. On the generation of mesoscale eddies and their contribution to the oceanic general circulation. II A parameter study. J Phys Oceanogr. 5:658–669.

Juza M, Renault L, Ruiz S, Tintoré J. 2013. Origin and pathways of winter intermediate water in the northwestern mediterranean Sea using observations and numerical simulation. J Geophys Res Oceans. 118:6621–6633.

Kang D, Curchitser EN. 2015. Energetics of Eddy–mean flow interactions in the Gulf stream region. J Phys Oceanogr. 45:1103–1120.

Marshall JC. 2006. Eddy-mean-flow interaction in a barotropic ocean model. Q J R Meteorol Soc. 110:573–590.

Mason E, Pascual A. 2013. Multiscale variability in the Balearic Sea: an altimetric perspective. J Geophys Res Oceans. 118:3007–3025.

Mason E, Pascual A, McWilliams JC. 2014. A new sea surface height-based code for oceanic mesoscale eddy tracking. J Atmos Ocean Technol. 31:1181–1188.

Parrilla G, Kinder TH. 1987. The physical oceanography of the Alboran Sea. Naval Ocean Res. Admin. (NORDA). Rep.184. p. 26.

Pascual A, Buongiorno NB, Larnicol G, Emelianov M, Gomis D. 2002. A case of an intense anticyclonic eddy in the Balearic Sea (western Mediterranean). J Geophys Res Oceans. 107:4–1.

Pinot JM, López-Jurado JL, Riera M. 2002. The CANALES experiment (1996–1998). Interannual, seasonal, and mesoscale variability of the circulation in the Balearic channels. Prog Oceanogr. 55:335–370.

Rio MH, Pascual A, Poulain PM, Menna M, Barceló B, Tintoré J. 2014. Computation of a new mean dynamic topography for the Mediterranean Sea from model outputs, altimeter measurements and oceanographic in situ data. Ocean Sci. 10:731–744.

Robinson AR, Leslie WG, Theocharis A, Lascaratos A. 2001. Mediterranean sea circulation. Ocean Curr Deriv Encycl Ocean Sci. 3:1689–1705.

Rubio A, Barnier B, Jordà G, Espino M, Marsaleix P. 2009. Origin and dynamics of mesoscale eddies in the Catalan Sea (NW Mediterranean): insight from a numerical model study. J Geophys Res. 114. doi:10.1029/2007JC004245.

Ruiz S, Pascual A, Garau B, Faugère Y, Alvarez A, Tintoré J. 2009. Mesoscale dynamics of the Balearic Front, integrating glider, ship and satellite data. J Mar Syst. 78:S3–S16.

Tintoré J, Vizoso G, Casas B, Heslop E, Pascual A, Orfila A, Ruiz S, Martínez-Ledesma M, Torner M, Cusí S, et al. 2013. SOCIB: the Balearic Islands coastal ocean observing and forecasting system responding to science, technology and society needs. Mar Technol Soc J. 47:101–117.

Viúdez Á, Haney RL. 1997. On the relative vorticity of the Atlantic jet in the Alboran Sea. J Phys Oceanogr. 27:175–185.

Section 4.4. Insights on the 2017 Marine Heatwaves in the Mediterranean Sea

Bensoussan N, Harmelin JG, Romano JC, Garrabou J. 2010. High resolution characterization of northwest Mediterranean coastal waters thermal regimes: to better understand responses of benthic communities to climate change. Estuarine Coast Shelf Sci. 87:431–441.

Crisci C, Bensoussan N, Romano JC, Garrabou J. 2011. Temperature anomalies and mortality events in marine communities: insights on factors behind differential mortality impacts in the NW Mediterranean. PloS One. 6(9): e23814. doi:10.1371/journal.pone.0023814.

Frölicher TL, Laufkötter C. 2018. Emerging risks from marine heat waves. Nat Commun. doi:10.1038/s41467-018-03163-6.

Galli G, Solidoro C, Lovato T. 2017. Marine heat waves hazard 3D maps and the risk for low motility organisms in a warming Mediterranean Sea. Front Mar Sci. doi:10.3389/fmars.2017.00136.

Garrabou J, Coma R, Bensoussan N, Bally M, Chevaldonné P, Cigliano M, Diaz D, Harmelin JG, Gambi MC, Kersting DK, et al. 2009. Mass mortality in NW Mediterranean rocky benthic communities: effects of the 2003 heat wave. Global Change Biol. doi:10.1111/j.1365-2486.2008.01823.x.

Hobday AJ, Alexander LV, Perkins SE, Smale DA, Straub SC, Oliver ECJ, Benthuysen J, Burrows MT, Donat MG, Feng M, et al. 2016. A hierarchical approach to defining marine heatwaves. Prog Oceanogr. doi:10.1016/j.pocean.2015.1012.1014.

Hobday AJ, Oliver ECJ, Sen Gupta A, Benthhuysen JA, Burrow MT, Donat MG, Holbrook NJ, Moore PJ, Thomsen MS, Wernberg T, Smale DA. 2018. Categorizing and naming marine heatwaves. Oceanography. 31(2). doi:10.5670/oceanog.2018.205.

Hughes TP, Barnes ML, Bellwood DR, Cinner JE, Cumming GS, Jackson JBC, Kleypas J, van de Leemput IA, Lough JM, Morrison TH, et al. 2017. Coral reefs in the anthropocene. Nature. 546(7656). doi:10.1038/nature22901.

Marbà N, Jordà G, Agustí S, Girard C, Duarte CM. 2015. Footprints of climate change on Mediterranean Sea biota. Front Mar Sci. 2:56. doi:10.3389/fmars.2015.00056.

Oliver ECJ, Donat MG, Burrows MT, Moore PJ, Smale DA, Alexander LV, Benthuysen JA, Feng M, Sen Gupta A, Hobday AJ, et al. 2018. Longer and more frequent marine heatwaves over the past century. Nat Commun. 9(1324). doi:10.1038/s41467-41018-03732-41469.

Schaeffer A, Roughan M. 2017. Subsurface intensification of marine heatwaves off southeastern Australia: the role of stratification and local winds. Geophys Res Lett. 44(10). doi:10.1002/2017GL073714.

Sparnocchia S, Schiano ME, Picco P, Bozzano R, Cappelletti A. 2006. The anomalous warming of summer 2003 in the surface layer of the central Ligurian Sea (western Mediterranean). Ann Geophys. 24:443–452.

Wernberg T, Bennett S, Babcock RC, de Bettignies T, Cure K, Depczynski M, Dufois F, Fromont J, Fulton CJ, Hovey RK, et al. 2016. Climate-driven regime shift of a temperate marine ecosystem. Science. 353:169–172.

Section 4.5. Reversal of the Northern Ionian Circulation in 2017

Bessiéres L, Rio MH, Dufau C, Boone C, Pujol MI. 2013. Ocean state indicators from MyOcean altimeter products. Ocean Sci. 9:545–560. doi:10.5194/os-9-545-2013.

Demirov E, Pinardi N. 2002. Simulation of the Mediterranean Sea circulation from 1979 to 1993: Part I. The interannual variability. J Mar Syst. 33–34:23–50. doi:10.1016/S0924-7963(02)00051-9.

Gačić M, Borzelli GLE, Civitarese G, Cardin V, Yari S. 2010. Can internal processes sustain reversals of the ocean

upper circulation? The Ionian Sea example. Geophys Res Lett. 37:L09608. doi:10.1029/2010GL043216.

Gačić M, Civitarese G, Eusebi Borzelli GL, Kovačević V, Poulain PM, Theocharis A, Menna M, Catucci A, Zarokanellos N. 2011. On the relationship between the decadal oscillations of the northern Ionian Sea and the salinity distributions in the eastern Mediterranean. J Geophys Res. 116:C12002. doi:10.1029/2011JC007280.

Gačić M, Civitarese G, Kovačević V, Ursella L, Bensi M, Menna M, Cardin V, Poulain PM, Cosoli S, Notarstefano G, Pizzi C. 2014. Extreme winter 2012 in the Adriatic: an example of climatic effect on the BiOS rhythm. Ocean Sci. 10:513–522. doi:10.5194/os-10-513-2014.

Kokkini Z, Notarstefano G, Poulain PM, Mauri E, Gerin R, Simoncelli S in von Schuckmann. 2017. Unusual salinity pattern in the South Adriatic Sea. The Copernicus marine environment monitoring service ocean state report. J Oper Ocean.

Lavigne H, Civitarese G, Gačić M, D'Ortenzio F. 2018. Impact of decadal reversals of the north Ionian circulation on phytoplankton phenology. Biogeosci. 15:4431–4445. doi:10.5194/bg-15-4431-2018.

Legeais JF, von Schuckmann K, Dagneaux Q, Melet A, Meyssignac B, Bonaduce A, Ablain M, Pérez Gomez B in von Schuckmann et al. 2016. Sea level. The Copernicus marine environment monitoring service ocean state report. J Oper Ocean. 9(sup2):s235–s320. doi:10.1080/1755876X.2016.1273446.

Legeais JF, von Schuckmann K, Melet A, Storto A, Meyssignac B in von Schuckmann. 2017. Sea level. The Copernicus marine environment monitoring service ocean state report. J Oper Ocean.

Pinardi N, Zavatarelli M, Adani M, Coppini G, Fratianni C, Oddo P, Simoncelli S, Tonani M, Lyubartsev V, Dobricic S, Bonaduce A. 2015. Mediterranean Sea large-scale low-frequency ocean variability and water mass formation rates from 1987 to 2007: a retrospective analysis. Prog Ocean. 132:318–332. ISSN 0079-6611. doi:10.1016/j.pocean.2013.11.003.

Poulain PM, Menna M, Mauri E. 2012. Surface geostrophic circulation of the Mediterranean Sea derived from drifter and satellite altimeter data. J Phys Ocean. 42(6):973–990. doi:10.1175/JPO-D-11-0159.1.

Pujol MI, Larnicol G. 2005. Mediterranean Sea eddy kinetic energy variability from 11 years of altimetric data. J Mar Syst. 58:121–142. doi:10.1016/j.jmarsys.2005.07.005.

Reale M, Salon S, Crise A, Farneti R, Mosetti R, Sannino G. 2017. Unexpected covariant behaviour of the Aegean and Ionian seas in the period 1987–2008 by means of a nondimensional sea surface height index. J Geophys Res Ocean. 122:8020–8033. doi:10.1002/2017JC012983.

Rio MH, Pascual A, Poulain PM, Menna M, Barcelò B, Tintoré J. 2014. Computation of a new mean dynamic topography for the Mediterranean Sea from model outputs, altimeter measurements and oceanographic in situ data. Ocean Sci. 110:731–744. doi:10.5194/os-10-731-2014.

Roether W, Manca BB, Klein B, Bregant D, Georgopoulos D, Beitzel V, Kovačević V, Luchetta A. 1996. Recent changes in eastern Mediterranean deep waters. Sci. 271:333–335.

Shabrang L, Menna M, Pizzi C, Lavigne H, Civitarese G, Gačić M. 2016. Long-term variability of the southern Adriatic circulation in relation to North Atlantic oscillation. Ocean Sci. 12(1):233–241. doi:10.5194/os-12-233-2016.

Simoncelli S, Fratianni C, Pinardi N, Grandi A, Drudi M, Oddo P, Dobricic S. 2014. Mediterranean Sea physical reanalysis (MEDREA 1987–2015) (Version 1). [Data set]. Copernicus Monitoring Environment Marine Service (CMEMS). doi:10.25423/medsea_reanalysis_phys_006_004.

Simoncelli S, Korres G, Pinardi N, Fratianni C, Clementi E, Tintoré J in von Schuckmann, et al. 2016. Mediterranean sea. The Copernicus marine environment monitoring service ocean state report. J Oper Ocean. 9(sup2):s235–s320. doi:10.1080/1755876X.2016.1273446.

Simoncelli S, Pinardi N, Fratianni C, Dubois C, Notarstefano G in von Schuckmann et al. 2017. Water mass formation processes in the Mediterranean Sea over the past 30 years. The Copernicus marine environment monitoring service ocean state report. J Oper Oceanogr.

Section 4.6. 'Silent' storm surge extremes in the western Baltic Sea on 4 January 2017

Gräwe U, Burchard H. 2012. Storm surges in the western Baltic Sea: the present and a possible future. Clim Dyn. 39:165. doi:10.1007/s00382-011-1185-z.

Kystdirektoratet. 2018. 'Højvandstatistikke 2017' Miljø – og Fødevareministeriet.

Madsen KS, Sørensen CS, Schmith T, Nielsen JW, Knudsen P. 2017. Determining storm surge return periods: the use of evidence of historic events. Abstract from International WCRP/IOC Conference 2017: Regional Sea Level Changes and Coastal Impacts, New York, United States.

Sztobryn M, Stigge H-J, Wielbińska D, Weidig B, Stanisławczyk I, Kańska A, Krzysztofiak K, Kowalska B, Letkiewicz B, Mykita M. 2005. Storm surges in the southern Baltic Sea (western and central Parts). Berichte des Bundesamtes für Seeschifffahrt und Hydrographie Nr. 39 / 2005, pp. 75.

Wolski T, Winiewski B, Giza A, Kalkowska H, Boman H, Grabbi-Kaiv S, Hammarklint T, Jürgen Holfort L. 2014. Extreme sea levels at selected stations on the Baltic Sea coast. Oceanologia. 56(2):259–290.

Section 4.7. The 2017 coastal El Niño

Dee DP, Uppala SM, Simmons AJ, Berrisford P, Poli P, Kobayashi S, Andrae U, Balmaseda MA, Balsamo G, Bauer P, et al. 2011. The ERA-interim reanalysis: configuration and performance of the data assimilation system. Quart J R Meteorol Soc. 137:553–597.

Echevin V, Colas F, Espinoza-Morriberon D, Vasquez L, Anculle T, Gutierrez D. 2018. Forcings and evolution of the 2017 coastal El Niño Off northern Peru and Ecuador. Front Mar Sci. 5:367. doi:10.3389/fmars.2018.00367.

Fraser B. 2017. Surprise El Niño causes devastation but offers lessons for ecologists. Nature. 544:405.

Garreaud RD. 2018. A plausible atmospheric trigger for the 2017 coastal El Niño. Int J Climatol. doi:10.1002/joc.5426.

Gasparin F, von Schuckmann K, Desportes C, Sathyendranath S, Prado S, Greiner E, Dubois C. 2017. The 2015–2016 El Niño southern oscillation, in Copernicus marine service ocean state report. J Oper Oceanogr. 11(sup1):s1–s142. doi:10.1080/1755876X.2018.1489208.

Guilyardi E, Wittenberg A, Fedorov A, Collins M, Wang C, Capotondi A, van Oldenborgh GJ, Stockdale T. 2009. Understanding El Niño in ocean-atmosphere general circulation models: progress and challenges. Bull Am Meteorol Soc. 90:325–340.

Pennington JT, Mahoney KL, Kuwahara VS, Kolber DD, Calienes R, Chavez FP. 2006. Primary production in the eastern tropical Pacific: a review. Prog Oceanogr. 69(2–4):285–317.

Ramírez IJ, Briones F. 2017. Understanding the El Niño Costero of 2017: the definition problem and challenges of climate forecasting and disaster responses. Int J Disaster Risk Sci. 8:489. doi:10.1007/s13753-017-0151-8.

Takahashi K, Martínez AG. 2017. The very strong coastal El Niño in 1925 in the far-eastern Pacific. Clim Dyn. 52:7389–7415.

Wang C, Deser C, Yu J-Y, DiNezio P, Clement A. 2017. El Niño and southern oscillation (ENSO): a review. Coral reefs of the eastern tropical Pacific: persistence and loss in a dynamic environment. In: Glynn PW, Manzello DP, Enoch IC, editors. Coral reefs of the world. Vol. 8. Springer; p. 85–106. doi:10.1007/978-94-017-7499-4_4.